# Discovery of pathogen virulence and plant defense mechanisms by proximity labelling

Camille-Madeleine Szymansky

A thesis submitted to the University of East Anglia
for the degree of Doctor of Philosophy

The Sainsbury Laboratory

March 2025

registration number: 100297364

**Abstract**

Plants detect pathogens through nucleotide-binding leucine-rich repeat (NLR) immune receptors, which activate effector-triggered immunity (ETI) after recognizing pathogen effectors. NLRs are classified into TIR NLRs (TNL), coiled-coil NLRs (CNL), and RPW8-like NLRs (RNL), and can function independently or in pairs, specializing in sensing pathogen effectors (sensor NLRs) or activating immune signalling (executor/helper NLRs). TNLs rely on EDS1, SAG101, and PAD4 for immune response activation, with the helper RNLs NRG1 and ADR1. In Solanaceous plants, many sensor CNLs depend on NRCs for immune signalling. Thus, plant immune responses involve complex protein-protein interactions (PPIs) in pathogen recognition and defense activation. This study aimed to explore these interactions using TurboID-based proximity labelling, which offers higher sensitivity for identifying PPIs compared to traditional approaches.

The first part of this work optimized TurboID for capturing effectors that interact with TurboID-tagged host proteins during native infection (Chapter 3). This knowledge was then applied to capture two previously reported *Phytophthora infestans* effectors, AVRamr1 and AVRamr3, recognized by the sensor CNLs Rpi-amr1 and Rpi-amr3 from *Solanum americanum*, respectively (Chapter 4). Additionally, we captured *Albugo candida* CCG effectors recognized by the sensor TNL WRR4A from *Arabidopsis thaliana*, identifying two novel effectors, CCG14 and CCG41, which had not been previously reported (Chapter 4). *A. candida* is particularly effective at suppressing TNL-mediate immunity. Therefore, we tested TurboID's ability to capture effectors targeting EDS1 signalling hubs downstream of TNLs, identifying CCG82, which may interfere with the EDS1-PAD4-ADR1 complex (Chapter 5). Lastly, TurboID captured the transient interaction between sensor CNLs and helper NRCs, shedding light on their dynamic communication (Chapter 6).

This work demonstrates TurboID's utility in enhancing our understanding of plant-pathogen interactions and establishes a foundation for future effector discovery.

## Table of contents

## List of tables

## List of figures

## List of supplementary figures

## List of appendices



## Acknowledgements

I am truly grateful to my two supervisors, Prof. Jonathan Jones and Dr. Frank Menke, for giving me the opportunity to conduct my PhD research under their supervision. I would like to thank them for their continued support, guidance, and for critically revising my work, which has helped me become a skilled and thoughtful scientist.

Thank you to the Norwich Research Park Doctoral Training Partnership (NRPDTP) for the opportunity to carry out my PhD at The Sainsbury Laboratory (TSL).

A huge thank you to my postdoctoral supervisors, Dr. Hee-Kyung Ahn and Dr. Jianhua Huang, for providing me with training on experimental protocols, as well as daily advice and support. Their mentorship helped me develop both my research ideas and technical skills.

Thank you to the Proteomics team, particularly Paul Derbyshire, for processing all my mass spectrometry samples.

I would also like to thank past and present members of Jonathan Jones' lab for their continued support in the lab, feedback on my research project, and for engaging in science-related discussions. In particularly, I would like to thank Dr. Joanna Feehan, Dr. Sophie Johnson, Renzo Villena Gaspar and Yordan Dolaptchiev.

Thank you also to the TSL students, the TSL community, and the support staff for making TSL such an amazing and special place to thrive. A special thanks to the horticultural services, particularly Timothy Wells, for taking care of my plants, and to the transformation team, especially Aleksandra Wawryk-Khamdavong, for generating all the Arabidopsis transformation lines for me. Also, thanks to Sara Perkins for her help with the BASTA spraying of my many transgenic lines.

I would also like to thank my previous supervisors, Dr. Clare Gough, with whom I did my first plant-microbe research project, and Dr. Charlotte Seal, with whom I published my first-author publication.

Thank you to my mother, Nathalie, for her love and encouragement in pursuing my goals. Without her, I probably wouldn't have accomplished so much in my life, including this PhD.

## Funding

This work was supported by the Biotechnology and Biology Sciences Research Council (BBSRC), the Norwich Research Park Doctoral Training Partnership (NRPDTP), and The Sainsbury Laboratory (TSL).

# Chapter 1

General introduction

# 1. General introduction

## 1.1 Plant defense mechanisms

Plants have evolved a dynamic and innate set of defense mechanisms to protect themselves against pathogenic organisms. The first line of defense consists of physical barriers, such as the cuticle and the plant cell wall (Hamann, 2012, Yeats and Rose, 2013), along with constitutive chemical defenses in the form of antimicrobial secondary metabolites called phytoanticipins (Piasecka et al., 2015, Vanetten et al., 1994). However, many fungal pathogens can penetrate the plant epidermis by mechanical rupture, often through the formation of an appressorium or by secreting a variety of plant cell wall-degrading enzymes (Mendgen et al., 1996). In contrast, bacteria typically enter the plant through natural openings, such as stomata (Melotto et al., 2008). Additionally, wounds caused by environmental conditions, pests, or herbivores provide alternative routes of entry for microbial pathogens. Once pathogens breach these pre-existing barriers, they must then contend with a second line of defense, the plant's immune system (Dodds and Rathjen, 2010, Jones and Dangl, 2006).

Plants have cell surface immune receptors localised to the plasma membrane called pattern recognition receptors (PRR), typically receptor like-kinases (RLKs) and receptor like-proteins (RLPs). These receptors can detect pathogen- or microbe-associated molecular patterns (PAMPs or MAMPs). PAMPs/MAMPs are often relatively invariant and well-conserved molecules that are released by microbial organisms into the environment. When PRRs detect PAMPs/MAMPs, they initiate a series of physiological responses in the plant cell, including burst of calcium ($Ca^{2+}$) and reactive oxygen species (ROS), ion fluxes, activation of mitogen-activated protein kinases (MAPKs), production of inducible antimicrobial compounds called phytoalexins (Paxton, 1981), cell wall thickening, and callose deposition. These events comprise pattern-triggered immunity (PTI) (Wu et al., 2014).

However, some pathogens can overcome this initial immune response by injecting virulence factors, called effectors, into the host cell cytosol. For bacteria, this is achieved through a needle-like structure known as the type-III secretion system (T3SS) (Cunnac et al., 2009). For filamentous pathogens, external appendages called haustoria, which are intimately associated with the host cell plasma membrane, facilitate the transfer of effectors (Catanzariti et al., 2007). The plant's recognition of these pathogenic proteins is mediated by intracellular immune receptors known as

nucleotide binding, leucine-rich repeats (NLR) proteins (Jacob et al., 2013, Wu et al., 2017). The detection of these effectors activates a second immune response, known as the effector-triggered immunity (ETI) (Cui et al., 2015). ETI triggers resistance (R)-gene-mediated defense, often leading to a hypersensitive response (HR), which involves the apoptosis of infected host cells to prevent pathogen spread to neighbouring cells (Greenberg and Yao, 2004).

Nevertheless, pathogens can evolve new, unrecognized effectors or modify existing ones to suppress ETI and successfully colonize the plant. This ongoing interaction is often described as a multi-level evolutionary arms race between plants and pathogens (Dodds and Rathjen, 2010, Jones and Dangl, 2006, Kanzaki et al., 2012). It is important to note that while PTI and ETI are often portrayed as two independent cellular processes, the distinction between them is increasingly blurred (Ngou et al., 2021, Thomma et al., 2011, Yuan et al., 2021).

### 1.2 NLR-mediated perception and response to pathogens

Once a pathogen is recognized by the plant, the activation of defense mechanisms involves a complex network of signalling pathways (Bigeard et al., 2015), many of which remain unclear, particularly in the case of the NLR-initiated ETI response. One possible reason for the lack of identified ETI signalling proteins is that the pathway is short.

Typical NLRs feature a variable N-terminal domain, which plays a key role in receptor activation and signalling, a central nucleotide-binding, apoptotic protease activating factor 1 (APAF-1), R-protein and cell death 4 (CED-4) domain (NB-ARC), which has an ATPase homology and functions as an ATP/ADP-exchange molecular switch (van der Biezen and Jones, 1998a, Van Ooijen et al., 2008), and a C-terminal leucine-rich repeats (LRR) domain that is involved in the direct or indirect recognition of pathogen effectors. NLRs are classified into three groups based on the architecture of their N-terminal domain (Shao et al., 2016): the toll/interleukin-1 receptor/resistance (TIR) NLRs (abbreviated TNL) which can function in various subcellular localizations, including the nucleus; the coiled-coil (CC) NLRs (abbreviated CNL) which, despite primarily functioning in association with the plasma membrane (Bentham et al., 2018), exhibit a vast and previously unsuspected diversity (Contreras et al., 2023a); and the resistance to powdery mildew 8 (RPW8)-like coiled-coil NLRs (abbreviated RNL) which support the function of many NLRs and therefore are often referred to as

helper NLRs (Feehan et al., 2020, Jubic et al., 2019). The role of helper NLRs is discussed in section 1.3.1.

NLRs can detect effectors in various ways. One mechanism involves direct interaction between the LRR domain of NLRs and the effectors, known as the “ligand-receptor model” (Catanzariti et al., 2010, Jia et al., 2000, Krasileva et al., 2010). Alternatively, NLRs can indirectly sense effectors by acting as guardians of host proteins targeted by effectors, as described by the “guard model” (Dangl and Jones, 2001, van der Biezen and Jones, 1998b). According to the guard hypothesis, NLRs recognize modifications to or perturbation of a host protein which typically plays a crucial role in defense and may therefore be repeatedly targeted by pathogen effectors. This strategy allows the plant to optimize a limited immune receptor repertoire. For example, the Arabidopsis RPS2 and RPM1 immune receptors monitor the status of the RIN4 protein, which is targeted by multiple different bacterial type III effectors. When RIN4 is cleaved by the AvrRpt2 protease, RPS2 activates immune responses (Axtell and Staskawicz, 2003, Mackey et al., 2003). In contrast, RPM1 triggers immunity upon detecting hyperphosphorylation of RIN4 by AvrRpm1, which disrupts its phospho-switch status (Mackey et al., 2002), as well as rhamnosylation of RIN4 by AvrB (Peng et al., 2024). Another mechanism is the “decoy model”, in which NLRs protect host proteins that have evolved to resemble those targeted by effectors. These proteins no longer serve indispensable defense functions but instead function solely to trap the effectors (Lewis et al., 2013, Ntoukakis et al., 2014, van der Hoorn and Kamoun, 2008). The ZAR1 immune receptor monitors the status of multiple RLCK-like proteins *via* intermediate pseudokinases, such as RKS1. For instance, the *Xanthomonas campestris* effector AvrAC uridylylates PBL2, which acts as a decoy for the true AvrAC target, BIK1 (Wang et al., 2015). Subsequently, the pseudokinase RKS1, in conjunction with ZAR1, interacts with the modified PBL2, leading to the activation of ZAR1 (Wang et al., 2019).

Some NLRs function independently in effector recognition and the execution of defense signalling. The activation of these so-called singleton NLRs, such as ZAR1 (CNL), ROQ1 (TNL), and RPP1 (TNL), upon detection of their cognate effectors, leads to their oligomerization into a wheel-like multimeric complex known as a resistosome (Ma et al., 2020, Martin et al., 2020, Wang et al., 2019). This oligomerization process usually involves the exchange of ADP for ATP at the NB domain of NLR proteins, which triggers the association of NB domains with one another, bringing their N-terminal signalling domains into proximity and allowing the initiation of signalling events. Once the N-terminal TIR domains are close to one another upon oligomerization, this activates an intrinsic

nicotinamide adenine dinucleotide hydrolases (NADases) activity in the TIR domain that hydrolyses NAD+ or ATP into small signalling molecules that can be detected by downstream signalling partners (Huang et al., 2022). RPP1 and Roq1 oligomerize to form tetramers (Ma et al., 2020, Martin et al., 2020), while ZAR1 constitutively forms a heterodimer with one of multiple pseudokinases, such as RKS1, which then binds to uridylylated PBL2, leading to the formation of ZAR1-RKS1-PBL2 complexes that oligomerize into a pentamer (Wang et al., 2019). These resistosomes harbour a funnel-shaped structure at their N-termini that can disrupt the plasma membrane integrity, creating cation channels and enabling $Ca^{2+}$ influx, inducing the expression of genes important for ETI and ultimately triggering HR (Bi et al., 2021).

Finally, some NLRs function in pairs, with one NLR acting as a sensor NLR that contains an integrated domain (ID) at its C-terminus, mimicking the effector target, and the other NLR acting as an executor NLR that converts effector recognition into defense activation. This is referred to as the "integrated decoy model" (Cesari et al., 2014). The first identified chromosomally adjacent Arabidopsis TNL gene pair, *RPP2A* and *RPP2B*, is required for conferring resistance to downy mildew (Sinapidou et al., 2004). Two of the most studied NLR-ID pairs are the Arabidopsis TNL pair RPS4/RRS1, in which RRS1 contains an integrated WRKY transcription factor domain that detects two unrelated bacterial effectors, AvrRps4 and PopP2, from *Pseudomonas syringae* and *Ralstonia solanacearum*, respectively (Le Roux et al., 2015, Sarris et al., 2015); and the rice CNL pair RGA4/RGA5, in which RGA5 carries an integrated HMA domain that interacts with *Magnaporthe orizae* effectors AVR-Pia and AVR1-CO39 (Cesari et al., 2013). It has not yet been shown whether NLR pairs oligomerize upon effector detection, like singleton NLRs.

Together, these mechanisms highlight the diverse strategies employed by NLRs to recognize and respond to pathogen effectors, ultimately orchestrating complex defense responses to protect plants from infection.

## 1.3 Additional signalling components in plant immunity: linking perception to defense activation

### 1.3.1 The role of helper NLRs downstream of sensor NLRs in plant defense

In addition to the sensor and executor NLRs, there are helper NLRs, and many NLR-mediated immune responses depend on their presence (Bonardi et al., 2011). Helper RNLs act as downstream

signalling hubs, enabling a wide range of sensor NLRs to activate subsequent signalling events. Two major RNL families in Arabidopsis and many other plants are the ACTIVATED DISEASE RESISTANCE 1 (ADR1) family (Dong et al., 2016), and the N REQUIRED GENE 1 (NRG1) family (Castel et al., 2019, Peart et al., 2005). These families belong to a small subclass of CNLs and carry a RPW8-like CC domain at their N-termini, which is related to the resistance protein RPW8 (Li et al., 2018, Xiao et al., 2001). Interestingly, homology has been observed between the RPW8 domain and the four-helical bundle (4HB) domain in the mammalian mixed-lineage kinase domain-like (MLKL) protein, as well as the fungal HeLo-like (HELL) domain (Daskalov et al., 2016). These domains play a role in pore-formation in the plasma membrane following aggregation, ultimately leading to cell death (Hildebrand et al., 2014, Seuring et al., 2012). Indeed, it has been shown that once activated, NRG1 and ADR1 oligomerize to form $Ca^{2+}$ influx channels at the plasma membrane (Feehan et al., 2023, Jacob et al., 2021, Wang et al., 2023), resembling the proposed pore-forming activity of the ZAR1 CC domain or the animal MLKL cation channel (Cai et al., 2014, Chen et al., 2014, Wang et al., 2019). In Arabidopsis, there are four paralogs of ADR1: ADR1, ADR1-L1, ADR1-L2, and the N-terminally truncated ADR1-L3; and three paralogs of NRG1: NRG1.1 (or NRG1-A), NRG1.2 (or NRG1-B), and N-terminally truncated NRG1.3 (or NRG1-C). Members of the NRG1 family are essential for TNL but not CNL receptor responses, whereas ADR1 family members function redundantly in signalling downstream of both TNLs and some CNLs (Wu et al., 2019). NRG1 and ADR1 functions are unequally redundant (Saile et al., 2020). Finally, NRG1 and ADR1 are essential for transcriptional reprogramming during TNL-mediated immunity, as 86% of genes induced 4 hours after AvrRps4 recognition are not activated in the *helperless* mutant or in the *eds1* mutant (Saile et al., 2020).

In Solanaceae, there is an additional class of helper NLRs, known as NLRs-required for cell death (NRCs), which support the function of many sensor CNLs (Wu et al., 2017). Several NRCs can either be specific or redundantly support the function of overlapping sets of sensor CNLs. For example, two CNLs, Rpi-amr1 and Rpi-amr3, from *Solanum americanum*, a wild relative of the potato that is resistant to blight, confer resistance to *Phytophthora infestans* in cultivated potatoes and are NRC-dependent (Witek et al., 2016, Witek et al., 2021). However, Rpi-amr1 can signal through NRC2 or NRC3, but not NRC4 (Witek et al., 2021), while Rpi-amr3 can signal through NRC2, NRC3 or NRC4 (Lin et al., 2022). The N-terminal region of NRCs carries a conserved MADA motif that is functionally exchangeable with the matching N-terminal region of ZAR1, which undergoes a conformational switch during resistosome activation (Adachi et al., 2019a). In contrast, sensor CNLs that depend on NRCs lack the MADA motif, suggesting that this motif has degenerated in sensor CNLs over

evolutionary time. It has been shown that members of the NRC family, NRC2 and NRC4, also oligomerize upon activation (Ahn et al., 2023, Contreras et al., 2023b). Notably, they form hexamers instead of pentamers, forming $Ca^{2+}$ channels, and the sensor CNLs are not incorporated into the NRC oligomers (Liu et al., 2024a, Ma et al., 2024, Madhuprakash et al., 2024). The precise molecular mechanisms by which activated sensor CNLs translate into activated helper NRCs, and consequently trigger disease resistance, remain to be determined.

### 1.3.2 Beyond NLRs: the role of lipase-like proteins in plant immunity

The RNLs function in concert with a family of EP domain (for EDS1 and PAD4-defined, (Feys et al., 2001)) containing signalling partners. This highly conserved C-terminal EP domain, shared by ENHANCED DISEASE SUSCEPTIBILITY 1 (EDS1), SENESCENCE ASSOCIATED GENE 101 (SAG101), and PHYTOALEXIN DEFICIENT 4 (PAD4) (Wiermer et al., 2005), is unique to plants and occurs only in conjunction with a lipase domain, thus defining the EDS1 family (Wagner et al., 2013). Both NRG1 and ADR1 proteins require the lipase-like protein EDS1 for function (Falk et al., 1999, Qi et al., 2018). EDS1 forms spatially distinct complexes with the two related lipase-like proteins SAG101 or PAD4 to mediate plant immunity (Cui et al., 2017, Feys et al., 2001, Feys et al., 2005, Gantner et al., 2019, Wagner et al., 2013). The EDS1-PAD4 complex localizes to both the nucleus and cytosol, while the EDS1-SAG101 complex localizes exclusively to the nucleus (Feys et al., 2005, García et al., 2010). Helper RNLs and lipase-like proteins form two distinct signalling complexes. In Arabidopsis, the EDS1-SAG101-NRG1 module is involved in eliciting host cell death, while the EDS1-PAD4-ADR1 module stimulates the accumulation of the plant hormone salicylic acid (SA), which is crucial for basal and systemic immunity, thereby restricting bacterial growth (Lapin et al., 2019). *At*EDS1-*At*SAG101 cannot signal in conjunction with *Nb*NRG1, indicating a molecular incompatibility between signalling components from different species. As a result, HR in the *epss N. benthamiana* mutant can only be triggered when alleles of EDS1, SAG101 and NRG1, all derived from Arabidopsis, are co-expressed (Lapin et al., 2019).

Conserved residues at the C-terminal EP domain (EPD) surfaces of PAD4 and SAG101, surrounding a cavity formed with EDS1, contribute to the function of EDS1 heterodimers and their association with the respective helper RNLs ADR1 and NRG1. These residues also play a role in recruiting other immune-related proteins upon NLR resistosome formation (Dongus et al., 2022). The N-terminal TIR domains of NLR resistosomes act as NADases releasing small molecules that were proposed to be

the signal perceived by the EPD surfaces of EDS1-PAD4 and EDS1-SAG101 heterodimers, thereby activating the helper RNLs ADR1 and NRG1, respectively (Horsefield et al., 2019, Huang et al., 2022, Jia et al., 2022, Wan et al., 2019). Recently, the molecular structures of both the EDS1-SAG101-NRG1 and the EDS1-PAD4-ADR1 signalling complexes have been resolved, revealing the nesting of TIR-catalyzed small molecules within the EPD cavity as predicted, which triggers conformational changes that lead to the recruitment of helper RNLs (Huang et al., 2025, Xiao et al., 2025, Yu et al., 2024).

### 1.4 Evasion of NLR-mediated defense mechanisms by pathogens

Pathogens introduce scores to hundreds of virulence factors, known as effectors, into plant cells to manipulate host cell biology. These effectors are often functionally redundant and can target and disrupt any phase of the plant immune response, thereby facilitating infection. In contrast, hosts only need to detect a single effector to mount a resistance response. Most plant *R* genes encode NLR proteins, while effector genes encode proteins with diverse biochemical functions.

NLRs are the primary sentinels for detecting intracellular effectors. Effectors recognized by NLRs are often referred to as “avirulence (AVR) effectors”, as their detection triggers ETI-mediated defense mechanisms that restrict pathogen growth (Cui et al., 2015). The robust immune response provided by NLRs exerts strong selection pressures on pathogens, driving host-pathogen coevolution. Pathogens that adapt to their hosts avoid or impair ETI through various strategies, including modification of *AVR* genes, acquisition of epistatic effectors, and modulation of plant’s guardees or decoys (Arnold and Jackson, 2011, Raffaele and Kamoun, 2012). The *AVR* gene repertoire of pathogens is frequently subject to change, with many effector-encoding genes located in highly plastic, repeat-rich genomic regions, enabling rapid evolution (Raffaele et al., 2010).

One or two amino acid substitutions can be enough to allow effector variants to escape recognition by NLRs. For example, a single amino acid change in the *Hyaloperonospora arabidopsidis* (*Hpa*) effector ATR1-Cala2, located at the centre of the interaction interface, is sufficient to disrupt its binding with the immune receptor RPP1-WsB, allowing it to escape RPP1 recognition (Chou et al., 2011). In another case, a single amino acid substitution in the nuclear localization signal of the *Hpa* effector RxL103 abolishes its accumulation in the nucleus. By altering its subcellular localization, this prevents recognition by the immune receptor RPP4 (Asai et al., 2018). Larger numbers of substitutions can also cause a recognized effector to become unrecognized. For instance, the *P.*

*infestans* effector AVR2 targets the host phosphatase BSU-LIKE PROTEIN 1 (BSL1), forming a complex that is recognized by the immune receptor R2 in *Solanum demissum*. An AVR2 variant, called "AVR2-like", contains 13 amino acid polymorphisms in the mature protein. Although AVR2-like still binds to BSL1, this complex can no longer be detected by R2 (Gilroy et al., 2011, Saunders et al., 2012).

Additionally, pathogens can avoid recognition by NLRs by modifying the expression of *AVR* genes. In virulent isolates of *Magnaporthe oryzae*, a transposon has inserted itself into the promoter region of *AVR-Pita1*, stopping its transcription (Kang et al., 2001, Zhou et al., 2007). *Avrvnt1* is silenced in *P. infestans* strains that overcome Rpi-vnt1-mediated resistance (Pais et al., 2018). Moreover, the expression of *AVR* genes can also be regulated by epigenetic modifications. The virulent isolate of *P. sojae* (P6496) harbours elevated methylation of histone H3 at the *Avr1b* locus, which reduces its expression (Wang et al., 2020).

Alternative strategies to evade the activation of ETI-mediated immune responses include the acquisition of epistatic effectors that bind to or regulate NLRs or other AVR effectors. The *Pseudomonas syringae* acetyltransferase type III effector HopZ3 binds to the AvrB3-RPM1 immune receptor complex and, through its acetylation activity, may inactivate the entire effector-immune complex (Lee et al., 2015). Moreover, the RIN4 protein, which is targeted by several effectors and guarded by two NLRs, RPS2 and RPM1, is also acetylated by HopZ3, suppressing RPM1-mediated resistance by interfering with RIN4's phosphorylation (Lee et al., 2015). Additionally, the *Leptosphaeria maculans*, the causal agent of oilseed rape stem canker, effector AvrLm4-7 is structurally similar to the AvrLm3 and AvrLm5-9, and can suppress their recognition by the immune receptors Rlm3 and Rlm9, respectively (Lazar et al., 2022).

Finally, some effectors have been shown to interfere with NLR regulatory elements or subvert immune signalling components. For example, an important regulator of NLR accumulation and activation, SUPPRESSOR OF G2 ALLELE OF skp1 (SGT1), interacts with the *Ralstonia solanacearum* type III effector RipAC, which blocks its phosphorylation, leading to attenuated SGT1-dependent ETI responses (Yu et al., 2020). Furthermore, a co-chaperone of SGT1, HEAT SHOCK CHAPERONE 90 (HSP90), which is required for the maturation of several NLRs, is targeted by the *P. syringae* type III effector HopBF1. HopBF1 mimics an HSP90 substrate, phosphorylates HSP90, and thereby inactivates it (Lopez et al., 2019). Pathogens have also convergently evolved effectors that target the NRC helper NLRs, which form a partially redundant signalling network downstream of sensor CNLs

in the Solanaceae, increasing the complexity and resilience of the plant immune system. Specifically, two effectors, the oomycete AVRcap1b and the nematode SPRYSEC15 effectors, were found to counteract the function of NRC2 and NRC3, thereby preventing the signal transmission of effector-activated sensor CNLs through these two NRCs (Derevnina et al., 2021). Surprisingly, despite the fact that the lipase-like proteins EDS1, SAG101, and PAD4 constitute a central signalling node linking TNL activation to the induction of resistance pathways, and are broadly conserved in plant genomes, making them ideal targets for effectors, only recently have a few effectors been identified that interfere with these key signalling proteins as a virulence strategy (Liu et al., 2024b, Qi et al., 2024).

Pathogens have evolved to evade plant immune responses through strategies like modifying effector proteins, altering *AVR* gene expression, and interfering with immune components like NLRs, boosting virulence and infection. However, the specific host targets and mechanisms used by many effectors remain unclear, as does how pathogens coordinate their effector repertoires to target key plant pathways.

### 1.5 Uncovering protein-protein interactions through proximity labelling

Protein-protein interactions (PPIs) are crucial to nearly all cellular processes, including the activation of plant defense mechanisms. Given the central role of proteins in plant-pathogen interactions, developing novel molecular techniques to identify protein interactors within various complexes is essential for their subsequent functional characterization.

Traditional methods for identifying PPIs include yeast-two-hybrid (Y2H) assays and biochemical techniques such as co-immunoprecipitation (Co-IP) and affinity purification (AP) coupled with mass-spectrometry (MS) (Struk et al., 2019). However, these techniques have notable limitations. The Y2H approach requires generation of cDNA libraries which can be labour-intensive and expensive and is performed in the nucleus of a heterologous single-cell eukaryotic organism, yeast. Biochemical approaches, such as Co-IP and AP-MS, on the other hand, are typically limited to detecting high-affinity interactions and often fail to capture weak or transient interactions unless paired with cross-linking (Chu et al., 2018). They also exhibit low efficiency in identifying interactors of membrane-associated proteins due to their low solubility and are not well-suited for low-abundance proteins. In addition, these conventional techniques are not representative of true cellular environments because they are conducted *in vitro* or under non-physiological conditions.

Enzyme-catalyzed proximity labelling (PL) methods have been developed to address some of the limitations of traditional PPI identification techniques. These approaches utilize an engineered enzyme, such as a biotin ligase, fused to a target protein of interest (POI) to catalyze the biotinylation of endogenous proteins in a proximity-dependent manner (Figure 1.1). In the presence of ATP and biotin, the biotin ligase generates reactive biotinyl-5'-AMP (bio-AMP), the active form of biotin, which covalently binds to nearby primary amines present on lysine residues of proteins within an estimated radius of 10 nanometres, as demonstrated in a study on the nuclear pore complex (Kim et al., 2014a), and up to 35 nanometres (May et al., 2020). The biotinylated proteins are subsequently isolated using streptavidin-based affinity purification and enriched under stringent washing conditions for identification by MS. PL techniques reveal unique spatial and temporal protein interaction networks by capturing weak, transient or hydrophobic PPIs in their native cellular environment, thereby providing deeper insights into specific biological processes (Gingras et al., 2019).

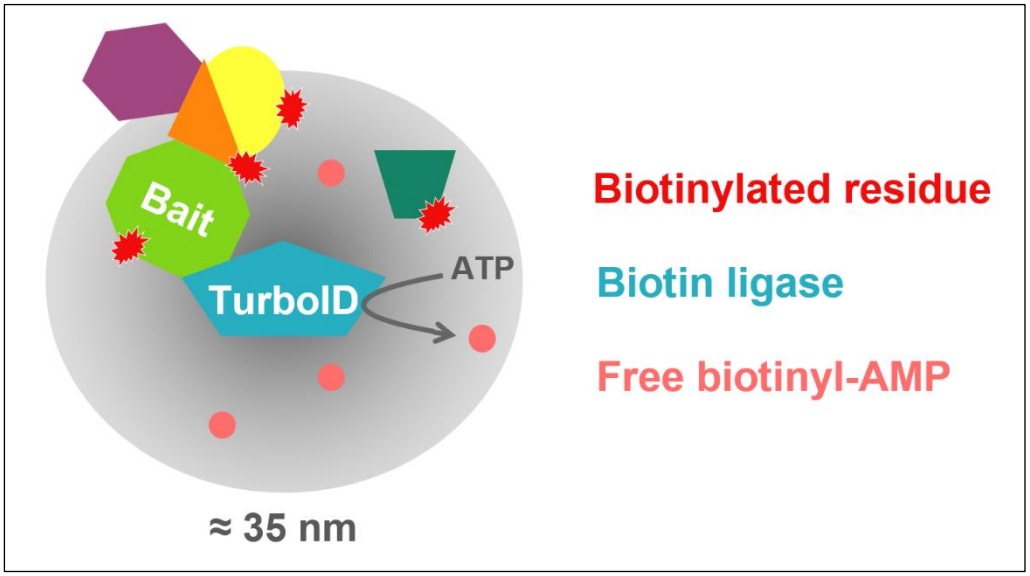


**Figure 1.1 TurboID-based identification of protein-protein interactions.**

TurboID enables the capture of transient or weak protein-protein interactions *in vivo* and at room temperature. In the presence of ATP and biotin, TurboID releases reactive free biotinyl-5'-AMP, which diffuses within a radius of up to 35 nm around the enzyme. Proteins that come in proximity with a TurboID-tagged bait are biotinylated, including direct and indirect interactors as well as proteins randomly passing by. The enzymatic reaction occurs within approximately 10 minutes, after which biotinylated proteins can be retrieved using streptavidin-based affinity purification. It is important to note that this approach reflects close proximity but does not confirm direct interactions.

Various PL enzymes have been developed, each with distinct advantages and disadvantages (Samavarchi-Tehrani et al., 2020). Two commonly used PL enzymes are engineered soybean ascorbate peroxidase (APEX) (Lam et al., 2015, Rhee et al., 2013), and *Escherichia coli* biotin ligase called BirA (Bifunctional ligase/repressor A) made by a point mutation (R118G) to generate BirA* (known as BioID) (Li et al., 2017b, Roux et al., 2012). Arginine (R) at position 118 plays a role in interacting with the biotin molecule, and replacing it with glycine (G), a smaller amino acid with a non-polar side chain, reduces steric interactions and lowers the affinity for biotin and bio-AMP. This mutation (R118G) improves the enzyme's efficiency in catalyzing the attachment of biotin to target proteins (Choi-Rhee et al., 2004). APEX offers rapid tagging kinetics, requiring only about one minute or less for labelling. However, its reliance on hydrogen peroxide ($H_2O_2$) as a substrate introduces toxicity, making it unsuitable for PL in plants. In contrast, BioID uses biotin as a substrate, which is non-toxic, but it requires a significantly longer incubation time (18-24 h) and higher temperature (37 °C) for efficient labelling. These conditions are suboptimal for *in planta* studies, limiting BioID's applicability in plant systems (Conlan et al., 2018, Khan et al., 2018, Lin et al., 2017). To address these

limitations, two improved variants of BioID, TurboID (35 kDa) and its truncated version miniTurbo (28 kDa), were developed through directed evolution of BirA (Branon et al., 2018). In this study, the authors found that R118S is approximately two-fold more active than R118G under identical conditions, and therefore selected R118S as their starting template for evolution. TurboID contains 15 mutations, while miniTurbo contains 13 mutations, relative to wild-type BirA. These variants exhibit enhanced catalytic activity, enabling biotinylation within 10 minutes, as well as improved thermal stability, allowing them to function at lower, more physiologically relevant temperatures (e.g., room temperature, 25 °C). As a result, TurboID and miniTurbo combine the advantages of APEX (speed) and BioID (non-toxicity), making them powerful tools for studying protein interactions in fast and dynamic cellular processes without compromising cell viability.

Therefore, PL methods offer significant advantages over traditional PPI techniques by capturing weak or transient protein interactions in their native cellular environment, which could provide deeper insights into plant defense mechanisms and pathogen virulence. The previous studies using TurboID in plant immunity are described in the introduction of Chapter 3.

## 1.6 Study aims and objectives

This project aimed to better understand pathogen virulence and the plant defense mechanisms involved in plant-pathogen interactions using enzyme-catalyzed proximity labelling. Proximity labelling enables the exploration of PPIs from a new perspective and achieves their detection with greater sensitivity than traditional approaches. Specifically, we aimed to investigate whether it would be possible to capture effectors during native infection, which would greatly facilitate effector discovery.

Chapter 3: The application of TurboID to better understand PPIs involved in plant-pathogen interactions was still in its infancy at the start of this project. One of the first tasks was to explore and identify experimental conditions that would allow us to successfully capture low-abundance proteins, such as effectors, despite the significant background noise generated by TurboID. This required optimization throughout the project to establish best practices.

Chapter 4: As a proof of concept, we aimed to capture two previously reported *Phytophthora infestans* effectors, AVRamr1 and AVRamr3, recognized by the sensor CNLs Rpi-amr1 and Rpi-amr3

from *Solanum americanum*, respectively. After further optimization, we successfully detected these effectors by mass spectrometry during native infection. We then captured *Albugo candida* CCG effectors recognized by the sensor TNL WRR4A from *Arabidopsis thaliana*, identifying two novel CCG effectors, CCG14 and CCG41, which had not been previously reported. These experiments demonstrated TurboID's ability to discover new effectors recognized by NLRs.

Chapter 5: The *Albugo*-Arabidopsis pathosystem offers an attractive model for studying broad-spectrum defense suppression by a biotrophic oomycete. *Albugo* species are highly effective at suppressing TNL-dependent immunity, and we hypothesized that they may have evolved effectors targeting TNL downstream signalling elements, such as EDS1. Using TurboID, we identified several CCG effectors, including CCG82, which AlphaFold2 predicts could potentially interfere with the EDS1-PAD4-ADR1 signalling complex by competing for ADR1 binding to PAD4. Additionally, the plant-proximal interactors of EDS1 identified in this experiment suggest its involvement in the host plant transcriptional and RNA processing machinery.

Chapter 6: Finally, the mode of communication between sensor CNLs and helper NRCs to activate plant immunity was unclear, particularly whether it would involve a transient interaction. TurboID enabled us to capture the interaction between sensor CNLs and helper NRCs, and we further attempted to characterize the dynamics of this interaction. Additionally, this exploration led us to hypothesize that the helper NRC2 could be phosphorylated, a hypothesis confirmed by mass spectrometry analysis. However, whether this post-translation modification plays a role in the interaction between sensor CNLs and helper NRCs remains to be determined.

# Chapter 2

## Materials and Methods

## 2. Materials and Methods

### 2.1 Golden Gate cloning

TSL Synbio has generated Golden Gate modules, which were used to generate the DNA constructs listed in Tables 4.1, 5.1, and 6.1. These constructs were employed for either transient expression assays in *N. benthamiana* and/or transformation into stable *A. thaliana* transgenic lines. The terminology of the various components used to assemble these constructs is also provided in the above-mentioned tables. Fusion of the TurboID enzyme (~ 35 kDa) to the C-terminal end of the target proteins is preceded by an eleven-amino acid linker, which may facilitate conformational rearrangements and prevent the TurboID fusion from interfering with the function of the bait proteins. Type IIS restriction enzymes were used to perform the DNA assembly reactions (Engler et al., 2008). The constructs were assembled following the protocol outlined below:

| | | |
|---|---|---|
| 30 s | 37 °C | |
| 3 min | 37 °C | |
| 4 min | 16 °C | ×35 |
| 5 min | 50 °C | |
| 5 min | 80 °C | |
| 1 min | 16 °C | |

The amount of acceptor plasmid used was 50-100 ng, with a 2:1 molar ratio of insert to acceptor. The reaction mixture included 0.5 µL of 20 U/µL of BpiI (BbsI) or BsaI (ThermoFisher), 1.5 µL of 10X Bovine Serum Albumin (BSA), 0.5 µL of 400 U/µL of T4 DNA ligase (NEB), and 1.5 µL of T4 ligase buffer (NEB) and water to a final volume of 10 µL. The resulting constructs were verified by generating digestion patterns using restriction enzymes other than BpiI (BbsI) or BsaI. For further confirmation, the constructs were analysed by Sanger sequencing to ensure the accuracy of the coding region of each protein of interest (POI). Finally, the constructs were transiently expressed in *N. benthamiana* to verify the protein sizes in kilodaltons (kDa).

## 2.2 Sanger sequencing of DNA

Sanger sequencing of the generated DNA constructs was performed by GENEWIZ. Pre-mixed reactions were prepared in distilled water ($dH_2O$) with 350 ng of plasmid DNA and 2.5 µL of 10 µM corresponding primer mixture, resulting in a final volume of 10 µL. The sequencing results were analysed using CLC Main Workbench software (version 20.0.4).

## 2.3 Bacterial transformation

Bacterial strains of *Erichia coli* (DH10β) were used for molecular biology, and *Agrobacterium tumefaciens* (GV3101:pMP90) for transformation in stable *A. thaliana* transgenic lines and/or transient expression in *N. benthamiana*. The *A. tumefaciens* GV3101:pMP90 strain harbours natural rifampicin antibiotic resistance and carries a nopaline-based Ti plasmid (pMP90), which contains a gentamycin resistance cassette for selectable antibiotic resistance. The *E. coli* DH10β strain harbours natural antibiotic resistance to streptomycin.

Electrocompetent *E. coli* cells were thawed on ice for 5-10 minutes before adding 0.5-1 µL of plasmid DNA. The resulting mixture was transferred into an ice-cool 1 mm gap electroporation cuvette. The cuvette was placed into a MicroPulser™ Electroporation Apparatus (Bio-Rad: 165-2100), and a single pulse of 1.8 kV was applied. The electrocompetent cells were then placed back on ice, resuspended in 200 µL of Lysogeny Broth (LB) liquid medium (L-media) [1% (w/v) tryptone, 0.5% (w/v) yeast extract, and 1% (w/v) sodium chloride, pH 7.0], and transferred to a 1.5 mL Eppendorf tube. The cells were incubated at 37 °C, shaking at 200-250 RPM for 20 minutes. Afterward, the cells were spread onto appropriate selection media on Petri dishes. The plates were incubated overnight (12-16 hours) at 37 °C to allow colony growth. For blue-white colony selection, when *LacZ* gene was present in the acceptor vector, 10 µL of 1M isopropyl β-D-1-thiogalactopyranoside (IPTG) and 20 µL of 50 mg/mL 5-bromo-4-chloro-3-indolyl β-D-galactopyranoside (X-gal) were added and spread onto selection plates.

Electrocompetent *A. tumefaciens* cells were prepared as described for electrocompetent *E. coli* cells, with the following modifications: the cells were incubated at 28 °C, shaken at 200-250 RPM for 20 minutes; and then placed in an incubator at 28 °C for 48 hours to allow colony growth.

To make glycerol stocks, single colonies were picked from selection plates and transferred to sterile 5 mL or 10 mL liquid L-media containing the appropriate antibiotic. The working concentrations of antibiotics used are listed below. The cultures were incubated at 37 °C for *E. coli* or 28 °C for *A. tumefaciens*, shaking at 200-250 RPM for 16-24 hours. After incubation, 700 µL of the culture solution was transferred to a 1.5 mL Eppendorf tube and combined with 700 µL of 60% sterile glycerol. The mixture was then stored at – 80 °C.

| | Working concentration (µg/mL) | |
|---|---|---|
| | *E. coli* | *A. tumefaciens* |
| Carbenicillin | 100 | 100 |
| Gentamicin | - | 20 |
| Kanamycin | 50 | 50 |
| Rifampicin | - | 50 |
| Spectinomycin | 50 | 50 |

## 2.4 Plasmid DNA isolation from *E. coli*

Single colonies were retrieved from selection plates and used to inoculate 10 mL sterile L-media containing the appropriate selection antibiotics. Cultures were grown overnight (12-16 hours) at 37 °C, shaking at 200-250 RPM. The cells were pelleted by centrifugation at 3,700 × g for 10 minutes. DNA was then purified using the Macherey-Nagel NucleoSpin® Plasmid Mini Kit (Ref: 740588.50) following the manufacturer's instructions. The concentration of plasmid DNA was measured using a Nanodrop™ spectrophotometer by measuring ultraviolet absorbance at 260 nm. Purified plasmids DNA were stored at – 20 °C.

## 2.5 Polymerase chain reaction

Polymerase chain reaction (PCR) was used to swap BpiI (BbsI) and BsaI restriction nucleotide sites in the different genes of interest without changing the resulting protein sequence, a process known as “gene domestication”. DNA oligonucleotide primers synthesized by Sigma-Aldrich were used for the PCR reactions. Lyophilized oligonucleotides were resuspended in water to a final concentration of 10 µM and stored at 4 °C. The Phusion high-fidelity DNA polymerase (ThermoFisher: 00975122) was used in 20 µL PCR reactions, which were run according to the following protocol:

| | | |
|---|---|---|
| 30 s | 98 °C | |
| 10 s | 98 °C | |
| 30 s | 56 °C | |
| 20 s/kb | 72 °C | ×30 |
| 5 min | 72 °C | |

For general PCR reactions, the Taq DNA polymerase (Qiagen: 163035150) was used in 20 µL PCR reactions, which were run according to the following protocol:

| | | |
|---|---|---|
| 3 min | 95 °C | |
| 30 s | 95 °C | |
| 30 s | 56 °C | |
| 1 min/kb | 72 °C | ×26/30 |
| 5 min | 72 °C | |

## 2.6 Agarose gel electrophoresis

Agarose gels for DNA electrophoresis were prepared using heated molecular biology grade agarose in TAE buffer, containing 40 mM Tris-acetate (pH 8.0) and 1 mM ethylenediaminetetraacetic acid (EDTA), to a final concentration of 1% (w/v). After the agarose solution cooled, ethidium bromide was added to a final concentration of 0.5 µg/mL. The molten agarose solution was poured into gel moulds with combs and allowed to cool at room temperature to facilitate agarose polymerization. DNA samples were mixed with 4 µL of 10X Orange G DNA Loading Buffer before being loaded into the gel. The GeneRuler 1kb Plus DNA Ladder (ThermoFisher: SM1331) was used as molecular weight marker, and 5 µL of the ladder was run alongside the DNA samples. Electrophoresis was carried out in TAE buffer, with an electrical current applied across the gel at 100-150 V. Finally, DNA bands were visualized using an ultraviolet transilluminator.

When necessary, DNA bands of interest were excised from the agarose gel using a scalpel on an ultraviolet trans-illuminator. DNA isolation and purification from the gel were performed using the Qiagen QIAquick® Gel Extraction Kit (Ref: 28704), following the manufacturer's instructions.

## 2.7 RT-PCR

The detection of *AVRamr1* and *AVRamr3* cDNAs from *Phytophthora infestans* was performed by first isolating the total RNA using the Qiagen RNeasy® Plant Mini Kit (Ref: 74904) and removing any genomic DNA (gDNA) with the ThermoFisher TURBO DNA-*free*™ Kit (Ref: AM1907). Complementary DNA (cDNA) fragments were then synthesized by reverse transcriptase (RT) using the ThermoFisher SuperScript™ IV Reverse Transcriptase (Ref: 18090050), following the manufacturer's instructions. Finally, the obtained cDNA fragments were amplified by PCR.

## 2.8 *N. benthamiana* transient assays

Glycerol stocks of *A. tumefaciens* strains carrying DNA constructs were streaked onto L-media agar plates containing the appropriate antibiotic selection. The plates were incubated at 28 °C for 48 hours. Cells were then scraped from the plates, resuspended in 2 mL of infiltration buffer consisting of $MgCl_2$-MES (pH 5.6) and 200 µM acetosyringone, and briefly vortexed. The resuspended cells were diluted 100-fold, and the optical density (OD) was measured using a spectrophotometer at a wavelength of 600 nm. The cells were then further diluted in infiltration buffer according to the experimental design. In some cases, a p19 RNA silencing suppressor expression construct (Kontra et al., 2016) was added to the *Agro*-infiltration mixes. Leaves from 4/6-week-old plants were infiltrated with the appropriate *Agro*-infiltration mixes using 1 mL plastic syringes and then blotted dry.

For cell death assays in *N. benthamiana*, leaves were spot-infiltrated and covered with foil envelopes to keep them in the dark (Schultink et al., 2017). The foil was removed 48 hours after infiltration. HR events were assessed up to 6 dpi, and photographs of the leaves were taken with a camera.

For protein purification from *N. benthamiana* leaves, tissues were harvested 48-72 hours after infiltration by removing central and lateral veins, and flash-freezing the samples in liquid nitrogen. The tissues were then stored at – 80 °C for future use.

## 2.9 *A. thaliana* transient assays

For cell death assays in *A. thaliana*, glycerol stocks of the non-pathogenic *Pseudomonas fluorescens Pf0*-1 strain (Thomas et al., 2009), either carrying the unrecognized AvrRps4$^{EEAA}$ (Ma et al., 2018) or

the recognized AvrRps4 bacterial effector, were streaked onto L-media agar plates containing the appropriate antibiotic selection. The plates were incubated at 28 °C for 24 hours. Cells were scraped from the plates, resuspended in autoclaved infiltration buffer consisting of $MgCl_2$-MES (pH 5.6), and diluted to an $OD_{600}$ of 0.2. The plants were watered from below for approximately 1 hour before the leaves were entirely infiltrated with 1 mL plastic syringes and then immediately blotted dry. HR events were assessed at 1 dpi, and photographs of the leaves were taken with a camera.

### 2.10 Protein extraction

Prior to tissues harvesting, two 3 mm tungsten carbide beads (Qiagen: 69997) were added to each tube. Tissues were ground and homogenized with Geno/Grinder® for 30 seconds at 1300 RPM, repeated twice, with cooling in liquid nitrogen between the first and second rounds of grinding. A 1:1 ratio (e.g., 100 g of tissue to 100 µL of extraction buffer) was used, with the extraction buffer consisting of 100 mM Tris-HCl (pH 8.0), 2% (w/v) sodium dodecyl sulphate (SDS), 10 mM dithiothreitol (DTT), and 1 tablet of EDTA-free protease inhibitor (Pi) cocktail (Roche: 11836170001) per 10 mL buffer, and was added to the tubes. Tubes were manually shaken regularly for 5 minutes at room temperature. The samples were then centrifuged for 2 minutes at 8,000 × g. The resulting supernatant was transferred to a new set of 1.5 mL Eppendorf tubes, and a 1:3 ratio of loading dye (made of 125 mM Tris-HCl (pH 6.8), 12% SDS (pH 7.2), 10% glycerol, 10 mM DTT, and 1% bromophenol blue; modified and adapted from (Martínez-García et al., 1999)) was added for visualization. The samples were briefly vortexed and heated at 95 °C for 5 minutes. Finally, lysates were centrifuged for 1 minute at 8,000 × g and stored at – 80 °C, if not used immediately.

### 2.11 TurboID-based proximity labelling

For TurboID-directed immunoprecipitation (TurboID-directed IP) experiments in *N. benthamiana*, leaves of four-week-old plants were infiltrated with agrobacteria carrying a TurboID construct. After 72 hours post-infiltration (hpi), 50 µM biotin in $dH_2O$, prepared from a 200 mM biotin stock solution made in the organic solvent dimethyl sulfoxide (DMSO) and stored at – 20 °C, was infiltrated into the leaves pre-infiltrated with TurboID constructs using 1 mL plastic syringes. The plants were maintained for an additional 30 minutes before the leaf tissue was harvested.

For TurboID coupled with MS experiments in *N. benthamiana*, leaves of four-week-old plants were infiltrated with agrobacteria carrying a TurboID construct. After 24 hpi, the leaves were infiltrated with 100,000 zoospores/mL of *P. infestans* (isolate 88069). Subsequently, 50 µM biotin in $dH_2O$ was infiltrated into the same leaves pre-infiltrated with TurboID constructs and *P. infestans* zoospores using 1 mL plastic syringes at 3, 4, and 5 dpi (Chapter 4, Figure 4.5). The plants were maintained for an additional 3 hours before the leaf tissue was harvested.

For TurboID coupled with MS experiments in *A. thaliana*, three-week-old transgenic lines transformed with TurboID constructs were spray-inoculated with *A. candida*$^{Ac2V}$ (100,000 oospores/mL) and maintained under the same growing conditions used for propagating *A. candida*, as described in section 2.20. Six days later, infected leaves were harvested, submerged into a beaker containing 200 mL of 100 µM biotin in $dH_2O$, vacuum-infiltrated for 5 minutes, and maintained for an additional 3 hours while rotating at 60-70 RPM (Chapter 4, Figure 4.18). The leaves were then rinsed with $dH_2O$ to wash off the biotin and blotted dry.

Plant tissues were weighed to obtain approximately 1 g of fresh weight (FW) leaf sample, which was placed in an aluminium foil pocket before being flash-frozen in liquid nitrogen. The frozen leaf material was ground to a fine powder in mortars with pestles and then stored in a 15 mL tube at –80 °C for subsequent use.

Protein extraction was performed by adding three times volume (here, 3 mL) of extraction buffer [150 mM Tris-HCl pH 7.5, 150 mM NaCl, 1 mM EDTA, 10% glycerol, 0.4% NP40 (v/v), 2% polyvinylpolypyrrolidone (PVPP), 0.1-0.5% deoxycholic acid (w/v), 10 mM DTT, 1 tablet of EDTA-free protease inhibitor (Pi) cocktail (Roche: 11836170001)] to each sample. The 15 mL tubes were placed on a rotator for 20 minutes at 4 °C before centrifuging at 4,000 × g for 20 minutes at 4 °C. The upper soluble fraction was then filtered through a piece of Miracloth (EMD Millipore Corporation: 475855-1R) placed above an equilibrated Zeba$^{TM}$ Spin Desalting Column (ThermoFisher: 89894). The desalting columns were centrifuged at 1,000 × g for 2 minutes at 4 °C to remove free biotin in the lysates. A 100 µL aliquot of the lysate was taken from the desalted extract and used to verify the protein expression of the different constructs used in the experiment by Western blot.

To enrich biotinylated proteins from the protein extracts, 150 µL of equilibrated streptavidin beads (ThermoFisher: 20361) were added to the desalted lysates and incubated on a rotator for 2 hours at

4 °C to affinity-purify the biotinylated proteins. The beads were precipitated by centrifugation at 1,000 × g for 2 minutes at 4 °C and washed twice with a minimal extraction buffer [150 mM Tris-HCl pH 7.5, 150 mM NaCl, 1 mM EDTA, 10% glycerol, 0.4% NP40 (v/v)]. The beads were initially washed sequentially once with *buffer I* [2% SDS (w/v)] for 5 minutes at room temperature, once with *buffer II* [1% Triton X-100, 0.1% deoxycholic acid (w/v), 150 mM Tris-HCl pH 7.5, 150 mM NaCl, 1 mM EDTA, 10% glycerol] for 5 minutes at 4 °C, once with *buffer III* [10 mM Tris-HCl pH 7.4, 1 mM EDTA, 250 mM lithium chloride (w/v), 1% NP40 (v/v), 0.1% deoxycholic acid (w/v)] for 5 minutes at 4 °C, twice with *buffer IV* [50 mM Tris-HCl pH 7.5] for 5 minutes each time at 4 °C to remove the detergent, and finally at least six times with *buffer V* [50 mM ammonium bicarbonate pH 8.0] for 2 minutes each time at 4 °C. However, after comparing and verifying that washing under urea conditions was equivalent to washing under SDS conditions (Chapter 3, Figure 3.5), the beads were sequentially washed once with 7 M urea (freshly made in *buffer V*) for 2 minutes at room temperature, twice with 4 M urea (freshly made fresh in *buffer V*) for 2 minutes each time at room temperature, and three times with *buffer V* [50 mM ammonium bicarbonate pH 8.0] for 2 minutes each time at 4 °C.

The washed beads were resuspended in 1 mL of *buffer V*. To confirm the successful enrichment of the biotinylated proteins, 100 µL of the suspension was aliquoted for Western blot analysis. The remaining beads were stored at – 80 °C for later MS analysis.

For TurboID-directed IP, the same steps were followed with the following modifications: lysates were not desalted, and 30 µL of equilibrated anti-Myc beads (Sigma-Aldrich: A5598) were added to each sample; after incubation, the beads were gently washed with minimal extraction buffer [150 mM Tris-HCl pH 7.5, 150 mM NaCl, 1 mM EDTA, 10% glycerol, 0.4% NP40 (v/v)] four times for 2 minutes each at 4 °C; finally, the beads were boiled at 95 °C for 5 minutes in 200 µL of minimal extraction buffer for Western bot analysis.

### 2.12 SDS-polyacrylamide gel electrophoresis (PAGE) assay and Western blot

PAGE resolution gels were prepared in the lab using two glass plates to cast 6%, 8%, 10% or 12% acrylamide resolving gels. The 4X resolution buffer was made by combining 1.5 mM Tris base, 20% SDS (w/v), and adjusting the pH to 8.8 with HCl before autoclaving. The 4X stacking buffer was prepared by mixing 0.5 M Tris base, 20% SDS (w/v), and adjusting the pH to 6.8 with HCl before autoclaving. Acrylamide was added to 1X resolution buffer along with 0.01% ammonium persulfate

(APS) and 0.05% Tetramethylenediamine (TEMED), then poured between the two glass plates and layered with isopropanol to remove bubbles. Gels were allowed to polymerize for about 20 minutes. After polymerization, the isopropanol was washed away with $dH_2O$. Next, 1X stacking buffer with acrylamide, 0.01% APS, and 0.1% TEMED was poured on top of the resolution gel. Combs were inserted, and the gels were left to set at room temperature for approximately 20 minutes. If the gels were not used immediately, they were stored at 4 °C in sealed plastic bags with moist blue-roll to maintain humidity.

Gels were assembled in tanks (Bio-Rad: Mini-PROTEAN® Tetra System) filled with 1X SDS buffer, consisting of 25 mM Tris, 200 mM Glycine, and 2% SDS (w/v) for Western blotting. Frozen samples were thawed at room temperature for about 5 minutes, briefly vortexed, and centrifuged at 8,000 × g for 1 minute. Samples were loaded into the gels alongside 5 µL of PageRuler™ Prestained Protein Ladder (10 to 180 kDa, ThermoFisher: 26616). Electrophoresis was run at 90 V for about 15-20 minutes, until the ladder had migrated through the stacking gel, then the voltage was increased to 110-120 V until the dye front reached the bottom of the gel.

Once protein migration was complete, semi-dry protein transfer to Immun-Blot® 0.2 µm PVDF (polyvinylidene difluoride) membranes (Bio-Rad: 1620177) was performed using the Bio-Rad Trans-Blot® Turbo™ Transfer System. The pre-programmed transfer protocol for 1.5 mm gels was used, with the transfer set for 10 minutes at 1.3 A for one gel or 2.5 A for two gels.

After transfer, the membranes were blocked for 1 hour in 20 mL of TBS-T (50 mM Tris-HCl, pH 8.0, 150 mM NaCl, 0.1 % Tween®-20) with either 5% (w/v) non-fat dry milk powder or 2% BSA (Bovine serum albumin). The membranes were then incubated with 15 mL of conjugated antibodies in 5% milk TBS-T, or HRP-conjugated streptavidin in 2% BSA, at a 1:10,000 dilution, either overnight at 4 °C or for 2 hours at room temperature, both while rotating at 60-70 RPM. After incubation, membranes were washed three times for 10 minutes each with TBS-T at room temperature, rotating at 60-70 RPM. Finally, membranes were incubated with either SuperSignal™ West Pico PLUS (Ref: 34580) or West Femto Maximum Sensitivity Substrate (Ref: 34096). Chemiluminescence signals were detected using the ImageQuant™ LAS 4000 from GE Healthcare or the Amersham™ ImageQuant™ 800 biomolecular imager, both of which are equipped with a chemiluminescence imaging analysis system.

## 2.13 Phos-tag SDS-PAGE

Part of the anti-Myc immunoprecipitated NRC2 proteins, as described in section 2.11, was run on Phos-tag SDS-PAGE gels. The aliquot of anti-Myc beads used for these gels was boiled at 65 °C for 5 minutes with shaking at 400 RPM just before running the gels. Phos-tag gels were prepared fresh by pouring resolution gel solution, which contained 6% (w/v) acrylamide, 50 µM Phos-tag™ Acrylamide AAL-107 (AlphaLabs), 375 mM Tris-HCl pH 8.8, 100 µM $MnCl_2$, 0.1% (w/v) SDS, 0.01% TEMED, and 0.05% (w/v) APS into 1.0 mm glass plates. Isopropanol was layered on top to prevent bubbles, and the gel was allowed to polymerize for 30 minutes at room temperature before the isopropanol was washed away with $dH_2O$. The stacking gel solution consisted of 4.5% (w/v) acrylamide, 125 mM Tris-HCl pH 6.8, 0.1% (w/v) SDS, 0.01% (w/v) TEMED, and 0.04% (w/v) APS, was poured on top of the resolving gel. Combs were inserted, and the gel was allowed to polymerize for 30 minutes at room temperature. The gel was then run under a constant current (15 mA/gel) for approximately 1 hour. Once electrophoresis was complete, the gel was soaked three times for 15 minutes each in 100 mL of 10X Tris/CAPS buffer, diluted to 1X, with 10 mM EDTA for 15 minutes twice to remove the manganese ions prior to transfer. The gel was then washed once in 100 mL of 10X Tris/CAPS buffer, diluted to 1X, for 10 minutes to remove EDTA before blotting onto a PVDF membrane.

## 2.14 Blue-native PAGE

The oligomerization of the miniTurbo-tagged *Nb*NRC2$^{EEE}$ construct was verified by performing blue native PAGE using pre-cast NativePAGE™ 3-12% Bis-Tris Mini Protein Gels (ThermoFisher: BN1001BOX). The samples were kept on ice to prevent dissociation or aggregation. To 50 µL of sample extract, 25 µL of NativePAGE™ Sample Buffer (4X) (ThermoFisher: BN2003) and 2.5 µL of NativePAGE™ 5% G-250 Sample Additive (ThermoFisher: BN2004), and $dH_2O$ were added to achieve a final volume of 100 µL. Electrophoresis was conducted in a cold room at 4 °C, and all buffers were cooled prior to use. The inner chamber of the tank was filled with cathode buffer, while the outer chamber was filled with anode buffer, using the NativePAGE™ Running Buffer Kit (ThermoFisher: BN2007). The samples were loaded and run alongside 5 µL NativeMark™ Unstained Protein Standard (ThermoFisher: LC0725). Electrophoresis was run at 150 V for approximately 45 minutes until the dye front had migrated about one-third of the way through the gel. The voltage was then increased to 250 V for about 1 hour until the dye front reached the bottom of the gel. The gel was subsequently transferred for 30 minutes at 20 V onto a PVDF membrane. The membrane was

incubated in 8% acetic acid for 15 minutes to fix the proteins, rinsed with water, and left to air-dry for a minimum of 1 hour. The membrane was then re-activated with 100% ethanol to visualize the molecular weight marker (labelled with a pencil) and to remove any residual Coomassie dye. The membrane was blocked and probed as described in section 2.12.

## 2.15 On-bead trypsin digestion

After washing and precipitating the biotinylated proteins as described in section 2.11, the frozen streptavidin beads were thawed on ice and transferred into assembled Mobicol columns (MoBiTec®: M1002), each inserted with a 10 µm pore size filter (MoBiTec®: M2110). The columns were centrifuged at 1,300 × g for 1 minute, followed by two washed with 600 µL of 50 mM Tris-HCl (pH 7.5) and two washes with 2 M urea in 50 mM Tris-HCl (pH 7.5). The columns were sealed with numpsy plugs, ensuring it did not touch the filter, and 80 µL of trypsin buffer (50 mM Tris-HCl pH 7.5, 1 M urea, 1 mM DTT) containing 200 ng of trypsin was added to each column. The columns were incubated at 25 °C with shaking at 300 RPM for 3 hours. After incubation, the numpsy plugs were removed, and the columns were transferred to fresh 1.5 mL low protein-binding Eppendorf tubes before being spun to collect the digest. To achieve a final volume of 200 µL, 60 µL of trypsin buffer (without trypsin) was added to each column, and the columns were spun again. The Mobicol columns were discarded, and 0.8 µL of DTT was added per sample to reach a final concentration of 4 mM. The samples were mixed, spun, and incubated at 25 °C for 30 minutes with shaking at 300 RPM. The digests were alkylated by adding iodoacetamide to a final concentration of 10 mM and incubating at 25 °C for 45 minutes with shaking at 300 RPM. Finally, another 200 ng of trypsin was added to each sample, mixed, spun, and incubated at 25 °C overnight (for approximately 14-16 hours) with shaking at 300 RPM.

After the overnight trypsin digestion, the digests were acidified with 2 µL of formic acid to achieve a final concentration of 1% and desalted using OMIX C18 pipette tips (Agilent: A57003100). The C18 desalting tips were activated by aspiring and dispensing 200 µL of buffer B2 (0.1% formic acid, 50% acetonitrile) two times and equilibrated by aspiring and dispensing 200 µL of buffer A2 (0.1% formic acid) four times. The peptides were bound to the C18 desalting tips by aspiring and dispensing the samples eight times. The peptides were then washed by aspiring and dispensing 200 µL of buffer A2 ten times and finally eluted by aspiring and dispensing 200 µL of buffer B2 into fresh 1.5 mL low protein-binding Eppendorf tubes ten times. The bottom part of the tubes containing the desalted

peptides was gently immersed in liquid nitrogen before being dried in a SpeedVac for about 2 hours and stored at – 80 °C for subsequent mass spectrometry analysis.

### 2.16 Mass spectrometry analysis

For each sample, 20% of the digested peptides were analysed by nanoLC-MS/MS on an Orbitrap Eclipse™ Tribrid™ mass spectrometer equipped with a FAIMS Pro Duo interface and coupled to an UltiMate® 3000 RSLCnano LC system (Thermo Fisher Scientific, Hemel Hempstead, UK). The samples were loaded onto a trap cartridge (PepMap™ Neo Trap Cartridge, C18, 5um, 0.3x5mm, Thermo) with 0.1% TFA at 15 µL min-1 for 3 min. The trap column was then switched in-line with the analytical column (Aurora Frontier TS, 60 cm nanoflow UHPLC column, ID 75 µm, reversed phase C18, 1.7 µm, 120 Å; IonOpticks, Fitzroy, Australia) for separation at 60°C using the following gradient of solvents A (water, 0.1% formic acid) and B (80% acetonitrile, 0.1% formic acid) at a flow rate of 0.26 µL min-1: 0-3 min 1% B (parallel to trapping); 3-10 min increase B (curve 4) to 8%; 10-102 min linear increase B to 48; followed by a ramp to 99% B and re-equilibration to 0% B, for a total of 140 min runtime. Mass spectrometry data were acquired with the FAIMS device set to three compensation voltages (-35V, -50V, -65V) at standard resolution for 1.0 s each with the following MS settings in positive ion mode: OT resolution 120 K, profile mode, mass range m/z 300-1600, normalized AGC target 100%, max inject time 50 ms; MS2 in IT Turbo mode: quadrupole isolation window 1 Da, charge states 2-5, threshold 1e4, HCD CE = 30, AGC target standard, max. injection time dynamic, dynamic exclusion 1 count for 15 s with mass tolerance of ±10 ppm, one charge state per precursor only.

Peak lists in the format of Mascot generic files were generated from raw files using MSConvert package (Matrix Science) and searched using Mascot (v2.5) against either Araport11 or in-house databases for *N. benthamiana*, *P. infestans*, *A. candida*, and contaminants. Searches were performed with peptide mass tolerance and fragment ion mass tolerance of 10 ppm and 0.8 Da, respectively, peptide charges of 2+, 3+ and 4+, and allowing for up to one missed tryptic cleavage. Carbamidomethylation of Cys residues was specified as a fixed modification, and oxidized Met as variable modification. The search results were assembled into Scaffold (v5.3.2; Proteome Software). Parameter settings were adjusted as follows: Protein Threshold - 1% FDR, Peptide Threshold - 1% FDR, Minimum # Peptides - 2, Display Options - Total Spectrum Count, and Required Modifications - No Filter. Under these parameters the data were exported in Excel (Microsoft Office) spreadsheets for further analysis.

## 2.17 Bioinformatics analyses

Three biological repeats of biotin labelling and MS analysis were performed. Proteins were considered proximal protein interactors if they were unique to Rpi-amr1, Rpi-amr3, WRR4A, or EDS1, or if they were enriched in biotinylation compared to the control mCherry (2x fold change, P-value < 0.05).

For plant-derived proximal interactors, volcano plots were used to represent the data. To generate the volcano plots, proteins with total spectral counts below 50 across the three replicates were excluded from the analysis. A Fisher's Exact Test was then applied using the exactTest() function from the edgeR (Empirical Analysis of Differential Gene Expression in R) package, version 4.2.1 (Chen et al., 2025).

For pathogen-derived proximal interactors, MA plots (M *versus* A plots) were used to represent the data. An MA plot is a scatter plot that displays the relationship between protein abundance (A), represented by the mean spectral counts, and the $\log_2$(fold change) in biotinylation (M). To generate the MA plots, the data were first normalized using cyclic loess-normalization *via* the edgeR package (Chen et al., 2025).

## 2.18 Plant material and growth conditions

Multi-parent advanced generation inter-cross (MAGIC) lines are a type of population generated by recombinant inbred lines (RILs) derived from multiple parents. These lines are created through several rounds of mating, followed by inbreeding to produce a stable panel of inbred lines, resulting in a mixed genome from the founder parents (Kover et al., 2009). The "Double MAGIC 10" (DM10) line is derived from a cross between MAGIC.329 and MAGIC.23, consisting of $F_4$ plants from independent $F_2$ lines that are susceptible to *A. candida* races (Cevik et al., 2019). Due to this susceptibility, the *A. thaliana* DM10 line was selected for the TurboID experiments.

Arabidopsis plants for pathogen assays were grown in a controlled environment room (CER) at 20-22 °C with 70% relative humidity and an 8-hour photoperiod. In contrast, plants used for seed collection were grown under similar conditions in a CER, but with a 16-hour photoperiod.

The *N. benthamiana* quadruple knock-out mutant of the EDS1-family genes (EDS1a, PAD4, SAG101a and SAG101b), referred to as *Nb_epss*, was generated by crossing *Nb_eds1a* with *Nb_pad4 sag101a sag101b* (*pss*) (Gantner et al., 2019, Lapin et al., 2019, Ordon et al., 2017), and was used in some of the cell death assays. The *nrc2/3/4* CRISPR knockout (KO) *N. benthamiana* mutant line was also employed in some experiments (Wu et al., 2020).

*N. benthamiana* plants used for *A. tumefaciens*-mediated transient transformation of leaf tissue and HR assays were grown in a CER at 20-22 °C, with 70% relative humidity and a 16-hour photoperiod.

### 2.19 *A. thaliana* transformation and T-DNA selection

*A. thaliana* stable transgenic lines were generated *via* flower dipping. Agrobacteria cultures were prepared in 100 mL L-media with the appropriate antibiotics, 5% sucrose, and 0.02% (v/v, 50 µl/l) Silwet L-77. The cultures were incubated for approximately 12-16 hours at 28 °C, with shaking at 200-250 RPM, until the $OD_{600}$ reached 0.4-0.8. Flowers were then submerged in the *Agro*-cultures for about 1 minute.

To select plants that have incorporated T-DNAs into their genomes, two selecting systems were employed: the FAST-Red (fluorescence-accumulating seed technology) selecting cassette (Shimada et al., 2010), which allows visualization of transgenic seeds emitting red fluorescence, and the BASTA selecting cassette (Lutz et al., 2001), which confers resistance to glufosinate (also known as phosphinothricin), a common herbicide active ingredient. FAST-Red seeds were screened using a Leica M165 fluorescent stereo microscope with DSR filter. Seeds with a red fluorescence were selected. BASTA-resistant seeds were sown in soil and sprayed three times with BASTA. The seeds from the plants that survived were then collected. T2 seeds were sterilized and evenly plated on ½MS media supplemented with 10 µg/mL of phosphinothricin (PTT) (Melford Duchefa: P0159.0250). Transgenic lines with a single insertion were selected by confirming a 3:1 segregation ratio in the T2 generation and were then grown to collect T3 seeds. T3 transgenic lines homozygous for Fast-Red fluorescence and BASTA resistance were selected.

For Arabidopsis seed sterilization, seeds were washed with a 1.2% hypochlorite solution for 30 seconds, followed by rinsing with sterile water. This process was repeated twice, after which the seeds were kept at 4 °C in the dark for 48 hours before being sown on plates.

## 2.20 Pathogens propagation and infection

*A. candida*$^{Ac2V}$, and *Hpa*$^{Emoy2}$ are obligate biotrophic pathogens and must be maintained on susceptible *A. thaliana* accessions and mutants on a weekly basis.

*A. candida*$^{Ac2V}$ was propagated approximately every two weeks. Infected leaves from infected plants were harvested, resuspended in water, and vortexed to release spores. The resulting spore mixture was then filtered and sprayed onto a new set of 2-week-old uninfected plants. The newly infected plants were placed in darkness at 4 °C overnight, followed by transfer to an incubator set at approximately 20 °C during the 10-hour light cycle and 16 °C during the 14-hour night cycle.

*Hpa*$^{Emoy2}$ was propagated weekly. Infected seedlings were harvested, and their roots were removed to prevent contamination. The remaining plant material was then resuspended in a 15 mL tube containing water, and the tube was shaken to release spores. The resulting mixture was filtered and sprayed onto 7-day-old uninfected seedlings. The newly infected seedlings were then placed in an incubator at 18 °C with a 12-hour photoperiod.

*P. infestans* (isolate 88069) was cultured and maintained on rye sucrose agar (RSA) media. All plates were incubated at 18 °C in darkness for 10 to 14 days before inoculating a new set of RSA plates by scraping off a small amount of oomycete from the 10-14 days-old plates. For subsequent infiltration into *N. benthamiana* leaves, sporangial suspensions were prepared by adding 10 mL of cold $dH_2O$ to each plate and gently shaking the plates for 2 hours at 4 °C to promote the release of motile zoospores.

Sporangial suspensions for all three pathogens were prepared on the day of inoculation, and their concentrations were determined by counting the spores under an optical microscope with a hemacytometer counting chamber. The concentration was then adjusted to the desired concentration of 100,000 spores/mL.

# Chapter 3

TurboID proximity labelling optimization for detection of pathogen virulence factors

# 3. TurboID proximity labelling optimization for detection of pathogen virulence factors

## 3.1 Introduction

### 3.1.1 Limitations associated with the use of proximity labelling

Proximity labelling (PL) technologies, such as TurboID and miniTurboID, provide valuable tools for studying protein interactions in plant systems. However, every method has specific limitations that can affect experimental outcomes. One advantage of TurboID is its sensitivity, but this also serves as its major drawback, as it generates significant background noise, which can make it difficult to distinguish the signal from the noise.

As the name suggests, miniTurboID is smaller than TurboID but exhibits only half its activity and has been reported as unstable (May et al., 2020). In contrast, TurboID demonstrates strong catalytic activity; however, this comes with the drawback of higher background labelling before biotin is introduced into the system. This issue arises because biotin is present in many plant cell compartments and is an essential cofactor for enzymes involved in the transfer of $CO_2$ during $HCO^-_3$-dependent carboxylation reactions (Alban et al., 2000). In pea leaves, biotin is distributed in roughly equimolar ratios across mitochondria, chloroplasts, and cytosol, with a total concentration of 1.1 ng/mg protein. However, biotin is not present in the same form across these compartments. The majority of free biotin is found in the cytosol of mesophyll cells, while protein-bound biotin (associated with biotin-dependent carboxylases) predominantly accumulates within organelles (Baldet et al., 1993). These biotin-dependent carboxylases in plants include cytosolic acetyl-CoA carboxylase, chloroplastic geranyl-CoA and acetyl-CoA carboxylases, and mitochondrial methylcrotonoyl-CoA carboxylase (Nikolau et al., 2003).

To reduce background biotinylation generated by TurboID and to potentially achieve greater control over the labelling window, two PL technologies, Split-TurboID and Pupylation-based interaction tagging (PUP-IT), are available. Split-TurboID involves dividing TurboID into two inactive fragments that reassemble into an active enzyme through protein-protein interactions (Cho et al., 2020). This method is based on the same principle as the split-GFP system, ensuring that labelling begins only after the enzyme is reconstituted. However, this technique requires prior knowledge of the protein targets whose interaction you wish to study. PUP-IT relies on a distinct concept, utilizing the bacterial

Pup protein-conjugation system. In this approach, the *pafA* gene, encoding a Pup ligase from mycobacteria, is fused to the bait protein (Liu et al., 2018). In the presence of ATP, the Pup ligase PafA catalyzes the conjugation of prokaryotic ubiquitin-like proteins (Pup) to lysine residues on target proteins. The PUP-IT approach enables precise labelling because the pupylation reaction, mediated by the PafA ligase, involves the enzymatic covalent attachment of Pup to lysine residues on nearby substrate proteins. This reaction occurs rapidly and specifically in the immediate vicinity of the PafA enzyme, which is tethered to the protein of interest. In contrast, during TurboID labelling, reactive bio-AMP diffuse freely away from the biotin ligase, forming a gradient of reactive bio-AMP around the enzyme. Unlike other proximity-tagging techniques, PUP-IT does not require the delivery of external substrates, as it relies on the inducible expression of Pup proteins. However, the relatively large size of both Pup (7 kDa) and PafA (54 kDa) restrict their diffusion across membranes. Although PUP-IT has not yet been widely applied in plants, a recent study successfully employed it to identify the interactome of the Arabidopsis plasma membrane-localized receptor kinase FERONIA (Lin et al., 2024).

TurboID, like BioID, has a molecular weight of 35 kDa, larger than GFP (26 kDa). This size may sometimes interfere with the proper localization or functionality of the fused proteins. To address this limitation, BioID2 was developed. Derived from *Aquifex aeolicus*, BioID2 at 26.4 kDa is smaller than TurboID, making it the smallest PL enzyme available at the time (Kim et al., 2016). Recently, two novel enzymes have surpassed BioID2 in size efficiency: microID, a truncated version of BioID2, and ultraID, a variant derived through directed evolution (Kubitz et al., 2022). These newly engineered enzymes have molecular weights below 20 kDa, making them the smallest PL enzymes available to date. Despite their reduced size, both microID and ultraID exhibit enzyme kinetics comparable to TurboID and maintain low background activity. However, their application in plant systems might present challenges due to their temperature dependence. Both enzymes show optimal activity at 55 °C, reduced activity at 37 °C, and even lower activity at 30 °C. These temperature requirements may limit their effectiveness in plant studies, where such high temperatures are typically unsuitable.

Overall, the most widely used PL techniques in plant systems so far are those based on biotin ligases. Despite their limitations, these methods remain the best suited for these organisms. However, the PUP-IT technology has the potential to be more widely adopted in the coming years.

### 3.1.2 TurboID and miniTurbo reveal plant protein-protein interactions

TurboID-based PL analysis has been successfully applied in mammalian cells, as well as in model organisms such as flies and worms. However, its implementation in plants has encountered several challenges due to unique plant characteristics, including the presence of a cuticle and a rigid cell wall, lower optimal growth temperatures, and their capacity to synthesize and store biotin, which can reduce biotinylation efficiency and/or specificity. While free biotin is low or even undetectable in bacterial and animal cells, plant cells contain a large pool of free biotin, which can interfere with the labelling process. Despite these challenges, the technique has since been optimized and extended to various plant systems, including *N. benthamiana*, *A. thaliana*, *Marchantia polymorpha*, and tomato hairy roots (Arora et al., 2020, Mair et al., 2019, Melkonian et al., 2022, Zhang et al., 2020).

Even though BioID was developed in 2012 (Roux et al., 2012), the first attempt to establish PL methods in plants was published in 2017, using BioID to identify interactors of the *Os*FD2 transcription factor in rice protoplasts (Lin et al., 2017). This was followed in 2018 by the mapping of the interactome of two membrane-localized effectors of *Pseudomonas syringae*, AvrPto and HopF2, in *Nicotiana benthamiana* and *Arabidopsis thaliana*, respectively (Conlan et al., 2018, Khan et al., 2018). Simultaneously, TurboID and miniTurbo were developed (Branon et al., 2018). Although the preceding studies used BioID, which is not the most optimal PL enzyme for plant systems, they laid the groundwork for subsequent efforts to establish TurboID-based PL methods.

TurboID has proven effective in *N. benthamiana* plants by identifying novel interactors with a nucleotide-binding leucine-rich repeat (NLR) immune receptor (Zhang et al., 2019). Research on the mechanisms of NLR protein interactions remains limited, as these receptors often present challenges for conventional methods due to their low abundance (which helps prevent autoimmunity and minimize negative effects on plant fitness (Tian et al., 2003)) and the transient or weak nature of their interactions. Additionally, the dynamic nature of the NLR regulatory network makes it challenging to identify proteins directly involved in the NLR signalling pathway (Sun et al., 2020). TurboID was used to identify the protein interactome of a *Tobacco mosaic virus* (TMV)-resistant NLR, referred to as N (Whitham et al., 1994). The researchers discovered that a putative E3 ubiquitin ligase, UBR7, directly interacts with the TIR domain of N, and that downregulation of UBR7 leads to increased accumulation of the N protein and enhanced TMV resistance. Furthermore, the TMV-p50

effector disrupts the N-UBR7 interaction and alleviates the negative regulation of N by UBR7 (Zhang et al., 2019). This study provided valuable insights into the complex regulation of N NLR protein homeostasis.

Following this success, other studies have also utilized the sensitivity of TurboID to further investigate PPIs involved in plant immunity. For example, TurboID was used to demonstrate that TIR signalling promotes the association of EDS1 and PAD4 with the "helper" NLR ADR1-L1, as well as the self-association of ADR1-L1s, suggesting probable oligomerization of ADR1-L1 for subsequent immune activation (Wu et al., 2021). TurboID also facilitated the discovery of a new interacting partner for the repressor proteins TOPLESS (TPL) and JAZ (NINJA) in tomato hairy roots (Gryffroy et al., 2023). This partner is the root oncogenic locus B (RolB) protein, which can directly interact with and mitigate the function of TPL, leading to specific changes in plant hormone signalling, immunity, growth, and developmental processes during infection by rhizogenic *Agrobacterium* strains. This study provided valuable insights into the pathogenesis of hairy root disease. Recently, TurboID and Split-TurboID were used in *N. benthamiana* to explore the interactome of SUPPRESSOR OF G2 ALLELE OF skp1 (SGT1), which plays a crucial role in growth, development, and immunity, during pre- and post-immune activation (Zhang et al., 2024). The researchers observed a dynamic shift from proteins associated with plant development to those linked with plant defense upon immune activation. One of the interactors, NECROTIC SPOTTED LESION 1 (NSL1), was further investigated, and their findings demonstrated that NSL1 negatively regulates NLR-mediated immunity by interfering with the salicylic acid (SA) signalling pathway. Moreover, they showed that SGT1 promotes the proteasomal degradation of NSL1 to facilitate immune activation. This study expanded our understanding of the regulatory landscape of SGT1 and revealed a new SGT1-NSL1 signalling module that regulates plant immunity. Finally, TurboID was used to unveil the interactome of the NONEXPRESSOR OF PR GENES 1 (NPR1) in Arabidopsis (Powers et al., 2024). The NPR1 signalling cascade has remained elusive due to difficulties in studying this transcriptional cofactor, whose chromatin association is indirect and likely transient. In this study, the researchers identified almost all known NPR1 interactors, as well as new components of transcription-related complexes, showing that chromatin remodelling and histone demethylation contribute to SA-induced resistance.

At the start of my project, PL methods had already been widely demonstrated as valuable tools for studying PPIs in animal systems, but their application in plants was still in its early stages. Even now,

there are relatively few well-executed and successful studies utilizing TurboID-based approaches in plant immunity.

We set out to test whether TurboID could be used as a tool to identify unknown effectors under native infection conditions. At the time, we did not realize that this would become one of the most challenging objectives to achieve with TurboID, requiring further optimization of the protocol to make it a reliable approach. While TurboID has fast labelling kinetics and does not require high-temperature catalysis, it is also the most promiscuous biotin ligase, which can lead to increased noise. In this chapter, I will focus on the various aspects of the protocol that can be adjusted and refined to reach this goal, with additional optimization details provided in the other chapters.

## 3.2 Results

While TurboID is highly efficient at attaching biotin to proteins, it biotinylates any target within a 20-35 nm range, leading to a high background of non-specific biotinylation. Additionally, plants naturally produce and store endogenous biotin in their cells, which contributes to a low biotinylation background even without exogenous biotin (i.e., before starting the experiment). This results in a lower signal-to-noise ratio, as the “noise” from non-specific labelling makes it difficult to detect and distinguish the proteins of interest (POI) from random proteins labelled due to the enzyme’s broad reactivity. In most cases, this background labelling can be ignored or eliminated with proper controls, but it has been a major challenge when attempting to capture effectors that are delivered by the pathogen under native infection conditions, especially due to their often extremely low abundance. Therefore, careful optimization was essential to increase the chances of successfully detecting low-abundance effectors (see Chapters 4 and 5).

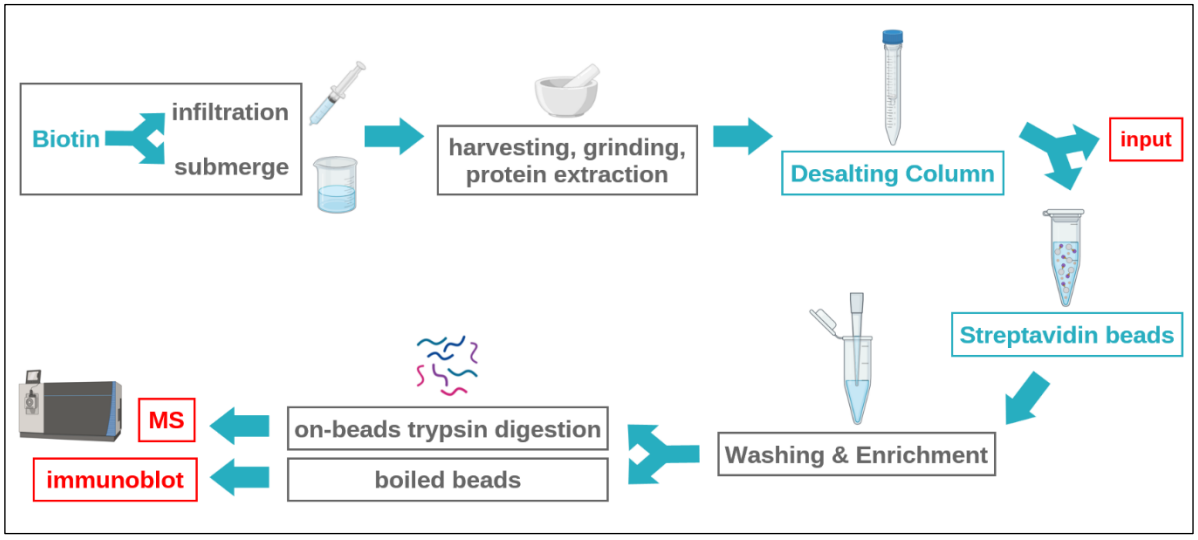


**Figure 3.1 Workflow for TurboID-based proximity labelling coupled with mass spectrometry in plants.**

4/5-week-old *A. thaliana* or *N. benthamiana* leaves are syringe-infiltrated with 50 µM biotin solution or submerged in 100 µM biotin solution for short (30 min) or long (3-5 h) labelling time. Leaf tissues are harvested, rinsed with cold water, dried and ground in liquid nitrogen. Total protein is extracted and excess free biotin is removed from crude extract by using desalting columns. Biotinylated proteins are pulled down using streptavidin-agarose beads. The beads are washed before being boiled for immunoblot analysis and/or subjected to on-bead digestion with trypsin. The resulting peptides are then sent for LC-MS/MS analysis. The figure was created with elements from BioRender (biorender.com).

At the start of this project, TurboID was a relatively new technology in plant research, and my first goal was to identify the best practices for its use. I thoroughly verified and optimized each key step of the protocol (Figure 3.1) for TurboID-based identification of plant interactomes, including 1) the removal of free biotin from crude extracts prior to streptavidin pull-down, 2) the capture of biotinylated proteins, 3) the washing of non-biotinylated proteins during the enrichment step, and 4) the effective release of biotinylated proteins from the beads. I conducted these optimization steps with different samples tested at the time; therefore, the TurboID-tagged baits across the different figures in this chapter are not necessarily consistent. The aim here is to compare different protocol parameters.

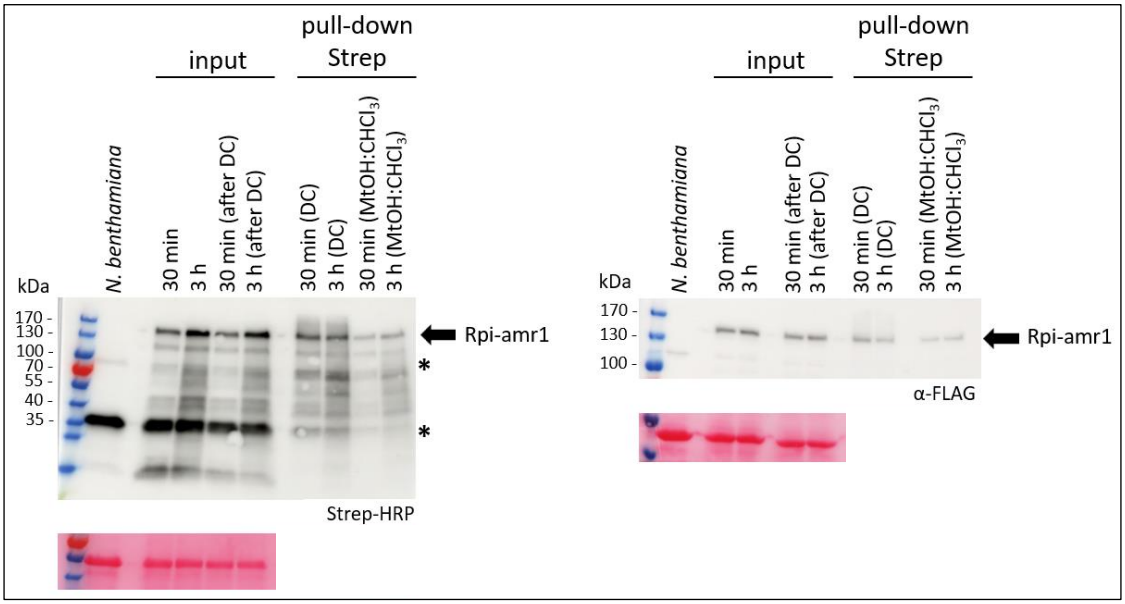


**Figure 3.2 Desalting columns effectively remove excess free biotin – part 1.**

Streptavidin pull-down and biotinylation of Rpi-amr1:TurboID-FLAG in WT *N. benthamiana*. *Agro*-infiltrations at $OD_{600}$ = 0.5 in 4-week-old *N. benthamiana* leaves in the presence of p19. Biotin-infiltration (50 µM) at 3 dpi and for 30 min to 3 h before tissue harvesting. Pull-down was carried out with streptavidin beads followed by 7 M urea washing conditions. A small fraction of the beads was boiled and analysed by SDS-PAGE, while the remaining beads were used for LC-MS/MS analysis. Biotinylated proteins were detected by using HRP-conjugated streptavidin labelling. Bands labelled with a black asterisk (*) correspond to endogenously biotinylated proteins. Each of the two samples (labelled 30 min and 3 h) was split in half, and each half was subjected to two different methods to remove excess free biotin prior to streptavidin pull-down: "DC" for desalting columns and "MtOH:$CHCl_3$" for methanol:chloroform precipitation. The "*N. benthamiana*" lane corresponds to non-infiltrated samples, meaning no TurboID-tagged baits were expressed and no biotin was added. It serves as control to show endogenous biotinylation.

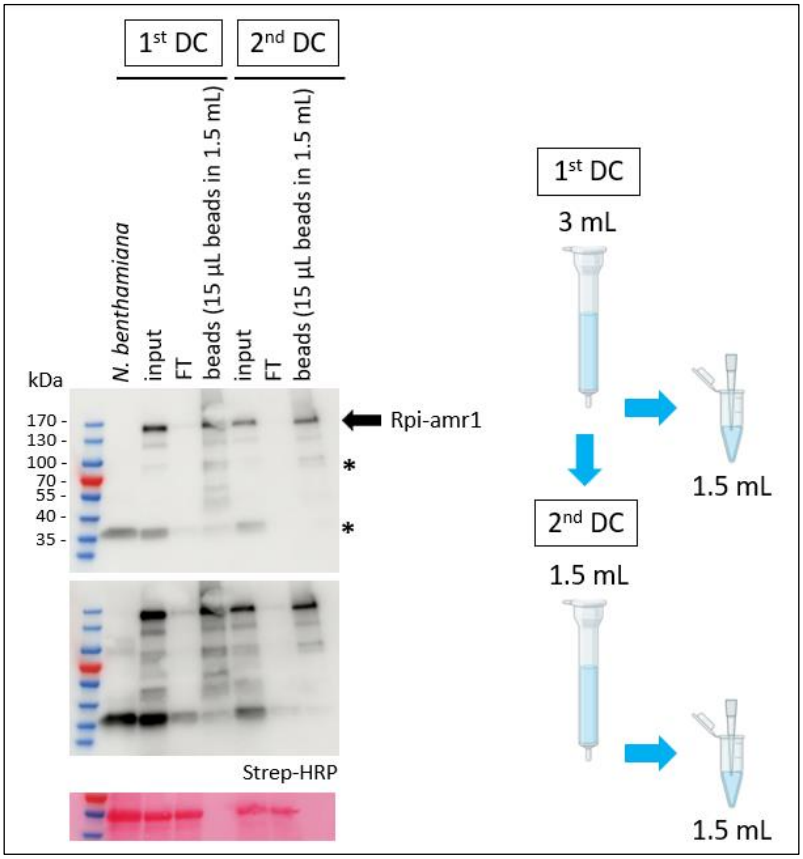


**Figure 3.3 Desalting columns effectively remove excess free biotin – part 2.**

Streptavidin pull-down and biotinylation of Rpi-amr1:TurboID-FLAG in WT *N. benthamiana*. *Agro*-infiltrations at $OD_{600}$ = 0.5 in 4-week-old *N. benthamiana* leaves in the presence of p19. Biotin-infiltration (50 µM) at 3 dpi and for 30 min before tissue harvesting. Pull-down was carried out with streptavidin beads followed by 7 M urea washing conditions. A small fraction of the beads was boiled and analysed by SDS-PAGE, while the remaining beads were used for LC-MS/MS analysis. Biotinylated proteins were detected by using HRP-conjugated streptavidin labelling. Bands labelled with a black asterisk (*****) correspond to endogenously biotinylated proteins. The sample was run through a first desalting column (1st DC), split in half, and beads were added to one half while the other half was run through a second desalting column (2nd DC) before adding the beads. The flowthrough (FT), collected after streptavidin pull-down, was loaded side by side with the boiled beads (beads) to estimate the amount of biotinylated proteins remaining in the crude extract. The "*N. benthamiana*" lane corresponds to non-infiltrated samples, meaning no TurboID-tagged baits were expressed and no biotin was added. It serves as control to show endogenous biotinylation.

Free biotin competes with binding to streptavidin beads, leading to a significantly reduced capture of biotinylated proteins. Conventional washes to remove free biotin, commonly used for human cell lines, are often insufficient for plant tissues (Chua et al., 2021). As a result, an additional desalting step using size-exclusion columns is typically employed in plant studies to remove free biotin (Zhang et al., 2019). Depletion of free biotin can also be achieved through protein precipitation, which provides cleaner results but carries the drawback of potential incomplete or inconsistent solubilization of precipitated proteins. Therefore, I aimed to test the efficiency of desalting columns for removing free biotin from the samples before adding the beads (Figure 3.2 and 3.3).

Firstly, the successful biotinylation of proteins by the TurboID enzyme was confirmed by blotting with HRP-conjugated streptavidin. In *N. benthamiana*, two characteristic bands, marked with an asterisk (*****), correspond to endogenously biotinylated proteins: one around 70-100 kDa and another around 35-40 kDa. Two different labelling periods were tested, 30 minutes and 3 hours, and, as expected, the longer labelling time resulted in a greater number of biotinylated proteins. Two methods were compared for removing free biotin: desalting columns and methanol:chloroform precipitation. The methanol:chloroform precipitation method resulted in a slightly lower enrichment compared to the desalting column method (Figure 3.2). This could be due to two reasons: first, not all the precipitated proteins may have been resolubilized, and second, the precipitation conditions may have been more denaturing than those used with desalting columns, as SDS is added to solubilize the precipitated proteins. In any case, desalting columns proved to be more efficient at removing excess free biotin, achieving strong enrichment, and this method was also faster than methanol:chloroform precipitation, thereby reducing the workload.

Furthermore, it was assessed whether running the same sample through desalting columns twice would improve their efficiency and remove any remaining free biotin (if still present after a single run), potentially resulting in even better enrichment (Figure 3.3). However, no significant improvement was observed when using two desalting columns instead of one. On the contrary, small molecular weight proteins were no longer eluted from the columns after the second run. Therefore, as long as the desalting columns are not overloaded with crude extract and a reasonable amount of biotin (50-100 µM) has been provided to the system, one desalting column is sufficient to effectively remove excess free biotin.

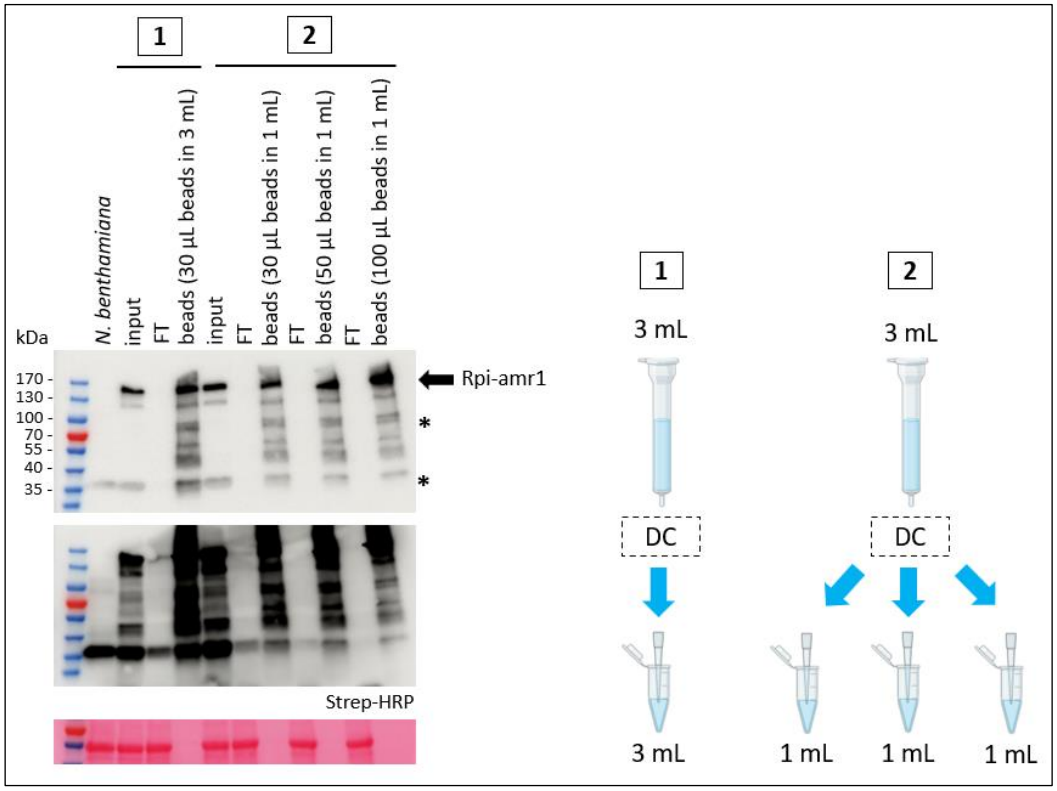


**Figure 3.4 At least 100 µL of beads are required to capture biotinylated proteins.**

Steptavidin pull-down and biotinylation of Rpi-amr1:TurboID-FLAG in WT *N. benthamiana*. *Agro*-infiltrations at $OD_{600}$ = 0.5 in 4-week-old *N. benthamiana* leaves in the presence of p19. Biotin-infiltration (50 µM) at 3 dpi and for 30 min before tissue harvesting. Pull-down was carried out with streptavidin beads followed by 7 M urea washing conditions. Lysates were resolved by SDS-PAGE. Biotinylated proteins were detected by using HRP-conjugated streptavidin labelling. Bands labelled with a black asterisk (*****) correspond to endogenously biotinylated proteins. Two samples (labelled 1 and 2) were run through a desalting column (DC); the second sample was split into three aliquots and different amount of beads were added (30, 50 and 100 µL). The flowthrough (FT), collected after streptavidin pull-down, was loaded side by side with the boiled beads (beads) to estimate the amount of biotinylated proteins remaining in the crude extract based on the amount of beads used. The "*N. benthamiana*" lane corresponds to non-infiltrated samples, meaning no TurboID-tagged baits were expressed and no biotin was added. It serves as control to show endogenous biotinylation.

To maximize the yield of enriching for biotinylated proteins, it is essential to identify the appropriate amount of streptavidin beads required for the experiment. This depends on the duration of the labelling period, the amount of plant tissues harvested, and the abundance of the bait protein. Hence, the amount of beads needed to capture most of the biotinylated proteins present in the samples was estimated (Figure 3.4). To achieve this, the flowthrough (FT), which is usually discarded

after performing streptavidin pull-down, was retained and run side by side with the boiled beads (beads) to determine how much biotinylated protein remained unbound.

Different bead volumes (30, 50 and 100 µL) were assessed, and it was found that at least 100 µL of beads per 1 mL of crude extract were required to capture most of the biotinylated proteins under these particular experimental conditions. When the membrane was overexposed, it was observed that when 30 µL of beads were added to 3 mL of crude extract, a significant amount of the TurboID-tagged bait (Rpi-amr1) was still detected in the flowthrough. Similarly, TurboID-tagged baits were present in the flowthrough when 30 µL of beads were added to 1 mL of crude extract, though in a lower proportion compared to the 3 mL condition. Only when 50 µL and then 100 µL of beads were added to 1 mL of crude extract did the flowthrough appear cleaner, although some endogenous biotinylated proteins were still detectable. In conclusion, the greater the number of biotinylated proteins in the samples, the more beads are required to ensure complete capture. This is particularly critical if target proteins are low-abundant, as there is a higher probability of abundant biotinylated proteins binding to the beads first, potentially leaving insufficient beads available to capture low-abundant proteins.

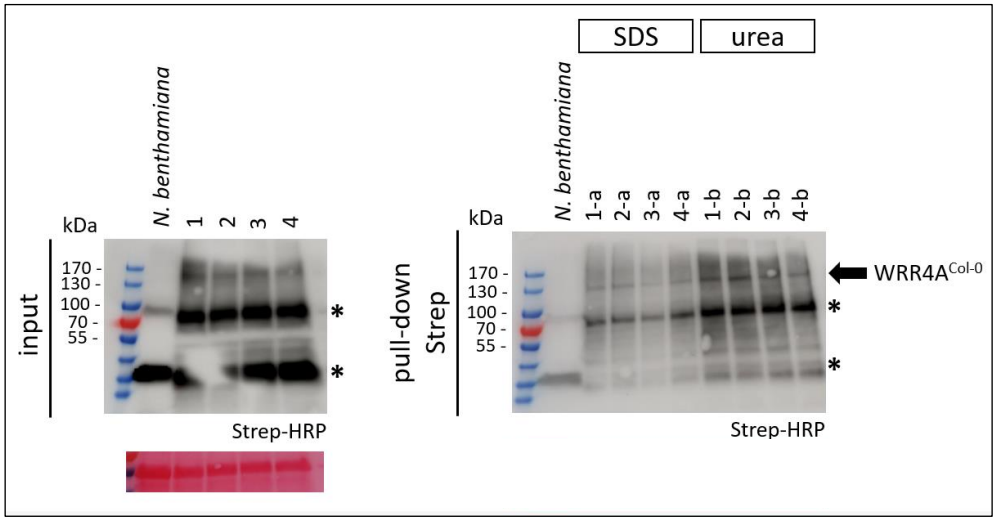


**Figure 3.5 7 M urea buffer is sufficient to effectively wash the beads.**

Streptavidin pull-down and biotinylation of WRR4A$^{Col-0}$:TurboID-V5 in *eds1 N. benthamiana*. *Agro*-infiltrations at $OD_{600}$ = 0.5 in 4-week-old *eds1 N. benthamiana* leaves in the presence of p19. Biotin-infiltration (50 µM) at 3 dpi and for 5 h before tissue harvesting. Pull-down was carried out with streptavidin beads. A small fraction of the beads was boiled and analysed by SDS-PAGE, while the remaining beads were used for LC-MS/MS analysis. Biotinylated proteins were detected by using HRP-conjugated streptavidin labelling. Bands labelled with a black asterisk (*****) correspond to endogenously biotinylated proteins. Each of the four samples (labelled 1, 2, 3 and 4) was split in half (labelled a and b) and each half was subjected to different washing conditions (2% SDS or 7 M urea). The "*N. benthamiana*" lane corresponds to non-infiltrated samples, meaning no TurboID-tagged baits were expressed and no biotin was added. It serves as control to show endogenous biotinylation.

The high-affinity interaction between biotin and streptavidin enables stringent washing conditions to remove any unbound proteins while retaining the captured biotinylated proteins. Ionic surfactants, such as SDS, are commonly used as they are among the strongest detergents. However, SDS is incompatible with MS analyses because it can inhibit enzymatic digestion and severely suppress the ionization of proteins and peptides. Consequently, additional downstream washing steps are necessary to ensure that all detergent is thoroughly removed from the sample before proceeding with MS analyses.

Therefore, different washing conditions were evaluated to shorten the workflow, comparing the use of 7 M urea to 2% SDS (Figure 3.5). The results showed that 7 M urea washing conditions were slightly less stringent than those with 2% SDS. However, while 2% SDS required at least eleven

washing steps, only six washes were needed with 7 M urea. As a result, 7 M urea was selected for all TurboID-directed IP and TurboID-MS experiments.

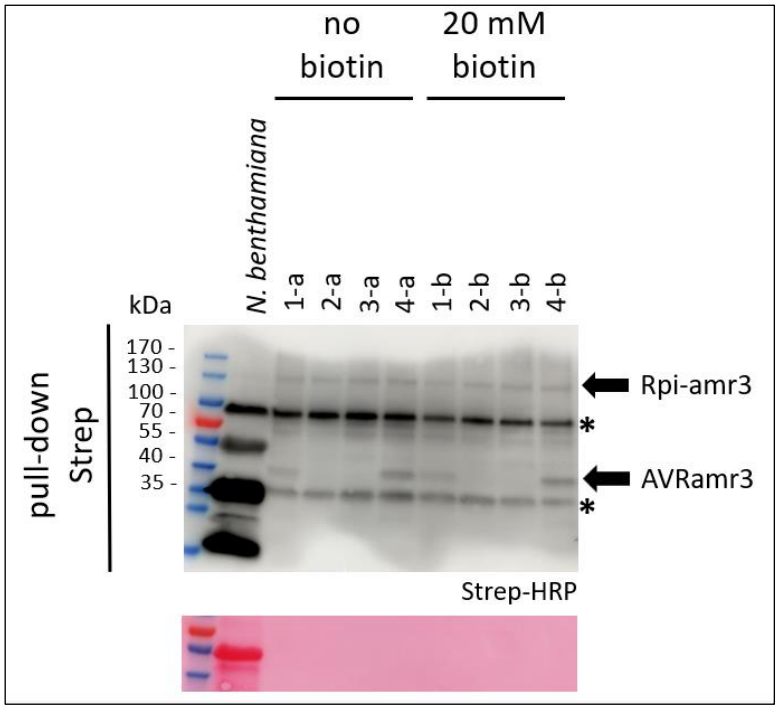


**Figure 3.6 Boiling the beads effectively releases biotinylated proteins.**

Streptavidin pull-down and biotinylation of Rpi-amr3:TurboID-FLAG with AVRamr3:V5 and *Nb*NRC2EEE:Myc in *nrc2/3/4 N. benthamiana*. *Agro*-infiltrations at $OD_{600}$ = 0.5 in 4-week-old *N. benthamiana* leaves in the presence of p19. Biotin-infiltration (50 µM) at 3 dpi and for 30 min before tissue harvesting. Pull-down was carried out with streptavidin beads followed by 7 M urea washing conditions. Lysates were resolved by SDS-PAGE. Biotinylated proteins were detected by using HRP-conjugated streptavidin labelling. Bands labelled with a black asterisk (*****) correspond to endogenously biotinylated proteins. The beads of the four samples (labelled 1, 2, 3 and 4) were split in half (labelled a and b) and each were subjected to different bead-boiling conditions: without adding biotin to the beads, or with 20 mM biotin added to the beads before boiling to verify that no biotinylated proteins re-attach to the beads. The "*N. benthamiana*" lane corresponds to non-infiltrated samples, meaning no TurboID-tagged baits were expressed and no biotin was added. It serves as control to show endogenous biotinylation.

Finally, it was confirmed that boiling the beads was sufficient to fully release all the captured biotinylated proteins when performing immunoblots. While the strong biotin-streptavidin interaction enables stringent washing conditions, it can also impede the efficient elution of biotinylated proteins from the beads. This is particularly true for highly biotinylated proteins, which can interact with multiple streptavidin molecules, making them especially difficult to elute.

To address this, two approaches were tested: boiling the beads without adding biotin and boiling them with 20 mM biotin added to the samples (Figure 3.6). The rationale behind adding biotin was that, once the proteins were eluted from the streptavidin molecules, the free biotin would competitively bind to streptavidin and prevent the proteins from reattaching. However, no significant improvement was observed with the addition of 20 mM biotin, indicating that boiling the beads alone is sufficient for efficient elution.

## 3.3 Discussion

In contrast to its widespread use in animal systems, the application of PL in plant immunity remains underexplored. PL methods are powerful and versatile tools, but the experimental design should be carefully tailored to align with your specific goals and identify the most relevant candidates for subsequent validation. While biotinylating proteins is relatively straightforward, the real challenge lies in performing the experiment under optimal conditions that distinguish genuine interactions from false positives while minimizing background noise. Below are some suggestions to consider when implementing TurboID, based on the experiments presented in this chapter as well as those in Chapter 4.

There are various methods to introduce biotin into a system, including syringe infiltration, vacuum infiltration, submerging plant tissues, or incorporating it into the growth media of the organism being studied. According to Mair et al. (2019), these methods show no significant differences in biotinylation efficiency. However, it is important to consider the amount of biotin provided to the system. While endogenous biotin concentrations in plants are sufficient to induce low-level protein labelling, most applications require strong enhancement and time-regulated labelling through the addition of exogenous biotin. Although excessive biotin does not affect immunoblots, it can interfere with protein purification using streptavidin beads. Specifically, free biotin (unbound to protein residues) must be removed from plant extracts before adding streptavidin beads, to ensure that the

beads capture only biotinylated proteins for successful enrichment (Figures 3.2 and 3.3). If excessive biotin is used, it may not be completely depleted from the samples, leading to inefficient enrichment. In our case, desalting columns were effective at depleting free biotin from the samples (Figures 3.2 and 3.3).

While increasing the amount of plant material may seem like an effective way to improve protein coverage, it also requires a corresponding increase in the amount of beads needed to ensure the effective retrieval of all biotinylated proteins (Figure 3.4). TurboID is highly effective at biotinylating a large pool of proteins, and to capture them all without loss, an increased amount of beads is necessary. The required amount of beads should be determined empirically (e.g., Figure 3.4). This is especially important if a target protein is low in abundance (such as native effectors in our case), as the beads will first become saturated with the most abundant biotinylated proteins.

Washing away non-biotinylated proteins during the enrichment step, which takes advantage of the high-affinity interaction between biotin and streptavidin, is crucial to limit false positives. This can be effectively achieved under 7 M urea conditions, which are safer for the mass spectrometry equipment and less labour-intensive (Figure 3.5).

The fusion of the PL enzyme to the bait protein is not expected to interfere with its localization or function. To confirm this, confocal microscopy and/or complementation tests should be performed to verify the correct targeting and functional maintenance of the tagged bait protein. We incorporated an 11-amino acid linker between the bait and TurboID, which may provide additional flexibility. However, we did not explicitly verify whether the absence of this short linker would affect the function of the baits. Nonetheless, all baits were tested and found to be functional, as demonstrated in the complementation experiments presented in the following chapters. If necessary, a short linker can be added between the bait protein and the PL enzyme to provide further flexibility. However, it is important that the linker remains relatively short to ensure that the enzyme stays in close proximity to the bait protein.

It is crucial to consider the abundance of the bait protein when using TurboID. If the bait protein is too low in abundance, it will be challenging to detect biotinylated candidates. Conversely, if the bait is too abundant, there is a risk of non-specific biotinylation as the cell may become saturated with TurboID-tagged baits. This can lead to random protein interactions without meaningful biological

output. This issue is illustrated in Chapter 4, where the specific biotinylation of the *Albugo candida* effector CCG28 by its corresponding TurboID-tagged sensor TNL WRR4A was observed only after switching from a high-expression 35S promoter-driven to a medium-expression pAt2 promoter-driven system (Chapter 4; Figures 4.15, 4.16, 4.17). Therefore, the choice of promoter for the tagged bait protein is critical to achieve optimal protein accumulation, neither too low nor too abundant. Ideally, the native promoter of the bait should be used to better reflect physiological conditions. Several stable Arabidopsis TurboID transgenic lines were generated, some of which are used in Chapters 4 and 5, with most baits expressed under their native promoters (Chapter 5, Table 5.1). Additionally, the abundance of the target proteins should also be considered, if predictable. Less abundant target proteins, like native effectors, are harder to detect by mass spectrometry, as detailed in Chapter 4.

PL techniques generate large datasets, so including appropriate controls and performing biological replicates is essential to reduce false positives and false negatives. The control protein should have a similar, or at least overlapping, localization pattern and an equivalent expression level to that of the bait protein. In our TurboID-MS experiments, we used commonly applied control proteins, such as fluorescent proteins tagged with a PL enzyme. Specifically, we used mCherry, which localized to the cytoplasm and nucleus, as the precise localization of our various baits was not determined (see Chapters 4 and 5). If available, a functional mutant of the corresponding bait protein can also serve as a control. It is important to match the expression levels between the bait and control proteins; a control with higher expression may lead to false negatives, while one with lower expression may lead to false positives. For this reason, all experiments presented in the following chapters were conducted with a control protein exhibiting protein accumulation as close as possible to that of the baits (see Chapter 5, Supplementary Figures 5.1 and 5.2 for the protein expression levels of the different Arabidopsis *thaliana* TurboID transgenic lines generated).

Lysines are the primary residues biotinylated by PL enzymes. However, if target proteins contain only a small number of lysines (e.g., small proteins like effectors), if these lysines are buried within the protein structure and inaccessible to the enzyme, or if they are modified by post-translational modifications such as ubiquitination or acetylation, biotinylation may not occur. This could potentially lead to false negatives.

In this study, trypsin, an enzyme that cleaves peptide bonds specifically at the carboxyl (C-terminal) side of lysine and arginine residues, was used to digest biotinylated proteins, even though TurboID predominantly biotinylates lysine residues, which could potentially interfere with trypsin's cleavage efficiency. Despite this modification, trypsin digestion did not appear to be significantly affected in our experiments. This may be because biotinylation occurs on the ε-amino group of lysines, while trypsin recognizes and cleaves at the peptide bond at the carboxyl end of the lysine residue, which may remain accessible. Alternatively, the steric hindrance caused by biotin may not be sufficient to block enzymatic access. In our TurboID method, we did not identify biotinylated peptides directly, but rather other peptides that enabled protein identification. Furthermore, while not all lysines are necessarily accessible for biotinylation, most become accessible to trypsin following denaturation. Other proteases, such as chymotrypsin, Asp-N, or Glu-C, can also be considered for protein digestion, depending on the experimental needs and the extent of lysine modification.

While TurboID has demonstrated robust performance in various cellular compartments, including those with slightly acidic to neutral pH such as the endoplasmic reticulum, nucleus, and mitochondria, highly acidic environments like the vacuole or apoplast in plant cells may not provide optimal conditions for its activity. Furthermore, fluctuations in pH during stress responses, for example during ROS bursts, could also impact the labelling efficiency of TurboID.

In previous studies using TurboID, labelling times ranged from 3 to 24 hours (Arora et al., 2020), despite the catalytic reaction itself takes only about 10 minutes. In general, it is not recommended to exceed 3 hours of labelling. Additionally, multiple short labelling periods (i.e., several time points) can be used instead of a single prolonged labelling period. Excessively long labelling times increase background biotinylation noise, making it more difficult to identify relevant candidates. In Chapter 4, specific biotinylation of the *Albugo candida* effector CCG28 by its corresponding TurboID-tagged sensor TNL WRR4A was observed not only by switching from a high-expression promoter-driven system to a medium-expression promoter-driven system, but also by shortening the labelling time from 5 hours to just 30 minutes (Chapter 4; Figures 4.15, 4.16, 4.17). For TurboID-MS experiments carried out in stable Arabidopsis transgenic lines under native promoter expression, a 3-hour labelling time was used (see Chapters 4 and 5). In contrast, for TurboID-directed IP experiments conducted transiently in *N. benthamiana*, often under 35S promoter-driven systems, a 30-minute labelling time was sufficient to observe the biotinylation of the expected candidate proteins (see Chapters 4 and 6). Therefore, to enhance the likelihood of capturing meaningful targets, shorter

labelling times, which can be combined with multiple time points, are more effective, especially since the precise timing of these potentially significant interactions is often unknown. Initially, 2 days post *P. infestans* zoospore infiltration was used to identify biotinylated native AVRamr effectors. However, we later found that this time point was too early, and it was only at 3 and 4 days post *P. infestans* zoospore infiltration that these effectors were detectable by mass spectrometry (see details in Chapter 4).

Optimizing experimental conditions for specific purpose can be achieved by adjusting the various aspects of the protocol mentioned above. Immunoblots are useful for testing different combinations and fine-tuning parameters to design experimental layout. However, this requires the effective release of biotinylated proteins from the beads, which can be accomplished by simply boiling the beads without adding biotin (Figure 3.6). It is important to note that the signal intensity observed on a Western blot does not necessarily reflect the overall amount of biotinylated protein, as proteins with multiple binding sites for streptavidin can amplify the signal. Additionally, the signal intensity will depend on the number of accessible biotinylation sites within a protein. As a result, the signal intensity does not directly correspond to the number of biotinylated proteins and is not a 1:1 ratio.

A study comparing PL-MS and IP-MS (Moreira et al., 2023), found surprisingly little concordance between the PPIs identified by these two approaches, even though both methods successfully identified meaningful PPIs. While affinity capture provides a snapshot of stable PPIs at the time of lysis, PL captures a history of protein interactions occurring during the labelling period, which may bias detection away from stable “core” complexes and toward more dynamic associations. Furthermore, the population of candidate proteins was observed to decrease as bait protein localization became more confined during pull-down experiments; however, this candidate population is less variable compared to PL approaches. Despite the variability in the precision and efficiency of PL techniques, which often leads to limited reproducibility in proteomic detection, PL generally generates larger interactomes. Overall, these findings highlight that the utility of each method is context-dependent, emphasizing that PL and affinity capture should be regarded as complementary approaches rather than interchangeable alternatives.

While the identification of known interactors helps validate the quality of the data, PL techniques primarily generate promising leads. Therefore, novel candidates identified through these methods require further validation using additional experiments, such as yeast two-hybrid (Y2H), co-

immunoprecipitation (Co-IP), bimolecular fluorescence complementation assays (BiFC), split luciferase assays, reciprocal PL-MS, or FRET-FLIM. However, conventional approaches may not consistently confirm candidates, particularly when analysing transient, weak, or hydrophobic PPIs due to their inherent limitations. Consequently, genetic assays may be necessary to demonstrate their biological relevance.

There is no single “perfect” method for all situations, and PL techniques have their own strengths and weaknesses. However, by focusing on leveraging these strengths and addressing their drawbacks, future advancements in PL methods hold significant promise. Further development and optimization could enable PL techniques to play an increasingly important role in tackling diverse biological questions in plant science. Moreover, integrating PL approaches with existing techniques will undoubtedly drive progress in the near future.

For instance, the combination of clustered regularly interspaced short palindromic repeats (CRISPR) with PL has already facilitated the study of protein-DNA interactomes at specific loci and enabled the mapping of RNA-binding protein complexes (Myers et al., 2018, Yi et al., 2020). PL techniques can also be combined with post-translational modification (PTM) studies to help dissect the regulatory mechanisms underlying dynamic changes. For example, this approach has been applied to track dynamic changes in protein complexes associated with *O*-GlcNac-modified targets, where a “GlycoID” system was developed by coupling miniTurboID with an *O*-GlcNac reader, GafD (Liu et al., 2022). Finally, PL methods can be integrated with cross-linking MS and single-cell proteomics to construct a plant cell atlas, which would be a valuable resource for the plant research community (Perkel, 2021, Petelski et al., 2021, Rhee et al., 2019).

# Chapter 4

## Capturing cognate effectors to NLRs during native infection by TurboID proximity labelling

# 4. Capturing cognate effectors to NLRs during native infection by TurboID proximity labelling

## 4.1 Introduction

### 4.1.1 Prediction and discovery of effectors

Plant-pathogen interactions are dynamic, with the behaviour of both plants and pathogens influencing each other in complex ways. Pathogens evolve to evade the plant's immune responses, while the plant's immune system works to counteract pathogen infections, creating a continuous back-and-forth interaction (Raffaele et al., 2010). Pathogens can secrete small virulence proteins, called effectors, which play a central role in determining the outcome of plant-pathogen interactions (Sánchez-Vallet et al., 2018). These effectors can manipulate the host and promote infection. However, they can be double-edged sword, as some effectors can be recognized by specific immune receptors that evolved to detect pathogen presence, triggering defense responses in disease-resistant plants (Hogenhout et al., 2009). Therefore, characterizing effector recognition by their cognate immune receptors and understanding the downstream immune signalling cascades are essential for gaining a deeper understanding of the mechanisms underlying pathogenicity and host resistance. This knowledge also contributes to the development of novel plant disease control strategies (Vleeshouwers and Oliver, 2014).

Effectors are classified into apoplastic or cytoplasmic effectors, depending on whether they perform their function in the apoplast or within the plant cell, respectively, after being translocated from the pathogen. Pathogens use various mechanisms to deliver effectors into host cells, with the type-III secretion system (T3SS) of Gram-negative bacterial pathogens being the best characterized. The T3SS encodes a syringe-like structure that directly injects effectors into plant cells (Green and Mecsas, 2016). However, this mechanism is not conserved across all bacteria; Gram-positive pathogens and certain phloem and xylem-colonizing bacteria lack the T3SS. In these bacteria, the secretion of effectors relies on the presence of an N-terminal signal peptide (SP) (Natale et al., 2008, Nielsen and Krogh, 1998). The identification of candidate secreted proteins was greatly enhanced through computational tools designed to predict SPs. The first publicly available program for SP prediction, SignalP, was released in 1998 (Nielsen and Krogh, 1998). The most recent version is SignalP 6.0 (Teufel et al., 2022). The identification of an N-terminal SP is also a key criterion for predicting

effectors in filamentous eukaryotic pathogens, including fungi and oomycetes (Petre and Kamoun, 2014). In fungi, most effectors are small and rich in cysteine residues. Although these features have not been directly linked to entry into host cells, they have been widely used as predictive markers for fungal effectors (Sperschneider et al., 2015). In contrast, the prediction of effectors in oomycete pathogens is more reliable, thanks to the discovery of host-targeting motifs in the N-terminal region of cytoplasmic effectors, downstream of the SP. Most of these effectors in downy mildews contain the RXLR-dEER motif, which is involved in translocation into plant cells (Birch et al., 2008, Whisson et al., 2007). Additional motifs, such as LFLAK and CHXC (unique to Albuginales), have also been identified and, when combined with the secretion SP, have contributed to defining effectors repertoires in oomycetes, particularly in *Phytophthora* species (Jiang et al., 2008), where these motifs have been most extensively characterized. No eukaryote-specific functional domain for the uptake of fungal effectors has been defined yet, which limits the effectiveness of motif-based database searches for identifying fungal effectors.

The rapid accumulation of pathogen genome data (Amselem et al., 2011, Cuomo et al., 2007, Dean et al., 2005, Haas et al., 2009), coupled with specialized bioinformatic pipelines and prediction software, has significantly improved the identification of secreted proteins involved in plant-pathogen interactions. Many of these secreted proteins, particularly those expressed during plant infection, are likely to function as effectors. However, predictions of effector proteins still require validation through experimental approaches. A notable example highlighting this is the *Magnaporthe oryzae* effector MC69, which is crucial for appressorium formation and was the only candidate among 1,306 putative secreted proteins found to be involved in pathogenicity following large-scale gene disruption (Saitoh et al., 2012).

Many effectors are recognized by host resistance proteins and can be identified in bioassays as molecules that trigger localized immune receptor-dependent cell death (hypersensitive response or HR), a defense mechanism that can limit pathogen spread. Such recognized effectors were called avirulence (Avr) proteins because they make the pathogen avirulent, preventing it from causing disease in resistant plants. Avirulence function can be assayed through transient Agrobacterium-mediated transformation (Vleeshouwers et al., 2008). This method allows testing the function of a candidate effector by heterologously expressing it *in planta*. These assays are often conducted in the model plant *N. benthamiana*, which is infiltrated with transformed *Agrobacterium* that delivers the effector gene into the plant cell for transient protein production (Ma et al., 2012). However, in the

absence of the corresponding resistance protein, many effectors cannot be identified based solely on their avirulence function. Therefore, demonstrating their virulence function remains the gold standard for validation. Genome-wide association studies (GWAS) and quantitative trait locus (QTL) mapping of the pathogen can identify loci associated with heritable phenotypic variations, such as virulence (Plissonneau et al., 2017). Nevertheless, functional screening of effectors that activate defense in resistant cultivars or wild relatives of crops has proven useful in identifying immune receptors, which can be incorporated into elite cultivars to enhance disease resistance (Lin et al., 2022).

### 4.1.2 Proximity labelling used for unbiased effector discovery *in planta*

While the translocation of many effectors has been demonstrated using overexpression reporter systems, these artificial conditions do not fully capture the dynamics of natural infection. A major challenge in confirming effectors during natural infection lies in the difficulty of detecting native effectors, which are often present in very low abundance within host cells. To address this, the sensitivity of proximity labelling (PL) techniques could be leveraged as a novel approach for identifying effectors under native conditions.

To date, relatively few studies have used PL to characterize effector-host interactions. Low effector protein levels *in planta* pose a significant challenge for identifying host target proteins, and conventional techniques often fail to capture the complexity, dynamics, and transient nature of effector-target interactions. One reported translocation assay used biotinylation of effectors in the host cytoplasm as a marker for their uptake (Lo Presti et al., 2017). This assay takes advantage of the bacterial biotin ligase BirA, which can biotinylate any protein carrying a short peptide tag (Avitag). It relies on the stable expression of BirA in the cytoplasm of maize plants and the engineering of *Ustilago maydis* strains in which two effectors are tagged with the Avitag. *Ustilago maydis* is a plant fungal pathogen responsible for corn smut in many important crops and grasses, including maize (*Zea mays*) (Doehlemann et al., 2008, Kahmann and Kämper, 2004). A biotinylated effector would confirm that the tagged effector had come into proximity with the biotin ligase in the host cytoplasm. Using this assay, the translocation of several effectors has been demonstrated (Lo Presti et al., 2017), although translocation to the host cell alone does not confirm effector function. *U. maydis* encodes approximately 460 effectors, though only a few have been functionally characterized (Lanver et al., 2017). Later, using the same *U. maydis*-maize system, researchers generated transgenic *U. maydis*

strains that secrete TurboID-tagged See1 effector directly into maize cells (Shi et al., 2023). In the absence of See1, *U. maydis* is unable to trigger tumour formation. Previous studies had already shown, through a yeast two-hybrid (Y2H) screen, that See1 interacts with maize SUPPRESSOR OF G2 ALLELE OF skp1 (SGT1), a protein involved in cell cycle transitions, and blocks its phosphorylation (Redkar et al., 2015). The researchers performed TurboID-based PL in combination with Co-IP and mass spectrometry analyses, identifying additional See1 interactors, including three proteins related to the ubiquitin-proteasome pathway (Shi et al., 2023). These findings offer deeper insight into the role of See1 in tumour formation during *U. maydis*-maize interaction. Recently, miniTurbo was shown to be valuable for identifying host targets of nematode effectors (Margets et al., 2024). CYSTEINE PROTEASE 1 (CPR1) from soybean cyst nematodes was predicted to be a secreted effector based on transcriptomic data, the presence of a signal peptide, and the absence of transmembrane domains. Moreover, CPR1 is conserved across all sequenced soybean cyst nematode isolates and suppresses RPS5-mediated cell death in *N. benthamiana*, suggesting its role in virulence. MiniTurbo-tagged CPR1, expressed in transgenic soybean roots, facilitated the identification of soybean BRANCHED-CHAIN AMINO ACID AMINOTRANSFERASE 1 (GmBCAT1) as a substrate for CPR1, which was confirmed by Co-IP and proteolytic cleavage assays (Margets et al., 2024).

One advantage of TurboID-tagging the effector is that by placing the PL enzyme on the effector, it enables the capture of interactions with multiple host proteins, which can disrupt single or various biological pathways to promote virulence. For example, the HopM1 effector from *Pseudomonas syringae* ensures full virulence by targeting five different Arabidopsis proteins related to the ubiquitin-proteasome system: MIN7, MIN10, UPL1, UPL3 and ECM29 (Üstün et al., 2016). Similarly, the *M. oryzae* effector AvrPiZ-t targets the Nup98 homolog APIP12 and the E3 ligases APIP6 and APIP10 in rice thus promoting disease (Park et al., 2012, Park et al., 2016, Tang et al., 2017). Additionally, placing the TurboID tag on the effector may help overcome the challenge of low effector abundance under native conditions by selectively enriching for host proteins. However, limitations of this approach include the need for prior knowledge of the effector being studied to explore its interactome, as well as the requirement that the pathogen be amenable to genetic recombination.

TurboID-tagging of R proteins or presumed host target proteins, rather than the effector itself, has not been attempted before. This novel approach could enable the identification of both known and unknown effectors. However, it comes with its own challenges, as it indiscriminately captures both pathogen-related and plant proteins. Since plant proteins are much more abundant than pathogen-

related ones, detecting potential effectors becomes more difficult. On the other hand, this approach not only captures the effector but also provides valuable insights into the plant's downstream signalling pathways.

First, we needed to establish the protocol and demonstrate its feasibility. To do so, we chose to work with nucleotide-binding leucine-rich repeat receptors (NLRs), which are typically responsible for the intracellular detection of effectors, while receptor-like proteins (RLPs) and receptor-like kinases (RLKs) play a role in pathogen recognition at the plant surface. As a proof of concept, we tested two different systems: 1) the transient *Agro*-mediated expression of two TurboID-tagged CNLs, Rpi-amr1 and Rpi-amr3, followed by infection by zoospore infiltration with *P. infestans* in *N. benthamiana*, and 2) the stable expression of a TurboID-tagged TNL, WRR4A, in a transgenic *Arabidopsis thaliana* line infected with *Albugo candida*.

## 4.2 Results

A major challenge in effector discovery during natural infection is their very low abundance within host cells. While TurboID is widely used to identify plant-related interactors, no one has yet attempted to exploit its sensitivity to capture effectors under native infection conditions. This is what we aimed to achieve by TurboID-tagging NLRs and utilizing either a transient system in *N. benthamiana* or a stable transgenic line in *A. thaliana*.

### 4.2.1 Identification of native AVRamr effectors through TurboID proximity labelling following *Phytophthora infestans* infection

*P. infestans* is an oomycete that causes late blight and is responsible for one of the most well-known plant disease outbreaks in human history, the Irish potato famine of the late 1840s. *P. infestans* continues to cause significant losses in global potato production today (Kamoun et al., 2015). In efforts to reduce these losses, breeders have sought resistance genes from wild potato relatives (Vleeshouwers et al., 2011). Unlike wild potatoes, many *Solanum* species are nonhost to *P. infestans*, meaning they are naturally resistant. Two Resistance to *P. infestans* (Rpi) genes, Rpi-amr1 and Rpi-amr3, encoding CNL proteins, were cloned from *Solanum americanum* and confer resistance to *P. infestans* in cultivated potatoes (Witek et al., 2016, Witek et al., 2021). The effector AVRamr1, recognized by Rpi-amr1, was identified through cDNA pathogen enrichment sequencing (Lin et al.,

2020), while AVRamr3, recognized by Rpi-amr3, was identified by screening an RXLR effector library (Lin et al., 2022). Co-IP experiments showed that AVRamr3 directly interacts with Rpi-amr3 (Lin et al., 2022). By transiently expressing TurboID-tagged Rpi-amr1 and Rpi-amr3 in *N. benthamiana*, we aimed to determine whether we could detect biotinylated AVRamr1 and AVRamr3, respectively, by mass spectrometry following *P. infestans* infection. If the pathosystem is reproducible in *N. benthamiana* through *Agro*-mediated transient expressing of TurboID-tagged baits, its fast turnover enables rapid testing before committing to the generation of transgenic lines, which can take time.

TurboID and miniTurbo (miniID) tagged Rpi-amr1 and Rpi-amr3 constructs were generated by Golden Gate cloning (Table 4.1). Their functionality was tested, and Rpi-amr1:TurboID supported HR in *N. benthamiana* without auto-activity (Figures 4.1). Rpi-amr3:TurboID also supported HR but was slightly auto-active (Figure 4.2); however, this low level of auto-activity was NRC-dependent and therefore not observed in the *nrc2/3/4* mutant background (Figure 4.3), making the construct suitable for use in that context. In addition, a miniTurbo-tagged version of Rpi-amr3 was generated, which supported HR without auto-activity (Figure 4.4).

**Table 4-1 List of the TurboID- or miniTurbo-tagged proteins generated by Golden Gate cloning and used in *N. benthamiana*.**

The promoters and terminators that were used to perform these DNA assemblies are as follow: p35S = cauliflower mosaic virus 35S promoter, t35S = cauliflower mosaic virus 35S terminator, tOCS = *Agrobacterium tumefaciens* octopine synthase gene terminator.

| Protein | Construct |
|---|---|
| *Sa*Rpi-amr1 | p35S:Rpi-amr1:TurboID-FLAG:tOCS |
| *Sa*Rpi-amr3 | p35S:Rpi-amr3:TurboID-FLAG:tOCS |
| *Sa*Rpi-amr3 | p35S:Rpi-amr3:V5-miniID:t35S |

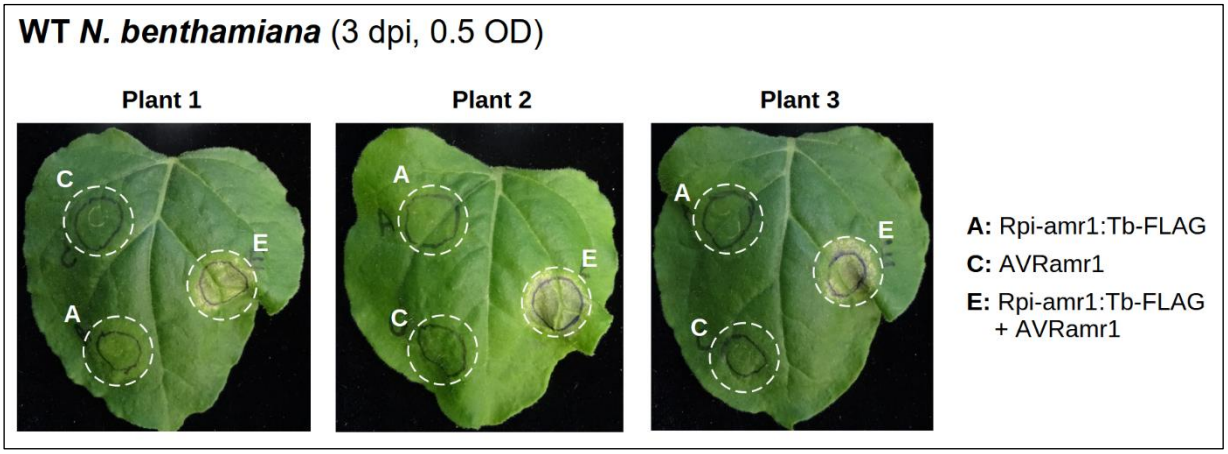


**Figure 4.1 Rpi-amr1:TurboID-FLAG supports HR in *N. benthamiana*.**

HR assays by *Agro*-infiltration at $OD_{600}$ = 0.5 in 4/5-week-old *N. benthamiana* leaves and at 3 dpi. The *P. infestans* effector AVRamr1 is recognized by the *S. americanum* NLR protein Rpi-amr1 (Lin et al., 2020). Co-delivery of 35S promoter-driven Rpi-amr1:TurboID-FLAG (Rpi-amr1:Tb-FLAG) with AVRamr1:V5 triggers HR in WT *N. benthamiana* leaves.

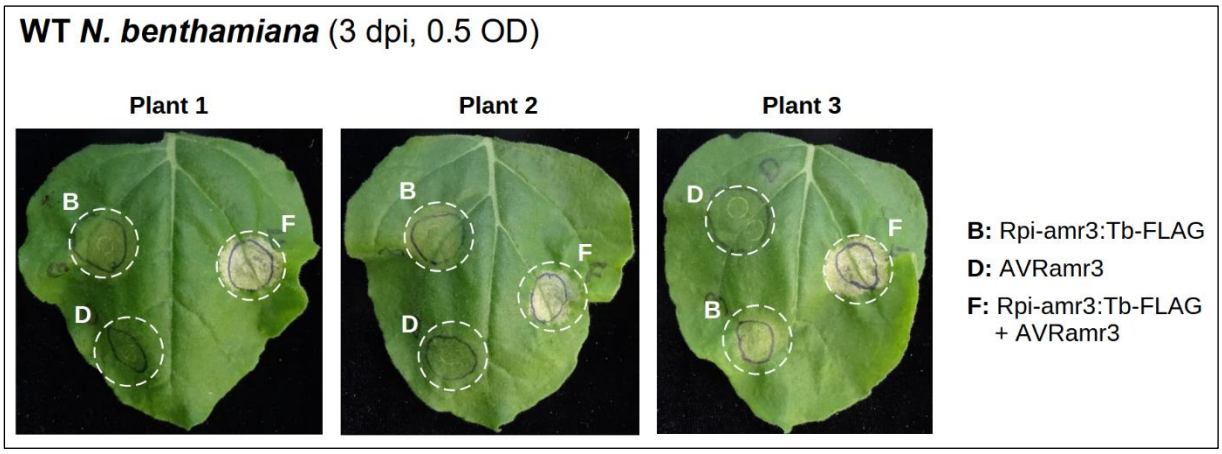


**Figure 4.2 Rpi-amr3:TurboID-FLAG supports HR in *N. benthamiana*.**

HR assays by *Agro*-infiltration at $OD_{600}$ = 0.5 in 4/5-week-old *N. benthamiana* leaves and at 3 dpi. The *P. infestans* effector AVRamr3 is recognized by the *S. americanum* NLR protein Rpi-amr3 (Lin et al., 2022). Co-delivery of 35S promoter-driven Rpi-amr3:TurboID-FLAG (Rpi-amr3:Tb-FLAG) with AVRamr3:V5 triggers HR in WT *N. benthamiana* leaves.

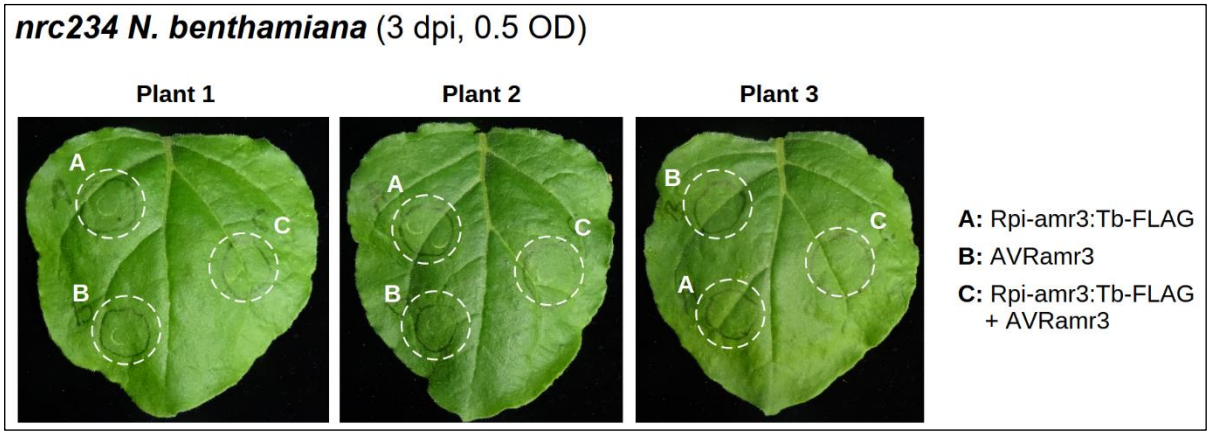


**Figure 4.3 Rpi-amr3:TurboID-FLAG alone does not trigger HR in *nrc2/3/4 N. benthamiana*.**

HR assays by *Agro*-infiltration at $OD_{600}$ = 0.5 in 4/5-week-old *nrc2/3/4 N. benthamiana* leaves and at 3 dpi. The *P. infestans* effector AVRamr3 is recognized by the *S. americanum* NLR protein Rpi-amr3 (Lin et al., 2022). Co-delivery of 35S promoter-driven Rpi-amr3:TurboID-FLAG (Rpi-amr3:Tb-FLAG) with AVRamr3:V5 does not trigger HR in *nrc2/3/4 N. benthamiana* leaves. As expected, Rpi-amr3:Tb-FLAG alone is insufficient to mediate immune recognition in the absence of NRCs.

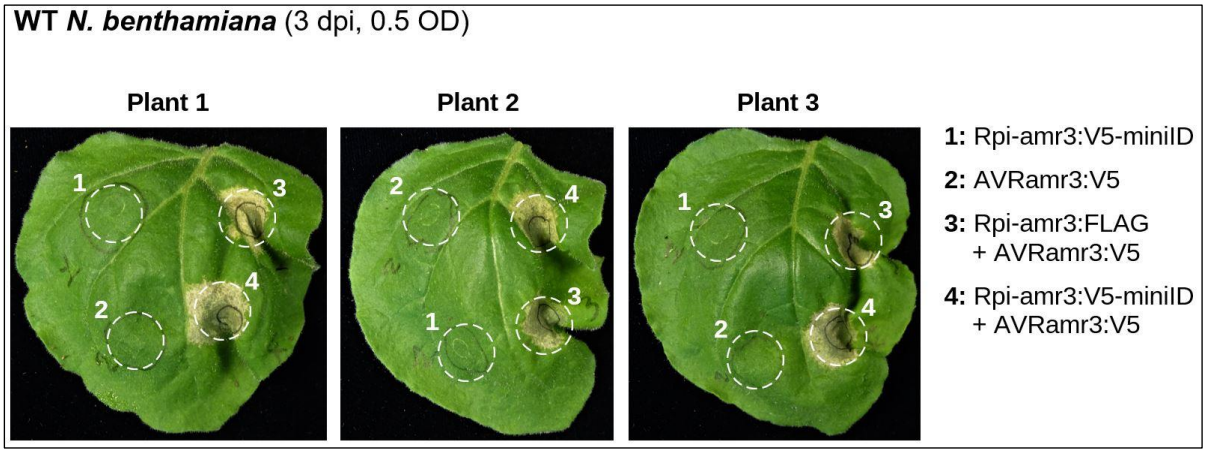


**Figure 4.4 Rpi-amr3:V5-miniTurbo supports HR in *N. benthamiana*.**

HR assays by *Agro*-infiltration at $OD_{600}$ = 0.5 in 4/5-week-old *N. benthamiana* leaves and at 3 dpi. The *P. infestans* effector AVRamr3 is recognized by the *S. americanum* NLR protein Rpi-amr3 (Lin et al., 2022). Co-delivery of 35S promoter-driven Rpi-amr3:FLAG or Rpi-amr3:V5-miniTurbo (Rpi-amr3:V5-miniID) with AVRamr3:V5 triggers HR in WT *N. benthamiana* leaves.

Once the functionality of the TurboID-tagged constructs was verified, we aimed to confirm that the small sizes of AVRamr1 (33 kDa) and AVRamr3 (28 kDa), which contain 28 and 31 lysine residues respectively (the protein residue primarily biotinylated by TurboID), were sufficient for biotinylation and detection *via* immunoblot. To test this, AVRamr1 with Rpi-amr1:TurboID and AVRamr3 with Rpi-

amr3:miniTurbo, all under 35S promoters, were transiently expressed in *nrc2/3/4 N. benthamiana* (Figure 4.5). Rpi-amr1 and Rpi-amr3 depend on the NRC class helper NLRs to trigger cell death (Lin et al., 2022, Witek et al., 2021). Therefore, *N. benthamiana nrc2/3/4* mutants were used to prevent HR from being triggered. AVRamr1 and AVRamr3 can be used as negative controls for each other. Since these effectors are specifically recognized by their cognizant NLRs, each effector was used as control for the other in a reciprocal manner to ensure recognition-specific biotinylation. After 30-minute labelling, the biotinylation of AVRamr1 and AVRamr3 by Rpi-amr1:TurboID and Rpi-amr3:miniTurbo, respectively, was detectable by immunoblot, indicating that these effectors can be biotinylated in a specific manner (Figure 4.5). However, this was achieved with an overexpression reporter system, which does not fully reflect natural infection. Therefore, we next aimed to detect these biotinylated effectors by mass spectrometry and under native infection conditions (Figure 4.6).

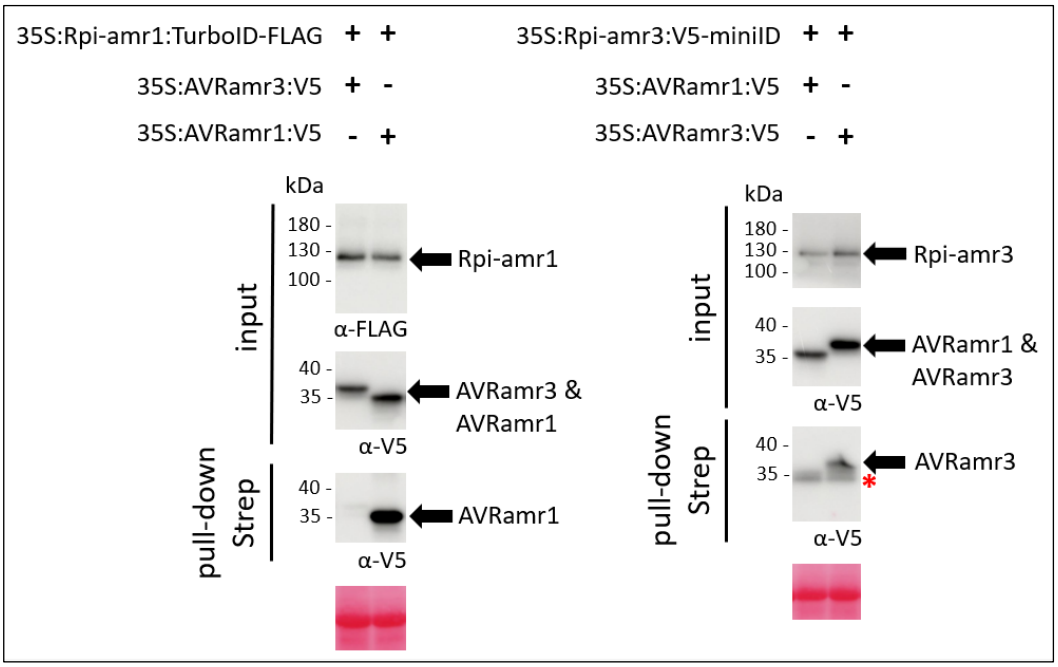


**Figure 4.5 TurboID and miniTurbo-tagged Rpi-amr1 and Rpi-amr3 specifically biotinylate AVRamr1 and AVRamr3 respectively.**

Streptavidin pull-down and biotinylation of AVRamr1:V5 and AVRamr3:V5 by Rpi-amr1:TurboID-FLAG and Rpi-amr3:V5-miniTurbo respectively in *nrc2/3/4 N. benthamiana* after 7 M urea washing conditions. *Agro*-infiltrations at $OD_{600}$ = 0.5 in 4-week-old *nrc2/3/4 N. benthamiana* leaves in the presence of p19. Biotin-infiltration (50 µM) at 3 dpi and for 30 min before tissue harvesting. Pull-down was carried out with streptavidin beads. Lysates were resolved by SDS-PAGE. Unspecific bands are indicated with a red asterisk (*).

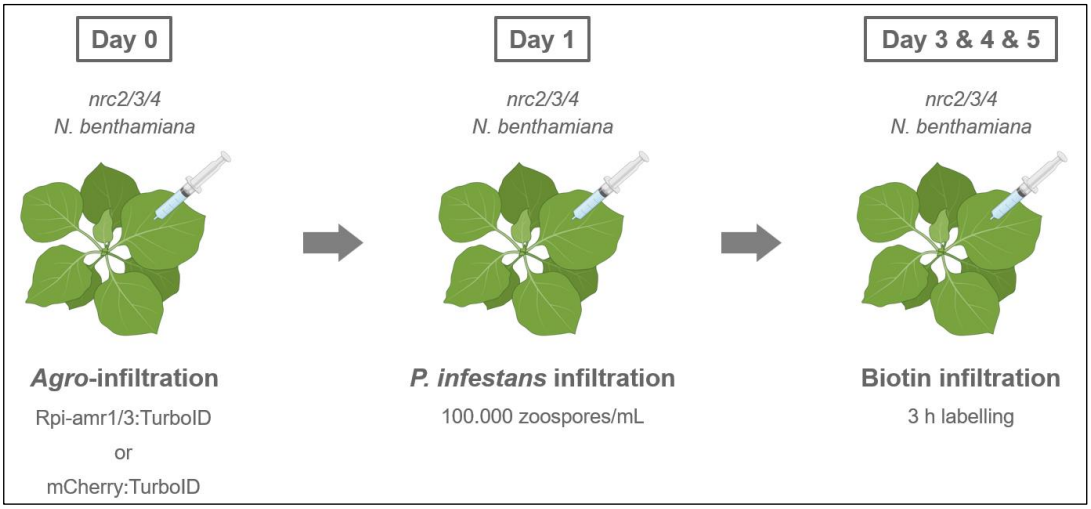


**Figure 4.6 Schematic representation of the experimental design used to identify pathogen and plant interactors of Rpi-amr1 and Rpi-amr3.**

*Agro*-infiltrations of 35S:Rpi-amr1:TurboID-FLAG, 35S:Rpi-amr3:TurboID-FLAG or pAt2:mCherry:TurboID-V5 at $OD_{600}$ = 0.5 in 4-week-old *nrc234 N. benthamiana* and in the presence of p19, followed by *P. infestans* (isolate 88069) infiltration (100,000 zoospores/mL) one day later. Biotin-infiltration (50 µM) was performed at 3, 4 and 5 days post *Agro*-infiltration (so 2, 3 and 4 days post *P. infestans* infiltration) and for 3 h before tissue harvesting.

TurboID-tagged Rpi-amr1 and Rpi-amr3 were again transiently expressed in *N. benthamiana nrc2/3/4*, but this time the *Agro*-infiltrated leaves were subsequently infiltrated with *P. infestans* zoospores, followed by mass spectrometry (Figure 4.6). In this experimental setup, the *P. infestans* effectors are delivered into the plant cells by the pathogen itself. Prior to my start in Jonathan Jones' Lab, Dr Xiao Lin, now a former team member, captured native AVRamr3 with Rpi-amr3:TurboID after *P. infestans* infection on one occasion, which was an encouraging result suggesting that capturing native effectors with TurboID could be feasible. One of the first things that needed to be done was to repeat this result. However, in my first two attempts, neither AVRamr1 nor AVRamr3 were detected in the MS data collected by the proteomic team. Biotin was initially infiltrated two days after *P. infestans* infiltration, and we suspected that the absence of the target effectors in the MS data could be due to the biotin being infiltrated at the wrong experimental time point (either too early or too late). It is known that the peak of *Avr* gene expression occurs at 2 dpi during *P. infestans* infection of a potato plant (Vleeshouwers et al., 2011), and the original experimental time point was based on that knowledge. However, after *Agro*-infiltrations, prior to *P. infestans* infection, it is not known exactly when *AVRamr1* and *AVRamr3* start to be expressed, and this 2 dpi time point might

no longer apply to *N. benthamiana* plants after their immune system has been primed by the *Agro*-infiltrations.

To test this hypothesis, an RT-PCR analysis of the *AVRamr1* and *AVRamr3* genes was conducted following *Agro*-infiltration of TurboID-tagged Rpi-amr1 and Rpi-amr3 (Supplementary Figure 4.1). The *AVRamr1* and *AVRamr3* cDNAs were undetectable at 2 days post *P. infestans* infection but were observed 3 days post *P. infestans* infection onwards. Genes used as positive controls were undetectable at 2 dpi, possibly due to the lower number of zoospores infiltrated into the leaves (8,700 zoospores/mL) compared to the usual amount (50,000 or 100,000 zoospores/mL), which may have affected pathogen growth. However, significant amounts of *AVRamr1* and *AVRamr3* were detected at 3 dpi. Based on these results, later time points (3 and 4 days post *P. infestans* infection) were incorporated into the experiment (Figure 4.6). In contrast to the previous experiment (Figure 4.5), where all proteins were overexpressed under 35S promoters and a 30-minute labelling time was used, a 3-hour labelling time was employed in this experiment to allow more time for capturing the native *P. infestans* effectors (Figure 4.6).

Before sending the samples for mass spectrometry (MS) analysis, a small fraction of the streptavidin beads used to pull down biotinylated proteins was boiled and analysed by Western blotting with HRP-conjugated streptavidin to detect biotinylated proteins and assess sample quality (Figure 4.7). TurboID-tagged mCherry, driven by the medium-expression *A. thaliana* small subunit ribosomal protein 16 (*SSR16*) gene promoter (pAt2), was used as a negative control. The baits themselves are biotinylated and are often easily identified on Western blots in the input samples. Both mCherry:TurboID and Rpi-amr1:TurboID showed similar protein accumulation, while Rpi-amr3:TurboID was less abundant and exhibited a lower overall level of biotinylation.

The samples were analysed using two different mass spectrometry systems. First, the Orbitrap Fusion LC-MS/MS system was employed to detect the effectors secreted by native infection, but this approach was unsuccessful. Subsequently, the Orbitrap Eclipse LC-MS/MS system with Field Asymmetric Ion Mobility Spectrometry (FAIMS) was used, which enabled the identification of eight spectral counts corresponding to AVRamr1 at 4 days post *P. infestans* infection (Table 4.2) with a protein sequence coverage of 32% and eight different peptides identified. However, AVRamr3 was not detected in this experiment. The Orbitrap Eclipse LC-MS/MS system comes with integrated FAIMS, which enhances ion mobility separation before ions enter the mass spectrometer. This

reduces background noise, improves ion separation in complex mixtures, reduces spectral overlap, and provides higher sensitivity and resolution compared to the Orbitrap Fusion system. Encouraged by this promising result, the experiment was repeated at both 3 and 4 days post *P. infestans* infection to assess the reproducibility of the technique.

In the subsequent repeats, several spectral counts corresponding to AVRamr1 were detected at both 3 and 4 dpi, with a higher number of spectral counts observed at 4 dpi compared to 3 dpi (Table 4.2). The increased number of spectral counts at 4 dpi can likely be explained by an increased pathogen biomass within the infected leaves, as well as the pathogen having colonized more plant cells. AVRamr1 was detected by mass spectrometry in four independent replicates at 3 and 4 dpi, whereas AVRamr3 was detected in only two replicates at 4 dpi (Table 4.2). AVRamr3 was detected with a protein sequence coverage of 22%, and five different peptides were identified. Neither AVRamr1 nor AVRamr3 were detected in samples containing mCherry:TurboID. The RT-PCR experiment (Supplementary Figure 4.1) confirmed that *AVRamr3* was expressed by *P. infestans* in *N. benthamiana* leaves at 3 dpi following *Agro*-infiltration, indicating that the absence of AVRamr3 detection at 3 dpi by mass spectrometry (Table 4.2) cannot be attributed to a lack of expression. However, the accumulation of Rpi-amr3:TurboID protein was lower compared to Rpi-amr1:TurboID (Figure 4.7), which may result in a lower overall level of biotinylation in these samples. This could explain why AVRamr3 was only detectable by mass spectrometry at 4 dpi, while AVRamr1 was detectable at both experimental time points. Therefore, it can be concluded that to maximize the chances of capturing native effectors, the bait must be sufficiently abundant, and shifting experimental time points to later stages of infection will increase the likelihood of pathogen growth within host cells and enhance the abundance of native effectors. Unfortunately, the repeats highlighted in red within Table 4.2 were affected by contamination issues and could not be included in the final analysis. However, I chose to include them here as they demonstrate that cognate effectors of Rpi-amr1 and Rpi-amr3 were captured by mass spectrometry multiple times in independent experiments.

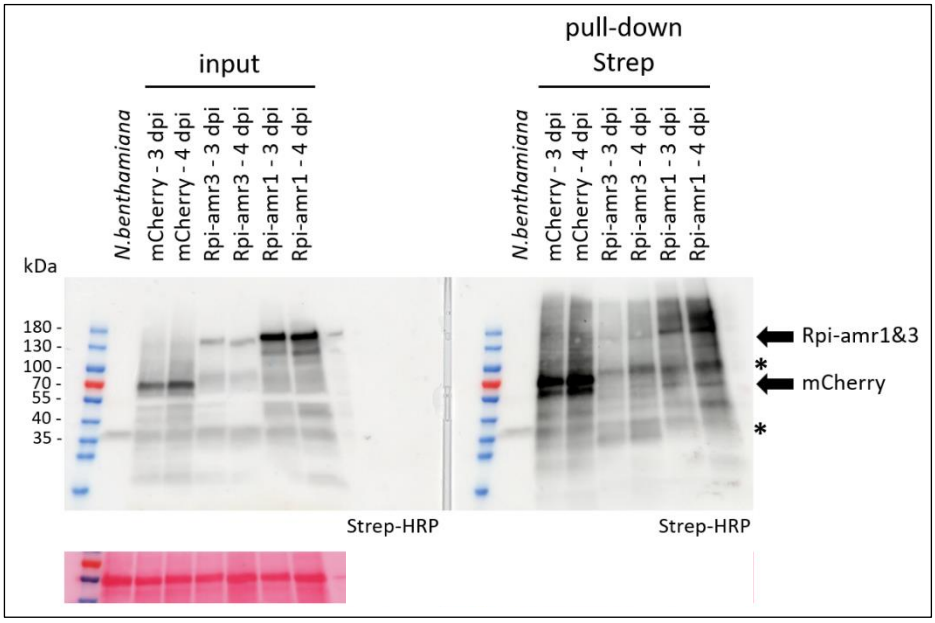


**Figure 4.7 Proximity biotinylation by Rpi-amr1:TurboID and Rpi-amr3:TurboID in *nrc2/3/4 N. benthamiana*.**

Streptavidin pull-down and biotinylation of 35S:Rpi-amr1:TurboID-FLAG, 35S:Rpi-amr3:TurboID-FLAG and pAt2:mCherry:TurboID-V5 in *nrc2/3/4 N. benthamiana*. *Agro*-infiltrations at $OD_{600}$ = 0.5 in 4-week-old *nrc234 N. benthamiana* and in the presence of p19, followed by *P. infestans* (isolate 88069) infiltration (100,000 zoospores/mL) at 1 day post *Agro*-infiltration. Biotin-infiltration (50 µM) at 3 and 4 days post *P. infestans* infiltration (dpi) (so at 4 and 5 days post *Agro*-infiltration) and for 3 h before tissue harvesting. Pull-down was carried out with streptavidin beads. A small fraction of the beads was boiled and resolved by SDS-PAGE to assess sample quality prior to LC-MS/MS analysis. Biotinylated proteins were detected by using HRP-conjugated streptavidin labelling. Bands labelled with a black asterisk (*****) correspond to endogenously biotinylated proteins. The "*N. benthamiana*" lane corresponds to non-infiltrated samples, meaning no TurboID-tagged baits were expressed and no biotin was added. It serves as control to show endogenous biotinylation.

**Table 4-2 Number of times *P. infestans* effectors AVRamr1 and AVRamr3 were detected by mass spectrometry with TurboID-tagged Rpi-amr1 and Rpi-amr3 in *nrc2/3/4 N. benthamiana*.**

In total, AVRamr1 was detected by mass spectrometry four times at 3 and 4 days post *P. infestans* infiltration (dpi), while AVRamr3 was detected twice at 4 dpi only. Detections highlighted in red are excluded from the final analysis due to a contamination issue. Detections highlighted in green represent repeats where the contamination issue was resolved and are therefore included in the final analysis. NA indicates that no spectral counts were detected.

| | **AVRamr1 (PITG_07569)** spectral counts | | | **AVRamr3 (PITG_21190)** spectral counts | |
|---|---|---|---|---|---|
| **MS detection:** | **3 dpi** | **4 dpi** | **MS detection:** | **3 dpi** | **4 dpi** |
| 1st | NA | 8 | 1st | NA | NA |
| 2nd | 3 | 6 | 2nd | NA | NA |
| 3rd | 2 | 5 | 3rd | NA | 2 |
| 4th | 5 | 13 | 4th | NA | 6 |

After the contamination issue was identified and resolved, three additional repeats were performed. In total, 8,123 proteins were identified across the three final repeats, including all proteins detected in samples from both bait constructs (Rpi-amr1:TurboID and Rpi-amr3:TurboID) as well as the mCherry:TurboID control. Of these, 7,578 proteins correspond to *N. benthamiana* and 545 to *P. infestans*. The *P. infestans* proteins account for approximately 7% of the total proteins detected. The *P. infestans* transcribed gene (PITG)-proteins that were uniquely detected in the Rpi-amr containing samples and absent from the mCherry control samples are summarized in Supplementary Figures 4.2, 4.3, 4.4 and 4.5. In two of these repeats (rep1 and rep2), *P. infestans* did not grow or colonize the plant tissues effectively, as indicated by the absence or low number of spectral counts corresponding to pathogen proteins. In contrast, the third repeat showed more pathogen infection, with a higher number of spectral counts corresponding to pathogen proteins. It was in this third repeat (highlighted in green in Table 4.2) that both AVRamr1 and AVRamr3 effectors were detected as biotinylated by the corresponding NLRs, but not in the mCherry:TurboID samples (Supplementary Figures 4.2, 4.3, 4.4 and 4.5).

Volcano plots are commonly used in mass spectrometry to visualize the relationship between fold changes and statistical significance, offering a way to identify key proteins that show significant differences between experimental conditions. A volcano plot displays $\log_2$(fold change) *versus* $-\log_{10}$(p-value) but does not account for the average expression level. Given that the total number of spectral counts for each effector is relatively low (with a maximum of 13 and 6 spectral counts for

AVRamr1 and AVRamr3, respectively, at 4 dpi), p-values calculated from this data would not be reliable due to the low signal-to-noise ratio and the potential lack of reproducibility at low counts. In other words, while statistical tests can provide p-values, these are prone to inaccuracies when applied to data with low or not reliably reproducible counts.

Therefore, we opted to use an MA plot, which is a scatter plot that displays the mean of the counts (typically the average counts per sample) against the $\log_2$(fold change). Originally, MA plots were developed in the context of microarray analysis in transcriptomics to visualize gene expression data. They were designed to examine the relationship between fold changes in gene expression and the mean expression level across experimental conditions. In this context, fold change refers to the difference in spectral counts between experimental conditions. The MA plot offers a clearer view of the data by focusing on the absolute change in expression (fold change) while accounting for the average expression level (here spectral counts) across conditions. This makes it particularly useful for visualizing data that may be noisy or close to the detection threshold. Unlike the volcano plot, the MA plot does not rely on statistical significance measures such as p-values, which can be unreliable for low-abundance or noisy data. This approach helps highlight patterns and trends in the data, making it easier to identify proteins or effectors with meaningful changes in abundance, regardless of statistical significance.

In the plot, each dot represents a protein. The top half displays proteins that are highly biotinylated in the Rpi-amr1:TurboID and Rpi-amr3:TurboID samples, while the bottom half shows those highly biotinylated in the control mCherry:TurboID samples. Dots further away from the Y-axis (both negative and positive) correspond to the most differentially biotinylated proteins between the two groups. Proteins with low abundance are positioned closer to 0 on the X-axis, while those with higher average counts are positioned further along the X-axis. For these more abundant proteins, extreme values on the Y-axis are not necessary to confirm differential biotinylation between the two groups.

As expected, the dots corresponding to AVRamr1 and AVRamr3 appear on the positive extreme of the Y-axis and closer to 0 on the X-axis (Figures 4.8 and 4.9). The PITG IDs for proteins that are highly biotinylated in experimental samples but with low A value (or low spectral counts) have been extracted and are presented in Tables 4.3, 4.4, 4.5, and 4.6. As anticipated, the p-values for these pathogen-related proteins are not significant due to their low abundance.

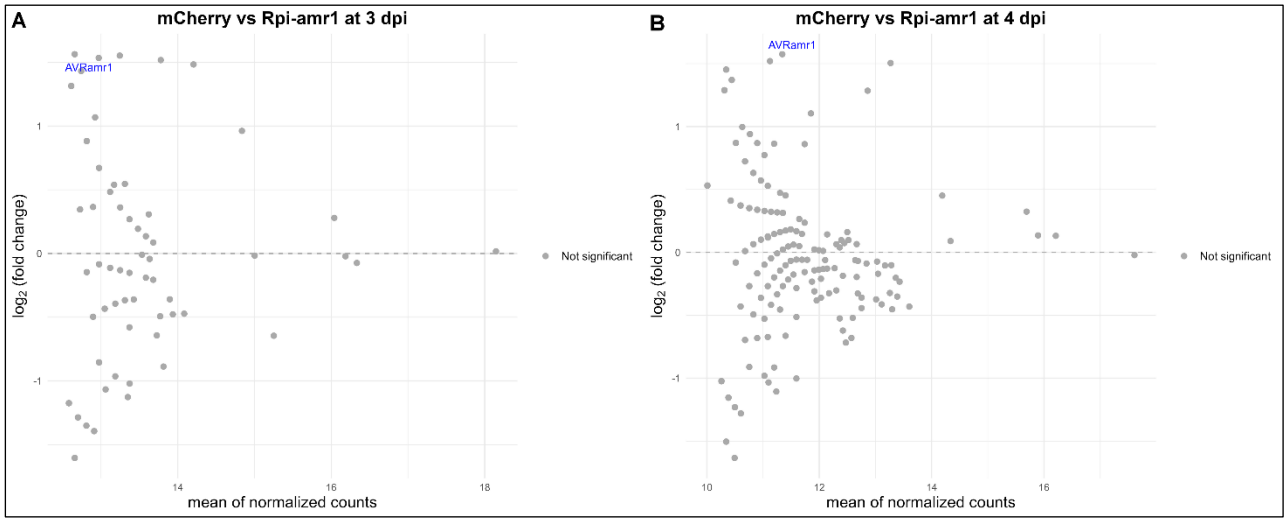


**Figure 4.8 TurboID-based identification of Rpi-amr1 proximal pathogen interactors.**

Rpi-amr1 proximal pathogen interactors identified by mass spectrometry at 3 (**A**) and 4 (**B**) days post *P. infestans* infiltration in *nrc2/3/4 N. benthamiana*. The MA plot (M *versus* A plot) displays the relationship between average protein abundance (A) and the $log_2$(FC) in biotinylation (M). Proteins with no significant differences in biotinylation are shown in grey. No proteins showed differential biotinylation compared to mCherry ($log_2$(FC) > 0 and P-value < 0.05). The data were normalized using cyclic loess normalization *via* the edgeR package (Chen et al., 2025). Proteins with values near 0 on the X-axis correspond to low-abundance proteins, while highly abundant proteins are located further from 0. Extreme values along the Y-axis represent promising interactors, and only small changes in biotinylation are sufficient for highly abundant proteins.

mCherry vs Rpi-amr1 at 3 dpi

ranked by p-value & log(FC) > 0

| Protein | p-value | log(FC) |
|---|---|---|
| PITG_15278T0 | 0.155 | 1.518 |
| PITG_04276T0 | 0.158 | 1.553 |
| AVRamr1 | 0.174 | 1.535 |
| PITG_04269T0 | 0.174 | 1.484 |

**Table 4-3 List of the Rpi-amr1 proximal pathogen interactors identified at 3 days post *P. infestans* infiltration in *nrc2/3/4 N. benthamiana*.**

Proteins are ranked by P-value < 0.2 and log(FC) > 0.

| mCherry vs Rpi-amr1 at 4 dpi<br>ranked by p-value & log(FC) > 0 | | |
|---|---|---|
| Protein | p-value | log(FC) |
| PITG_04276T0 | 0.056 | 1.520 |
| PITG_04658T0 | 0.094 | 0.324 |
| AVRamr1 | 0.135 | 1.575 |
| PITG_04269T0 | 0.149 | 1.505 |
| PITG_08809T0 | 0.182 | 0.861 |
| PITG_11215T0 | 0.187 | 1.105 |
| PITG_15278T0 | 0.197 | 1.285 |

**Table 4-4 List of the Rpi-amr1 proximal pathogen interactors identified at 4 days post *P. infestans* infiltration in *nrc2/3/4 N. benthamiana*.**

Proteins are ranked by P-value < 0.2 and log(FC) > 0.

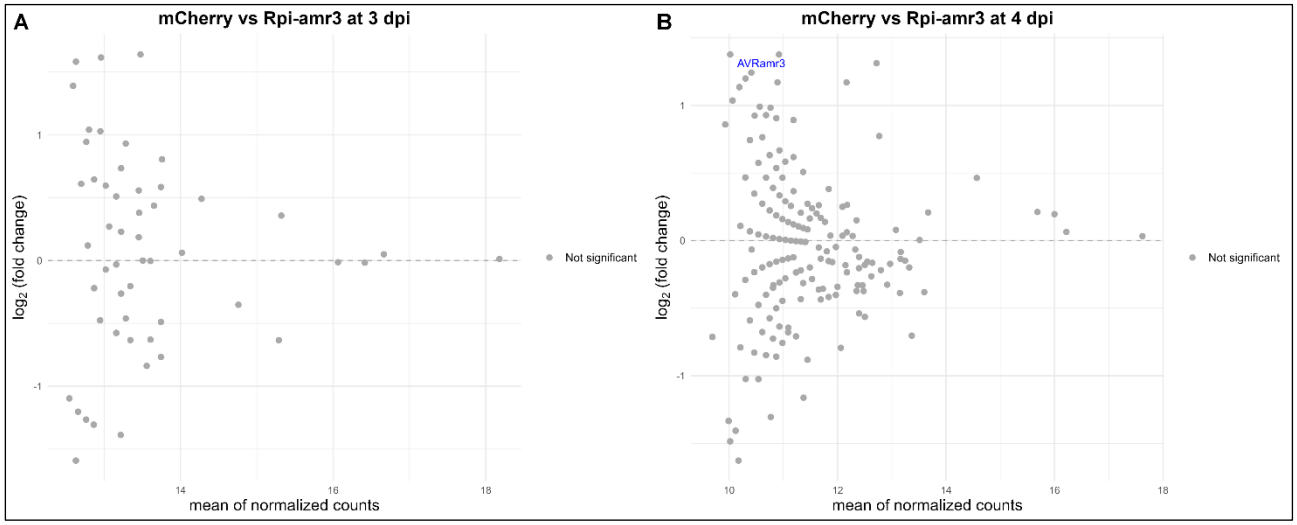


**Figure 4.9 TurboID-based identification of Rpi-amr3 proximal pathogen interactors.**

Rpi-amr3 proximal pathogen interactors identified by mass spectrometry at 3 (**A**) and 4 (**B**) days post *P. infestans* infiltration in *nrc2/3/4 N. benthamiana*. The MA plot (M *versus* A plot) displays the relationship between average protein abundance (A) and the $\log_2$(FC) in biotinylation (M). Proteins with no significant differences in biotinylation are shown in grey. No proteins showed differential biotinylation compared to mCherry ($\log_2$(FC) > 0 and P-value < 0.05). The data were normalized using cyclic loess normalization *via* the edgeR package (Chen et al., 2025). Proteins with values near 0 on the X-axis correspond to low-abundance proteins, while highly abundant proteins are located further from 0. Extreme values along the Y-axis represent promising interactors, and only small changes in biotinylation are sufficient for highly abundant proteins.

| mCherry vs Rpi-amr3 at 3 dpi<br>ranked by p-value & log(FC) > 0 | | |
|---|---|---|
| Protein | p-value | log(FC) |
| PITG_04269T0 | 0.142 | 1.640 |
| PITG_11215T0 | 0.160 | 1.616 |
| PITG_01940T0 | 0.190 | 0.806 |

**Table 4-5 List of the Rpi-amr3 proximal pathogen interactors identified at 3 days post *P. infestans* infiltration in *nrc2/3/4 N. benthamiana*.**

Proteins are ranked by P-value < 0.2 and log(FC) > 0.

| mCherry vs Rpi-amr3 at 4 dpi<br>ranked by p-value & log(FC) > 0 | | |
|---|---|---|
| Protein | p-value | log(FC) |
| PITG_04276T0 | 0.085 | 1.376 |
| PITG_06449T0 | 0.132 | 0.464 |
| PITG_04269T0 | 0.147 | 1.312 |
| PITG_00693T0 | 0.162 | 1.171 |
| PITG_11215T0 | 0.177 | 1.170 |
| PITG_15786T0 | 0.181 | 0.892 |
| PITG_17993T0 | 0.192 | 0.983 |
| PITG_06619T0 | 0.195 | 1.243 |
| AVRamr3 | 0.195 | 1.243 |
| PITG_01036T0 | 0.200 | 0.906 |

**Table 4-6 List of the Rpi-amr3 proximal pathogen interactors identified at 4 days post *P. infestans* infiltration in *nrc2/3/4 N. benthamiana*.**

Proteins are ranked by P-value < 0.2 and log(FC) > 0.

In addition to the cognate AVRamr1 and AVRamr3 effectors, other *P. infestans* proteins were captured. To assess whether these proteins also function as effectors, we analysed all pathogen proteins uniquely detected in samples containing Rpi-amr1 and Rpi-amr3 (Supplementary Figures 4.2, 4.3, 4.4 and 4.5), along with the highly-biotinylated PITG proteins identified from the MA plots (Tables 4.3, 4.4, 4.5 and 4.6), using SignalP 6.0 to predict the presence of a signal peptide (Table 4.7). Three additional pathogen proteins were identified as having a predicted signal peptide with Rpi-amr1:TurboID, and six with Rpi-amr3:TurboID. PITG_15278 was the only protein common to both CNLs, detected at both 3 and 4 dpi with Rpi-amr1:TurboID. All other pathogen proteins containing a predicted signal peptide were detected at only one time point, either 3 dpi or 4 dpi. Interestingly, PITG_15278 has been previously reported to suppress Rpiblb2-mediated cell death (Derevnina et al., 2021). Rpi-blb2 is a CNL from *Solanum bulbocastanum* that confers resistance to *P. infestans* (Oh et al., 2009). Conceivably, PITG_15278 has evolved to interact with many NLRs and to attenuate their activity. Additionally, PITG_09216 has been identified as a mitochondria-associated effector (Breeze

et al., 2023, Zuluaga et al., 2016). However, no information is available in the literature regarding the other PITG_proteins with a predicted signal peptide, which were identified through TurboID (Table 4.7). These may represent newly identified effectors, though further testing is required to confirm this. Moreover, it is also important to note that the physical proximity of two proteins does not necessarily imply a functional relationship.

**Table 4-7 *P. infestans* proteins identified using TurboID-tagged Rpi-amr1 and Rpi-amr3 that contain a predicted signal peptide.**

Amount all the PITG_proteins detected by mass spectrometry, three additional PITG_proteins with a predicted signal peptide were identified with Rpi-amr1, and six additional PITG_proteins with a predicted signal peptide were identified with Rpi-amr3. YES indicates that a signal peptide was predicted by the SignalP 6.0 software (Teufel et al., 2022), whereas NA indicates that no spectral counts were detected.

| | **Rpi-amr1** signal peptide (SP) | | | **Rpi-amr3** signal peptide (SP) | |
|---|---|---|---|---|---|
| **Protein:** | **3 dpi** | **4 dpi** | **Protein:** | **3 dpi** | **4 dpi** |
| **PITG_15278** | YES | YES | **PITG_15278** | YES | NA |
| **PITG_09216** | YES | NA | **PITG_02231** | YES | NA |
| **PITG_16959** | NA | YES | **PITG_02909** | NA | YES |
| | | | **PITG_09817** | NA | YES |
| | | | **PITG_03335** | NA | YES |
| | | | **PITG_03694** | NA | YES |

In these PL experiments, TurboID was used to capture pathogen proteins during infection; however, plant proteins were also identified. These plant proteins may be involved in regulating NLRs and downstream signalling pathways that activate defense responses.

The 7,578 *N. benthamiana* biotinylated proteins identified with TurboID-tagged Rpi-amr1 and Rpi-amr3 were bioinformatically analysed using the edgeR (Empirical analysis of Differential Gene Expression in R) package, version 4.2.1. This package compares expression counts across different experimental datasets and uses the Fisher's Exact Test *via* the exactTest() function to identify differentially expressed genes (in this case, differentially biotinylated proteins) (Chen et al., 2025). Fisher's Exact Test is particularly suited for genomic datasets with small, discrete counts, such as spectral counts in our analysis, as it is specifically designed to handle such count-based data.

Proteins with total spectral counts below 50 across the three replicates were excluded from the analysis to ensure more reliable estimates and reduce the influence of low counts. Higher spectral counts provide more confidence in the results, especially when calculating fold changes. This threshold helps avoid unreliable conclusions that can arise from small counts, where a 3-fold change might be based on minimal differences (e.g., 1 vs. 3 counts), whereas larger counts offer a more robust basis for interpreting significant changes. Volcano plots of the resulting p-values were generated (Figures 4.10, 4.11, 4.12 and 4.13) and the top significant proximal interactors are listed in Tables 4.8, 4.9, 4.10 and 4.11.

Majority of the identified proximal interactors of Rpi-amr1 and Rpi-amr3 were shared between 3 and 4 days post *P. infestans* infection (Figure 4.14), demonstrating a substantial overlap between the two time points. However, the proximal plant interactors identified for Rpi-amr1 and Rpi-amr3 were distinct to each CNL, with only 12 proteins common to both, most of which corresponded to chaperones and co-chaperones (Tables 4.8, 4.9, 4.10 and 4.11). This observation underscores the specificity of TurboID in identifying potential interactors for these two CNLs. A greater number of proteins were identified as proximal interactors with Rpi-amr3, with a total of 122 proteins, compared to 21 proteins for Rpi-amr1 (Figure 4.14). A GO-term analysis could not be performed on the proteins identified in *N. benthamiana*; therefore, the closest homologs in Arabidopsis were manually searched using the BLAST function in the Arabidopsis database, TAIR (Tables 4.8, 4.9, 4.10 and 4.11).

Among the top proximal interactors identified as significant candidates (Tables 4.8, 4.9, 4.10 and 4.11), several chaperones and co-chaperones, including HSP70, HSP90, and HOP3, are shared by both Rpi-amr1 and Rpi-amr3. These proteins are known to play a critical role in regulating NLR stability and preventing autoimmunity, which, if not tightly regulated, can be detrimental to growth and development (Berka et al., 2022, Courbier, 2021, Mayor et al., 2007, Shirasu, 2009).

In addition to these chaperones, an ARGONAUTE (AGO) protein, AGO2, was identified in proximity to Rpi-amr1 (Tables 4.8 and 4.9). AGO proteins bind to small-interfering (si)RNAs and micro (mi)RNAs to mediate target cleavage and translation inhibition, and can also be involved in RNA silencing mechanisms against viruses (Harvey et al., 2011). This is particularly intriguing given the effector from *P. infestans*, AVRamr1, recognized by Rpi-amr1, has been reported to have an alternative

splicing function (Huang et al., 2020). It is therefore assumed that AVRamr1 must be localized in the nucleus to carry out its function. This raises the possibility that Rpi-amr1 may also localize to the nucleus, where it could potentially function as a guardee for AGO2, which might be modified by AVRamr1. However, this hypothesis requires further investigation.

Unexpectedly, a CINNAMYL ALCOHOL DEHYDROGENASE (CAD) was also found in the proximity to Rpi-amr1 (Tables 4.8 and 4.9). CADs are contributing to structural lignification during development, and several are strongly induced during infection, playing a role in localized lignification that serves as a barrier against infection. A phylogenetic analysis revealed that the CAD7 subfamily of cinnamaldehyde dehydrogenases, which includes *At*CAD6, *At*CAD7, and *At*CAD8, is expanded across several plant genomes (Li et al., 2019). Using RT-PCR, they demonstrated that transcript levels of *AtCAD6*, *AtCAD7*, and *AtCAD8* were increased during *P. capsici* infection of Arabidopsis leaves. Additionally, yeast-two-hybrid (Y2H), bimolecular fluorescence complementation (BiFC), and co-immunoprecipitation (Co-IP) assays identified members of the CAD7 subfamily, including *At*CAD6, as targets of multiple Avr3a-like effectors from *Phytophthora* pathogens. Finally, *At*CAD7 was stabilized by Avr3a-like effectors and involved in the suppression of PTI, including callose deposition, ROS burst, and *WRKY33* expression. These findings suggest that CAD7 subfamily proteins act as negative regulators of plant immunity, which are exploited by multiple Avr3a-like effectors to promote infection (Li et al., 2019). Given these findings, it is possible that Rpi-amr1 may monitor CAD proteins and act as a guardee, though this hypothesis would need to be tested.

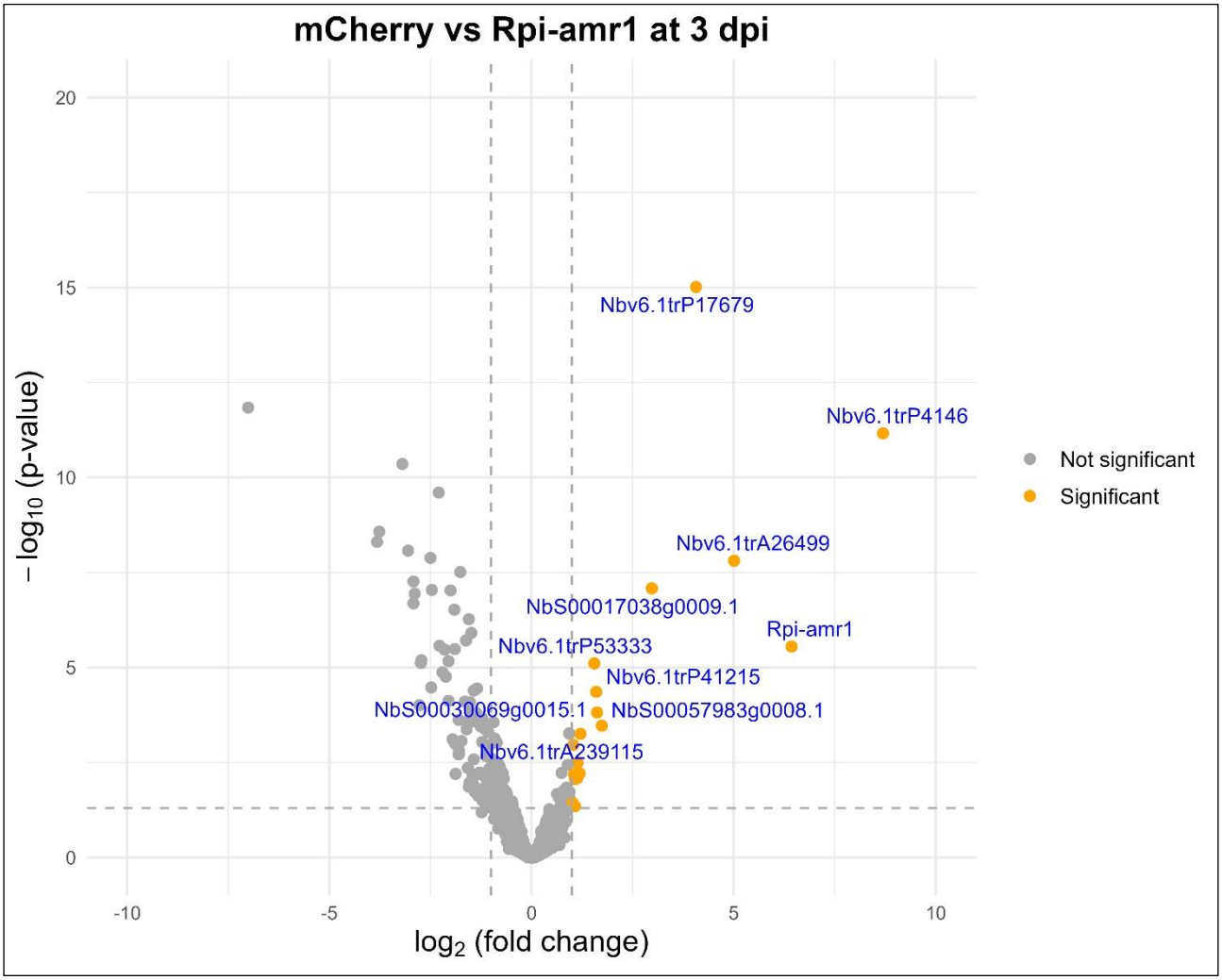


**Figure 4.10 TurboID-based identification of Rpi-amr1 proximal plant interactors at 3 days post *P. infestans* infiltration in *nrc2/3/4 N. benthamiana*.**

Proteins highlighted in orange were considered as Rpi-amr1 proximal plant interactors if they exhibited a 2-fold change increase in biotinylation compared to mCherry and had a statistically significant difference (P-value < 0.05). Proteins with no significant difference in biotinylation are shown in grey. The grey dotted threshold lines indicate a P-value of 0.05 (horizontal) and a $\log_2$(fold change) of –1 and 1 (vertical). The top 10 significantly biotinylated proteins are labelled with their identification numbers. Proteins with a total spectral count below 50 were excluded from the analysis. Statistical significance was determined using Fisher's Exact Test, implemented in the edgeR package (Chen et al., 2025).

**Table 4-8 List of the Rpi-amr1 proximal plant interactors identified at 3 days post *P. infestans* infiltration in *nrc2/3/4 N. benthamiana*.**

Proteins are ranked by P-value and log(FC) > 1. The closest homologous proteins in Arabidopsis were identified through a BLAST search of the corresponding *N. benthamiana* amino acid sequences in the database TAIR.

| Protein | P-value | log(FC) | Closest homologous in Arabidopsis | Description |
|---|---|---|---|---|
| Nbv6.1trP17679 | 9.73E-16 | 4.067 | AT5G02500 | HSP70, encodes a member of heat shock protein 70 family |
| Nbv6.1trP4146 | 6.89E-12 | 8.694 | AT4G12400 | HOP3, encodes one of the 36 TPR proteins with potential to interact with Hsp90/Hsp70 as co-chaperones |
| Nbv6.1trA26499 | 1.55E-08 | 5.01 | AT5G52640 | HSP90, encodes a cytosolic heat shock protein which interacts with disease resistance signalling components SGT1b and RAR1 and is required for RPS2-mediated resistance |
| NbS00017038g0009.1 | 8.26E-08 | 2.977 | AT1G48850 | EMB1144, flavoenzyme-encoding gene essential for embryo development |
| Rpi-amr1 | 2.81E-06 | 6.431 | | Rpi-amr1 |
| Nbv6.1trP53333 | 7.82E-06 | 1.551 | AT5G02500 | HSP70, encodes a member of heat shock protein 70 family |
| Nbv6.1trP41215 | 4.38E-05 | 1.6 | AT3G12580 | HSP70, cytoplasmically localized member of the heat shock protein 70 family |
| NbS00030069g0015.1 | 1.52E-04 | 1.62 | AT4G37970 | CAD6, cinnamyl alcohol dehydrogenase 6 |
| NbS00057983g0008.1 | 3.39E-04 | 1.737 | AT2G47960 | TRAPPC13, part of multi-protein complex, acting as guanine nucleotide exchange factors (GEFs) and possibly as tethers, regulating intracellular trafficking |
| Nbv6.1trA239115 | 5.56E-04 | 1.209 | AT3G44110 | ATJ3, homologous to the co-chaperone DNAJ protein from *E. coli* and member of the HSP40 family |
| Nbv6.1trA61448 | 1.09E-03 | 1.033 | AT5G53400 | BOB1, encodes a non-canonical small heat shock protein required for both development and thermotolerance |
| Nbv6.1trP58215 | 3.22E-03 | 1.138 | AT1G30070 | possibly involved in response to heat stress |
| NbS00000946g0007.1 | 6.15E-03 | 1.191 | AT3G51680 | SDR2, NAD(P)-binding Rossmann-fold superfamily protein |
| Nbv6.1trP9009 | 6.43E-03 | 1.051 | AT1G31280 | AGO2, encodes Argonaute gene that binds viral siRNAs, is involved in antiviral defense response and regulates innate immunity |
| Nbv6.1trA27087 | 8.06E-03 | 1.133 | AT4G13010 | CEQORH, oxidoreductase, zinc-binding dehydrogenase family protein |
| Nbv6.1trP26183 | 8.57E-03 | 1.073 | AT4G02450 | P23-1, encodes one of two isoforms of a co-chaperone of HSP90 that is required for root growth |
| Nbv6.1trA104511 (+1) | 3.66E-02 | 1.015 | AT1G59900 | E1-alpha, encodes the E1-alpha subunit of the pyruvate dehydrogenase complex (PDC) |
| NbS00032243g0025.1 | 4.44E-02 | 1.073 | AT3G26300 | CYP71B34, putative cytochrome P450 |

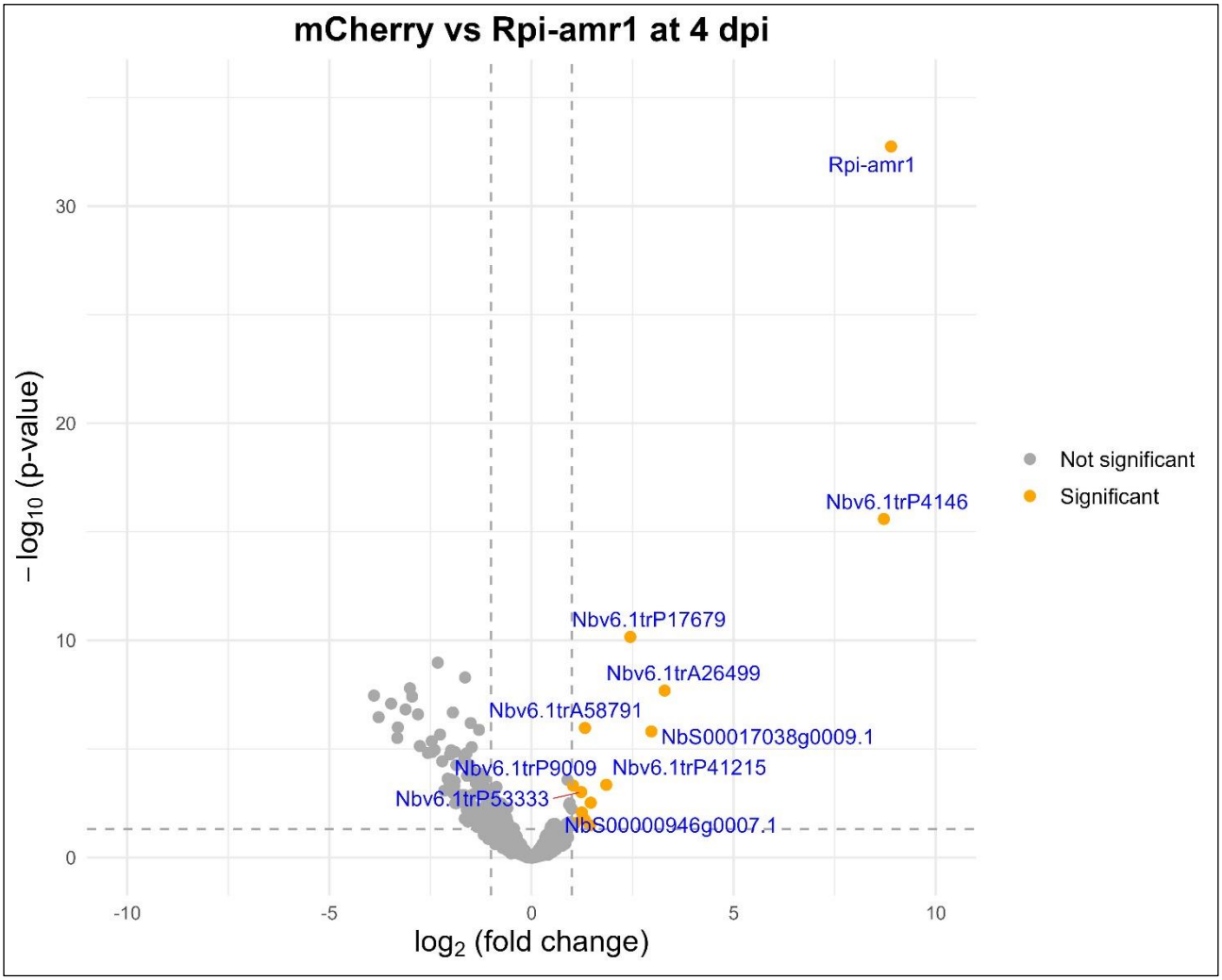


**Figure 4.11 TurboID-based identification of Rpi-amr1 proximal plant interactors at 4 days post *P. infestans* infiltration in *nrc2/3/4 N. benthamiana*.**

Proteins highlighted in orange were considered as Rpi-amr1 proximal plant interactors if they exhibited a 2-fold change increase in biotinylation compared to mCherry and had a statistically significant difference (P-value < 0.05). Proteins with no significant difference in biotinylation are shown in grey. The grey dotted threshold lines indicate a P-value of 0.05 (horizontal) and a $\log_2$(fold change) of –1 and 1 (vertical). The top 10 significantly biotinylated proteins are labelled with their identification numbers. Proteins with a total spectral count below 50 were excluded from the analysis. Statistical significance was determined using Fisher's Exact Test, implemented in the edgeR package (Chen et al., 2025).

**Table 4-9 List of the Rpi-amr1 proximal plant interactors identified at 4 days post *P. infestans* infiltration in *nrc2/3/4 N. benthamiana*.**

Proteins are ranked by P-value and log(FC) > 1. The closest homologous proteins in Arabidopsis were identified through a BLAST search of the corresponding *N. benthamiana* amino acid sequences in the database TAIR.

| Protein | P-value | log(FC) | Closest homologous in Arabidopsis | Description |
|---|---|---|---|---|
| Rpi-amr1 | 1.81E-33 | 8.894 | | Rpi-amr1 |
| Nbv6.1trP4146 | 2.57E-16 | 8.715 | AT4G12400 | HOP3, encodes one of the 36 TPR proteins with potential to interact with Hsp90/Hsp70 as co-chaperones |
| Nbv6.1trP17679 | 6.95E-11 | 2.443 | AT5G02500 | HSP70, encodes a member of heat shock protein 70 family |
| Nbv6.1trA26499 | 2.06E-08 | 3.293 | AT5G52640 | HSP90, encodes a cytosolic heat shock protein which interacts with disease resistance signalling components SGT1b and RAR1 and is required for RPS2-mediated resistance |
| Nbv6.1trA58791 | 1.08E-06 | 1.322 | AT3G51680 | SDR2, NAD(P)-binding Rossmann-fold superfamily protein |
| NbS00017038g0009.1 | 1.57E-06 | 2.964 | AT1G48850 | EMB1144, flavoenzyme-encoding gene essential for embryo development |
| Nbv6.1trP41215 | 4.49E-04 | 1.849 | AT3G12580 | HSP70, cytoplasmically localized member of the heat shock protein 70 family |
| Nbv6.1trP9009 | 4.86E-04 | 1.027 | AT1G31280 | AGO2, encodes Argonaute gene that binds viral siRNAs, is involved in antiviral defense response and regulates innate immunity |
| Nbv6.1trP53333 | 9.71E-04 | 1.228 | AT5G02500 | HSP70, encodes a member of heat shock protein 70 family |
| NbS00000946g0007.1 | 3E-03 | 1.464 | AT3G51680 | SDR2, NAD(P)-binding Rossmann-fold superfamily protein |
| Nbv6.1trP58215 | 8.45E-03 | 1.244 | AT1G30070 | possibly involved in response to heat stress |
| NbS00030069g0015.1 | 1.83E-02 | 1.313 | AT4G37970 | CAD6, cinnamyl alcohol dehydrogenase 6 |
| NbS00036003g0011.1 | 2.68E-02 | 1.072 | AT4G01100 | ADNT1, adenine nucleotide transporter, located in mitochondrion, loss of function mutants exhibit reduced root growth and respiration |
| Nbv6.1trP73156 | 3.27E-02 | 1.443 | AT1G53350 | disease resistance protein (CC-NBS-LRR class) family |

A distinct set of proximal interactors was identified with Rpi-amr3 compared to Rpi-amr1. Among them, SUPPRESSOR OF rps4-RLD1 (SRFR1), a known negative regulator of NLRs, was detected in proximity to Rpi-amr3 (Tables 4.10 and 4.11). SRFR1 has been previously identified as a negative regulator of ETI and has been shown to interact with the TNL resistance proteins SNC1, RPS4, and RPS6 (Bhattacharjee et al., 2011, Kim et al., 2010, Li et al., 2010). In *srfr1* mutant plants, the accumulation of several NLR proteins including SNC1, RPS2, and RPS4, is increased. It has also been

demonstrated that SRFR1 interacts with SGT1 (Li et al., 2010), a co-chaperone of HSP90 (Kadota et al., 2008, Liu et al., 2004, Takahashi et al., 2003), suggesting that SRFR1 regulates NLR stability through SGT1. SRFR1 is localized in both the cytoplasm and the nucleus (Kim et al., 2010). Excluding SRFR1 from the nucleus prevents complementation of the *srfr1* phenotype, emphasizing the importance of its nuclear localization for regulation of plant immunity (Kim et al., 2014b). Additionally, SRFR1 contains a conserved TPR domain, which shares high sequence similarity with TPR domains found in transcriptional repressors in other organisms. This suggests that SRFR1 might also negatively regulate ETI through transcriptional control (Kim et al., 2014b). Indeed, SRFR1 has been shown to interact with multiple TEOSINTE BRANCHED1/CYCLOIDEA/PCF (TCP) transcription factors that positively regulate ETI mediated by several NLRs (Kim et al., 2014b). Therefore, SRFR1 might functions as an important negative regulator in NLR-mediated immunity by interacting with various NLR-interacting proteins, including molecular co-chaperones and transcription factors, thus preventing the auto-activation of plant immunity. SRFR1 may also be modulating Rpi-amr3 activity, although no CNLs have been reported to be regulated by SRFR1 so far.

Syntaxins are also found to be proximal interactors of Rpi-amr3. Syntaxins are soluble *N*-ethylmaleimide-sensitive-factor-attachment protein receptors (SNAREs) involved in the fusion of transport vesicles to target membranes (Sanderfoot et al., 2001, Ungar and Hughson, 2003). Intriguingly, two syntaxins have been implicated in mediating defense-related secretion in plants: SYP132 for resistance to bacteria (Kalde et al., 2007), and SYP121/ROR2 for resistance against powdery mildew fungus (Assaad et al., 2004, Bhat et al., 2005). Notably, Kalde et al. (2007) found that, in *N. benthamiana*, silencing *Nb*SYP132 inhibited the accumulation of antimicrobial PATHOGENESIS-RELATED 1 (PR1) protein in the apoplast. This suggests that syntaxins could mediate defense-related secretion against *P. infestans* through Rpi-amr3.

Proteins associated with the phosphate (Pi) starvation response (PSR) were also detected in the vicinity of Rpi-amr3. Notably, PHOSPHATE STARVATION RESPONSE 1 (PHR1), a master transcription factor involved in Pi starvation in Arabidopsis, regulates the coordination between nutrition and defense (Bustos et al., 2010, Castrillo et al., 2017). In the absence of pathogens, plants prioritize nutritional stress over defense. It has been reported that PHR1 directly binds to the promoters of RAPID ALKALINIZATION FACTOR (RALF) genes and activates their expression under Pi-starvation conditions (Tang et al., 2022). RALFs, in turn, suppress the assembly of receptor kinase complexes during PTI through the malectin-like receptor kinase FERONIA (FER), which normally acts as a

scaffold (Stegmann et al., 2017). This facilitates the suppression of immunity *via* the PHR1-RALF-FERONIA axis (Tang et al., 2022). Therefore, Rpi-amr3 might help alleviate the repression of defense responses by PHR1.

Moreover, a PHOSPHATE TRANSPORTER 5 (PHT5) was found in the neighbourhood of Rpi-amr3 at 4 days post *P. infestans* infection. PHT5 functions as a vacuolar Pi transporter, and plant vacuoles are known to serve as the primary intracellular compartments for inorganic Pi storage (Liu et al., 2016). It has been reported that the plasma membrane Pi transporter PHT1-mediated phosphate uptake is repressed upon activation of PTI, and that this inhibition depends on the receptor-like cytoplasmic BOTRYTIS-INDUCED KINASE 1 (BIK1) and PBS1-like KINASE 1 (PBL1), both of which phosphorylate PHT1 (Dindas et al., 2022). This further suggests that Rpi-amr3 could be another plant immune-related protein linking plant defense responses and cytoplasmic Pi homeostasis.

Interestingly, another kind of vacuole-localized transporter, the ALUMINUM-ACTIVATED MALATE TRANSPORTER 4 (ALMT4), was detected with Rpi-amr3. In Arabidopsis, these transporters are ion channels that can mediate malate-release from the vacuole and are required for stomatal closure in response to abscisic acid (ABA) (Eisenach et al., 2017, Kovermann et al., 2007). Rpi-amr3 could thus also be involved in regulating the cytosolic malate homeostasis.

Finally, several of the Rpi-amr3 proximal proteins are associated with vacuolar functions or transport or are localized to the vacuole. This suggests that Rpi-amr3-mediated defense responses may involve vacuolar-based defense mechanisms, or it could simply indicate that Rpi-amr3 is localized within this endomembrane compartment, as proximity does not necessarily imply functionality. Recently, a cell-death function at the vacuole was identified in an atypical but conserved Arabidopsis potentially membrane localized NLR (PML), named PML5 (Sunil et al., 2024). Active PML5 oligomers localize to the Golgi membranes and the tonoplast, where they alter vacuole morphology and induce cell death, potentially by releasing calcium from the vacuole. This suggests that NLR-triggered cell death and calcium influx may also occur at the vacuole.

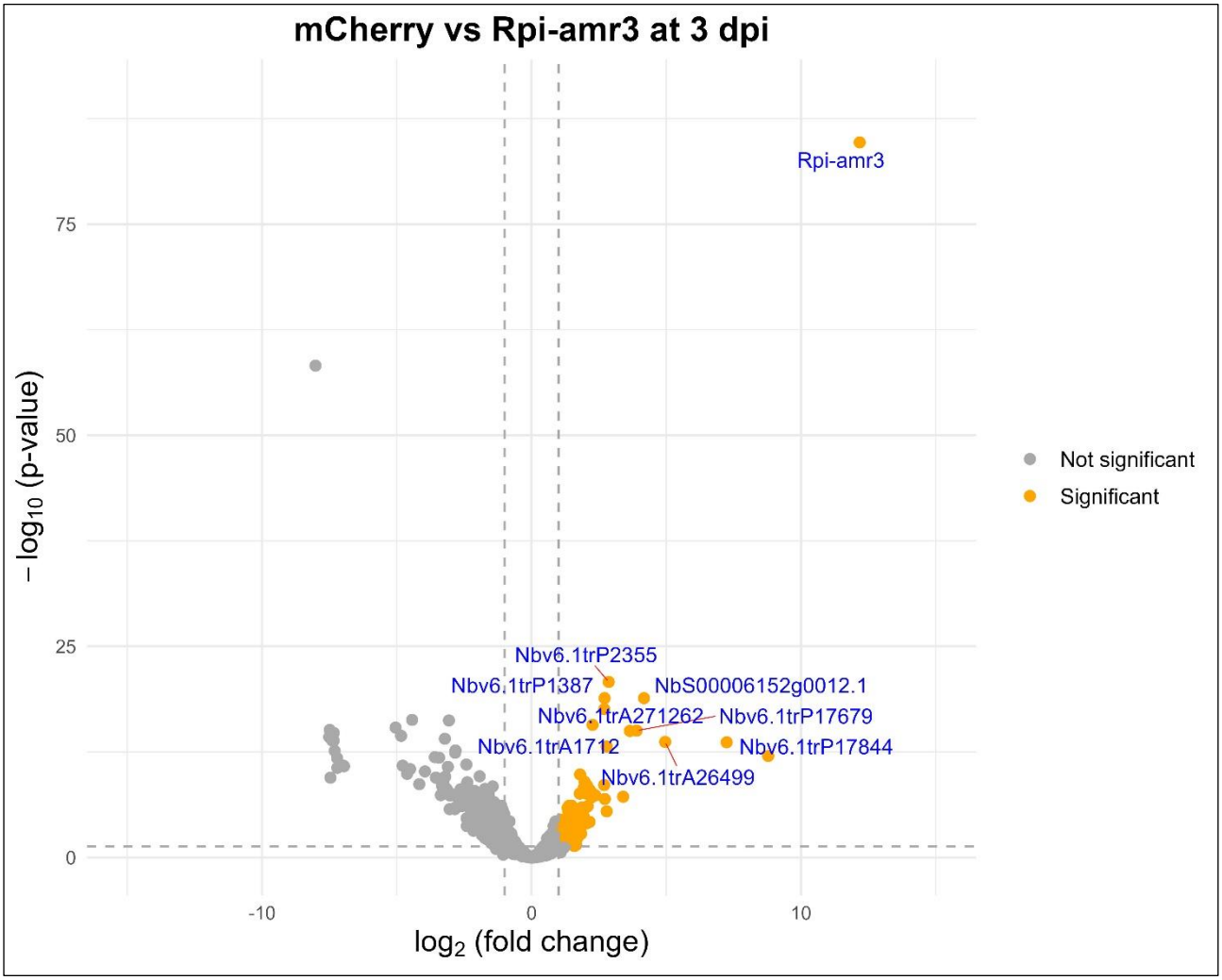


**Figure 4.12 TurboID-based identification of Rpi-amr3 proximal plant interactors at 3 days post *P. infestans* infiltration in *nrc2/3/4 N. benthamiana*.**

Proteins highlighted in orange were considered as Rpi-amr1 proximal plant interactors if they exhibited a 2-fold change increase in biotinylation compared to mCherry and had a statistically significant difference (P-value < 0.05). Proteins with no significant difference in biotinylation are shown in grey. The grey dotted threshold lines indicate a P-value of 0.05 (horizontal) and a $\log_2$(fold change) of –1 and 1 (vertical). The top 10 significantly biotinylated proteins are labelled with their identification numbers. Proteins with a total spectral count below 50 were excluded from the analysis. Statistical significance was determined using Fisher's Exact Test, implemented in the edgeR package (Chen et al., 2025).

**Table 4-10 List of the Rpi-amr3 proximal plant interactors identified at 3 days post *P. infestans* infiltration in *nrc2/3/4 N. benthamiana*.**

Proteins are ranked by P-value and log(FC) > 2. The closest homologous proteins in Arabidopsis were identified through a BLAST search of the corresponding *N. benthamiana* amino acid sequences in the database TAIR.

| Protein | P-value | log(FC) | Closest homologous in Arabidopsis | Description |
|---|---|---|---|---|
| Rpi-amr3 | 2.06E-85 | 12.176 | | Rpi-amr3 |
| Nbv6.1trP2355 | 1.6E-21 | 2.863 | AT1G16240 | SYP51, encodes one of 24 Arabidopsis syntaxins |
| NbS00006152g0012.1 | 1.34E-19 | 4.173 | AT5G36250 | PP2C74, encodes a myristoylated 2C-type protein **phosphatase** that interacts with the catalytic subunit of **SnRK1** |
| Nbv6.1trP1387 | 1.34E-19 | 2.711 | AT4G28610 | PHR1, weakly responsive to phosphate starvation, acts upstream of PHO2 in **phosphate signalling** |
| Nbv6.1trA271262 | 2.71E-18 | 2.697 | AT4G31750 | WIN2, encodes HopW1-1-Interacting protein 2, interacts with the *P. syringae* effector HopW1-1, it has protein **phosphatase activity** and modulates plant defenses against bacteria |
| Nbv6.1trP67644 | 1.96E-16 | 2.264 | AT1G16240 | SYP51, encodes one of 24 Arabidopsis syntaxins |
| Nbv6.1trP17679 | 9.43E-16 | 3.9 | AT5G02500 | HSP70, encodes a member of heat shock protein 70 family |
| Nbv6.1trA1712 | 1.02E-15 | 3.648 | AT1G31480 | SGR2, encodes a novel protein that may be part of a gene family represented by bovine phosphatidic acid-preferring phospholipase A1 (PA-PLA1) containing a putative transmembrane domain, it is involved in the formation and function of the **vacuole** |
| Nbv6.1trA26499 | 2.04E-14 | 4.958 | AT5G52640 | HSP90, encodes a cytosolic heat shock protein which interacts with disease resistance signalling components SGT1b and RAR1 and is required for RPS2-mediated resistance |
| Nbv6.1trP17844 | 2.28E-14 | 7.240 | AT5G48570 | ROF2, encodes one of the 36 TPR proteins with potential to interact with Hsp90/Hsp70 as co-chaperones |
| Nbv6.1trA35551 | 7.26E-14 | 2.788 | AT5G40740 | AUG6, encodes a conserved AUGMIN subunit 6 which is known to be involved in microtubule nucleation |
| Nbv6.1trP4146 | 9.38E-13 | 8.782 | AT4G12400 | HOP3, encodes one of the 36 TPR proteins with potential to interact with Hsp90/Hsp70 as co-chaperones |
| Nbv6.1trP58215 | 2.62E-09 | 2.695 | AT1G30070 | possibly involved in response to heat stress |
| Nbv6.1trA239115 | 3.17E-09 | 2.057 | AT3G44110 | ATJ3, homologous to the co-chaperon DNAJ protein from *E. coli* and member of the HSP40 family |
| Nbv6.1trA43927 | 9.05E-09 | 2.147 | AT1G08190 | VPS41, might be involved in protein sorting to the **vacuole** |
| Nbv6.1trA60305 | 1.61E-08 | 2.138 | AT2G38020 | VCL1, MVB-to-**vacuole trafficking** protein |

| | | | | |
|---|---|---|---|---|
| NbS00013010g0005.1 | 2.84E-08 | 2.282 | AT1G25480 | ALMT4, encodes a phosphorylation-dependent anion channel that can mediate **malate release** from the **vacuole** and is required for stomatal closure in response to abscisic acid |
| Nbv6.1trP26183 | 4.33E-08 | 2.367 | AT4G02450 | P23-1, encodes one of two isoforms of a co-chaperone of HSP90 that is required for root growth |
| Nbv6.1trP48754 | 6.34E-08 | 3.398 | AT4G31750 | WIN2, encodes HopW1-1-Interacting protein 2, interacts with the *P. syringae* effector HopW1-1, it has protein **phosphatase activity** and modulates plant defenses against bacteria |
| NbS00033525g0004.1 | 7.69E-08 | 2.218 | AT2G39570 | ACR9, encodes a ACT domain-containing protein which is a regulatory domain that serves as an amino acid-binding site in feedback-regulated amino acid metabolic enzymes |
| Nbv6.1trP2672 | 1.19E-07 | 2.718 | AT4G37460 | SRFR1, encodes a tetratricopeptide repeat domain containing protein that shows sequence similarity to those of transcriptional repressors in other organisms, it is involved in mediating effector-triggered immunity |
| Nbv6.1trP41215 | 8.48E-07 | 2.083 | AT3G12580 | HSP70, cytoplasmically localized member of the heat shock protein 70 family |
| NbS00007736g0001.1 | 1.02E-06 | 2.056 | AT4G32150 | VAMP711, member of Synaptobrevin-like *At*VAMP7C, v-SNARE protein family, VAMP7C is **vacuolar-localized** |
| Nbv6.1trP2196 | 3.4E-06 | 2.789 | AT1G60160 | KT12, member of the KT/KUP/HAK family of proton-coupled **potassium transporters** which have potential effect on cellular expansion |
| Nbv6.1trP71383 | 6.08E-05 | 2.154 | AT5G56000 | HSP81, member of heat shock protein 90 |
| Nbv6.1trA254080 | 8.38E-05 | 2.07 | AT3G46530 | RPP11, RPP13, encodes an NBS-LRR type R protein with a putative amino-terminal leucine zipper, confers resistance to the biotrophic oomycete, *Peronospora parasitica*, fungal protein ATR13 induces RPP13 gene expression and disease resistance |

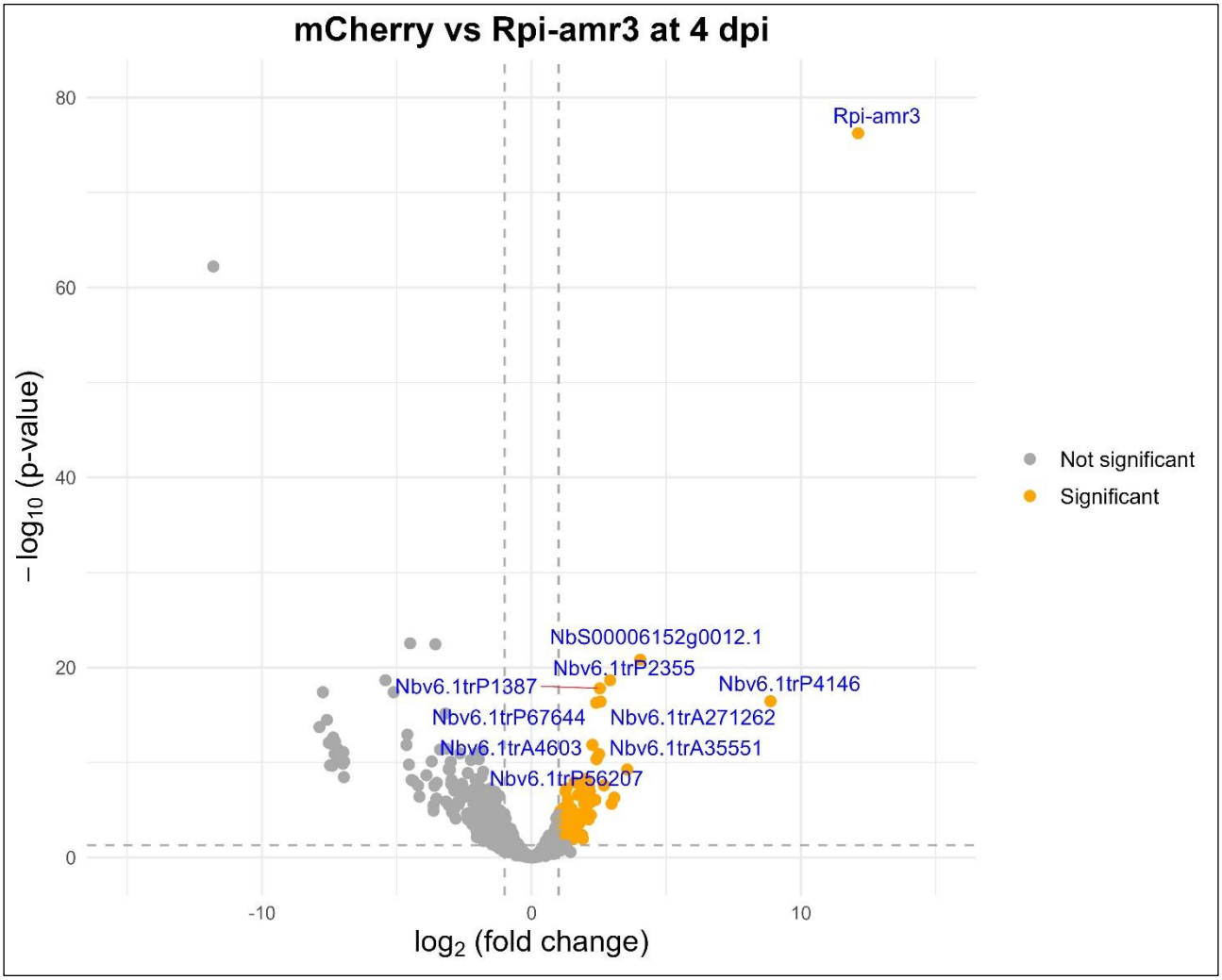


**Figure 4.13 TurboID-based identification of Rpi-amr3 proximal plant interactors at 4 days post *P. infestans* infiltration in *nrc2/3/4 N. benthamiana*.**

Proteins highlighted in orange were considered as Rpi-amr1 proximal plant interactors if they exhibited a 2-fold change increase in biotinylation compared to mCherry and had a statistically significant difference (P-value < 0.05). Proteins with no significant difference in biotinylation are shown in grey. The grey dotted threshold lines indicate a P-value of 0.05 (horizontal) and a $\log_2$(fold change) of –1 and 1 (vertical). The top 10 significantly biotinylated proteins are labelled with their identification numbers. Proteins with a total spectral count below 50 were excluded from the analysis. Statistical significance was determined using Fisher's Exact Test, implemented in the edgeR package (Chen et al., 2025).

**Table 4-11 List of the Rpi-amr3 proximal plant interactors identified at 4 days post *P. infestans* infiltration in *nrc2/3/4 N. benthamiana*.**

Proteins are ranked by P-value and log(FC) > 2. The closest homologous proteins in Arabidopsis were identified through a BLAST search of the corresponding *N. benthamiana* amino acid sequences in the database TAIR.

| Protein | P-value | log(FC) | Closest homologous in Arabidopsis | Description |
|---|---|---|---|---|
| Rpi-amr3 | 5.78E-77 | 12.119 | | Rpi-amr3 |
| NbS00006152g0012.1 | 1.49E-21 | 4.033 | AT5G36250 | PP2C74, encodes a myristoylated 2C-type protein **phosphatase** that interacts with the catalytic subunit of **SnRK1** |
| Nbv6.1trP2355 | 2.18E-19 | 2.914 | AT1G16240 | SYP51, encodes one of 24 Arabidopsis syntaxins |
| Nbv6.1trP1387 | 1.55E-18 | 2.534 | AT4G28610 | PHR1, similar to phosphate starvation response gene from Chlamydomonas, weakly responsive to phosphate starvation, acts upstream of PHO2 in **phosphate signalling** |
| Nbv6.1trP4146 | 3.51E-17 | 8.868 | AT4G12400 | HOP3, encodes one of the 36 TPR proteins with potential to interact with Hsp90/Hsp70 as co-chaperones |
| Nbv6.1trA271262 | 3.89E-17 | 2.559 | AT5G19280 | RAG1, kinase associated protein **phosphatase** |
| Nbv6.1trP67644 | 5.2E-17 | 2.401 | AT1G16240 | SYP51, encodes one of 24 Arabidopsis syntaxins |
| Nbv6.1trA4603 | 1.39E-12 | 2.258 | AT4G22990 | PHT5, encodes a member of the **PHOSPHATE TRANSPORTER** 5 family (PHT5;3), overexpression of PHT5:3 leads to Pi sequestration into **vacuoles** and altered regulation of Pi starvation-responsive genes |
| Nbv6.1trA35551 | 1.31E-11 | 2.504 | AT5G40740 | AUG6, encodes a conserved AUGMIN subunit 6 which is known to be involved in microtubule nucleation |
| Nbv6.1trP56207 | 4.44E-11 | 2.411 | AT4G39420 | spatacsin carboxy-terminus protein |
| Nbv6.1trA26499 | 5.46E-10 | 3.55 | AT5G52640 | HSP90, encodes a cytosolic heat shock protein which interacts with disease resistance signalling components SGT1b and RAR1 and is required for RPS2-mediated resistance |
| Nbv6.1trA59943 | 5.43E-09 | 2.011 | AT2G25730 | zinc finger FYVE domain protein |
| Nbv6.1trA1712 | 2.52E-08 | 2.688 | AT1G31480 | SGR2, encodes a novel protein that may be part of a gene family represented by bovine phosphatidic acid-preferring phospholipase A1 (PA-PLA1) containing a putative transmembrane domain, it is involved in the formation and function of the **vacuole** |
| Nbv6.1trA60305 | 2.63E-08 | 2.061 | AT2G38020 | VCL1, MVB-to-**vacuole trafficking** protein |
| Nbv6.1trP17679 | 3.22E-08 | 2.131 | AT5G02500 | HSP70, encodes a member of heat shock protein 70 family |
| Nbv6.1trP58215 | 1.08E-07 | 2.164 | AT1G30070 | possibly involved in response to heat stress |
| Nbv6.1trP26183 | 2.49E-07 | 2.006 | AT4G02450 | P23-1, encodes one of two isoforms of a co-chaperone of HSP90 that is required for root growth |

| | | | | |
|---|---|---|---|---|
| Nbv6.1trP48754 | 4.97E-07 | 3.07 | AT5G19280 | RAG1, kinase associated protein **phosphatase** |
| Nbv6.1trA1558 | 8.64E-07 | 2.368 | AT3G12520 | SULTR4, encodes a **sulfate transporter** that in induced under sulfate limitation |
| NbS00013010g0005.1 | 1.42E-06 | 2.217 | AT1G25480 | ALMT4, encodes a phosphorylation-dependent anion channel that can mediate **malate release** from the **vacuole** and is required for stomatal closure in response to abscisic acid |
| Nbv6.1trP2672 | 2.19E-06 | 2.969 | AT4G37460 | SRFR1, encodes a tetratricopeptide repeat domain containing protein that shows sequence similarity to those of transcriptional repressors in other organisms, it is involved in mediating effector-triggered immunity |
| Nbv6.1trA14713 | 7.94E-06 | 2.023 | AT2G13560 | NAD-ME1, encodes an NAD-dependent **malic enzyme** (NAD-ME) |
| Nbv6.1trP41215 | 3.42E-05 | 2.198 | AT3G12580 | HSP70, cytoplasmically localized member of the heat shock protein 70 family |
| NbS00024585g0001.1 | 9.74E-05 | 2.115 | AT1G75220 | ERDL6, encodes a **vacuolar glucose exporter** that is induced in response to factors that activate vacuolar glucose pools |

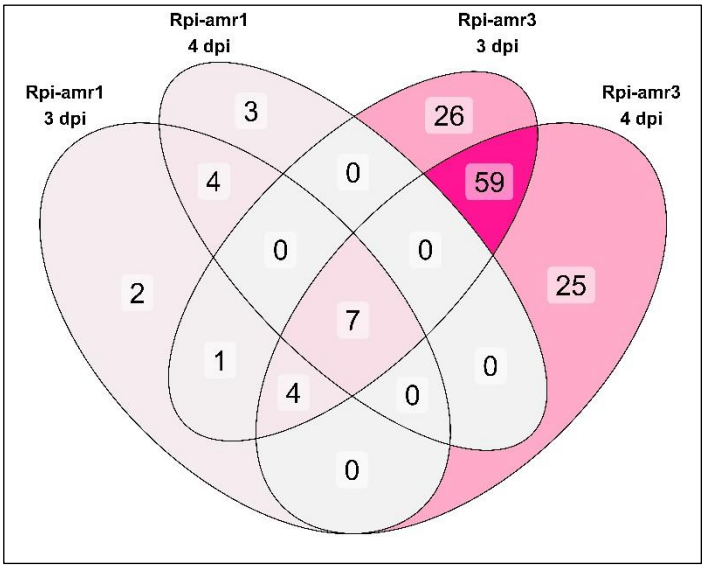


**Figure 4.14 Most proximal plant interactors are unique to Rpi-amr1 or Rpi-amr3.**

Proteins were considered as proximal plant interactors for each treatment if they showed at least a 1-fold change increase in biotinylation compared to mCherry and a statistically significant difference (P-value < 0.05). Proximal plant interactors for each treatment were compared to generate a Venn diagram. The pink gradient corresponds to counts ranging from a lower to higher number of proteins.

### 4.2.2 Identification of native CCG effectors through TurboID proximity labelling following *Albugo candida* infection

In the previous results section, I described how we successfully detected *P. infestans* AVRamr1 and AVRamr3 effectors under native infection conditions using the transient expression of TurboID-tagged Rpi-amr1 and Rpi-amr3 in *N. benthamiana*, respectively. In this section, we aimed to capture native effectors using a TurboID-tagged NLR, but this time in a stable TurboID transgenic line of *A. thaliana*.

*A. candida* is an oomycete pathogen that causes white blister rust disease in plants, particularly in members of the Brassicaceae family (Choi et al., 2009). It is an obligate biotroph, meaning it requires living host cells to complete its life cycle. *Albugo* species mainly encode CCG ($C_{x2}C_{x5}G$) effectors, instead of RXLR effectors (Furzer et al., 2022). The white rust resistance gene 4 (WRR4) provides resistance to multiple *A. candida* races (Borhan et al., 2008), and the WRR4A$^{Col-0}$ TNL protein can recognize eight different CCG effectors: CCG28, CCG30, CCG33, CCG40, CCG67, CCG71, CCG79, and CCG104 (Redkar et al., 2023). These effectors were identified by screening a CCG effector library. Co-IP experiments demonstrated that WRR4A$^{Col-0}$ directly interacts with the N-terminal region of the recognized CCG28, CCG30 and CCG71 effectors (Redkar et al., 2023). By generating a TurboID-tagged WRR4A$^{Col-0}$ stable Arabidopsis transgenic line, we aimed to test whether we could detect biotinylated CCGs by mass spectrometry following *A. candida* infection.

A complementation test was performed in *N. benthamiana* plants with the p35S:*At*WRR4A$^{Col-0}$:TurboID-V5 construct generated by Golden Gate cloning to assess its functionality *via* HR (Figure 4.15). TurboID-tagged WRR4A$^{Col-0}$, co-delivered with the recognized CCG28 effector, triggered HR, confirming the functionality of the TurboID-tagged protein (Figure 4.15). The p35S:*At*WRR4A$^{Col-0}$:TurboID-V5 construct was then transformed into the confirmed *eds1*$^{Ws-2}$ mutant background (see Chapter 5, Supplementary Figure 5.4) and was intended to be used for detecting the eight CCG effectors recognized by WRR4A$^{Col-0}$ following infection with *A. candida* isolate Ac2V. The Ac2V isolate was chosen because its genome was re-sequenced using PacBio long reads, and an assembly was constructed with the addition of Illumina reads (Furzer et al., 2022). As a negative control, the pAt2:mCherry:TurboID-V5 construct was transformed into the same *eds1*$^{Ws-2}$ mutant background (see Chapter 5, Table 5.1). *A. thaliana* TurboID transgenic lines with similar protein expression were

selected for TurboID-tagged WRR4A$^{Col-0}$ and mCherry (See Chapter 5, Supplementary Figures 5.1 and 5.2).

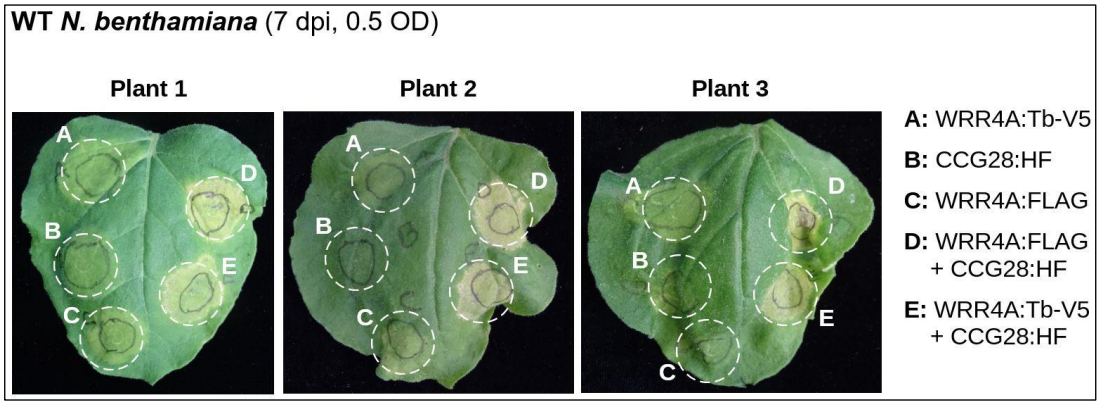


**Figure 4.15 WRR4A$^{Col-0}$:TurboID-V5 supports HR in *N. benthamiana*.**

HR assays by *Agro*-infiltration at $OD_{600}$ = 0.5 in 4/5-week-old *N. benthamiana* leaves in the presence of p19 and at 7 dpi. The *A. candida* effector CCG28 is recognized by the Arabidopsis NLR protein WRR4A$^{Col-0}$ (Redkar et al., 2023). Co-delivery of 35S promoter-driven WRR4A$^{Col-0}$:FLAG or WRR4A$^{Col-0}$:TurboID-V5 (WRR4A:Tb-V5) with CCG28 triggers HR in WT *N. benthamiana* leaves.

While the *A. thaliana* TurboID transgenic lines were being selected, I also attempted to capture CCG28 with TurboID-tagged WRR4A$^{Col-0}$ in the *N. benthamiana eds1* mutant background by transiently expressing these proteins *via* Agrobacterium infiltration under 35S promoters (Figures 4.16, 4.17 and 4.18). WRR4A$^{Col-0}$ relies on the expression of the *EDS1* gene to activate defense responses, and working in an *eds1* mutant background prevents HR from being triggered. We aimed to confirm that biotinylated CCG28, which is 61 kDa in size and contains 28 lysines (6 of which are in its N-terminal region within the secreted protein sequence), could be detectable by immunoblot. CCG34 was used as a negative control, as it is not recognized by WRR4A$^{Col-0}$ (Redkar et al., 2023).

In the first attempt, a 5-hour labelling time was used, and the TurboID-tagged WRR4A$^{Col-0}$ protein biotinylated itself, as expected, along with the recognized CCG28 and the unrecognized CCG34 (Figure 4.16). Since CCG34 is neither recognized by nor directly interacts with WRR4A$^{Col-0}$ (Redkar et al., 2023), it was not expected to be biotinylated, suggesting that the experiment might not have revealed recognition-dependent biotinylation.

The experiment was repeated with additional negative controls, including the effector AVRamr3 from *P. infestans* and the non-functional WRR4A Niederzenz-1 allele ($WRR4A^{Nd-1}$), which differs from $WRR4A^{Col-0}$ by 22 amino acid residues and does not recognize these CCGs (Pucker et al., 2019) (Figure 4.17). Additionally, the full-length CCG28 and CCG34 effectors were replaced with their N-terminal regions only ($CCG28^{N-ter}$ and $CCG34^{N-ter}$), as these were used in the Co-IP experiments in Redkar et al. (2023). Finally, a 30-minute labelling time was employed to increase specificity. However, despite these experimental changes, $CCG28^{N-ter}$, $CCG34^{N-ter}$ and AVRamr3 were all biotinylated by the TurboID-tagged $WRR4A^{Col-0}$ and $WRR4^{Nd-1}$, suggesting that the experimental parameters were still not optimal (Figure 4.17). Despite the N-terminal regions of CCG28 and CCG34 containing only six lysines, their biotinylation was detectable, likely due to the Myc-E9 tag, which consists of an additional sequence containing 24 lysine residues.

I realized that $WRR4A^{Col-0}$ was highly expressed in *N. benthamiana*, which might have increased the chances of the TurboID enzyme being randomly near proteins that would subsequently be biotinylated, even if their proximity with the bait had no biological significance. To test this, the 35S promoter was switched to a pAt2 promoter with lower expression, which significantly reduced the protein accumulation of $WRR4A^{Col-0}$, and the experiment was repeated. In this third attempt, specific biotinylation of $CCG28^{N-ter}$ by TurboID-tagged $WRR4A^{Col-0}$ was detected, and as expected, no biotinylation of $CCG34^{N-ter}$ occurred (Figure 4.18). This demonstrated that TurboID is sensitive to bait protein abundance: too little bait protein can make it hard to detect biotinylated residues, while too much can lead to non-specific biotinylation. The biotinylation pattern observed for the N-terminal regions of these CCGs aligns with the previously reported Co-IP experiments (Redkar et al., 2023). However, both full-length CCG28 and CCG34 were still biotinylated, even though $CCG34^{Nter}$ was no longer biotinylated under these new experimental conditions (shorter labelling time and reduced bait protein accumulation) (Figure 4.18). The fact that full-length CCG34 remains biotinylated by $WRR4A^{Col-0}$ under these experimental conditions suggests a weak or transient interaction between these two proteins, even though CCG34 does not trigger HR with $WRR4A^{Col-0}$. Such interactions can be detected by PL techniques, which are more sensitive than traditional Co-IPs. This could indicate that not all protein-protein interactions necessarily lead to a biological outcome (see Chapter 6 for more discussion on this). However, this may also be an artifact of transient overexpression in *N. benthamiana*.

After confirming that specific biotinylation of CCG28$^{Nter}$ by WRR4A$^{Col-0}$ was achievable in an overexpression reporter system, we aimed to detect biotinylated CCG effectors by mass spectrometry under native infection conditions in Arabidopsis (Figure 4.19).

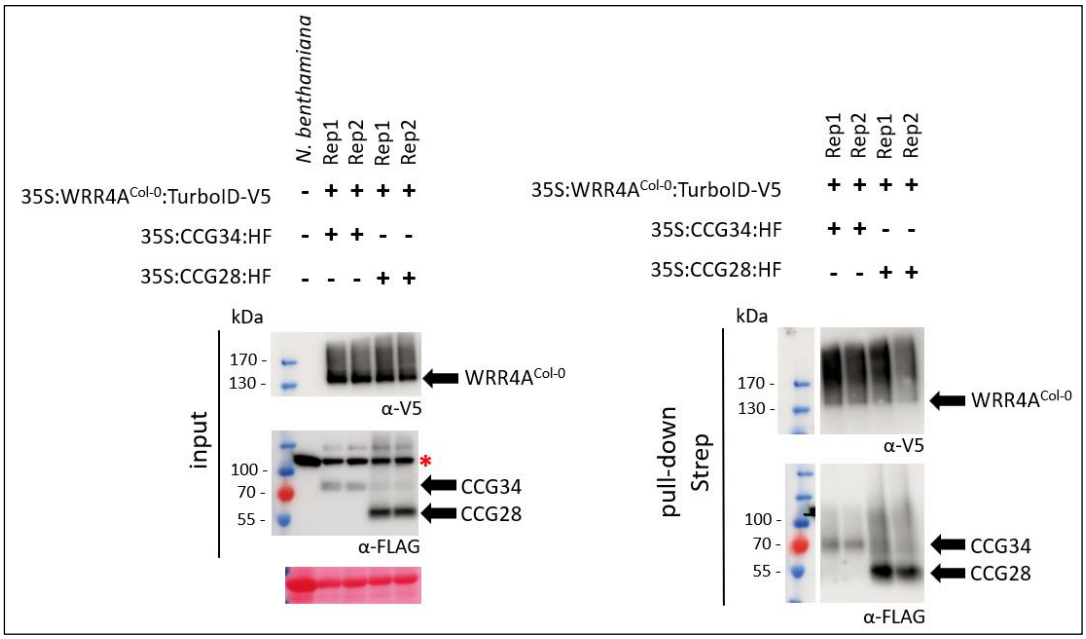


**Figure 4.16 Proximity biotinylation of *At*WRR4A$^{Col-0}$ by TurboID in *eds1 N. benthamiana*.**

Steptavidin pull-down and biotinylation of full length CCG28$^{AcNc2}$:HF and CCG34$^{AcBot}$:HF by WRR4A$^{Col-0}$:TurboID-V5 in *eds1 N. benthamiana* after 7 M urea washing conditions. *Agro*-infiltrations at $OD_{600}$ = 0.5 in 4-week-old *eds1 N. benthamiana* leaves in the presence of p19. Biotin-infiltration (50 µM) at 3 dpi and for 5 h before tissue harvesting. Pull-down was carried out with streptavidin beads. Lysates were resolved by SDS-PAGE. HF-tagged proteins contain both a His-tag and a FLAG-tag, enabling versatile options for protein purification and detection. Bands labelled with a red asterisk (*) correspond to unspecific bands. Each repeat corresponds to two different plants infiltrated with the same *Agro*-infiltration mixture.

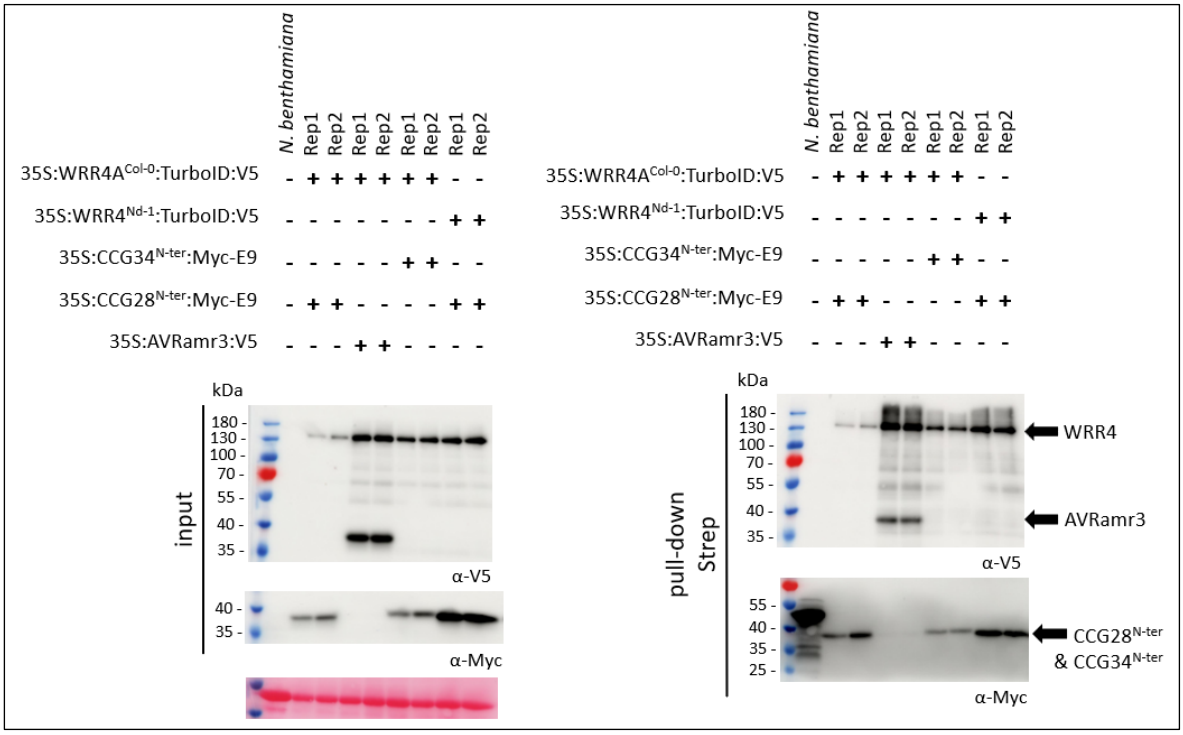


**Figure 4.17 Proximity biotinylation of *At*WRR4A$^{Col-0}$ and *At*WRR4A$^{Nd-1}$ by TurboID in *eds1 N. benthamiana*.**

Streptavidin pull-down and biotinylation of AVRamr3:V5, CCG28$^{N-ter}$:Myc-E9 and CCG34$^{N-ter}$:Myc-E9 by WRR4A$^{Col-0}$:TurboID-V5 and WRR4A$^{Nd-1}$:TurboID-V5 in *eds1 N. benthamiana* after 7 M urea washing conditions. *Agro*-infiltrations at $OD_{600}$ = 0.5 in 4-week-old *eds1 N. benthamiana* leaves in the presence of p19. Biotin-infiltration (50 µM) at 3 dpi and for 30 min before tissue harvesting. Pull-down was carried out with streptavidin beads. Lysates were resolved by SDS-PAGE. Each repeat corresponds to two different plants infiltrated with the same *Agro*-infiltration mixture.

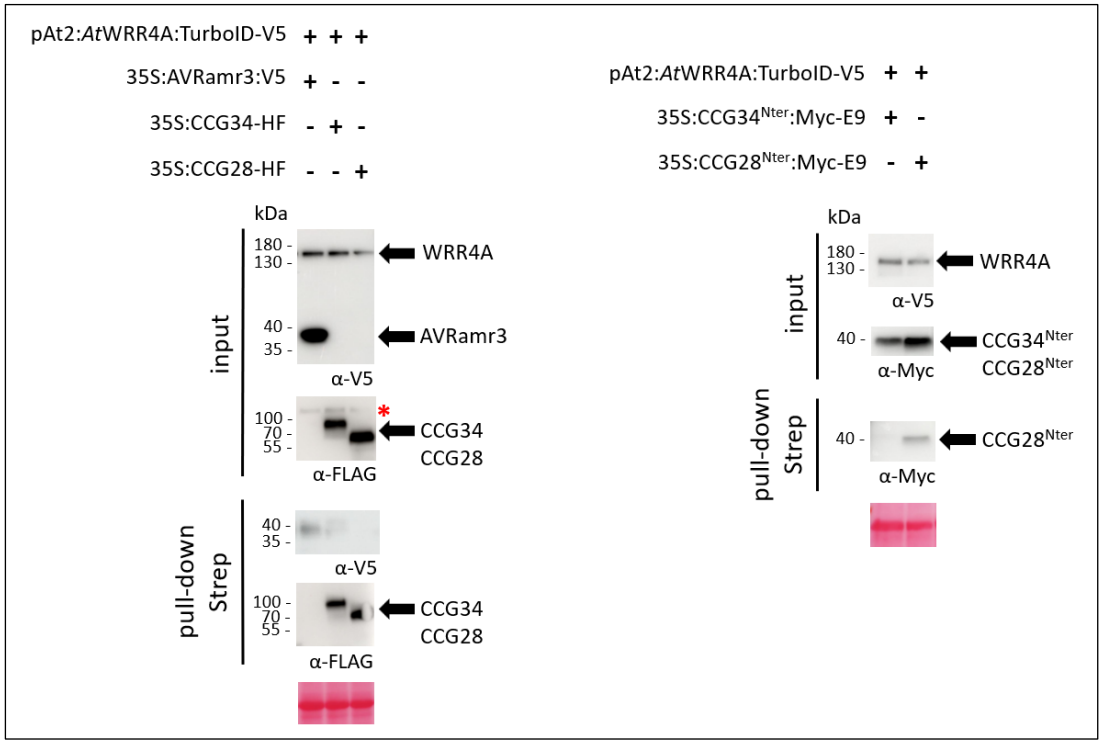


**Figure 4.18 The pAt2 promoter-driven TurboID-tagged *At*WRR4A$^{Col-0}$ specifically biotinylates CCG28$^{N-ter}$ but not the full-length CCG28 in *eds1 N. benthamiana*.**

Streptavidin pull-down and biotinylation of AVRamr3:V5, full-lenght CCG28:HF, full-lenght CCG34:HF, CCG28$^{N-ter}$:Myc-E9 and CCG34$^{N-ter}$:Myc-E9 by pAt2:WRR4A$^{Col-0}$:TurboID-V5 in *eds1 N. benthamiana* after 7 M urea washing conditions. *Agro*-infiltrations at $OD_{600}$ = 0.5 in 4-week-old *eds1 N. benthamiana* leaves in the presence of p19. Biotin-infiltration (50 µM) at 3 dpi and for 30 min before tissue harvesting. Pull-down was carried out with streptavidin beads. Lysates were resolved by SDS-PAGE. HF-tagged proteins contain both a His-tag and a FLAG-tag, enabling versatile options for protein purification and detection. Bands labelled with a red asterisk (*) correspond to unspecific bands.

Both transgenic Arabidopsis lines, transformed with WRR4A$^{Col-0}$ and mCherry fused with TurboID, were spray-inoculated with *A. candida*$^{Ac2V}$. Six days later, leaves were harvested, vacuum-infiltrated with biotin, and left submerged for 3 hours (Figure 4.19). The quality of the samples was assessed by Western blotting with HRP-conjugated streptavidin to detect biotinylated proteins within the samples (Figure 4.20). The baits themselves are biotinylated and can be identified in the input samples on the Western blot. Both mCherry:TurboID and WRR4A$^{Col-0}$:TurboID showed similar protein accumulation and biotinylation levels (Figure 4.20). These samples were sent for analysis using the Orbitrap Eclipse LC-MS/MS system with FAIMS, as this system was the only one capable of detecting native *P. infestans* AVRamr effectors.

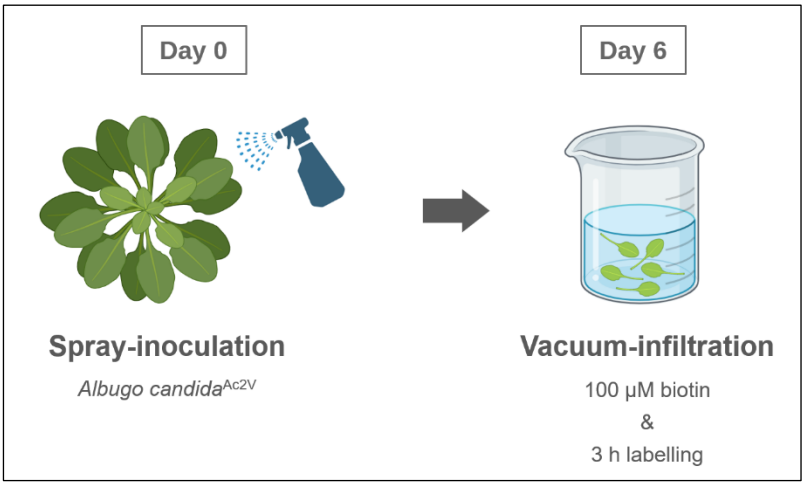


**Figure 4.19 Schematic representation of the experimental design used to identify pathogen and plant interactors of WRR4A$^{Col-0}$.**

2/3-week-old transgenic *A. thaliana* lines, 35S:*WRR4A*$^{Col-0}$:TurboID-V5 in the *eds1*$^{Ws-2}$ mutant background, were sprayed with *A. candida*$^{Ac2V}$ (100,000 oospores/mL). Six days post-inoculation, infected leaves were harvested, vacuum-infiltrated with biotin (100 µM) and subsequently submerged in biotin (100 µM) for 3 h.

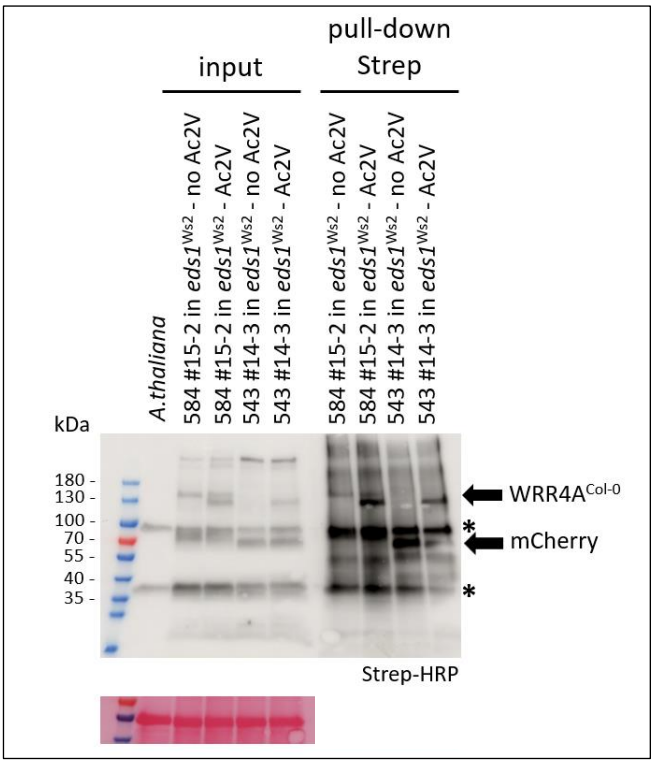


**Figure 4.20 Proximity biotinylation by *At*WRR4A$^{Col-0}$:TurboID in *eds1*$^{Ws-2}$ *A. thaliana*.**

Streptavidin pull-down and biotinylation of 35S:WRR4A$^{Col-0}$:TurboID-V5 (584) and pAt2:mCherry:TurboID-V5 (543) in *eds1*$^{Ws-2}$ *A. Thaliana*. 2/3-week-old *eds1*$^{Ws-2}$ *A. thaliana* TurboID transgenic lines were sprayed with *A. candida*$^{Ac2V}$ (100,000 oospores/mL). Leaves were harvested at 6 days post-inoculation, vacuum-infiltrated with biotin (100 µM), and submerged in biotin (100 µM) for 3 h. Pull-down was carried out with streptavidin beads. A small fraction of the beads was boiled and resolved by SDS-PAGE to assess sample quality prior to LC-MS/MS analysis. Biotinylated proteins were detected by using HRP-conjugated streptavidin labelling. Bands labelled with a black asterisk (*****) correspond to endogenously biotinylated proteins. The "*A. thaliana*" lane corresponds to non-infiltrated samples, meaning no TurboID-tagged baits were expressed and no biotin was added. It serves as control to show endogenous biotinylation.

In total, 5,809 proteins were identified across the three repeats, including all proteins detected in samples from the bait construct WRR4A$^{Col-0}$:TurboID and the mCherry:TurboID control. Of these,

4,948 proteins correspond to *A. thaliana* and 861 to *A. candida*$^{Ac2V}$. The *A. candida*$^{Ac2V}$ proteins account for approximately 15% of the total proteins detected. The pathogen-related proteins (referred to as Ac2V_proteins) that were uniquely detected in the WRR4A$^{Col-0}$ containing samples and absent from the mCherry control samples are summarized in Supplementary Figure 4.6. *A. candida* grew and colonized the plant tissues effectively in all three repeats, as indicated by the presence of spectral counts corresponding to pathogen proteins, which were homogeneously distributed across the repeats.

In addition to extracting all the pathogen-related proteins uniquely found with WRR4A$^{Col-0}$ (Supplementary Figure 4.6), an MA plot was created to represent the data (Figure 4.21). Overall, more pathogen-related proteins were detected in this experiment compared to the TurboID experiment carried out in *N. benthamiana* with Rpi-amr1 and Rpi-amr3. Therefore, in this case, dots on the positive end of the Y-axis, highlighted in orange, represent Ac2V_proteins that were significantly differentially biotinylated in the WRR4A$^{Col-0}$ samples compared to the mCherry samples (Figure 4.21). The identification numbers of the proteins highlighted in orange on the MA plot and their corresponding p-values are presented in Table 4.12. None of the eight CCGs previously reported to be recognized by WRR4A$^{Col-0}$ were detected in this experiment (Redkar et al., 2023). However, two new CCGs appeared as potential candidates. CCG41 emerged as a potential candidate in the MA plot analysis (Figure 4.21), and CCG14 was found in the list of Ac2V_proteins uniquely identified with WRR4A$^{Col-0}$ (Supplementary Figure 4.6). CCG41 and CCG14 were detected with protein sequence coverages of 27% and 8%, respectively, and with eleven and three peptides identified.

CCG41 does not appear in the list of Ac2V_proteins uniquely identified with WRR4A$^{Col-0}$ (Supplementary Figure 4.6) because it is more abundant (with five, six, and ten spectral counts detected in rep1, rep2, and rep3, respectively) than CCG14 and was also detected in the mCherry-containing samples (with two and four spectral counts detected in rep1 and rep3, respectively). Although CCG41 was detected in mCherry samples, it was significantly more biotinylated by WRR4A$^{Col-0}$, making it a significant candidate. On the other hand, CCG14 does not appear in the MA plot analysis (Figure 4.21) because it is less abundant (with two and three spectral counts detected in rep2 and rep3, respectively, Supplementary Figure 4.6) than CCG41. As a result, CCG14 does not emerge as a significantly differentially biotinylated candidate, even though it is completely absent from mCherry-containing samples. Since some of these Ac2V_proteins are not abundant enough to

emerge as significant candidates, it is also important to examine the raw data (Supplementary Figure 4.6).

Along with these two CCGs, several other pathogen proteins were also captured, some of which might play a role as effectors. To explore this further, we analysed all pathogen proteins uniquely detected in samples containing WRR4A$^{Col-0}$ (Supplementary Figure 4.6), and the top Ac2V_proteins identified in the MA plots (Table 4.12), using SignalP 6.0 to predict the presence of a signal peptide (Table 4.13). Three additional pathogen proteins were identified as having a predicted signal peptide. However, no information is available regarding these three Ac2V_proteins identified through TurboID (Table 4.13). These may represent newly identified effectors, although further testing is required to confirm this.

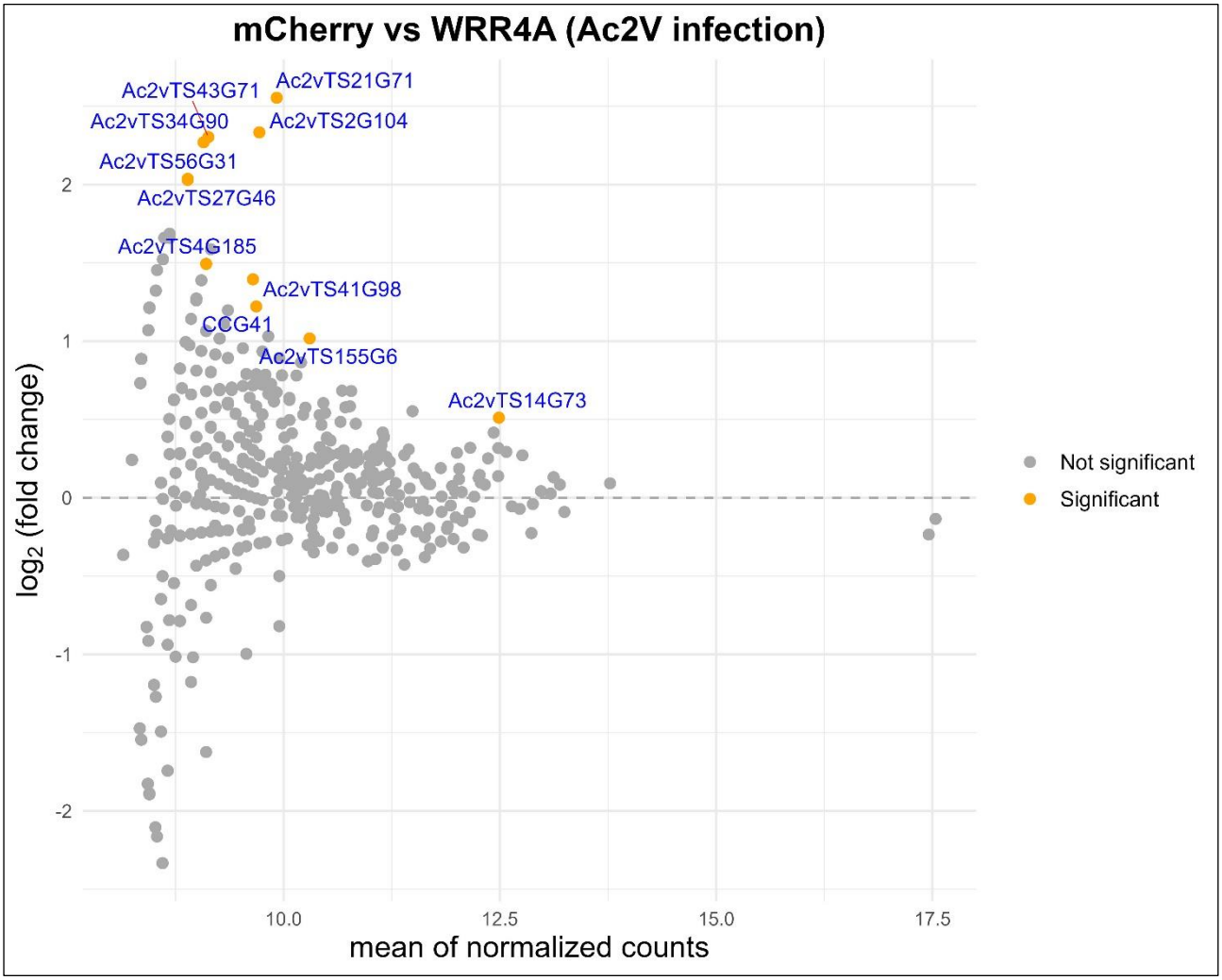


**Figure 4.21 TurboID-based identification of WRR4A$^{Col-0}$ proximal pathogen interactors.**

WRR4A$^{Col-0}$ proximal pathogen interactors identified by mass spectrometry at 6 days post *A. candida*$^{Ac2V}$ infection in *eds1*$^{Ws-2}$ *A. thaliana*. The MA plot (M *versus* A plot) displays the relationship between average protein abundance (A) and the $log_2$(FC) in biotinylation (M). Proteins highlighted in orange represent the most differentially biotinylated proteins compared to mCherry ($log_2$(FC) > 0 and P-value < 0.05), while proteins with no significant differences in biotinylation are shown in grey. The data were normalized using cyclic loess normalization *via* the edgeR package (Chen et al., 2025). Proteins with values near 0 on the X-axis correspond to low-abundance proteins, while highly abundant proteins are located further from 0. Extreme values along the Y-axis represent promising interactors, and only small changes in biotinylation are sufficient for highly abundant proteins.

| mCherry vs WRR4A (Ac2V infection)<br>ranked by p-value & log(FC) > 0 | | |
|---|---|---|
| Protein | p-value | log(FC) |
| Ac2vTS21G71 | 0.0002 | 2.5539 |
| Ac2vTS2G104 | 0.0018 | 2.3329 |
| Ac2vTS34G90 | 0.0090 | 2.2695 |
| Ac2vTS43G71 | 0.0175 | 2.3028 |
| Ac2vTS155G6 | 0.0228 | 1.0170 |
| Ac2vTS56G31 | 0.0229 | 2.0363 |
| CCG41 | 0.0255 | 1.2211 |
| Ac2vTS41G98 | 0.0278 | 1.3947 |
| Ac2vTS27G46 | 0.0329 | 2.0297 |
| Ac2vTS14G73 | 0.0351 | 0.5107 |
| Ac2vTS4G185 | 0.0447 | 1.4930 |

**Table 4-12 List of the WRR4A$^{Col-0}$ proximal pathogen interactors identified at 6 days post *A. candida*$^{Ac2V}$ infection in *eds1*$^{Ws-2}$ *A. thaliana*.**

Proteins are ranked by P-value < 0.05 and log(FC) > 0.

**Table 4-13 *A. candida* proteins identified using TurboID-tagged WRR4A$^{Col-0}$ that contain a predicted signal peptide.**

Amount all the Ac2V_proteins detected by mass spectrometry, three additional Ac2V_proteins with a predicted signal peptide were identified with WRR4A$^{Col-0}$. YES indicates that a signal peptide was predicted by the SignalP 6.0 software (Teufel et al., 2022).

| **Protein:** | **WRR4A$^{Col-0}$**<br>signal peptide (SP) |
|---|---|
| **Ac2vTS2G104** | YES |
| **Ac2vTS41G98** | YES |
| **Ac2vTS31G30** | YES |

Protein proximity provides weak evidence of a functional relationship, which is why we further tested CCG14 and CCG41 to verify that they were recognized by WRR4A$^{Col-0}$. First, we performed an

*in silico* prediction of the potential interaction between CCG41 and CCG14 with WRR4A$^{Col-0}$ using AlphaFold2 (Figures 4.22 and 4.23) (Jumper et al., 2021). For the structural model, only the N-terminal regions of these two CCGs, along with the leucine-rich repeat (LRR) domain and C-terminal jellyroll immunoglobulin domain (C-JID) of WRR4A$^{Col-0}$, were used. The software predicted that CCG41 and CCG14 are highly likely to interact with WRR4A$^{Col-0}$ with ipTM scores of 0.79 and 0.816 respectively (Figures 4.22 and 4.23). Furthermore, we performed HR assays in *N. tabacum* (Figure 4.24), and both CCG41 and CCG14 triggered cell death in the presence of WRR4A$^{Col-0}$, similar to the cell death triggered by CCG40, which is already reported to be recognized by WRR4A$^{Col-0}$ (Redkar et al., 2023). Therefore, these two promising CCG candidates identified by TurboID have been validated, bringing the total number of CCGs recognized by WRR4A$^{Col-0}$ from eight to ten. This further demonstrates that effector discovery under native conditions can be facilitated and achieved with TurboID.

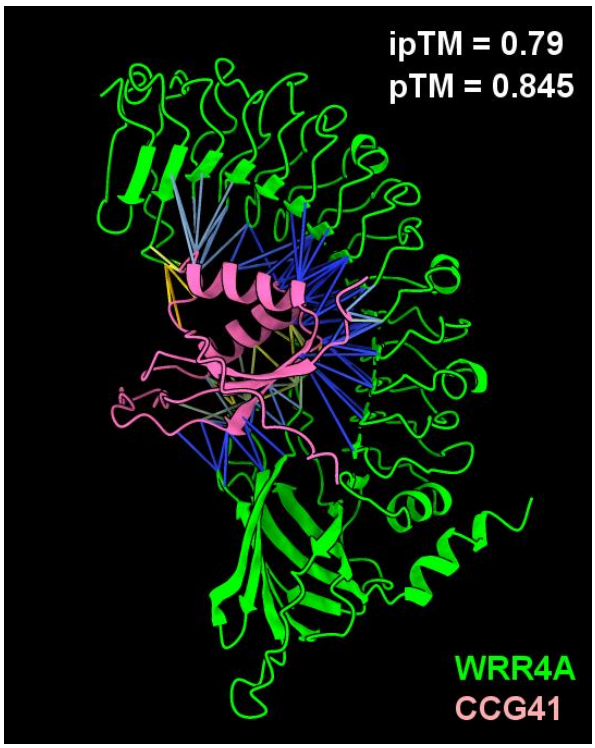


**Figure 4.22 TurboID-identified CCG41 is predicted to interact with WRR4A$^{Col-0}$.**

AlphaFold2 prediction of the interaction between CCG41$^{Nter}$ (pink) and WRR4A$^{Col-0}$ (green). For the structural model of WRR4A$^{Col-0}$, only the leucine-rich repeat (LRR) domain and C-terminal jellyroll immunoglobulin domain (C-JID) were used. Predicted interaction sites between the two proteins are represented as straight lines, with blue indicating high-confidence predictions and red indicating low-confidence predictions. The model shown represents the highest-scoring prediction among the five models generated.


**Figure 4.23 TurboID-identified CCG14 is predicted to interact with WRR4A$^{Col-0}$.**

AlphaFold2 prediction of the interaction between CCG14$^{Nter}$ (pink) and WRR4A$^{Col-0}$ (green). For the structural model of WRR4A$^{Col-0}$, only the leucine-rich repeat (LRR) domain and C-terminal jellyroll immunoglobulin domain (C-JID) were used. Predicted interaction sites between the two proteins are represented as straight lines, with blue indicating high-confidence predictions and red indicating low-confidence predictions. The model shown represents the highest-scoring prediction among the five models generated.

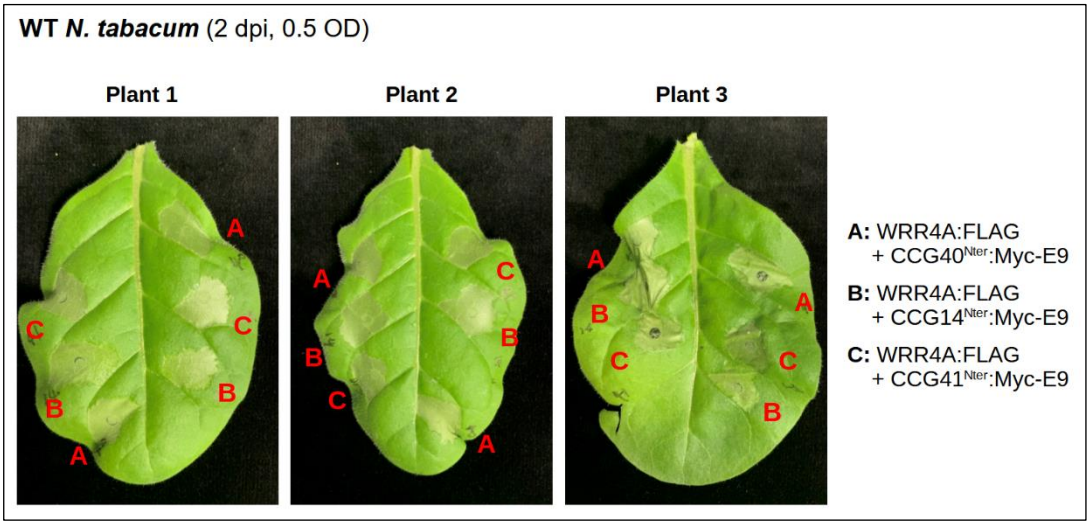


**Figure 4.24 CCG14$^{Nter}$ and CCG41$^{Nter}$ are recognized by WRR4A$^{Col-0}$ in *N. tabacum*.**

HR assays by *Agro*-infiltration at $OD_{600}$ = 0.5 in 4/5-week-old *N. tabacum* leaves and at 2 dpi. The *A. candida* effector CCG40 is recognized by the Arabidopsis NLR protein WRR4A$^{Col-0}$ (Redkar et al., 2023). Co-delivery of 35S promoter-driven WRR4A$^{Col-0}$:FLAG with CCG14$^{Nter}$:Myc-E9 and CCG41$^{Nter}$:Myc-E9 triggers HR in WT *N. tabacum* leaves. Colleague Dr He Zhao performed this experiment.

The experiment not only captured pathogen-related proteins but also identified WRR4A$^{Col-0}$ plant interactors, offering valuable insights into NLR regulation and signalling. A total of 4,948 *A. thaliana* biotinylated proteins were identified with TurboID-tagged WRR4A$^{Col-0}$ and were bioinformatically analysed using the same pipeline applied to *N. benthamiana* proteins associated with Rpi-amr1 and Rpi-amr3. Volcano plots of the resulting p-values were generated (Figures 4.25 and 4.26) and the top significant proximal interactors are summarized in Tables 4.14 and 4.15.

Most of the identified proximal interactors of WRR4A$^{Col-0}$ were shared between *A. candida*-infected and uninfected conditions, with a total of 54 proteins, while 37 were unique to the infected samples (Figure 4.27). The GO-term analysis highlighted the prominence of chaperones and co-chaperones in the proximity of WRR4A$^{Col-0}$, which are typically involved in regulating NLR stability (Figure 4.28). Chaperones and co-chaperones were also observed in the proximity of Rpi-amr1 and Rpi-amr3, suggesting that they are a common feature of NLRs, as seen in the previous results section.

In addition to chaperones, another important regulator of NLRs, SRFR1, was detected in the proximity of WRR4A$^{Col-0}$ (Tables 4.14 and 4.15). SRFR1 was also observed in the presence of TurboID-tagged Rpi-amr3, as described in the previous results section. As negative regulator of NLR-mediated

immunity, SRFR1 interacts with various NLR-associated proteins, including molecular co-chaperones and transcription factors, thereby preventing the auto-activation of plant immunity. SRFR1 may also regulate the activity of both WRR4A$^{Col-0}$ and Rpi-amr3.

Furthermore, the experiment identified a less conventional protein in the proximity of WRR4A$^{Col-0}$: a PHOSPHOENOLPYRUVATE CARBOXYKINASE (PCK1) involved in gluconeogenesis (Leegood and Walker, 2003). A study reported that the pepper (*Capsicum annuum*) *PEPCK* gene, *CaPEPCK1*, was rapidly and strongly induced in pepper plants infected with *Xanthomonas campestris* pv. v*esicatoria* (*Xcv*) (Choi et al., 2015). Silencing of *CaPEPCK1* in pepper increased susceptibility to both virulent and avirulent *Xcv* infections, impaired the induction of basal defense-marker genes, including *CaPR1* (*pathogenesis-related 1 protein*), *CaPR10* (*pathogenesis-related 10 protein*), and *CaDEF1* (*defensin*), and reduced salicylic acid (SA) accumulation. In contrast, overexpression of *CaPEPCK1* in Arabidopsis enhanced resistance to *Pseudomonas syringae* pv. *tomato* (*Pst*) and *Hyaloperonospora arabidopsidis* (*Hpa*) infections. Additionally, the T-DNA insertion mutant of the Arabidopsis ortholog, *pck1*, exhibited greater susceptible to *Pst* and *Hpa* infection compared to wild-type plants. These findings suggest that PEPCK1 plays a positive role in plant immunity against bacterial and oomycete pathogens in both pepper and Arabidopsis (Choi et al., 2015).

Lastly, a few spectral counts corresponding to the transcription factor WRKY2 were detected in the *A. candida*-infected WRR4A$^{Col-0}$ samples (with 3, 2, and 4 spectral counts in rep1, rep2, and rep3, respectively), but not in the non-infected WRR4A$^{Col-0}$ samples or the mCherry samples. Due to the low number of spectral counts, this candidate was excluded from the bioinformatic analysis; however, it was uniquely found in the proximity of WRR4A$^{Col-0}$ in infected tissues. *WRKY* genes encode transcription factors (TFs) that belong to a large family involved in various developmental and physiological processes, including plant responses to pathogen infections (Javed and Gao, 2023). A subset of plant NLRs has been shown to directly interact with TFs or cofactors to regulate defense gene expression. The rice CNL Pb1, upon activation, confers blast resistance through its interaction with *Os*WRKY45 in the nucleus (Inoue et al., 2013). Similarly, the rice CNL BPH14 modulates gene expression with *Os*WRKY46/*Os*WRKY72 (Hu et al., 2017), while the chickpea CNL *Ca*RGA interacts with *Ca*WRKY64 (Chakraborty et al., 2018). An example of WRKY2 involvement into plant immunity is the constitutive expression of grapevine (*Vitis vinifera*) *VvWRKY2* in *N. tabacum*, which resulted in enhanced resistance to three types of necrotrophic fungi: *B. cinerea*, *Alternaria tenuis*, and *Pythium*

(Mzid et al., 2007). These findings suggest that WRKY2 may be involved in the downstream signalling pathway of WRR4A$^{Col-0}$.

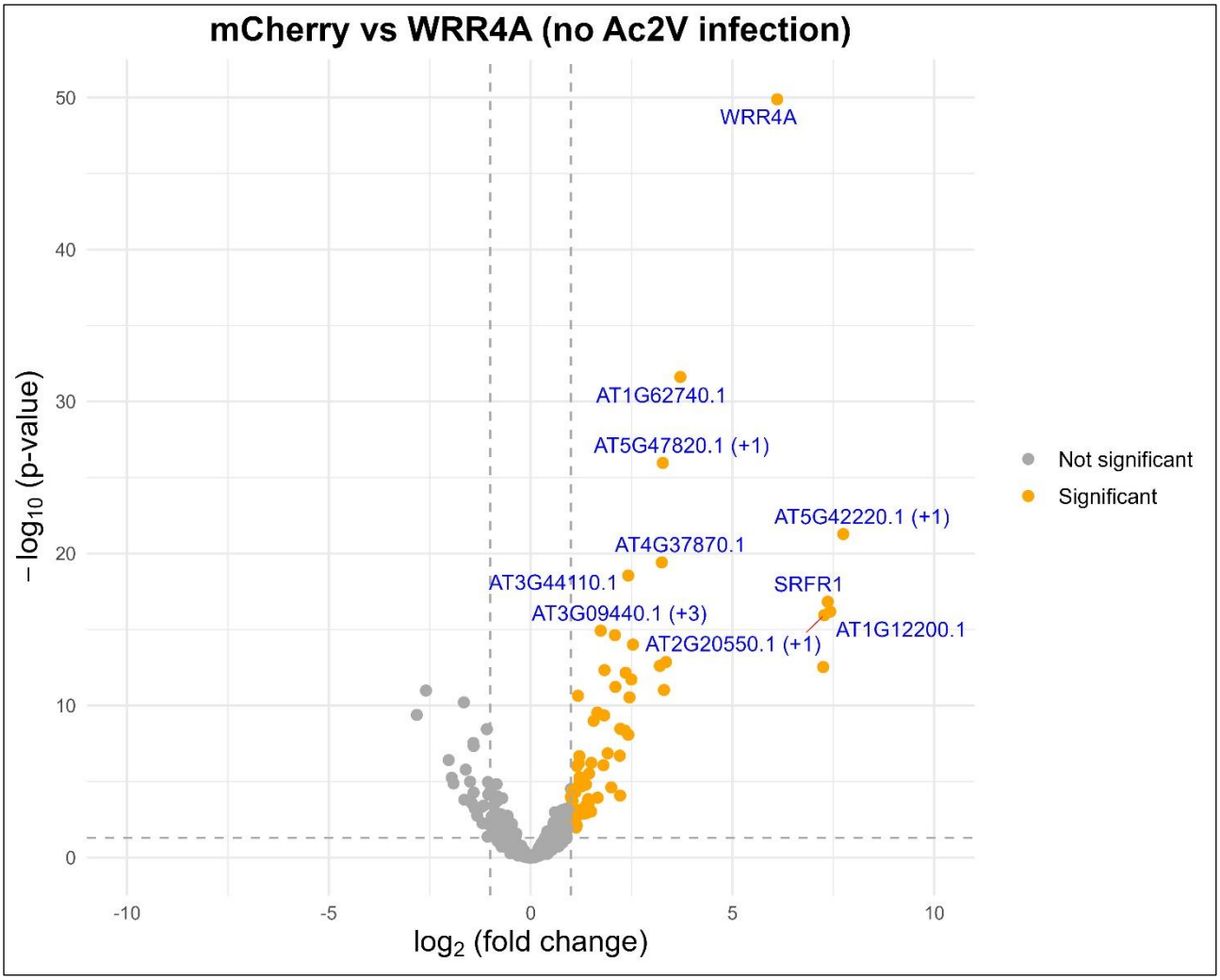


**Figure 4.25 TurboID-based identification of WRR4A$^{Col-0}$ proximal plant interactors in *eds1*$^{Ws-2}$ *A. thaliana* without *A. candida*$^{Ac2V}$ infection.**

Proteins highlighted in orange were considered as WRR4A$^{Col-0}$ proximal plant interactors if they exhibited a 2-fold change increase in biotinylation compared to mCherry and had a statistically significant difference (P-value < 0.05). Proteins with no significant difference in biotinylation are shown in grey. The grey dotted threshold lines indicate a P-value of 0.05 (horizontal) and a log2(fold change) of –1 and 1 (vertical). The top 10 significantly biotinylated proteins are labelled with their identification numbers. Proteins with a total spectral count below 50 were excluded from the analysis. Statistical significance was determined using Fisher's Exact Test, implemented in the edgeR package (Chen et al., 2025).

**Table 4-14 . List of the WRR4A$^{Col-0}$ proximal plant interactors identified in *eds1*$^{Ws-2}$ *Arabidopsis thaliana* without *A. candida*$^{Ac2V}$ infection.**

Proteins are ranked by P-value and log(FC) > 2.

| Protein | P-value | log(FC) | Description |
|---|---|---|---|
| AT1G56510 | 1.32E-50 | 6.108 | WRR4A |
| AT1G62740 | 2.42E-32 | 3.709 | HOP2, encodes one of the 36 TPR proteins with potential to interact with Hsp90/Hsp70 as co-chaperones |
| AT5G47820 | 1.1E-26 | 3.273 | FRA1, encodes a kinesin-like protein with an N-terminal microtubule binding motor domain |
| AT5G42220 | 5.27E-22 | 7.745 | Ubiquitin-like superfamily protein |
| AT4G37870 | 3.86E-20 | 3.248 | PCK1, encodes a phosphoenolpyruvate carboxykinase that localizes to the cytosol |
| AT3G44110 | 2.83E-19 | 2.418 | ATJ3, homologous to the co-chaperon DNAJ protein from *E. coli*, member of the HSP40 family, interacts with HSP70 to mediate heat shock response |
| AT4G37460 | 1.5E-17 | 7.363 | SRFR1, encodes a tetratricopeptide repeat domain containing protein that shows sequence similarity to those of transcriptional repressors in other organisms, it is involved in mediating effector-triggered immunity |
| AT1G12200 | 6.56E-17 | 7.422 | FMO, putative flavin monooxygenase |
| AT2G20550 | 1.13E-16 | 7.273 | HSP40/DnaJ peptide-binding protein |
| AT4G02450 | 2.35E-15 | 2.086 | P23-1, encodes one of two isoforms of a co-chaperone of HSP90 that is required for root growth |
| AT1G56440 | 9.85E-15 | 2.534 | TPR5, encodes one of the 36 TPR proteins with potential to interact with Hsp90/Hsp70 as co-chaperones |
| AT5G12430 | 1.37E-13 | 3.353 | TPR16, encodes one of the 36 TPR proteins with potential to interact with Hsp90/Hsp70 as co-chaperones |
| AT4G09420 | 2.47E-13 | 3.202 | TN15, disease resistance protein (TIR-NBS class) |
| AT4G12400 | 2.94E-13 | 7.247 | HOP3, encodes one of the 36 TPR proteins with potential to interact with Hsp90/Hsp70 as co-chaperones |
| AT3G19190 | 7.04E-13 | 2.353 | ATG2, encodes autophagy-related 2, autophagy controls guard cell ROS homeostasis by eliminating oxidized peroxisomes, thereby allowing stomatal opening |
| AT1G68530 | 1.94E-12 | 2.494 | KCS6, member of the 3-ketoacyl-CoA synthase family involved in the biosynthesis of VLCFA (very long chain fatty acids) |
| AT5G53400 | 5.93E-12 | 2.099 | BOB1, encodes a non-canonical small heat shock protein required for both development and thermotolerance |
| AT5G40740 | 9.54E-12 | 3.303 | AUG6, encodes a conserved AUGMIN subunit 6 which is known to be involved in microtubule nucleation |
| AT1G30070 | 2.93E-11 | 2.448 | possibly involved in response to heat stress |
| AT4G39800 | 3.39E-09 | 2.221 | MIPS1, myo-inositol-1-phosphate synthase isoform 1 |
| AT5G17270 | 4.47E-09 | 2.333 | protein prenylyltransferase superfamily protein |
| AT2G24020 | 8.44E-09 | 2.419 | STIC2 was identified in a screen for suppressors of chloroplast protein import defect in tic40 |
| AT4G22670 | 2.01E-07 | 2.208 | TPR11, encodes one of the 36 TPR proteins with potential to interact with Hsp90/Hsp70 as co-chaperones |
| AT2G44230 | 8.38E-05 | 2.216 | hypothetical protein (DUF946) |

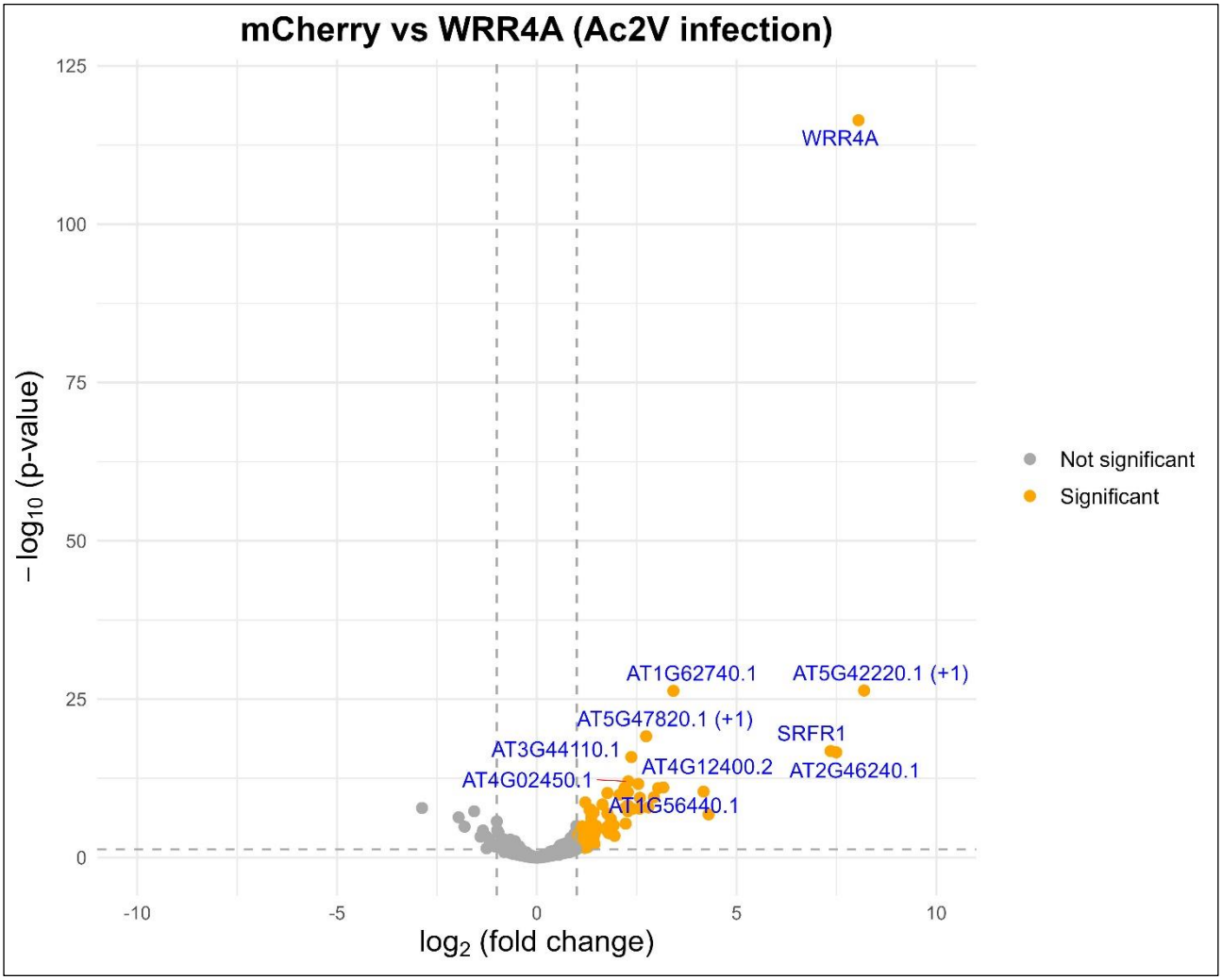


**Figure 4.26 TurboID-based identification of WRR4A$^{Col-0}$ proximal plant interactors at 6 days post *A. candida*$^{Ac2V}$ infection in *eds1*$^{Ws-2}$ *A. thaliana*.**

Proteins highlighted in orange were considered as WRR4A$^{Col-0}$ proximal plant interactors if they exhibited a 2-fold change increase in biotinylation compared to mCherry and had a statistically significant difference (P-value < 0.05). Proteins with no significant difference in biotinylation are shown in grey. The grey dotted threshold lines indicate a P-value of 0.05 (horizontal) and a log2(fold change) of –1 and 1 (vertical). The top 10 significantly biotinylated proteins are labelled with their identification numbers. Proteins with a total spectral count below 50 were excluded from the analysis. Statistical significance was determined using Fisher's Exact Test, implemented in the edgeR package (Chen et al., 2025).

**Table 4-15 List of the WRR4A$^{Col-0}$ proximal plant interactors identified at 6 days post *A. candida*$^{Ac2V}$ infection in *eds1*$^{Ws-2}$ *Arabidopsis thaliana*.**

Proteins are ranked by P-value and log(FC) > 2.

| Protein | P-value | log(FC) | Description |
|---|---|---|---|
| AT1G56510 | 3.94E-117 | 8.053 | WRR4A |
| AT5G42220 | 4.36E-27 | 8.193 | Ubiquitin-like superfamily protein |
| AT1G62740 | 4.84E-27 | 3.419 | HOP2, encodes one of the 36 TPR proteins with potential to interact with Hsp90/Hsp70 as co-chaperones |
| AT5G47820 | 7.08E-20 | 2.737 | FRA1, encodes a kinesin-like protein with an N-terminal microtubule binding motor domain |
| AT4G37460 | 1.55E-17 | 7.355 | SRFR1, encodes a tetratricopeptide repeat domain containing protein that shows sequence similarity to those of transcriptional repressors in other organisms, it is involved in mediating effector-triggered immunity |
| AT2G46240 | 2.49E-17 | 7.497 | BAG6, member of Arabidopsis BAG (Bcl-2-associated athanogene) proteins, plant homologs of mammalian regulators of apoptosis |
| AT3G44110 | 1.38E-16 | 2.367 | ATJ3, homologous to the co-chaperon DNAJ protein from *E. coli*, member of the HSP40 family, interacts with HSP70 to mediate heat shock response |
| AT4G02450 | 9.4E-13 | 2.29 | P23-1, encodes one of two isoforms of a co-chaperone of HSP90 that is required for root growth |
| AT1G56440 | 2.41E-12 | 2.541 | TPR5, encodes one of the 36 TPR proteins with potential to interact with Hsp90/Hsp70 as co-chaperones |
| AT4G12400 | 8.78E-12 | 3.166 | HOP3, encodes one of the 36 TPR proteins with potential to interact with Hsp90/Hsp70 as co-chaperones |
| AT5G53400 | 1.07E-11 | 2.198 | BOB1, encodes a non-canonical small heat shock protein required for both development and thermotolerance |
| AT5G40740 | 1.1E-11 | 3.04 | AUG6, encodes a conserved AUGMIN subunit 6 which is known to be involved in microtubule nucleation |
| AT2G20550 | 3.92E-11 | 4.175 | HSP40/DnaJ peptide-binding protein |
| AT3G19190 | 4.76E-11 | 2.279 | ATG2, encodes autophagy-related 2, autophagy controls guard cell ROS homeostasis by eliminating oxidized peroxisomes, thereby allowing stomatal opening |
| AT2G35630 | 1.22E-10 | 2.073 | MOR1, member of the MAP215 family of microtubule-associated proteins required to establish interphase arrays of cortical microtubules |
| AT5G17270 | 3.18E-10 | 2.932 | protein prenylyltransferase superfamily protein |
| AT4G22670 | 3.78E-10 | 2.581 | TPR11, encodes one of the 36 TPR proteins with potential to interact with Hsp90/Hsp70 as co-chaperones |
| AT1G68530 | 6.03E-09 | 2.278 | KCS6, member of the 3-ketoacyl-CoA synthase family involved in the biosynthesis of VLCFA (very long chain fatty acids) |
| AT2G24020 | 1.23E-08 | 2.792 | STIC2 was identified in a screen for suppressors of chloroplast protein import defect in tic40 |
| AT4G39800 | 1.62E-08 | 2.206 | MIPS1, myo-inositol-1-phosphate synthase isoform 1 |
| AT5G12430 | 1.94E-08 | 2.571 | TPR16, encodes one of the 36 TPR proteins with potential to interact with Hsp90/Hsp70 as co-chaperones |
| AT1G30070 | 2.14E-08 | 2.391 | possibly involved in response to heat stress |
| AT5G02490 | 4.93E-08 | 2.282 | HSP70, member of the cytosolic heat shock 70 protein family |
| AT5G24280 | 1.55E-07 | 4.3 | GMI1, a structural-maintenance-of-chromosomes-hinge domain-containing protein involved in homologous recombination |
| AT1G24020 | 4.48E-06 | 2.225 | MLP423, MLP-like protein 423 |

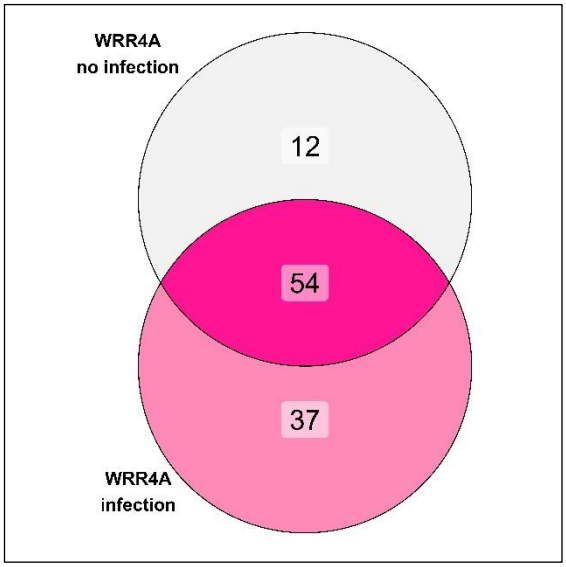


**Figure 4.27 Most WRR4A$^{Col-0}$ proximal plant interactors are shared between uninfected and infected tissues.**

Proteins were considered as proximal plant interactors for each treatment if they showed at least a 1-fold change increase in biotinylation compared to mCherry and a statistically significant difference (P-value < 0.05). Proximal plant interactors for each treatment were compared to generate a Venn diagram. The pink gradient corresponds to counts ranging from a lower to higher number of proteins.

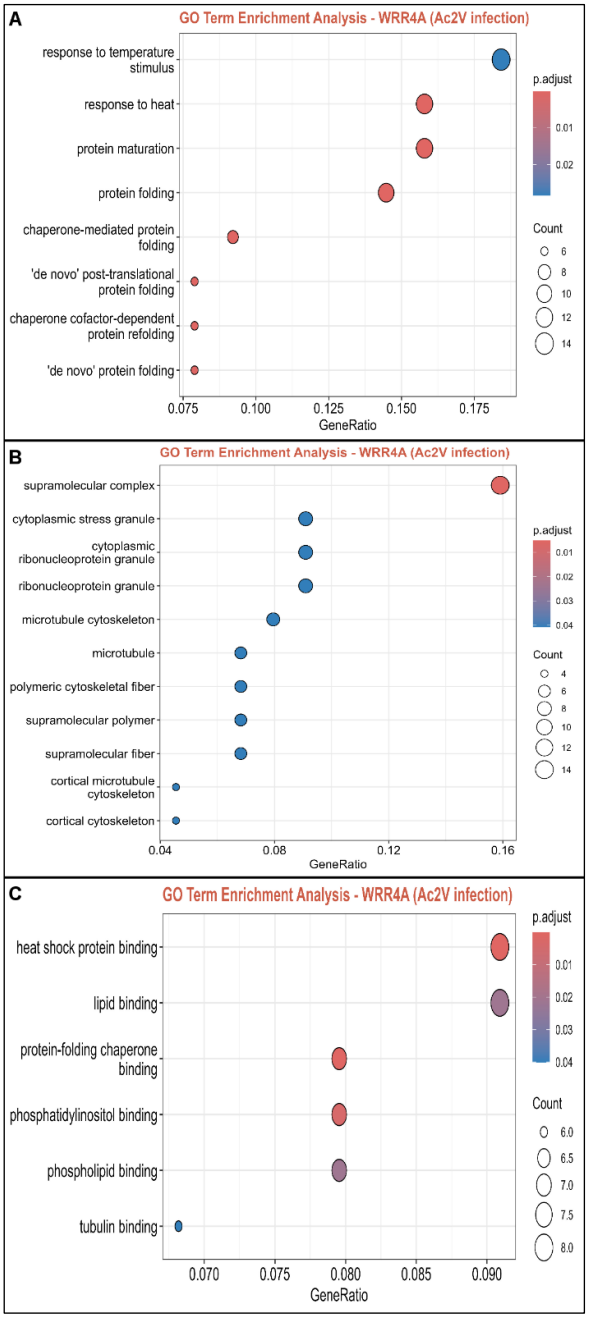


**Figure 4.28 GO-term enrichment analysis of WRR4A$^{Col-0}$ proximal plant interactors.**

Gene ontology (GO) categories analysed included biological process (**A**), cellular component (**B**) and molecular function (**C**). GO terms within each category were ranked in descending order of significance (P-value < 0.05) and visualized by count (represented by circle size). The analysis compared proteins in the proximity to WRR4A$^{Col-0}$ during infection with all Arabidopsis proteins detected by mass spectrometry.

## 4.3 Discussion

To successfully use TurboID-mediated proximity labelling to detect effectors under native infection conditions, several additional optimizations to the experimental parameters, beyond those discussed in Chapter 3, were required. These included: 1) incorporating extended experimental time points to allow the pathogen to proliferate more within the plant, 2) using a more sensitive mass spectrometry machine, and 3) ensuring that the TurboID-tagged bait had optimal protein accumulation (neither too high nor too low). All these adjustments were made to maximize the chances of capturing low-abundance native effectors.

Thanks to these adjustments, AVRamr1 and AVRamr3, which were previously reported to be recognized by the CNLs Rpi-amr1 and Rpi-amr3, respectively, were successfully detected by mass spectrometry in a transient assay conducted in *N. benthamiana* leaves infected with *P. infestans* (Table 4.2; Figures 4.8 and 4.9). AVRamr1 was detected at both experimental time points, 3 and 4 days post *P. infestans* infection, while AVRamr3 was only detected at 4 dpi. This was most likely due to the lower abundance of the Rpi-amr3 TurboID bait protein compared to the Rpi-amr1 TurboID bait (Figure 4.7). Nonetheless, this result demonstrated the feasibility of capturing native effectors with TurboID.

Subsequently, two CCG effectors, CCG14 and CCG41, which had not previously been reported to be recognized by the TNL WRR4A$^{Col-0}$, were identified as promising effector candidates in *A. thaliana* stable transgenic line following infection with *A. candida* (Figure 4.21 and Supplementary Figure 4.6). Both newly identified WRR4A$^{Col-0}$-recognized CCG effectors were predicted to interact with WRR4A$^{Col-0}$ using AlphaFold2 (Figures 4.22 and 4.23) and validated by HR assay (Figure 4.24). Of the two promising CCG candidates identified with TurboID, both were validated as NLR-recognized effectors, resulting in a 100% success rate in this particular experiment. However, none of the previously reported CCG effectors recognized by WRR4A$^{Col-0}$ were detected. This may be due to the fact that only a single time point, 6 days post *A. candida* infection, was examined, and these effectors might have been secreted during different stages of infection.

In Furzer et al. (2022), the expression levels of CCG effectors were measured across all colonization time points, ranging from 2 to 8 dpi, in mustard plants and grouped into distinct expression clusters. The CCG effectors exhibited a broad spectrum of expression patterns, varying from exclusive early

expression to constitutive or late expression during infection. Notably, these expression patterns appeared to be independent of the genomic clusters. Interestingly, both CCG14 and CCG41 are part of expression cluster number 7, indicating they belong to the early-expressed CCGs, with peak expression occurring at 2 and 4 dpi, and decreasing by 6 dpi. Although infected tissues were harvested at 6 dpi in our experimental setup, we were still able to capture early expressed CCGs. In the Furzer et al. (2022) study, trypan blue staining of the Ac2V infection of *B. juncea* at 2, 4, 6, and 8 dpi, corresponding to the RNA extraction time points, showed that the peak of colonization begins at 6 dpi, with 40.4% of the plant tissues colonized by the pathogen, and continues at 8 dpi with 47% of the plant tissues colonized. This could reflect the fact that, at the leaf scale, not all cells are at the same stage of infection, and that at 6 dpi, the plant-pathogen interface is larger as the overall pathogen biomass reaches its peak, potentially making it easier to detect native effectors. In comparison, the previously reported WRR4A$^{Col-0}$-recognized CCG effectors belong to different expression clusters: CCG28 and CCG79 are part of expression cluster number 7 (expressed at 2 and 4 dpi), CCG67 and CCG104 belong to expression cluster number 5 (expressed at 4 and 6 dpi), CCG30 and CCG71 are part of expression cluster number 1 (expressed at 4, 6 and 8 dpi). It is possible that, to detect the previously reported CCG effectors, we are either not examining the right time point or that their expression levels are simply too low. Nevertheless, these findings further demonstrate that TurboID can be a valuable tool for effector discovery, enabling relatively rapid identification of new effectors under native conditions.

In addition to the previously identified pathogen-related proteins as effectors, additional pathogen-related proteins containing predicted signal peptides were detected in both the transient *N. benthamiana* and stable Arabidopsis TurboID transgenic line systems (Tables 4.7 and 4.13). These proteins may represent novel pathogen virulence factors that warrant further investigation.

Overall, more pathogen-related proteins were identified in the stable *A. thaliana* TurboID transgenic line compared to the transient system in *N. benthamiana*. The higher number of pathogen-related proteins identified in Arabidopsis allowed for the estimation of significant p-values (Figures 4.8 and 4.9 vs. Figure 4.21).

This new TurboID-based approach for capturing native effectors could be applied to a wide range of plant pathogens, including oomycetes, fungi, bacteria, aphids, and even beneficial microorganisms. However, its implementation may be more challenging with necrotrophic pathogens, which kill host

cells rapidly, potentially limiting pathogen biomass accumulation in plant tissues and hindering effector detection. Here, we have only tested this approach with the hemi-biotrophic oomycete *P. infestans* and the biotrophic oomycete *A. candida*.

These experiments not only provided valuable information about effector-host interactions but also offered insights into the NLR-interacting proteins. All three NLRs, Rpi-amr1, Rpi-amr3, and WRR4A$^{Col-0}$, shared a common feature: their association with chaperones and co-chaperones, particularly HEAT SHOCK PROTEIN 90 (HSP90), HEAT SHOCK PROTEIN 70 (HSP70), and HSP70-HSP90 ORGANIZING PROTEIN 3 (HOP3). Chaperones, well known for regulating protein folding, stability, and degradation, play essential roles in NLRs as well and some have been shown to modulate plant immune responses.

Specifically, the chaperone complex consisting of the proteins HSP90 and the two co-chaperones, SUPPRESSOR OF THE G2 ALLELE OF skp1 (SGT1) and REQUIRED FOR MLA12 RESISTANCE 1 (RAR1), facilitates NLR folding and accumulation, and is crucial for the proper activation of several NLRs in different plant species (Shirasu, 2009). In Arabidopsis, different HSP90 family members play specific roles in various NLR-mediated defense responses: HSP90.3 negatively regulates SNC1 accumulation (Huang et al., 2014a), while HSP90.2 enhances RPM1 stability (Hubert et al., 2003). Other NLRs, including barley MLA1, potato Rx, and tobacco N, also interact with HSP90 (Bieri et al., 2004, Botër et al., 2007, Liu et al., 2004). HSP90 and its co-chaperones thus regulate NLR protein accumulation, either by promoting folding or facilitating degradation. However, the mechanisms by which these proteins recognize different NLRs and regulate their fates in response to environmental signals remain unclear. Interestingly, it has been found that the bacterial effector HopBF1 mimics an HSP90 client to phosphorylate and inactivate HSP90, preventing NLR activation and undermining the plant defense response (Lopez et al., 2019).

Moreover, HOP proteins are a family of co-chaperones containing three tetratricopeptide repeat (TPR) domains, which mediate interactions with the molecular chaperones HSP70 and HSP90. It has been reported that inhibition of HSP70 and HSP90 results in decreased jasmonic acid (JA) sensitivity and down-regulation of JA-responsive genes, raising questions about the role of their interactor, HOP3, in the regulation of JA signalling (Zhang et al., 2015). Indeed, the *HOP3* gene has been shown to be induced in response to the necrotrophic pathogen *Botrytis cinerea* and the two-spotted spider mite *Tetranychus urticae* attack, and to play a role in the induction of JA-mediated defense in Arabidopsis (Muñoz et al., 2021).

The TurboID NLR datasets highlight that chaperones and co-chaperones are likely a common feature in the regulation of NLRs, either stabilizing immune receptors for defense or limiting their number to prevent autoimmunity. Notably, these HSP proteins were absent from the mCherry:TurboID control samples or were significantly differentially biotinylated compared to the mCherry:TurboID control. This suggests that their presence in the NLR datasets is not due to non-specific binding or the general "stickiness" of HSPs, but rather indicates that HSPs may have a targeted and functional role in the regulation of NLRs, rather than simply acting as passive contaminants. Additionally, no HSPs were detected in the EDS1:TurboID experiment described in Chapter 5.

Beyond chaperones, other proteins such as ubiquitin-like proteins (UBLs) also regulate NLR stability. UBLs are best known for their role in regulating protein degradation, and a few E3 ubiquitin ligases (E3 ligases) have been found to associate with NLRs to regulate their stability (Duplan and Rivas, 2014). For example, the TurboID-identified E3 ligase UBR7 acts as a negative regulator of the tobacco TNL N-mediated immunity by mediating the degradation of N proteins, and downregulation of UBR7 enhances resistance to tobacco mosaic virus (TMV) (Zhang et al., 2019). Notably, one UBL protein was found in the proximity of WRR4A$^{Col-0}$, which could function as a negative regulator of this TNL (Tables 4.14 & 4.15). Indeed, the over accumulation of NLRs can lead to inappropriate activation, thus their stability must be tightly regulated, such as through the ubiquitin-mediated protein degradation pathway, to maintain relatively low levels and ensure NLR homeostasis.

Another NLR-regulating protein, SUPPRESSOR OF rps4-RLD1 (SRFR1), was found in the vicinity of Rpi-amr3 and WRR4A$^{Col-0}$, but not of Rpi-amr1. SRFR1 has been shown to interact with multiple NLRs, including SNC1, RPS4, and RPS6 (Bhattacharjee et al., 2011, Kim et al., 2010, Li et al., 2010). It has also been demonstrated that SRFR1 interacts with SGT1 (Li et al., 2010), a co-chaperone of HSP90 (Kadota et al., 2008, Liu et al., 2004, Takahashi et al., 2003), suggesting that SRFR1 regulates NLR stability through SGT1. Additionally, SRFR1 interacts with multiple TEOSINTE BRANCHED1/CYCLOIDEA/PCF (TCP) transcription factors, which positively regulate ETI mediated by several NLRs (Kim et al., 2014b). Thus, SRFR1 serves as a negative regulator of NLRs by interacting with various NLR-interacting proteins, including molecular co-chaperones and transcription factors, thereby preventing the auto-activation of plant immunity.

Additionally, other types of proteins, apart from those regulating NLR stability, were also detected. A transcriptional regulator, WRKY2, was uniquely found in the Ac2V-infected WRR4A$^{Col-0}$ samples

and could potentially be involved in WRR4A downstream signalling pathways. AGO2 is a promising candidate for Rpi-amr1 and could act as a guardee, potentially targeted by AVRamr1 in the nucleus. On the other hand, Rpi-amr3 could be involved, directly or indirectly, in one or more biological processes, including defense-related secretion *via* syntaxins, linking the phosphate starvation response with defense activation through the transcription factor PHR1, and possibly some yet-unknown vacuole-related defense mechanisms, potentially involving the release of malate. However, regarding the vacuole-related proteins, it is also possible that they merely reflect the fact that Rpi-amr3 localizes to the vacuole.

In conclusion, the identified plant proteins in the proximity of these three NLRs participate in various aspects of NLR-mediated defense responses, such as regulating NLR stability, acting as potential guardees, contributing to downstream signalling, and potentially through other, yet unknown mechanisms. These findings emphasize that a single NLR can associate with multiple NLR regulators. A prime example of this is the SNC1 TNL protein, for which at least seven different NLR regulators have been implicated: bHLH84, a transcription factor (Xu et al., 2014); CPR1, a E3 ligase (F-box) (Cheng et al., 2011); TPR1, a transcriptional corepressor (Zhu et al., 2010); SRFR1, a TPR domain-containing protein (Kim et al., 2010); MUSE13, a TRAF domain-containing protein (Huang et al., 2016); MUSE3, a E4 ligase (Huang et al., 2014b); and HSP90.3, a molecular chaperone (Huang et al., 2014a).

These TurboID-based NLR datasets highlight the sophisticated regulatory networks that control NLR activity, which must be carefully balanced to optimize disease resistance without incurring fitness costs. Overaccumulation of NLRs can result in significant growth and yield penalties. As such, effectively manipulating NLR regulation is key for enhancing crop resilience.

## 4.4 Supplementary figures

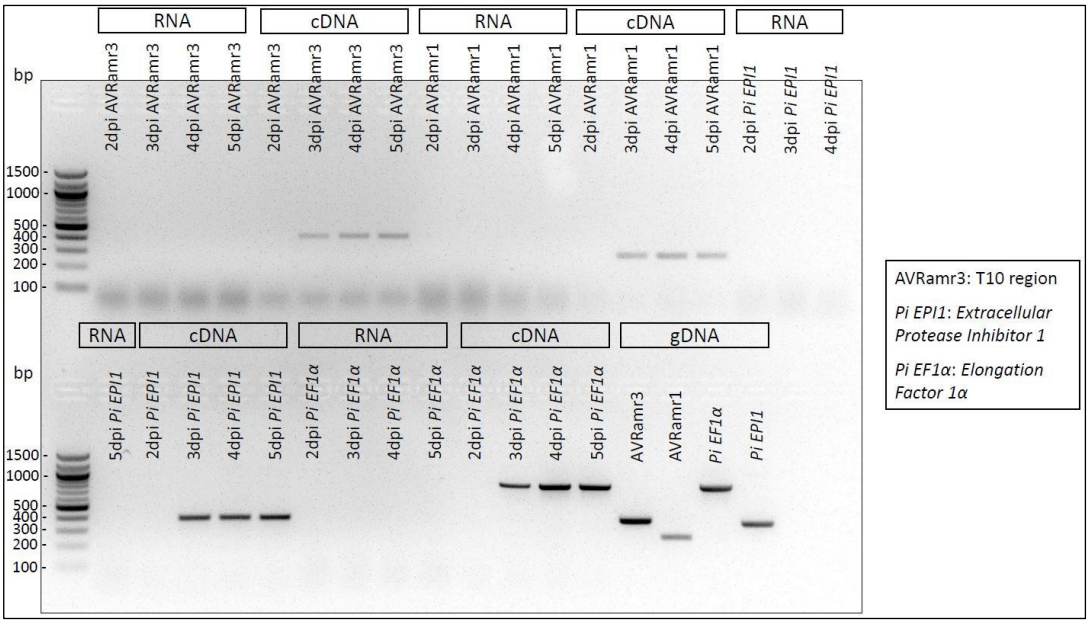


**Supplementary Figure 4-1 Detection of *AVRamr3* and *AVRamr1* cDNA after *P. infestans* infection of *nrc234 N. benthamiana*.**

RT-PCR of *P. infestans* AVRamr3 and AVRamr1 genes. *Agro*-infiltrations of Rpi-amr3:TurboID:FLAG at $OD_{600}$ = 0.5 in 4-week-old *nrc234 N. benthamiana* and in the presence of p19, followed by *P. infestans* (isolate 88069) infiltration (8,700 zoospores/mL) at 1 day post *Agro*-infiltration. Tissues were harvested at 2, 3, 4 and 5 days post *P. infestans* infection (so at 3, 4, 5 and 6 days post *Agro*-infiltration). *P. infestans EPI1* (Tian et al., 2004) and *EF1*α genes were used as positive controls.

| mCherry vs Rpi-amr1 at 3 dpi<br>spectral count of PITG_proteins > 1 & present in Rpi-amr1 but not in mCherry | | | | |
|---|---|---|---|---|
| Protein | rep 1 | rep 2 | rep 3 | Total spectral counts |
| PITG_04269T0 | NA | NA | 25 | 25 |
| PITG_15278T0 | NA | NA | 16 | 16 |
| PITG_04276T0 | NA | NA | 8 | 8 |
| AVRamr1 | NA | NA | 5 | 5 |
| PITG_15398T0 | NA | NA | 3 | 3 |
| PITG_17069T0 | NA | 2 | NA | 2 |
| PITG_11215T0 | NA | NA | 2 | 2 |
| PITG_00133T0 | NA | NA | 2 | 2 |
| PITG_14175T0 | NA | NA | 2 | 2 |
| PITG_09556T0 | NA | NA | 2 | 2 |
| PITG_15786T0 | NA | NA | 2 | 2 |
| PITG_22839T0 | NA | NA | 2 | 2 |
| PITG_01852T0 | NA | NA | 2 | 2 |
| PITG_01932T0 | NA | NA | 2 | 2 |
| PITG_07340T0 | NA | NA | 2 | 2 |
| PITG_09216T0 | NA | NA | 2 | 2 |
| PITG_01810T0 | NA | 2 | NA | 2 |
| PITG_14008T0 | NA | NA | 2 | 2 |
| PITG_16507T0 | 2 | NA | NA | 2 |

**Supplementary Figure 4-2 List of proximal pathogen proteins identified with Rpi-amr1 at 3 days post *P. infestans* infiltration *in nrc2/3/4 N. benthamiana*.**

Proteins are ranked by total number of spectral counts across the three replicates, with a minimum of two spectral counts detected by mass spectrometry for each protein. Only proteins uniquely detected in the Rpi-amr1 samples, but absent from mCherry control samples, are included. Results from each experimental replicate are shown.

| mCherry vs Rpi-amr1 at 4 dpi<br>spectral count of PITG_proteins > 2 & present in Rpi-amr1 but not in mCherry | | | | |
|---|---|---|---|---|
| Protein | rep 1 | rep 2 | rep 3 | Total spectral counts |
| AVRamr1 | NA | NA | 13 | 13 |
| PITG_04276T0 | 3 | NA | 7 | 10 |
| PITG_16005T0 | NA | NA | 3 | 3 |
| PITG_02740T0 | NA | NA | 3 | 3 |
| PITG_16959T0 | NA | NA | 3 | 3 |
| PITG_03936T0 (+1) | NA | NA | 3 | 3 |

**Supplementary Figure 4-3 List of proximal pathogen proteins identified with Rpi-amr1 at 4 days post *P. infestans* infiltration in *nrc2/3/4 N. benthamiana*.**

Proteins are ranked by total number of spectral counts across the three replicates, with a minimum of two spectral counts detected by mass spectrometry for each protein. Only proteins uniquely detected in the Rpi-amr1 samples, but absent from mCherry control samples, are included. Results from each experimental replicate are shown.

| mCherry vs Rpi-amr3 at 3 dpi<br>spectral count of PITG_proteins > 1 & present in Rpi-amr3 but not in mCherry | | | | |
|---|---|---|---|---|
| Protein | rep 1 | rep 2 | rep 3 | Total spectral counts |
| PITG_04269T0 | NA | NA | 11 | 11 |
| PITG_11215T0 | NA | NA | 5 | 5 |
| PITG_17069T0 | NA | NA | 2 | 2 |
| PITG_04276T0 | NA | NA | 2 | 2 |
| PITG_15278T0 | NA | NA | 2 | 2 |
| PITG_11038T0 | NA | NA | 2 | 2 |
| PITG_05367T0 | NA | NA | 2 | 2 |
| PITG_15398T0 | NA | NA | 2 | 2 |
| PITG_08746T0 | NA | NA | 2 | 2 |
| PITG_02231T0 | NA | NA | 2 | 2 |
| PITG_18354T0 | NA | NA | 2 | 2 |
| PITG_00879T0 | NA | NA | 2 | 2 |
| PITG_22743T0 | NA | NA | 2 | 2 |
| PITG_00089T0 (+1) | NA | NA | 2 | 2 |
| PITG_16008T0 | NA | NA | 2 | 2 |
| PITG_00407T0 | 2 | NA | NA | 2 |

**Supplementary Figure 4-4 List of proximal pathogen proteins identified with Rpi-amr3 at 3 days post *P. infestans* infiltration in *nrc2/3/4 N. benthamiana*.**

Proteins are ranked by total number of spectral counts across the three replicates, with a minimum of two spectral count detected by mass spectrometry for each protein. Only proteins uniquely detected in the Rpi-amr3 samples, but absent from mCherry control samples, are included. Results from each experimental replicate are shown.

| mCherry vs Rpi-amr3 at 4 dpi<br>spectral count of PITG_proteins > 2 & present in Rpi-amr3 but not in mCherry | | | | |
|---|---|---|---|---|
| Protein | rep 1 | rep 2 | rep 3 | Total spectral counts |
| PITG_04276T0 | NA | 2 | 10 | 12 |
| PITG_06619T0 | NA | NA | 6 | 6 |
| AVRamr3 | NA | NA | 6 | 6 |
| PITG_09400T0 | NA | NA | 5 | 5 |
| PITG_02909T0 | NA | NA | 5 | 5 |
| PITG_02740T0 | NA | NA | 5 | 5 |
| PITG_10142T0 | NA | NA | 5 | 5 |
| PITG_06595T0 | NA | NA | 4 | 4 |
| PITG_02259T0 | NA | NA | 4 | 4 |
| PITG_07056T0 | NA | NA | 4 | 4 |
| PITG_13831T0 | NA | NA | 4 | 4 |
| PITG_22391T0 | NA | NA | 4 | 4 |
| PITG_09284T0 | NA | NA | 4 | 4 |
| PITG_02533T0 | NA | NA | 4 | 4 |
| PITG_09817T0 | NA | NA | 4 | 4 |
| PITG_06320T0 | NA | NA | 3 | 3 |
| PITG_03148T0 | NA | NA | 3 | 3 |
| PITG_03335T0 | NA | NA | 3 | 3 |
| PITG_12193T0 | NA | NA | 3 | 3 |
| PITG_00203T0 | NA | NA | 3 | 3 |
| PITG_16005T0 | NA | NA | 3 | 3 |
| PITG_03694T0 | NA | NA | 3 | 3 |
| PITG_03463T0 | NA | NA | 3 | 3 |
| PITG_03550T0 (+1) | NA | NA | 3 | 3 |
| PITG_03936T0 (+1) | NA | NA | 3 | 3 |
| PITG_01549T0 | NA | NA | 3 | 3 |
| PITG_02347T0 | NA | NA | 3 | 3 |
| PITG_05464T0 | NA | NA | 3 | 3 |
| PITG_03828T0 | NA | NA | 3 | 3 |

**Supplementary Figure 4-5 List of proximal pathogen proteins identified with Rpi-amr3 at 4 days post *P. infestans* infiltration in *nrc2/3/4 N. benthamiana*.**

Proteins are ranked by total number of spectral counts across the three replicates, with a minimum of two spectral count detected by mass spectrometry for each protein. Only proteins uniquely detected in the Rpi-amr3 samples, but absent from mCherry control samples, are included. Results from each experimental replicate are shown.

| mCherry vs WRR4A (Ac2V infection)<br>spectral count of Ac2V_proteins > 2 & present in WRR4A but not in mCherry | | | | |
|---|---|---|---|---|
| Protein | rep 1 | rep 2 | rep 3 | Total spectral counts |
| Ac2vTS43G71 | NA | 3 | 11 | 14 |
| Ac2vTS34G90 | 2 | 4 | 7 | 13 |
| Ac2vTS27G46 | 4 | NA | 6 | 10 |
| Ac2vTS56G31 | 2 | 2 | 6 | 10 |
| Ac2vTS39G92 | 2 | NA | 5 | 7 |
| Ac2vTS2G210 | 4 | NA | 3 | 7 |
| Ac2vTS54G24 | 2 | NA | 5 | 7 |
| Ac2vTS27G16 | 3 | 2 | 2 | 7 |
| Ac2vTS101G12 | 3 | NA | 3 | 6 |
| Ac2vTS32G33 | 3 | NA | 3 | 6 |
| Ac2vTS29G162 | 2 | 2 | 2 | 6 |
| Ac2vTS94G13 | NA | 3 | 3 | 6 |
| Ac2vTS13G91 | 2 | NA | 4 | 6 |
| CCG14 | NA | 2 | 3 | 5 |
| Ac2vTS17G128 | 2 | NA | 3 | 5 |
| Ac2vTS29G54 | 2 | NA | 3 | 5 |
| Ac2vTS50G10 | NA | 2 | 2 | 4 |
| Ac2vTS49G74 | 2 | 2 | NA | 4 |
| Ac2vTS12G155 | 2 | NA | 2 | 4 |
| Ac2vTS14G123 | NA | 2 | 2 | 4 |
| Ac2vTS31G30 | NA | 2 | 2 | 4 |
| Ac2vTS32G22 | 2 | NA | 2 | 4 |
| Ac2vTS102G25 | 2 | NA | 2 | 4 |

**Supplementary Figure 4-6 List of proximal pathogen proteins identified with WRR4A$^{Col-0}$ at 6 days post *A. candida*$^{Ac2V}$ infection in *eds1*$^{Ws-2}$ *A. thaliana*.**

Proteins are ranked by total number of spectral counts across the three replicates, with a minimum of two spectral counts detected by mass spectrometry for each protein. Only proteins uniquely detected in the WRR4A$^{Col-0}$ samples, but absent from mCherry control samples, are included. Results from each experimental replicate are shown.

# Chapter 5

## Identification of a host defense hub targeted by pathogen effectors through TurboID proximity labelling

# 5. Identification of a host defense hub targeted by pathogen effectors through TurboID proximity labelling

## 5.1 Introduction

### 5.1.1 Pathogen effectors converge on plant signalling hubs

Pathogens deploy virulence effector proteins into host cells, where they physically interact with host proteins to modulate defense responses. These host targets can include signalling components, transcription factors (Bi and Zhou, 2017, Gimenez-Ibanez et al., 2014, Janik et al., 2017), metabolic enzymes (Zhou et al., 2011), or susceptibility (S) factors (Antony et al., 2010, He et al., 2018, Yang et al., 2017a). In turn, the targeting of host proteins by pathogen effectors can lead to inhibition of host target activity, degradation, or hijacking of the signalling pathways on which the pathogen effector acts (He et al., 2020). Large-scale interactomic studies have revealed that effectors from pathogens across different kingdoms of life primarily converge on a limited set of conserved, defense-related host targets to maximize their impact on negating host defense mechanisms. These commonly targeted plant host proteins are often part of hub proteins that play central roles in numerous plant processes by interacting with multiple proteins.

An interaction network of plant-pathogen effectors has been constructed from two pathogens, *Pseudomonas syringae*, a Gram-negative bacterium, and *Hyaloperonospora arabidopsidis*, an obligate biotrophic oomycete, that employ vastly different mechanisms to colonize plants (Mukhtar et al., 2011). It was observed that effectors target an overlapping subset of plant proteins, including those involved in interactions with many other proteins. This observation confirmed that effectors from evolutionarily distinct pathogens tend to converge on key cellular hubs, manipulating a variety of crucial plant processes and thereby facilitating disease. Additionally, it was noted that the recognition of cognate effectors by plant immune receptors are often indirect and typically mediated by another protein (Mukhtar et al., 2011). Altogether, these findings are consistent with the guard hypothesis and argue against the potential decoy role for these targeted proteins, although the decoy hypothesis may apply in some cases. Indeed, the decoy hypothesis suggests that decoy proteins would have few, if any, additional cellular functions and, as a result, would likely interact with fewer partners in the host protein interaction network.

Therefore, the host proteins targeted by pathogen tend to be highly connected and centrally positioned in the plant protein-protein interaction network (Li et al., 2017a, Wessling et al., 2014). Centrality was previously often linked to lethality, meaning that perturbations to these highly connected hubs could have detrimental effects on plant fitness (Jeong et al., 2001). However, contrasting findings have shown no correlation between centrality and lethality. In fact, centralized hub proteins often exhibit functional redundancy by gene duplication, which helps protect their essential functions from perturbations or mutations (Vandereyken et al., 2018). Multiple members of a single family can be identified as hubs for effector targeting, as it is the case for the TEOSINTE BRANCHED1/CYCLOIDEA/PROLIFERATING CELL FACTOR (TCP) family and the JASMONATE-ZIM DOMAIN (JAZ) family of transcriptional regulators, which are also reported to be plant signalling hubs (Gimenez-Ibanez et al., 2014, Lopez et al., 2015).

TCPs are conserved and interact with diverse groups of proteins, such as kinases, transporters, immunity regulators, and transcriptional regulators, thereby influencing various plant processes. Additionally, most plant signalling pathways converge onto TCP family members, making them attractive effector targets for a variety of pathogens (Lopez et al., 2015). Effectors may target different TCPs to modulate the same processes at different levels, thus inhibiting redundant TCP activities. Notably, TCP14 is targeted by effectors from three evolutionarily diverse pathogens, including the bacterium *P. syringae*, the oomycete *H. arabidopsidis*, and the fungus *Golovinomyces orontii* (Wessling et al., 2014, Yang et al., 2017a). Furthermore, SAP11, an effector from insect-transmitted bacterial pathogens known as phytoplasmas, has been shown to bind to and destabilize TCP transcription factors, leading to changes in the morphology of Arabidopsis plants (Sugio et al., 2011).

JAZ proteins are negative regulators of jasmonate response and play a key role in regulating numerous processes, including plant defense, growth, and development. JAZ proteins contain different domains that facilitate interactions with diverse partners, and these protein-protein interacting domains are targeted by different effectors. For example, the *P. syringae* HopBB1 effector targets the Jas domain of JAZ3, while the HopX1 effector mediates proteasomal degradation of most JAZ repressors by interacting with the ZIM domain (Gimenez-Ibanez et al., 2014, Yang et al., 2017a). Thus, different effectors from the same bacterial pathogen can target different members of the same protein family by interacting with distinct domains. Moreover, it has also been showed that the effector HARP1 from the cotton bollworm (*Helicoverpa armigera*) and REPAT38, a homolog in

*Spodoptera exigua*, stabilize JAZ3 through direct interaction, thereby preventing its interaction with the E3 ubiquitin ligase complex and the F-box protein COI1, which marks it for proteasomal degradation (Chen et al., 2019). Hence, the JAZ family may represent an attractive and conserved virulence strategy for both pathogens and pests, aimed at interfering with the JA signalling pathway.

Given that EDS1 is a key convergence point for defense signalling cascades (Wagner et al., 2013), it is surprising that only recently a few pathogen effectors have been reported to target or interfere with its downstream TNL signalling functions. This delay may be due to the limitations of traditional techniques for identifying plant-pathogen PPIs, which may not have been sensitive enough to detect these interactions effectively. TurboID proximity labelling offers a new approach for capturing these dynamic and low-abundance interactions.

It is reasonable to hypothesize that EDS1 could be targeted by several pathogen effectors from different kingdoms of life. For example, two effectors, the SPRYSEC15 nematode effector and the oomycete AVRcap1b effector, have been reported to counteract redundant nodes of the NRC immune receptor network, NRC2 and NRC3 (Derevnina et al., 2021). Similarly to EDS1, NRCs are central components in a complex defense network against multiple pathogens, representing up to half of the NLRome in *Solanaceous* plants (Wu et al., 2017). Recently, it was reported that the *Ralstonia solanacearum* type III effector RipV2 ubiquitinates and degrades the tomato (*Solanum lycopersicum*) *Sl*NRG1-*Sl*EDS1-*Sl*SAG101 immune complex, thereby dampening resistance in the tomato cultivar Hawaii 7996 (Qi et al., 2024). RipV2, which encodes an E3 ubiquitin ligase, suppresses immune responses and TNL-mediated cell death. Notably, RipV2 is essential for *R. solanacearum* virulence in Hawaii 7996, but not in *SlNRG1*-silenced tomato, highlighting that *Sl*NRG1 is a virulence target of RipV2. Moreover, a recent preprint utilizing TurboID reported that cathepsins B (CathB) in the oral secretion of aphids (*Myzus persicae*) recruit the *At*EDS1-*At*PAD4-*At*ADR1 immune complex to processing bodies (p-bodies), thereby suppressing plant defense in Arabidopsis (Liu et al., 2024b).

Since *Albugo* species are particularly effective at suppressing the TNL-dependent immunity (Belhaj et al., 2017, Cooper et al., 2008, Prince et al., 2017), we hypothesized that they might have evolved effectors targeting TNL downstream signalling elements, such as EDS1, SAG101, PAD4, NRG1, and ADR1, given their central role in activating plant defense mechanisms. To test this hypothesis, we

selected the *Albugo*-Arabidopsis pathosystem and combined it with a proximity-labelling proteomic approach using the engineered biotin ligase TurboID.

### 5.1.2 The *Albugo*-Arabidopsis pathosystem

The *Albugo*-Arabidopsis pathosystem provides an attractive model to explore the molecular basis of broad-spectrum defense suppression by a biotrophic oomycete, as *Albugo* species are particularly efficient at suppressing TNL-mediated immunity. Plants typically benefit from a basal resistance to most pathogens, known as non-host resistance (NHR) (Heath, 2000), which is considered a relatively durable, multi-gene defense mechanism. In contrast, host resistance protects against specific pathogens and is generally controlled by single *R* genes, making it potentially less durable than NHR (Gill et al., 2015, Schulze-Lefert and Panstruga, 2011).

Most plant pathogens are adapted to a limited number of related host species, particularly obligate biotrophic pathogens that can only reproduce on living tissues. These pathogens are intimately associated with their hosts, often leading to host specialization (Dong et al., 2014, Thines, 2014). However, broad host-range pathogens also exist and exhibit virulence on a diverse range of plant hosts. Some of these broad host-range pathogens became “generalist” by evolving multiple specialized races capable of infecting different hosts. This is the case with the filamentous oomycete order Albuginales. Its largest genus, *Albugo*, comprises about 50 species, each typically specific to a plant host, causing white blister rust disease (Choi and Priest, 1995, Ploch et al., 2010, Ploch and Thines, 2011). For example, *Albugo laibachii* specializes in infecting Arabidopsis (Thines et al., 2009). However, *Albugo candida* includes several specialized physiological races that infect a wide range of plant species, including members of the *Brassicaceae*, *Cleomaceae*, and *Capparaceae* (Choi et al., 2009).

Furthermore, *Albugo* species are capable of strongly suppressing host innate immunity, thereby enhancing susceptibility to secondary infections by non-adapted pathogens to which the plant would normally exhibit NHR. For example, *Arabidopsis thaliana* is naturally resistance to *P. infestans* (Huitema et al., 2003), but pre-inoculation with *A. laibachii* or *A. candida* renders Arabidopsis susceptible to *P. infestans* (Belhaj et al., 2017, Prince et al., 2017). Similarly, *Brassica juncea* and resistant Arabidopsis accessions, when pre-inoculated with *A. candida*, can be infected by the biotrophic downy mildew pathogen *H. arabidopsidis*, which shares an overlapping host range with

*Albugo* species (Cooper et al., 2008). It has been proposed that *Albugo* species' ability to suppress plant immunity may allow cohabitation of *A. candida* races with non-overlapping host ranges, facilitating genetic exchanges *via* sexual reproduction and enabling the colonization of new hosts (Adhikari et al., 2003, Jouet et al., 2019, McMullan et al., 2015).

Several Arabidopsis *R* genes encoding TNL proteins have been identified that confer resistance to *A. candida*. These are resistance to *A. candida* 1 (*RAC1*), which offers resistance to *A. laibachii* (originally reported as *A. candida* due to the lack of distinction between the two *Albugo* species at the time) (Borhan et al., 2004, Thines et al., 2009), the white rust resistance gene 4 (*WRR4*) locus (Borhan et al., 2008), which confers resistance to multiple *A. candida* races and carries two paralogs, *WRR4A* and *WRR4B*. Additional resistance genes include *WRR8*, *WRR9* and *WRR12* (previously reported as SOC3) (Cevik et al., 2019). These TNL genes are dependent on *EDS1*.

The *WRR4* locus in *A. thaliana* accession Col-0 contains three paralogues. The Col-0 alleles of *WRR4A* and *WRR4B* confer resistance to four (AcEm2, Ac2V, Ac7V and Ac9V) and three (Ac2V, Ac7V and AcBoT) different *A. candida* races respectively (Borhan et al., 2008, Cevik et al., 2019). However, the AcEx1 isolate of race 4 can sufficiently overcome both resistant *WRR4* alleles to enable growth and reproduction, though AcEx1 grows better on a *WRR4A* mutant of Col-0. The *A. thaliana* accession Ws-2 lacks *WRR4A* but contains the two other *WRR4* paralogues (Van de Weyer et al., 2019), one of which is the Ws-2 allele of *WRR4B*, conferring resistance to Ac2V (Cevik et al., 2019).

*Albugo* species primarily encode CCG effectors, a class of secreted proteins characterized by a $CX_2CX_5G$ motif, abbreviated as "CCG", which was initially termed CHXC (Kemen et al., 2011, Links et al., 2011). The genome of the Ac2V isolate of *A. candida* was re-sequenced using PacBio long reads, revealing a two-fold expansion of CCG effector-like proteins, which now represent 10% of the secretome of *A. candida* races (Furzer et al., 2022). CCG effectors exhibit diverse transcriptional profiles, with some being constitutively expressed or expressed at specific time points (early or late) during infection (Furzer et al., 2022).

Finally, the $WRR4A^{Col\text{-}0}$ and $WRR4B^{Col\text{-}0}$ paralogous TNL proteins are reported to recognize eight and four different CCG effectors, respectively (Castel et al., 2021, Redkar et al., 2023). Moreover, as discussed in Chapter 4, we identified two additional CCGs recognized by $WRR4A^{Col\text{-}0}$, bringing the total number of CCGs it can recognize to ten. The broad-spectrum resistance provided by these two

distinct *WRR4* paralogues to *A. candida* could be explained by their ability to recognize multiple CCG effectors.

However, the mechanisms by which *Albugo* species broadly suppress plant immunity, including the suppression of the ETI response activated by NLR proteins, remain poorly understood. This led us to hypothesize that one such mechanism could involve targeting the EDS1 signalling hubs.

## 5.2 Results

After demonstrating in Chapter 4 that it is possible to capture native effectors during pathogen infection, we applied this approach to test whether effectors can also target plant defense signalling hubs. We chose to work with *A. candida*, as it is highly effective at suppressing TNL-mediated defense responses (Belhaj et al., 2017, Cooper et al., 2008, Prince et al., 2017), which rely on the EDS1-SAG101-NRG1 or EDS1-PAD4-ADR1 signalling nodes (Huang et al., 2025, Xiao et al., 2025, Yu et al., 2024). EDS1 is at the core of these two signalling pathways, therefore we generated an Arabidopsis EDS1:TurboID transgenic line. Additionally, we created TurboID transgenic lines for all its signalling partners, including SAG101, PAD4, NRG1.2 and ADR1-L1 (Table 5.1).

The functionality of the TurboID-tagged signalling elements involved in triggering cell death was verified through HR assays. TurboID-tagged EDS1, SAG101 and NRG1.2 were all able to trigger HR in *epss N. benthamiana* leaves (Figures 5.1. 5.2 and 5.3). The *N. benthamiana epss* mutant corresponds to the quadruple knockout mutant *eds1a pad4 sag101a sag101b* (Lapin et al., 2019). In all these HR assays, the *At*EDS1:TurboID-V5, *At*SAG101:TurboID-V5 and *At*NRG1.2:TurboID-V5 proteins were co-delivered with the genetically compatible *At*EDS1 and/or *At*SAG101 and/or *At*NRG1.2 proteins in the presence of the bacterial effector HopQ1, recognized by the NLR protein Roq1 (Schultink et al., 2017). An eleven amino acid linker was included between the end of the bait coding region and the start of the TurboID enzyme coding region, potentially allowing for more flexible protein conformational arrangements.

These constructs were subsequently transformed into Arabidopsis, as listed in Table 5.1. For each protein, either the corresponding Arabidopsis mutant background was used to enable future complementation tests, or the Arabidopsis DM10 line was employed. Two multiparent advanced generation inter-cross (MAGIC) lines, which exhibited different levels of susceptibility to the *A.*

*candida* race Ac2V, were crossed to generate the resulting Double MAGIC 10 (DM10) line, which is fully susceptible to *A. candida* races AcBoT, Ac2V and Ac7V (Cevik et al., 2019, Kover et al., 2009).

*A. thaliana* transgenic lines overexpressing the TurboID-tagged signalling genes were selected by assessing their protein expression. The protein expression levels of the different *A. thaliana* TurboID transgenic lines were quantified by Western blot in the T1 generation, and the individuals with the highest protein expression were selected. For each transgenic line, two independent insertion events were chosen, with protein expression levels as similar as possible. Protein expression was quantified in each plant generation (T1, T2 and T3) to look for potential silencing events (Supplementary Figures 5.1 and 5.2). For unknown reasons, 35S:ADR1-L1:TurboID-V5 was detectable in 14-day-old seedlings but not in 4/5-week-old plants of the T3 generation. Therefore, the ADR1-L1 transgenic line was not prioritized for TurboID experiments. Finally, in the T3 generation, homozygous lines were identified by sowing seeds on BASTA selection plates and looking for fully resistant individuals (Supplementary Figure 5.6). All these TurboID transgenic lines are nearly complete, and the progress to date is summarized in Table 5.2.

**Table 5-1 List of the TurboID-tagged proteins generated by Golden Gate cloning and transformed into *A. thaliana*.**

mCherry and NLS-GFP are the chosen negative controls. All constructs were transformed in the *A. thaliana* DM10 line. Additionally, these constructs were transformed in their corresponding *A. thaliana* mutant backgrounds to carry out complementation tests and verify the functionality of proteins. One of these constructs was not generated by me and the person who did so is mentioned. The promoters and terminators that were used to perform these DNA assemblies are as follow: p35S = cauliflower mosaic virus 35S promoter, pAt2 = *A. thaliana* small subunit ribosomal protein 16 (SSR16) gene promoter, t35S = cauliflower mosaic virus 35S terminator, tNOS = *Agrobacterium*

*tumefaciens* nopaline synthase gene terminator, tOCS = *Agrobacterium tumefaciens* octopine synthase gene terminator.

| Protein | Construct | *A. thaliana* genetic background |
|---|---|---|
| EDS1 | pEDS1:EDS1:TurboID-V5:tNOS (construct made by colleague Dr Sophie Johnson) | *eds1-12* & DM10 |
| SAG101 | pSAG101:SAG101:TurboID-V5:t35S | *sag101-2* & DM10 |
| PAD4 | pPAD4:PAD4:TurboID-V5:t35S | *pad4-1* & DM10 |
| NRG1.2 (NRG1-B) | pNRG1.2:NRG1.2:TurboID-V5:tNRG1.2 | *nrg1-a/b* & DM10 |
| ADR1-L1 | p35S:ADR1-L1:TurboID-V5:t35S | *adr1* triple mutant & DM10 |
| $WRR4A^{Col-0}$ | p35S:$WRR4A^{Col-0}$:TurboID-V5:tOCS | $eds1^{Ws-2}$ |
| mCherry | pAt2:mCherry:TurboID-V5:t35S | $eds1^{Ws-2}$ & DM10 |
| NLS-GFP | pAt2:NLS-GFP:TurboID-V5:t35S | DM10 |

**Table 5-2 Table showing the progress of the generation of the *A. thaliana* TurboID transgenic lines to date.**

mCherry and NLS-GFP are the chosen negative controls. A cross indicates that the task is completed while "in progress" means that the task is currently being carried out, and an empty box means the task has yet to be performed. One of these lines was not entirely generated by me, and the person who did so is mentioned. The stage at which I have inherited it and started carrying it further is also indicated.

| Protein | Protein expression in T3 seedlings | Protein expression in T3 leaves | Seed bulk: T3 & T4 | Complementation test: (*Hpa* infection) |
|---|---|---|---|---|
| EDS1 (T2 seeds from colleague Dr Sophie Johnson) | X | X | X | X |
| SAG101 | X | X | X | in progress |
| PAD4 | X | X | X | in progress |
| NRG1.2 (NRG1-B) | X | X | X | X |
| ADR1-L1 | X | - | | |
| $WRR4A^{Col-0}$ | X | X | X | X |
| mCherry | X | X | X | NA |
| NLS-GFP | X | X | X | NA |

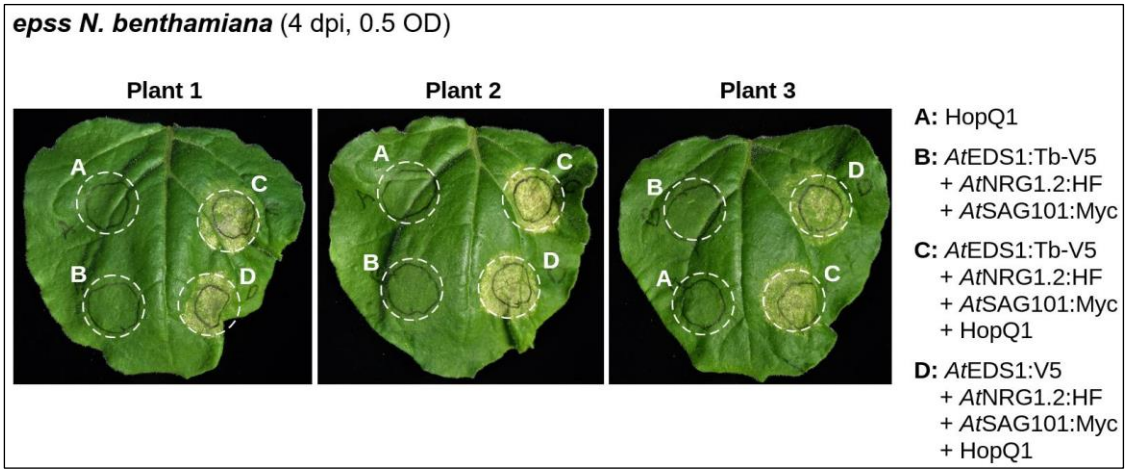


**Figure 5.1 *At*EDS1:TurboID-V5 supports HR with *At*NRG1.2 and *At*SAG101.**

HR assays by *Agro*-infiltration at $OD_{600}$ = 0.5 in 4/5-week-old *epss N. benthamiana* leaves and at 4 dpi. The *Pseudomonas* type III effector HopQ1 is recognized by the native *N. benthamiana* NLR protein Roq1 (Schultink et al., 2017). Co-delivery of 35S promoter-driven *At*NRG1.2-HF, *At*SAG101-Myc, and *At*EDS1-V5 or *At*EDS1:TurboID-V5 (*At*EDS1:Tb-V5) with HopQ1 triggers HR in *epss* mutant leaves. HF-tagged proteins contain both a His-tag and a FLAG-tag, enabling versatile options for protein purification and detection.

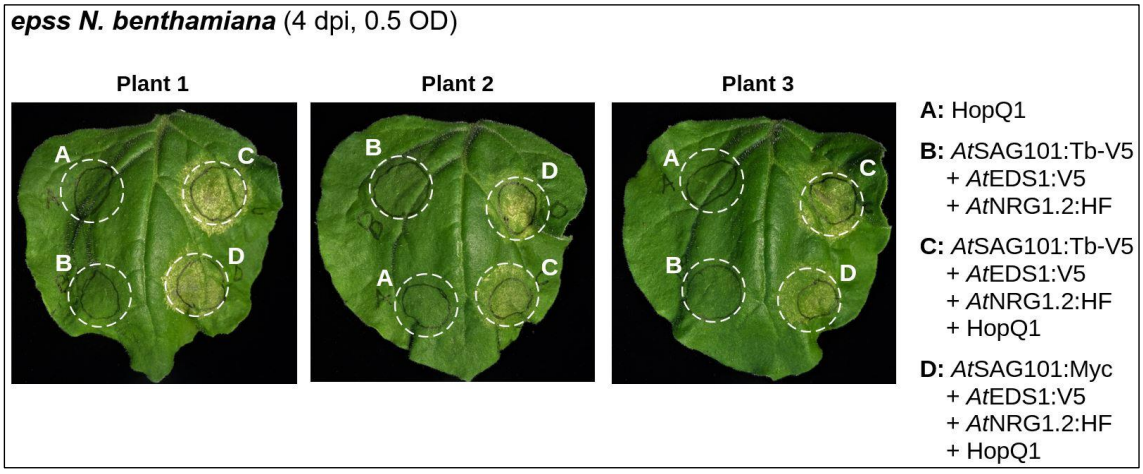


**Figure 5.2 *At*SAG101:TurboID-V5 supports HR with *At*EDS1 and *At*NRG1.2.**

HR assays by *Agro*-infiltration at $OD_{600}$ = 0.5 in 4/5-week-old *epss N. benthamiana* leaves and at 4 dpi. The *Pseudomonas* type III effector HopQ1 is recognized by the native *N. benthamiana* NLR protein Roq1 (Schultink et al., 2017). Co-delivery of 35S promoter-driven *At*EDS1-V5, *At*NRG1.2-HF, and *At*SAG101-Myc or *At*SAG101:TurboID-V5 (*At*SAG101:Tb-V5) with HopQ1 triggers HR in *epss* mutant leaves. HF-tagged proteins contain both a His-tag and a FLAG-tag, enabling versatile options for protein purification and detection.

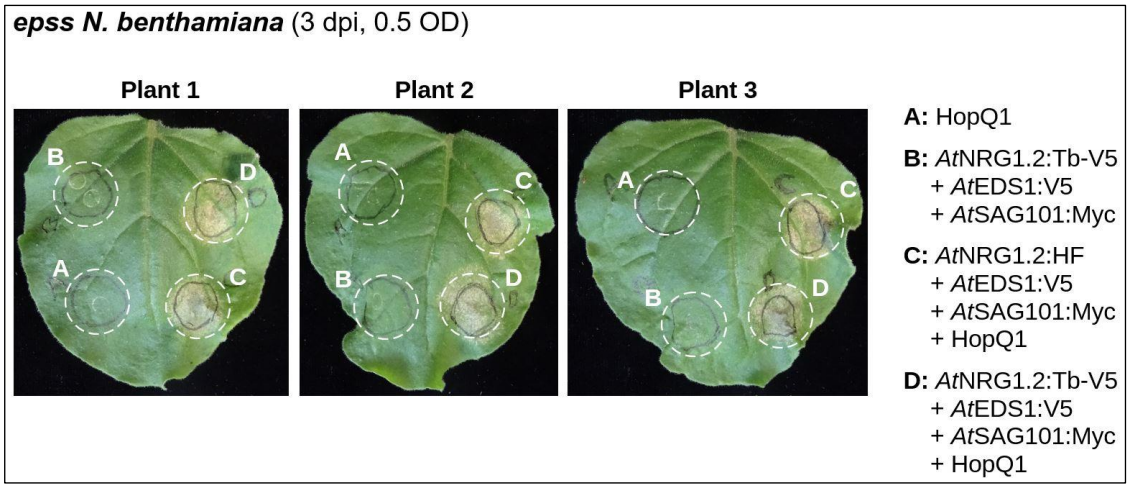


**Figure 5.3 *At*NRG1.2:TurboID-V5 supports HR with *At*EDS1 and *At*SAG101.**

HR assays by *Agro*-infiltration at $OD_{600}$ = 0.5 in 4/5-week-old *epss N. benthamiana* leaves and at 3 dpi. The *Pseudomonas* type III effector HopQ1 is recognized by the native *N. benthamiana* NLR protein Roq1 (Schultink et al., 2017). Co-delivery of 35S promoter-driven *At*EDS1-V5, *At*SAG101-Myc, and *At*NRG1.2-HF or *At*NRG1.2:TurboID-V5 (*At*NRG1.2:Tb-V5) with HopQ1 triggers HR in *epss* mutant leaves. HF-tagged proteins contain both a His-tag and a FLAG-tag, enabling versatile options for protein purification and detection.

Since EDS1 is the common protein between the EDS1-SAG101-NRG1 and EDS1-PAD4-ADR1 signalling hubs, the EDS1:TurboID transgenic line was prioritized for performing TurboID experiments. To confirm the functionality of this transgenic line, the transformed *eds1-12 A. thaliana* mutant background was inoculated with *Hyaloperonospora arabidopsidis* (*Hpa*) (Supplementary Figure 5.3). This transgenic line fully restored the *Hpa*-resistant phenotype, thereby confirming the functionality of the TurboID-tagged protein.

Similar to the WRR4A$^{Col\text{-}0}$ TurboID experiment described in Chapter 4, the EDS1 and mCherry TurboID transgenic Arabidopsis lines transformed into DM10 were spray-inoculated with *A. candida*$^{Ac2V}$. Six days later, they were vacuum-infiltrated with biotin and left submerged for 3 hours (Figure 5.4). As mentioned in Chapter 4, we chose to work with *A. candid*a race Ac2V because it has the most complete sequencing data (Furzer et al., 2022). The mCherry:TurboID transgenic line was used as a negative control.

Before sending the samples for mass spectrometry analysis, their quality was assessed by Western blot (Figure 5.5). The overall biotinylation level of the EDS1-containing samples was slightly higher

than that of the mCherry control samples, even though I selected transgenic lines with protein levels as similar as possible. Nonetheless, the EDS1 noninfected samples can serve as an additional negative control to identify overlapping proteins between noninfected and infected plant tissues, as well as those unique to infection. The samples were sent for analysis using the Orbitrap Eclipse LC-MS/MS system with FAIMS, as this system was used to detect native *P. infestans* and *A. candida* effectors, as described in Chapter 4.

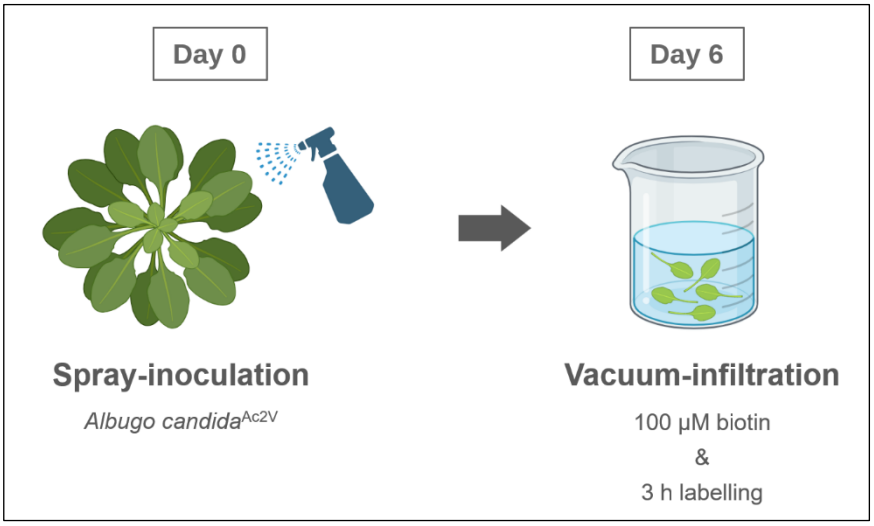


**Figure 5.4 Schematic representation of the experimental design used to identify pathogen and plant interactors of EDS1.**

2/3-week-old transgenic *A. thaliana* lines, *pEDS1*:*EDS1*:TurboID-V5 in DM10 plants, were sprayed with *A. candida*$^{Ac2V}$ (100,000 oospores/mL). Six days post-inoculation, infected leaves were harvested, vacuum-infiltrated with biotin (100 µM) and subsequently submerged in biotin (100 µM) for 3 h.

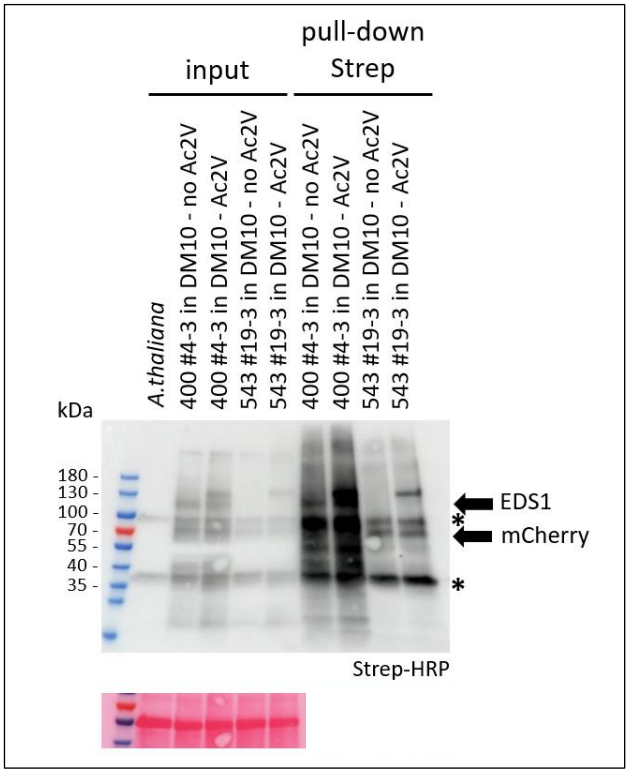


**Figure 5.5 Proximity biotinylation by *At*EDS1 in DM10 *A. thaliana*.**

Streptavidin pull-down and biotinylation of *pEDS1*:*EDS1*:TurboID-V5 (400) and pAt2:mCherry:TurboID-V5 (543) in DM10 *A. thaliana*. 2/3-week-old DM10 *A. thaliana* TurboID transgenic lines were sprayed with *A. candida*$^{Ac2V}$ (100,000 oospores/mL). Leaves were harvested at 6 days post-inoculation, vacuum-infiltrated with biotin (100 µM), and submerged in biotin (100 µM) for 3 h. Pull-down was carried out with streptavidin beads. A small fraction of the beads was boiled and resolved by SDS-PAGE to assess sample quality prior to LC-MS/MS analysis. Biotinylated proteins were detected by using HRP-conjugated streptavidin labelling. Bands labelled with a black asterisk (*****) correspond to endogenously biotinylated proteins. The "*A. thaliana*" lane corresponds to non-infiltrated samples, meaning no TurboID-tagged baits were expressed and no biotin was added. It serves as control to show endogenous biotinylation.

In total, 5,630 proteins were identified across the three repeats, including all proteins detected in samples from the bait construct EDS1:TurboID and the mCherry:TurboID control. Of these, 4,784

proteins correspond to *A. thaliana* and 846 to *A. candida*$^{Ac2V}$. The number of plant- and pathogen-related protein detected in this experiment is very similar, if not almost identical, to the total number of proteins identified in the WRR4A$^{Col-0}$ TurboID experiment described in Chapter 4. Again, the *A. candida*$^{Ac2V}$ proteins accounted for approximately 15% of the total proteins captured. The pathogen-related proteins (referred to as Ac2V_proteins) that were uniquely detected in the EDS1-containing samples and absent from the mCherry control samples are summarized in Supplementary Figure 5.5. In one of these repeats (rep2), *A. candida*$^{Ac2V}$ did not proliferate effectively within the plant tissues, as indicated by the absence or low number of spectral counts corresponding to pathogen proteins. However, the first and third repeats showed more pathogen infection, with higher numbers of spectral counts corresponding to pathogen proteins.

In addition to extracting all the pathogen-related proteins uniquely found with EDS1 (Supplementary Figure 5.5), an MA plot was created to represent the data (the rationale for using MA plots is explained in Chapter 4) (Figure 5.6). Overall, sufficient pathogen-related proteins were detected in this experiment, and dots on the positive end of the Y-axis highlighted in orange represent Ac2V_proteins that were significantly differentially biotinylated in the EDS1 samples compared to the mCherry samples (Figure 5.6). The identification numbers of the dots highlighted in orange on the MA plot and their corresponding p-values are presented in Table 5.3. Interestingly, three CCGs appeared as potential candidates. CCG82 and CCG31 emerged as potential candidates in the MA plot analysis (Figure 5.6), and CCG32 was found in the list of Ac2V_proteins uniquely identified with EDS1 (Supplementary Figure 5.5). CCG82, CCG31, and CCG32 were detected with protein sequence coverages of 28%, 9%, and 33%, respectively, and with eleven, four, and sixteen peptides identified.

CCG31 does not appear in the list of Ac2V_proteins uniquely identified with EDS1 (Supplementary Figure 5.5) because it is more abundant (with twelve, two, and sixteen spectral counts detected in rep1, rep2, and rep3, respectively) than CCG82 and CCG32 and it was also detected in the mCherry-containing samples (with seven spectral counts detected in rep3 only). Although CCG31 was detected in mCherry samples, it was significantly more biotinylated by EDS1, making it a significant candidate. On the other hand, CCG32 does not appear in the MA plot analysis (Figure 5.6) because it is less abundant (with four and three spectral counts detected in rep1 and rep3, respectively, Supplementary Figure 5.5) than CCG31 and CCG82. As a result, CCG32 does not emerge as a significantly differentially biotinylated candidate, even though it is completely absent from mCherry-containing samples. Finally, CCG82 appears in both the list of Ac2V_proteins uniquely identified with

EDS1 (Supplementary Figure 5.5) and in the MA plot analysis (Figure 5.6) because it is both abundant enough (with five and fifteen spectral counts detected in rep1 and rep3, respectively) and absent from the mCherry samples. Since some of these Ac2V_proteins are not abundant enough to emerge as significant candidates, these two methods of extracting information from the raw data are complementary. These three CCG effectors may potentially target EDS1 to interfere with its signalling pathways, which could explain why *Albugo* species are so effective at suppressing TNL-mediated defense responses.

In addition to these three CCGs, other pathogen proteins were captured, some of which may also function as effectors. Therefore, all pathogen proteins uniquely detected in samples containing EDS1 (Supplementary Figure 5.5), along with the top Ac2V_proteins identified from the MA plots (Table 5.3), were analysed using SignalP 6.0 to predict the presence of a signal peptide (Table 5.4). Two additional pathogen proteins were identified as having a predicted signal peptide. However, no further information was available regarding these two Ac2V_proteins identified through TurboID (Table 5.3). These proteins may represent newly identified effectors, though additional experiments are necessary to validate this.

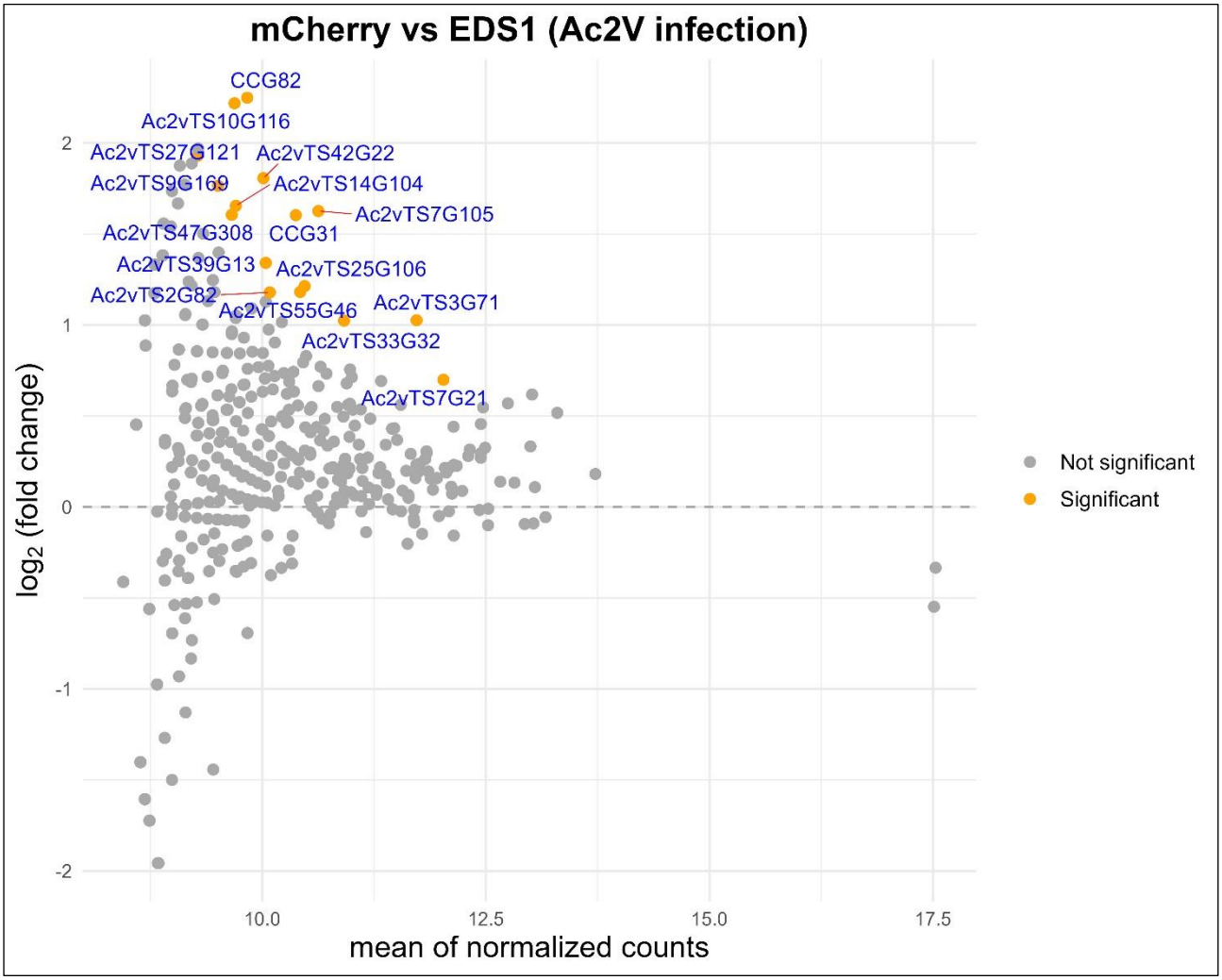


**Figure 5.6 TurboID-based identification of *At*EDS1 proximal pathogen interactors.**

*At*EDS1 proximal pathogen interactors identified by mass spectrometry at 6 days post *A. candida*$^{Ac2V}$ infection in *eds1*$^{Ws\text{-}2}$ *A. thaliana*. The MA plot (M *versus* A plot) displays the relationship between average protein abundance (A) and the $log_2$(FC) in biotinylation (M). Proteins highlighted in orange represent the most differentially biotinylated proteins compared to mCherry ($log_2$(FC) > 0 and P-value < 0.05), while proteins with no significant differences in biotinylation are shown in grey. The data were normalized using cyclic loess normalization *via* the edgeR package (Chen et al., 2025). Proteins with values near 0 on the X-axis correspond to low-abundance proteins, while highly abundant proteins are located further from 0. Extreme values along the Y-axis represent promising interactors, and only small changes in biotinylation are sufficient for highly abundant proteins.

| mCherry vs EDS1 (Ac2V infection) ranked by p-value & log(FC) > 0 | | |
|---|---|---|
| Protein | p-value | log(FC) |
| Ac2vTS10G116 | 0.005 | 2.219 |
| CCG31 | 0.006 | 1.604 |
| CCG82 | 0.006 | 2.249 |
| Ac2vTS7G105 | 0.008 | 1.626 |
| Ac2vTS3G71 | 0.008 | 1.026 |
| Ac2vTS42G22 | 0.013 | 1.807 |
| Ac2vTS47G308 | 0.018 | 1.605 |
| Ac2vTS33G32 | 0.018 | 1.024 |
| Ac2vTS9G169 | 0.021 | 1.765 |
| Ac2vTS27G121 | 0.022 | 1.930 |
| Ac2vTS14G104 | 0.024 | 1.655 |
| Ac2vTS55G46 | 0.025 | 1.182 |
| Ac2vTS39G13 | 0.026 | 1.341 |
| Ac2vTS25G106 | 0.037 | 1.214 |
| Ac2vTS7G21 | 0.041 | 0.699 |
| Ac2vTS2G82 | 0.049 | 1.179 |

**Table 5-3 List of the *At*EDS1 proximal pathogen interactors identified at 6 days post *A. candida*$^{Ac2V}$ infection in DM10 *A. thaliana*.**

Proteins are ranked by P-value < 0.05 and log(FC) > 0.

**Table 5-4 *A. candida* proteins identified using TurboID-tagged *At*EDS1 that contain a predicted signal peptide.**

Amount all the Ac2V_proteins detected by mass spectrometry, two additional Ac2V_proteins with a predicted signal peptide were identified with *At*EDS1. YES indicates that a signal peptide was predicted by the SignalP 6.0 software (Teufel et al., 2022).

| **Protein:** | ***At*EDS1** signal peptide (SP) |
|---|---|
| **Ac2vTS14G104** | YES |
| **Ac2vTS3G71** | YES |

As undertaken for WRR4A with CCG14 and CCG41 in Chapter 4, an *in silico* prediction was conducted to assess the potential interaction between CCG31, CCG32, or CCG82, and EDS1 using AlphaFold2 (Jumper et al., 2021). For the structural model, the full-length of these three CCG effectors and EDS1 were used. The software predicted that, among the three CCGs, only CCG82 is highly likely to interact with EDS1, with an ipTM score of 0.806 (Figure 5.7). Interestingly, the N-terminal interface of EDS1, which mediates heterodimer formation with its signalling partners SAG101 and PAD4, is predicted to be targeted by CCG82 (Wagner et al., 2013). This interaction could impair EDS1-SAG101 and/or EDS1-PAD4 dimerization, potentially disrupting their downstream signalling pathways. In this prediction, with monomer EDS1, CCG82 does not appear to interfere with the binding of small molecules within the EP domain (EPD) surface surrounding the cavity formed by the heterodimer, nor with its association with the helper NLRs ADR1 and NRG1 (Dongus et al., 2022, Huang et al., 2025, Xiao et al., 2025, Yu et al., 2024).

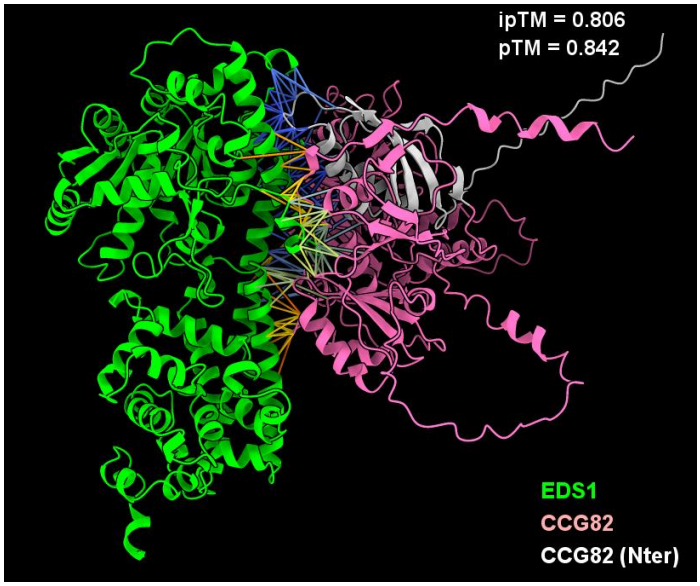


**Figure 5.7 TurboID-identified CCG82 is predicted to interact with EDS1.**

AlphaFold2 prediction of the interaction between CCG82 (pink) and EDS1 (green). The N-terminal region of CCG82 is highlighted in white. Predicted interaction sites between the two proteins are shown as straight lines, with blue indicating high-confidence predictions and red indicating low-confidence predictions. The model displayed corresponds to the highest-scoring prediction out of the five generated models.

Subsequently, we simulated whether CCG82 would also be predicted to interfere with EDS1 signalling in the presence of SAG101 and PAD4. To do so, we inputted these three proteins, CCG82 with either EDS1 and SAG101, or EDS1 and PAD4, into AlphaFold2 (Figures 5.8 and 5.9). In both scenarios, CCG82 was not predicted to disturb the dimerization of EDS1 with either SAG101 or PAD4. In the presence of SAG101, CCG82 is predicted to interact with EDS1, but when this prediction is compared to the resolved molecular structure of EDS1-SAG101-NRG1 complex (Xiao et al., 2025, Yu et al., 2024), its predicted binding site would not impair small molecule binding or the association with the helper NLR NRG1 (Figure 5.8). Interestingly, in the presence of PAD4, CCG82 is predicted to primarily interact with PAD4 rather than EDS1, and when this prediction is overlapped with the published molecular structure of EDS1-PAD4-ADR1 module (Yu et al., 2024), the predicted position of CCG82 aligns perfectly with the PAD4-ADR1 association site (Figure 5.9). These additional predictions suggest that CCG82 could specifically target the EDS1-PAD4-ADR1 signalling pathway, but not the EDS1-SAG101-NRG1 module, by competing for and/or obstructing ADR1's association with PAD4. Moreover, according to this prediction, CCG82 appears to target PAD4 instead of EDS1. Since EDS1 carries the TurboID at its C-terminal end, this places the enzyme in close proximity to CCG82's predicted PAD4 target site. This does not exclude the possibility that CCG82 also interfere with EDS1 monomer (Figure 5.7), although monomeric EDS1 is likely less abundant in cells compared to its heterodimerized forms with either SAG101 or PAD4.

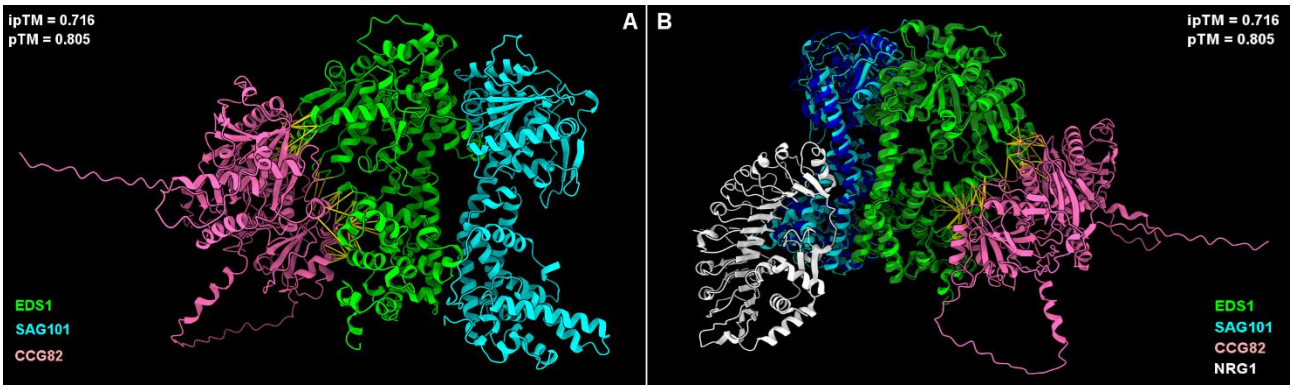


**Figure 5.8 Prediction of the interaction between CCG82 and the EDS1-SAG101 heterodimer.**

AlphaFold2 prediction of the interaction between CCG82 (pink), EDS1 (light green), and SAG101 (light blue). The model shown represents the highest-scoring prediction out of the five generated models. Predicted interaction sites between CCG82 and EDS1 are indicated by straight lines, with blue denoting high-confidence predictions, orange denoting medium-confidence predictions, and red denoting low-confidence predictions (**A**). The overlap of the predicted model (**A**) with the published molecular structure of the EDS1 (dark green), SAG101 (dark blue), and NRG1 (white) heterotrimer is presented in (**B**) (Huang et al., 2025, Xiao et al., 2025).

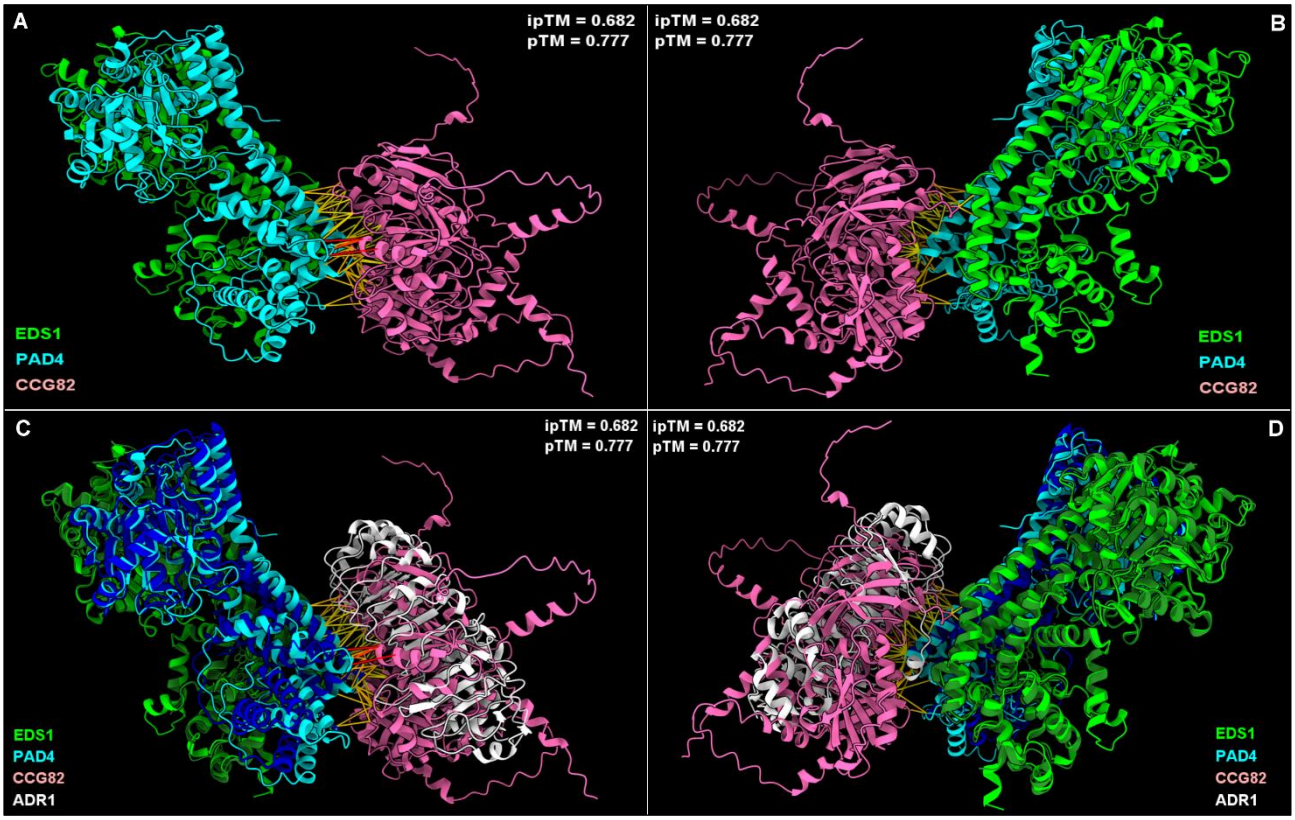


**Figure 5.9 Prediction of the interaction between CCG82 and the EDS1-PAD4 heterodimer.**

AlphaFold2 prediction of the interaction between CCG82 (pink), EDS1 (light green), and PAD4 (light blue). The model shown represents the highest-scoring prediction out of the five generated models, from either the PAD4 side of the heterodimer (**A**) or the EDS1 side of the heterodimer (**B**). Predicted interaction sites between CCG82 and PAD4 are indicated by straight lines, with blue representing high-confidence predictions, orange representing medium-confidence predictions, and red representing low-confidence predictions (**A**) and (**B**). The overlap of the predicted model with the published molecular structure of the EDS1 (dark green), PAD4 (dark blue), and ADR1 (white) heterotrimer is presented in (**C**) and (**D**) (Yu et al., 2024).

In addition to capturing pathogen-derived proteins, EDS1-proximal plant interactors were also identified, providing valuable insights into its role during pathogen infection. A total of 4,784 *A. thaliana* biotinylated proteins were identified with TurboID-tagged EDS1 and were bioinformatically analysed using the same pipeline described in Chapter 4. Volcano plots of the resulting p-values were generated (Figures 5.10 and 5.11) and the top significant proximal interactors are summarized in Tables 5.5 and 5.6.

Most of the identified proximal interactors of EDS1 were shared between *A. candida*-infected and uninfected conditions, totalling 187 proteins, while 78 were unique to the infected samples (Figure 5.12). GO-term analysis revealed a prominent presence of chromatin and transcriptional regulators in proximity to EDS1, which are typically involved in transcriptional processes (Figure 5.13). Notably, none of these proteins were found in proximity to any of the NLRs examined in Chapter 4, including Rpi-amr1, Rpi-amr3, or $WRR4A^{Col-0}$. For instance, CHROMATIN REGULATOR 28 (CHR28) was found near EDS1 (Tables 5.5 and 5.6); CHR28 is involved in chromatin remodelling and negative regulation of transcription. Mutants of *CHR28* show increased transcript levels, suggesting that it typically functions to suppress transcription, thus playing a role in regulating gene expression (Han et al., 2014).

It is well established that EDS1 forms spatially distinct complexes with two related lipase-like proteins, SAG101 and PAD4, to mediate plant immunity (Feys et al., 2001, Feys et al., 2005). As such, these proteins serve as positive controls in this experiment. As anticipated, SAG101 and PAD4 exhibited the highest biotinylation levels among all EDS1 proximal interactors, a pattern that was consistent regardless of pathogen infection (Tables 5.5 and 5.6). Furthermore, EDS1-PAD4 and EDS1-SAG101 heterodimers activate the “helper” RNLs ADR1 and NRG1, respectively (Dongus et al., 2022). Interestingly, the N-terminally truncated ADR1-L3 was identified as a significantly biotinylated proximal interactor with EDS1 only upon infection (Table 5.6). Similar to NRG1.3, ADR1-L3 lacks the N-terminal RPW8 domain. However, in contrast to NRG1.3, ADR1-L3 retains the full NB domain. Unlike NRG1.3, which has been reported to antagonize the immunity mediated by its full-length counterparts NRG1.1 and NRG1.2 (Huang et al., 2025, Xiao et al., 2025), ADR1-L3 does not appear to play a role in TNL-mediated autoimmunity and defense (Wu et al., 2022). Therefore, it is intriguing to observe ADR1-L3 emerging as a promising candidate in this context. A few spectral counts corresponding to ADR1-L1 (with three, two, and two spectral counts in rep1, rep2, and rep3 of infected tissues, respectively, as well as five and two spectral counts in rep1 and rep2 of uninfected tissues) and to NRG1.1 (with two spectral counts in rep1 of uninfected tissues) were detected. However, ADR1-L1 and NRG1.1 do not appear in the list of significant proximal interactors, as their total spectral counts are too low. The detection of a few spectral counts corresponding to NRG1.1 and ADR1-L1 in both uninfected and infected samples is inconsistent with the infection-dependent association of RNLs with the EDS1-SAG101 or EDS1-PAD4 heterodimers (Feehan et al., 2023, Sun et al., 2021). However, TurboID is more sensitive than traditional PPI techniques, which could explain why NRG1.1 and ADR1-L1 were detected in both uninfected and infected plant tissues in our

experiment. This suggests that the interactions between these RNLs and lipase-like proteins may be low in abundance and/or transient, enabling rapid downstream signalling and activation of defense responses, in contrast to the relatively strong and stable interactions observed between the lipase-like proteins themselves.

The transcription factor WRKY2 was identified as a significantly biotinylated proximal interactor with EDS1, but only upon infection (Table 5.6). Its potential role in immunity was previously discussed in Chapter 4, where a few spectral counts were captured in the presence of the TNL WRR4A$^{Col-0}$.

MEDIATOR COMPLEX SUBUNIT 14 (MED14), a component of the Arabidopsis Mediator complex that functions as a transcriptional coactivator in RNA polymerase II (RNAPII)-mediated transcription, was found to be in proximity to EDS1 in both uninfected and *A. candida*-infected tissues (Tables 5.5 and 5.6). It has been reported to positively regulate plant immunity (Zhang et al., 2013). Mutants lacking *MED14* were shown to be more susceptible to *Pseudomonas syringae* DC3000, exhibiting compromised salicylic acid (SA) responsiveness and impaired induction of systemic acquired resistance (SAR). Furthermore, it was also shown that MED14 positively influences immune responses by regulating key defense genes, such as *EDS1*, *ICS1*, *PAD4*, and *SAG101*, all of which are critical for plant defense (Zhang et al., 2013). EDS1 may stabilize MED14 protein levels, while MED14, in turn, sustains *EDS1* expression during pathogen infection.

Surprisingly, multiple molecular players positively regulating the expression of the major flowering repressor locus *FLOWERING LOCUS C* (*FLC*) and, consequently, the timing of flowering in Arabidopsis, were specifically detected in *A. candida*-infected tissues in close proximity to EDS1 (Table 5.6):

- SUPPRESSORS OF MEC-8 AND UNC-52 1 (SMU1): A conserved subunit of the spliceosomal B complex and key player in cold-induced processing of the long noncoding RNA, collectively called *COOLAIR*, which suppresses the flowering repressor gene *FLC* (Long et al., 2024). Cold exposure triggers the production of *COOLAIR* isoforms through the action of SMU1, which are necessary for proper regulation of *FLC* and thereby modulates the timing of flowering in *Arabidopsis*.

- EARLY FLOWERING 7 (ELF7): A component of the Paf1 complex, which is required for the recruitment of histone modification and chromatin remodelling factors, as well as small RNA-mediated gene silencing, and plays a role in regulating the transcription of the flowering repressor

*FLC*. Mutations in *ELF7* result in early flowering, as *FLC* expression is repressed in *elf7* mutants (Cao et al., 2015, He et al., 2004).

- ENHANCED SILENCING PHENOTYPE (ESP) proteins, including ESP3 and ESP4: These cofactors are involved in RNA splicing and interact with the CLEAVAGE POLYADENYLATION SPECIFICITY COMPLEX (CPSF), a key factor in RNA cleavage and polyadenylation. Mutants of *ESP4* and *ESP5* display early flowering, suggesting that defects in RNA processing accelerate flowering time, potentially through enhanced RNA silencing mechanisms (Herr et al., 2006).

- LYSINE-SPECIFIC DEMETHYLASE 1-LIKE 3 (LDL3): A major H3K4me2 demethylase involved in co-transcriptional demethylation, playing a role in removing the H3K4me2 histone modification from active genes. In the *ldl3* mutant, *FLC* is expressed at lower levels due to a reduction in H3K4me2, promoting earlier flowering. LDL3 works by binding to phosphorylated RNAPII and regulating the chromatin landscape at the *FLC* locus (Mori et al., 2023).

In summary SMU1, ELF7, LDL3, ESP3, and ESP4 all interact with transcriptional or chromatin processes to positively regulate *FLC* expression, which represses flowering. These factors influence flowering through mechanisms such as RNA splicing, transcription termination, chromatin modification, and RNA processing. The integration of these processes enables plants to respond to environmental signals and regulate their developmental timing, particularly flowering. This set of proximal interactors suggests that EDS1 may play a role in either enhancing or inhibiting flowering in infected plants, ensuring reproduction occurs before the plant potentially succumbs to disease, or prioritizing immunity. It may achieve one of these outcomes by disrupting or activating a broad range of positive regulators of *FLC*, thereby lifting or maintaining the *FLC*-mediated repression of flowering genes.

Proteins involved in modulating the coordination of growth and immunity were also identified in the vicinity of EDS1.

Notably, CONSTITUTIVE PHOTOMORPHOGENIC 1 (COP1), was found to be specifically localized near EDS1 in uninfected tissues (Table 5.5). Both COP1 and DE-ETIOLATED 1 (DET1) are key regulators of light signalling pathways that negatively regulate immunity, playing an essential role in immune modulation in response to photoperiod and temperature changes (Gangappa and Kumar, 2018). It

has been demonstrated that defense gene expression and disease resistance are strongly influenced by day length, with the transcription factor PHYTOCHROME INTERACTING FACTOR 4 (PIF4), a downstream target of COP1 and DET1, serving as a central regulator. Moreover, PIF4 has been shown to suppress immunity under short photoperiods, while COP1 and DET1 are critical for the suppression of defense responses at elevated temperatures. Collectively, these findings suggest that the DET1-COP1-PIF4 module acts as a central hub for coordinating growth and immunity in response to seasonal signals (Gangappa and Kumar, 2018), with EDS1 potentially playing a role in maintaining developmental processes and inhibiting defense responses in the absence of pathogens.

On the other hand, RETINOBLASTOMA-RELATED 1 (RBR1) was specifically identified in the proximity of EDS1 upon *A. candida* infection (Table 5.6). RBR1 has been shown to undergo hyperphosphorylation during ETI, leading to the over-activation of the core cell-cycle regulator, E2F transcription factor. This results in programmed cell-death (PCD) instead of normal cell-cycle progression (Wang et al., 2014). *e2f* mutants display compromised ETI responses induced by both TNL and CNL classes of immune receptors. This impairment is likely due to CYCLIN-DEPENDENT KINASE INHIBITORS (CKIs)-mediated hyperphosphorylation of RBR1. These findings suggest that canonical cell-cycle regulators, like RBR1, also have noncanonical roles in plant immunity (Zebell and Dong, 2015). EDS1 may be involved in this cell-cycle-related signalling pathway to initiate the reallocation of energy from growth to defense.

Finally, SUPPRESSOR OF ACTIVATED PROTEIN KINASE 3B (SAC3B) was identified in close proximity to EDS1, a component of the mRNA export complex TREX-2 (transcription/export), which facilitates the transport of mRNA from the nucleus to the cytoplasm. SAC3B plays a role in preventing gene silencing in Arabidopsis and is involved in small RNA biogenesis and chromatin methylation, which are essential processes for gene regulation (Yang et al., 2017b). The function of SAC3B can be disrupted by the fungal pathogen *Verticillium dahliae*, which produces an effector that interferes with the export of the AGO1–microRNA complex, a crucial component of post-transcriptional gene silencing (Zhu et al., 2022). By blocking this export, the effector suppresses miRNA function, weakening the plant's immune response and promoting pathogen infection. EDS1 may be involved in the export of certain immune-related mRNAs through this complex.

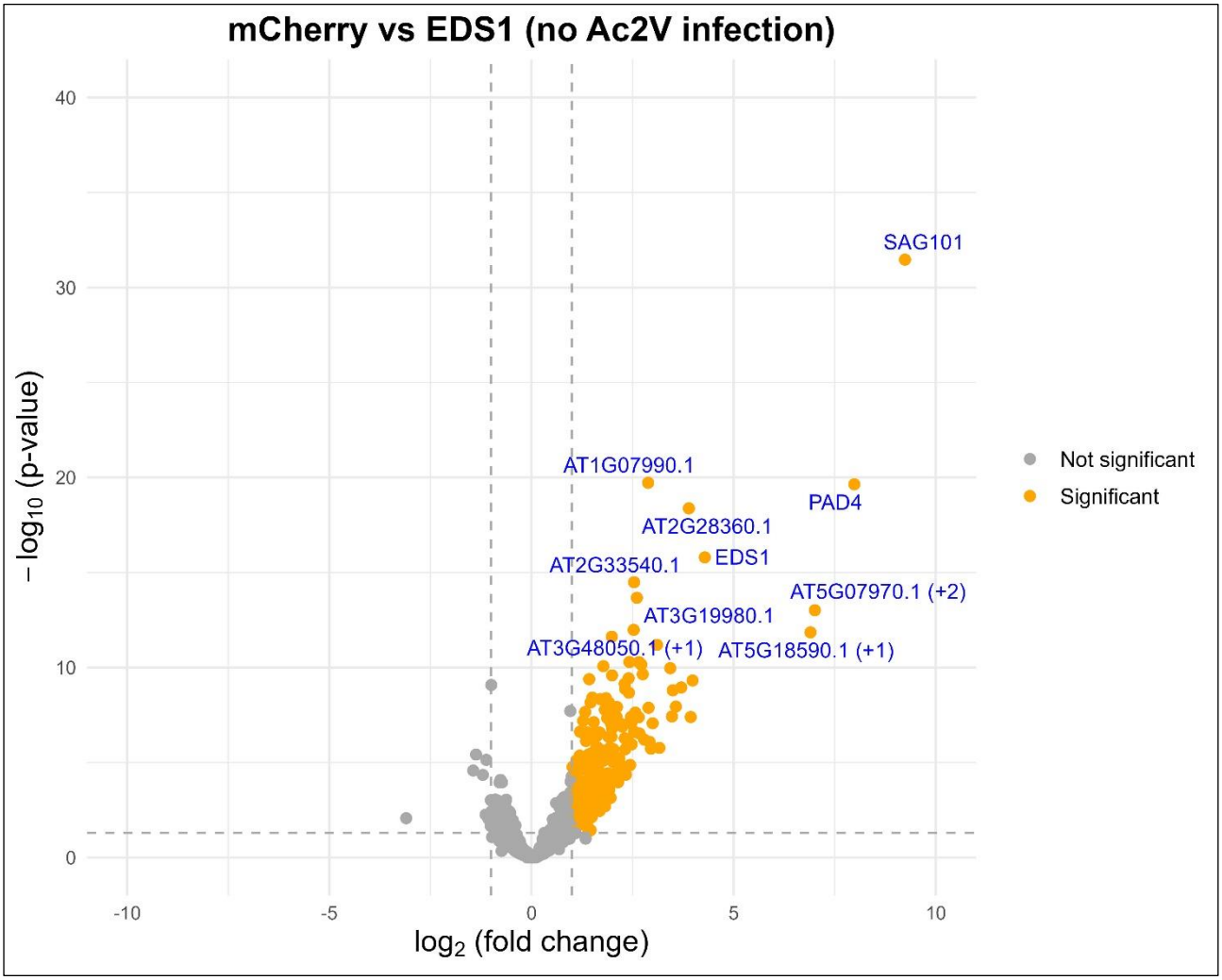


**Figure 5.10 TurboID-based identification of *At*EDS1 proximal plant interactors in DM10 *A. thaliana* without *A. candida*$^{Ac2V}$ infection.**

Proteins highlighted in orange were considered as *At*EDS1 proximal plant interactors if they exhibited a 2-fold change increase in biotinylation compared to mCherry and had a statistically significant difference (P-value < 0.05). Proteins with no significant difference in biotinylation are shown in grey. The grey dotted threshold lines indicate a P-value of 0.05 (horizontal) and a log2(fold change) of –1 and 1 (vertical). The top 10 significantly biotinylated proteins are labelled with their identification numbers. Proteins with a total spectral count below 50 were excluded from the analysis. Statistical significance was determined using Fisher's Exact Test, implemented in the edgeR package (Chen et al., 2025).

**Table 5-5 List of the *At*EDS1 proximal plant interactors identified in DM10 *A. thaliana* without *A. candida*$^{Ac2V}$ infection.**

Proteins are ranked by P-value and log(FC) > 3.

| Protein | P-value | log(FC) | Description |
|---|---|---|---|
| AT5G14930 | 3.42E-32 | 9.238 | SAG101 |
| AT3G52430 | 2.28E-20 | 7.984 | PAD4 |
| AT2G28360 | 4.21E-19 | 3.892 | SIT4 phosphatase-associated family protein |
| AT3G48090 | 1.59E-16 | 4.285 | EDS1 |
| AT5G07970 | 9.66E-14 | 7.008 | SYS2, identified as a specific subunit of SYD-associated SWI/SNF (SAS) complexes |
| AT5G18590 | 1.41E-12 | 6.9 | galactose oxidase/kelch repeat superfamily protein |
| AT5G07940 | 6.41E-12 | 3.102 | SYS1, identified as a specific subunit of SYD-associated SWI/SNF (SAS) complexes |
| AT3G04740 | 1.09E-10 | 3.431 | MED14, encodes a protein with similarities to subunits of the Mediator complex, required for RNA polymerase II recruitment at target promoters in response to specific activators |
| AT5G01400 | 4.83E-10 | 3.983 | ESP4, encodes a Symplekin/Pta1 homologue which would have the potential to interact with either ESP1 or AtCstF64 |
| AT1G50410 | 1.12E-09 | 3.703 | CHR28, encodes a member of the SNF2 family of helicase-like proteins and is involved in RNA-directed DNA methylation |
| AT2G32950 | 1.58E-09 | 3.494 | COP1, represses photomorphogenesis and induces skotomorphogenesis in the dark, contains a ring finger zinc-binding motif, a coiled-coil domain, and several WD-40 repeats, similar to G-beta proteins |
| AT4G33240 | 1.58E-09 | 3.494 | FAB1A, encodes a protein that is predicted to act as a 1-phosphatidylinositol-3-phosphate (PtdIns3P) 5-kinase based on its homology to Fab1 from yeast |
| AT3G06290 | 1.14E-08 | 3.571 | SAC3B, encodes a component of the conserved TREX-2 complex that couples mRNA transcription with nucleo-cytoplasmic export |
| AT5G38840 | 3.78E-08 | 3.473 | SMAD/FHA domain-containing protein |
| AT1G13120 | 4.03E-08 | 3.937 | GLE1, nucleoporin GLE1-like protein |
| AT3G63500 | 1.69E-06 | 3.162 | OBE4, encodes a PHD-finger protein that, with TTA2, is redundantly required for MP-dependent embryonic root meristem initiation |

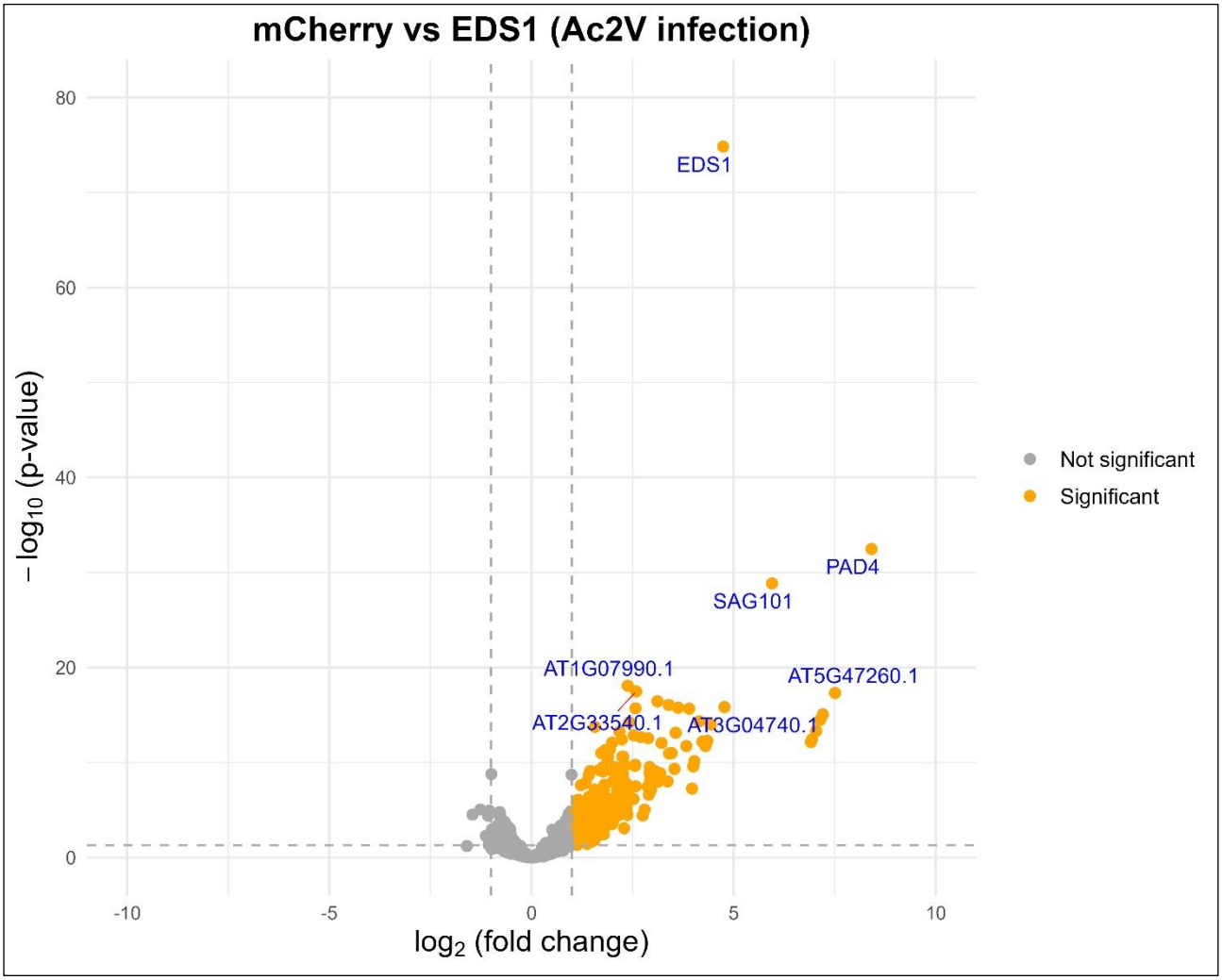


**Figure 5.11 TurboID-based identification of *At*EDS1 proximal plant interactors at 6 days post *A. candida*$^{Ac2V}$ infection in DM10 *A. thaliana*.**

Proteins highlighted in orange were considered as *At*EDS1 proximal plant interactors if they exhibited a 2-fold change increase in biotinylation compared to mCherry and had a statistically significant difference (P-value < 0.05). Proteins with no significant difference in biotinylation are shown in grey. The grey dotted threshold lines indicate a P-value of 0.05 (horizontal) and a log2(fold change) of –1 and 1 (vertical). The top 10 significantly biotinylated proteins are labelled with their identification numbers. Proteins with a total spectral count below 50 were excluded from the analysis. Statistical significance was determined using Fisher's Exact Test, implemented in the edgeR package (Chen et al., 2025).

**Table 5-6 List of the *At*EDS1 proximal plant interactors identified at 6 days post *A. candida*$^{Ac2V}$ infection in DM10 *A. thaliana*.**

Proteins are ranked by P-value and log(FC) > 3.

| Protein | P-value | log(FC) | Description |
|---|---|---|---|
| AT3G48090 | 1.46E-75 | 4.741 | EDS1 |
| AT3G52430 | 3.34E-33 | 8.411 | PAD4 |
| AT5G14930 | 1.4E-29 | 5.948 | SAG101 |
| AT5G47260 | 4.77E-18 | 7.507 | NLR gene, together with AT5G47280 controls broad-spectrum quantitative partial resistance to the root pathogen *P. brassicae* |
| AT2G46020 | 3.58E-17 | 3.114 | CHR2, encodes a SWI/SNF chromatin remodelling ATPase that upregulates transcription of all three CUC genes and is involved in the formation and/or maintenance of boundary cells during embryogenesis |
| AT5G07940 | 8.75E-17 | 3.393 | SYS1, identified as a specific subunit of SYD-associated SWI/SNF (SAS) complexes |
| AT3G04740 | 1.46E-16 | 4.771 | MED14, encodes a protein with similarities to subunits of the Mediator complex, required for RNA polymerase II recruitment at target promoters in response to specific activators |
| AT4G25520 | 1.71E-16 | 3.629 | SLK1, SEUSS-like 1 |
| AT1G50410 | 2.15E-16 | 3.898 | CHR28, encodes a member of the SNF2 family of helicase-like proteins and is involved in RNA-directed DNA methylation |
| AT1G24190 | 8.61E-16 | 7.206 | SIN3, enhances *At*ERF7-mediated transcriptional repression, RNAi lines show ABA hypersensitivity, interacts with ERF7 and HDA19 |
| AT5G47280 | 3.31E-15 | 7.137 | ADR1-L3 |
| AT4G16310 | 4.63E-15 | 4.148 | LDL3, FAD-dependent lysine-specific histone demethylase involved in the control of **flowering time**, major **H3K4me2** demethylase |
| AT5G07970 | 9.73E-15 | 4.432 | SYS2, identified as a specific subunit of SYD-associated SWI/SNF (SAS) complexes |
| AT3G07790 | 4.87E-14 | 7.041 | DGCR14-like protein |
| AT1G73720 | 7.39E-14 | 3.566 | SMU1, a protein involved in RNA splicing |
| AT5G56270 | 3.65E-13 | 6.936 | WRKY2, encodes WRKY transcription factor 2, a zinc-finger protein |
| AT1G03280 | 5.17E-13 | 4.346 | transcription initiation factor TFIIE subunit alpha |
| AT5G16680 | 6.45E-13 | 4.225 | PHD2, PHD protein which cooperates with AIPP2 and BAH domain protein AIPP3 to read **H3K4** histone marks |
| AT2G46510 | 7.13E-13 | 6.909 | JAM1, encodes a nuclear localized BLH domain containing transcriptional activator involved in response to ABA |
| AT3G51120 | 8.78E-13 | 3.214 | ATC3H44, zinc finger CCCH domain-containing protein 44 |
| AT3G12280 | 1.8E-12 | 4.301 | RBR1, encodes a retinoblastoma homologue RETINOBLASTOMA-RELATED protein (RBR or RBR1) |
| AT2G47330 | 1.84E-12 | 3.827 | P-loop containing nucleoside triphosphate hydrolases superfamily protein |
| AT2G46340 | 1E-11 | 3.468 | SPA1, encodes a member of the suppressor of phyA-105 protein family (SPA1-SPA4) |
| AT5G15020 | 1.1E-11 | 3.402 | SNL2, encodes a homolog of the transcriptional repressor SIN3 |
| AT5G01400 | 7.27E-11 | 4.026 | ESP4, encodes a Symplekin/Pta1 homologue which would have the potential to interact with either ESP1 or AtCstF64 |
| AT1G79730 | 2.56E-10 | 3.999 | ELF7, encodes a PAF1 homolog that is involved in the control of **flowering time** by elevating **FLC expression** to a level that creates the vernalization-responsive, winter-annual habit |
| AT4G18130 | 4.64E-10 | 3.536 | PHYE, member of Histidine Kinase |
| AT1G32490 | 4.64E-10 | 3.535 | ESP3, encodes a homolog of the yeast PRP2 protein, one of four related DEAH RNA helicases identified as essential cofactors for RNA splicing |

| | | | |
|---|---|---|---|
| AT3G49600 | 8.04E-10 | 3.056 | UBP26, encodes a ubiquitin-specific protease which catalyzes deubiquitination of histone H2B and is required for heterochromatin silencing |
| AT3G06290 | 1.34E-09 | 3.182 | SAC3B, encodes a component of the conserved TREX-2 complex that couples mRNA transcription with nucleo-cytoplasmic export, that is required for prevention of epigenetic gene silencing and has additional roles in regulating siRNAs and DNA methylation |
| AT5G20610 | 9.62E-09 | 3.364 | PMIR1, encodes a member of a plant specific C2 domain containing gene family |
| AT5G13010 | 1.07E-08 | 3.128 | CUV, encodes a nuclear localized DEAH-box containing protein that is involved in miRNA biogenesis |
| AT1G15780 | 5.56E-08 | 3.97 | MED15A, mediator of RNA polymerase II transcription subunit 15a-like protein |

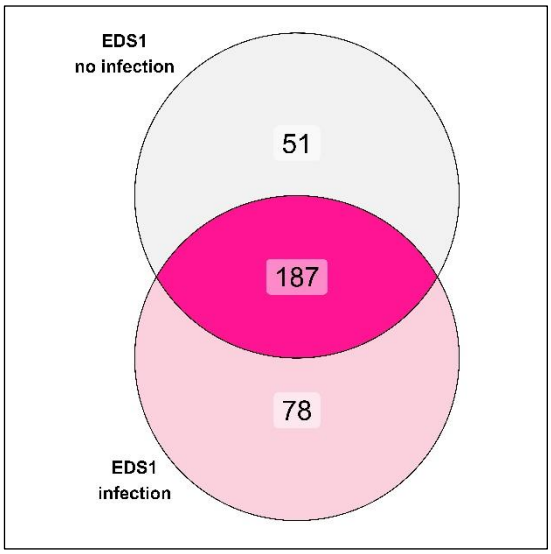


**Figure 5.12 Most *At*EDS1 proximal plant interactors are shared between uninfected and infected tissues.**

Proteins were considered as proximal plant interactors for each treatment if they showed at least a 1-fold change increase in biotinylation compared to mCherry and a statistically significant difference (P-value < 0.05). Proximal plant interactors for each treatment were compared to generate a Venn diagram. The pink gradient corresponds to counts ranging from a lower to higher number of proteins.

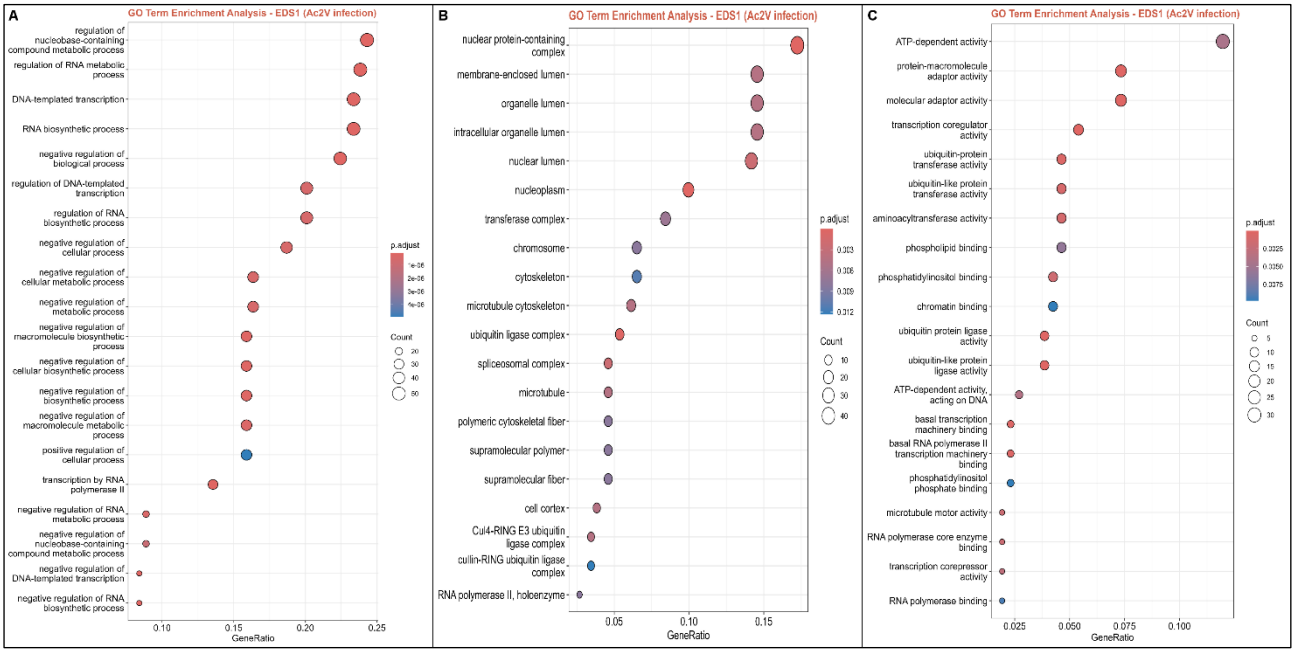


**Figure 5.13 GO-term enrichment analysis of *At*EDS1 proximal plant interactors.**

Gene ontology (GO) categories analysed included biological process (**A**), cellular component (**B**) and molecular function (**C**). GO terms within each category were ranked in descending order of significance (P-value < 0.05) and visualized by count (represented by circle size). The analysis compared proteins that were significantly enriched during infection and in proximity to *At*EDS1 with all Arabidopsis proteins detected by mass spectrometry.

## 5.3 Discussion

After establishing the experimental conditions to capture native CCG effectors from *A. candida* using the TurboID-tagged TNL WRR4A$^{Col-0}$ in Arabidopsis transgenic lines, as described in Chapter 4, we applied this system to test whether some CCGs might target EDS1, which play a central role in TNL signalling.

We detected three promising CCG candidates, CCG82, CCG31 and CCG32, that could potentially interfere with EDS1 functions (Figure 5.6 and Supplementary Figure 5.5). In Redkar et al. (2023), several CCG candidates were cloned and tested in high-throughput transient screens to identify effectors recognized by the broad-spectrum NLRs WRR4A and WRR4B. CCG82 and CCG31 were part of that screen and were found not to be recognized by these TNLs, which supports the hypothesis that they might evade NLR recognition and target EDS1. Furthermore, the potential interactions between CCG82, CCG31, CCG32, and EDS1 were evaluated using AlphaFold2. Among these predicted interactions, only CCG82 was identified as potentially interacting with EDS1 at its N-terminal

interface, which is involved in dimerization with either SAG101 or PAD4 (Wagner et al., 2013) (Figure 5.7). The predicted interaction between CCG82 and EDS1 was then tested in the presence of EDS1's signalling partners, SAG101 and PAD4 (Figures 5.8 and 5.9). In the presence of SAG101, CCG82 was still predicted to bind to EDS1, without disrupting any of the EDS1-SAG101 heterodimer signalling functions (Huang et al., 2025, Xiao et al., 2025) (Figure 5.8). However, when PAD4 was present, CCG82 was predicted to bind to PAD4 instead of EDS1, with its binding site perfectly matching the site where ADR1 associates with PAD4 (Yu et al., 2024) (Figure 5.9). Thus, CCG82 may specifically interfere with the EDS1-PAD4-ADR1 signalling complex by out-competing ADR1 for binding to PAD4. However, further experiments are needed to test this hypothesis.

According to Furzer et al. (2022), like the two CCGs, CCG14 and CCG41, identified in the WRR4A$^{Col-0}$ TurboID experiment (see Chapter 4), CCG82 and CCG31 belong to the early-expressed CCGs (expression cluster number 7), which are primarily expressed at 2 and 4 dpi. Among the five CCGs detected in total with our TurboID approach, only CCG32 is part of the late-expressed CCGs (expression cluster number 1), which begin being expressed at 4 dpi and continue up to 8 dpi. Therefore, this system seems to mainly capture early-expressed effectors, although more experiments with additional time points are needed to establish a clear pattern (only the 6 dpi time point was explored here).

In addition to identifying effectors recognized by NLR proteins (see Chapter 4), this approach also appears capable of identifying effectors that target susceptible host proteins or those involved in important downstream signalling hubs responsible for activating defense responses. Since we have also generated Arabidopsis TurboID transgenic lines for other signalling components, including SAG101, PAD4, NRG1.2 and ADR1-L1, which are signalling partners of EDS1, it would be interesting to perform this experiment with these proteins to gain a more comprehensive overview of the extent to which this essential signalling platform may be targeted by effectors. Additionally, these transgenic lines could be infected with other plant pathogens to determine whether their potential targeting is a common feature or specific to *Albugo* species. Ultimately, this could enhance our understanding of pathogen virulence by defining the core set of effectors required for pathogenicity and, consequently, identifying the key plant immune components necessary to trigger defense mechanisms.

Pathogen infection in plants triggers large-scale transcriptional changes, with EDS1 heterodimers being recruited by TNLs to activate resistance pathways. However, the exact mechanisms by which NLRs converge on transcriptional reprogramming, and how the balance between maintaining growth, triggering flowering, and activating immunity is regulated, remains to be elucidated. Indeed, both flowering and immunity are energy-consuming processes that must be tightly controlled and balanced with developmental processes. Given that several key players in these signalling pathways were detected in proximity to EDS1 (Tables 5.5 and 5.6), it is possible that EDS1 serves as an important hub, linking these processes and regulating the transition from developmental and/or flowering stages to defense responses.

Interestingly, many of the identified proximal interactors of EDS1 were found to localize to the nuclear pore complex (NPC), whose local and global associated proteome was recently characterized using TurboID (Tang et al., 2024). These EDS1 proximal interactors include mRNA splicing and processing regulators such as SMU1 and ESP4, mediators like MED14 and MED15, the transcription regulator SLK1, histone modifiers LDL3 and SNL2, chromatin remodelers CHR2, CHR28, PHD2 and RBR1, as well as nuclear mRNA exporters SAC3B and GLE1, all localized in the nucleoplasm. In contrast, the translation regulatory machineries are recruited on the cytoplasmic side. The NPC is vital for nucleocytoplasmic communication, and the Tang et al. (2024) study underscores its significant role in orchestrating gene expression regulation, beyond simply serving as a conduit for cargo transport. Therefore, EDS1-mediated transcriptional reprogramming in response to pathogen attacks may involve the NPC. Moreover, it has been reported that the plant NPC central barrier undergoes phase separation, a critical process that determines NPC permeability. This mechanism regulates the selective nucleocytoplasmic transport of immune regulators, such as MPK3, which contributes to resistance against *Botrytis cinerea* (Wang et al., 2023).

Surprisingly, several positive regulators of the major flowering repressor locus *FLC*, which is involved in repressing flowering, were identified through TurboID-tagged EDS1. These proximal interactors include ESP4, ESP3, ELF7, LDL3, and SMU1 (Table 5.6). It has been shown that the Y-complex (Nup107-160 complex), a subcomplex of the NPC, modulates *FLC* transcription by tethering the locus at the nuclear periphery and altering its histone modification (Huang et al., 2024b). Additionally, it was demonstrated that Y-complex nucleoporins interact with RNA polymerase II, increasing its occupancy at the *FLC* locus and facilitating its transcription. Therefore, our EDS1 TurboID dataset

suggests that EDS1 could be involved in inhibiting flowering processes, thereby allocating energy toward defense rather than reproduction.

The link between flowering time and pathogen defense has been explored using the *A. thaliana* and the fungal pathogen *Fusarium oxysporum* (Lyons et al., 2015). The study found that *F. oxysporum* infection delays flowering in *A. thaliana*, and late-flowering mutants exhibited increased resistance to the pathogen. However, this association was independent of vernalization and the flowering repressor *FLC*. Through RNA-seq, the authors further explored the mechanism underlying enhanced resistance in late-flowering mutants and identified flowering-time genes responsive to *F. oxysporum* infection. Notably, the photoperiodic pathway regulator GIGANTEA (GI) was found to promote susceptibility to the pathogen.

Moreover, two studies conducted simultaneously in rice found that a pair of E3 ubiquitin ligases enhanced immunity by negatively controlling flowering (Xu et al., 2024, Yi et al., 2024). AvrPiz-t-INTERACTING PROTEIN 6 (APIP6) forms homo- or hetero-oligomers with IDEAL PLANT ARCHITECTURE 1 INTERACTOR 1 (IPI1) to target two rice homologs of the flowering regulator EARLY FLOWERING 3 (ELF3) for degradation *via* the 26S proteasome, thereby regulating both rice immunity and flowering. Surprisingly, overexpression of *IPI1* in *Nipponbare* resulted in significantly late-flowering phenotypes, similar to the *elf3-1* mutant, which also enhances resistance against the rice blast fungus *Magnaporthe oryzae* (Xu et al., 2024). In contrast, *IPI4* knockout plants displayed early flowering phenotypes and compromised resistance to the rice pathogen (Yi et al., 2024). It was found that IPI1 and APIP6 synergistically modulate the degradation of *Os*ELF3s, fine-tuning blast disease resistance by targeting *Os*ELF3-2, while IPI1 controls both disease resistance and flowering by targeting *Os*ELF3-1, a paralog of *Os*ELF3-2. These studies uncovered a molecular mechanism that balances rice immunity and flowering.

Finally, COP1, which regulates light signalling pathways and negatively affects immunity, was identified as a proximal interactor of EDS1 when no pathogens are present (Table 5.5). COP1 and DET1 influence defense gene expression and disease resistance through the transcription factor PIF4, which suppresses immunity under short photoperiods and helps suppress defense responses under high temperatures (Gangappa and Kumar, 2018). Thus, COP1, DET1, and PIF4 form a central module that coordinates growth and immunity, with EDS1 potentially helping to regulate these processes in the absence of pathogens. In contrast, upon infection with *A. candida*, RBR1 was found near EDS1

(Table 5.6). Unlike COP1, RBR1 is involved in the cell cycle, and its hyperphosphorylation during immune responses leads to programmed cell death instead of normal cell-cycle progression (Wang et al., 2014). EDS1 may play a role in this cell-cycle-related signalling, reallocating energy from growth to defense during immune responses.

The mechanism by which EDS1 contributes to TIR-NLR-dependent elevation of mRNA levels for key defense genes such as *SARD1*, *ICS1* and *FMO1*, remains mysterious. It is questionable whether this role can be solely due to its promotion of ADR1 or NRG1 oligomerization and association with plant membranes to form calcium channels. Taken together, these proximal interactors identified through TurboID suggest that EDS1 may also elevate transcription *via* its interactions with the host plant transcriptional and RNA processing machinery. It would be interesting to use the SAG101 and PAD4 TurboID transgenic lines to determine whether these proximal interactors are involved in the EDS1-SAG101 or the EDS1-PAD4 heterodimer signalling pathways.

## 5.4 Supplementary figures

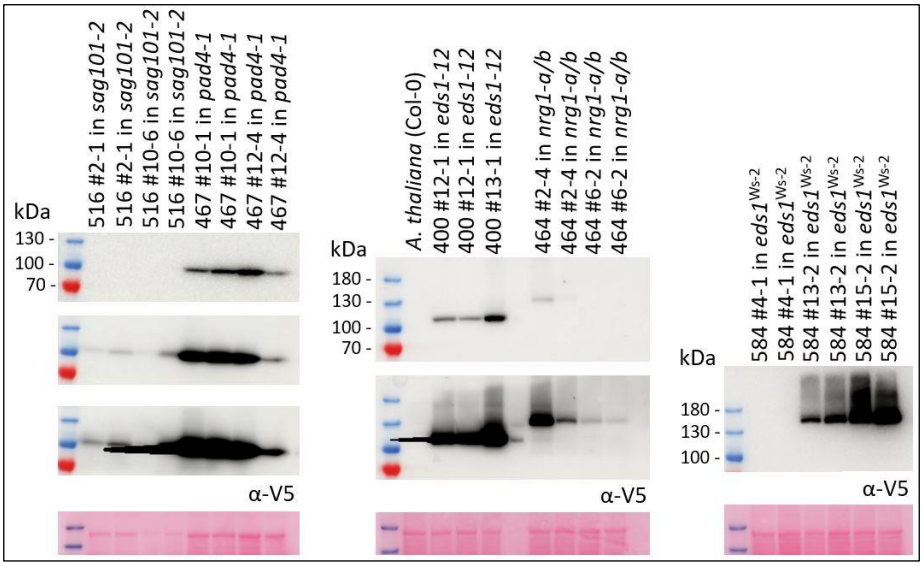


**Supplementary Figure 5-1 Protein expression of the *A. thaliana* TurboID transgenic lines in the T3 generation – part 1.**

Western blot of *pEDS1*:*EDS1*:TurboID-V5 (400), *pSAG101*:*SAG101*:TurboID-V5 (516), *pPAD4*:*PAD4*:TurboID-V5 (467), *pNRG1.2*:*NRG1.2*:TurboID-V5 (464), 35S:*WRR4A*$^{Col-0}$:TurboID-V5 (584) in 4/5-week-old *eds1-12*, *sag101-2*, *pad4-1*, *nrg1-a/b* and *eds1*$^{Ws-2}$ *A. thaliana* plants. Lysates were resolved by SDS-PAGE and bands were visualized by anti-V5 antibody labelling.

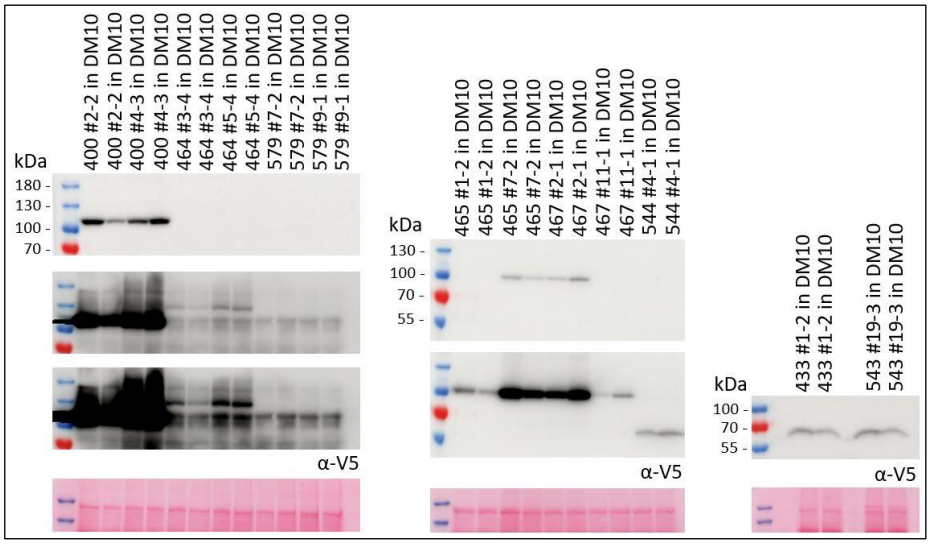


**Supplementary Figure 5-2 Protein expression of the *A. thaliana* TurboID transgenic lines in the T3 generation – part 2.**

Western blot of *pEDS1*:*EDS1*:TurboID-V5 (400), *pSAG101*:*SAG101*:TurboID-V5 (465), *pPAD4*:*PAD4*:TurboID-V5 (467), 35S:*ADR1-L1*:TurboID-V5 (579), *pNRG1.2*:*NRG1.2*:TurboID-V5 (464), pAt2:mCherry:TurboID-V5 (543), p35S:mCherry:TurboID-V5 (433) and pAt2:NLS-GFP:TurboID-V5 (544) in 4/5-week-old DM10 *A. thaliana* plants. Lysates were resolved by SDS-PAGE and bands were visualized by anti-V5 antibody labelling.

***Hpa*** $^{Emoy2}$ **infection** (50,000 oospores/mL; 10 dpi)

Rep1

| | 1 | 2 | 3 | 4 | 5 |
|---|---|---|---|---|---|
| **Col-0** | 100% | | | | |
| ***eds1-12*** | | 5% | | | 95% |
| **EDS1:Tb-V5 #12-1** | 100% | | | | |
| **EDS1:Tb-V5 #13-1** | 100% | | | | |

Rep2

| | 1 | 2 | 3 | 4 | 5 |
|---|---|---|---|---|---|
| **Col-0** | 100% | | | | |
| ***eds1-12*** | 2.5% | 2.5% | | 5% | 90% |
| **EDS1:Tb-V5 #12-1** | 100% | | | | |
| **EDS1:Tb-V5 #13-1** | 100% | | | | |

Rep3

| | 1 | 2 | 3 | 4 | 5 |
|---|---|---|---|---|---|
| **Col-0** | 100% | | | | |
| ***eds1-12*** | | | 2.5% | 5% | 92.5% |
| **EDS1:Tb-V5 #12-1** | 100% | | | | |
| **EDS1:Tb-V5 #13-1** | 100% | | | | |

**1**: no leaves infected
**2**: 1 leaf infected and less than 5 spores
**3**: 1 leaf infected and more than 5 spores
**4**: 2 leaves infected and less than 5 spores
**5**: 2 or more leaves infected and more than 5 spores

**Supplementary Figure 5-3 *At*EDS1:TurboID-V5 confers resistance to *Hpa* in *A. thaliana eds1-12*.**

Quantification of *Hpa* isolate Emoy2 growth on T3 14-day-old *A. thaliana* seedlings at 10 dpi ($5.10^4$ spores/mL) by counting conidiospores. Wild-type Col-0 *A. thaliana* accession infected with *Hpa*$^{Emoy2}$ is fully resistant. Indeed, the Arabidopsis R gene *RPP4* confers resistance to *Hpa*$^{Emoy2}$ (van der Biezen et al., 2002). The growth of the pathogen was evaluated according to five categories from 1 to 5: 1 corresponding to no infection, and 5 to strongly infected seedlings. For each genotype, conidiospores were counted on 40 seedlings.

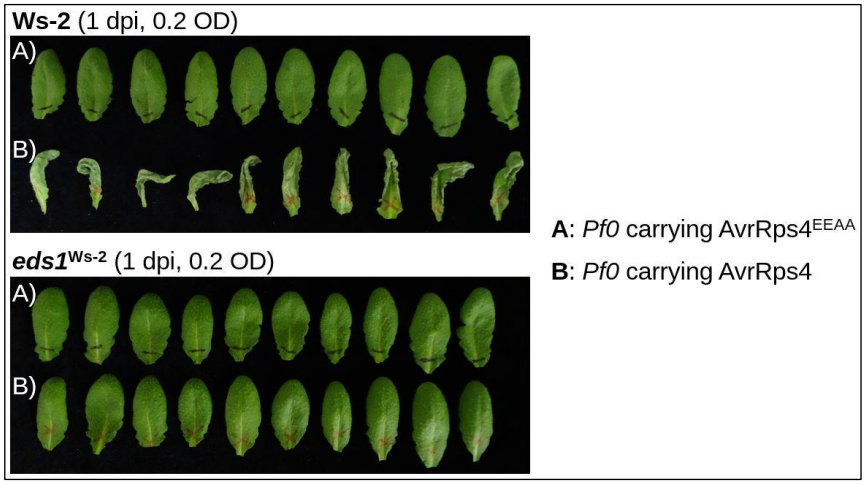


**Supplementary Figure 5-4 Confirmation of the *eds1*$^{Ws-2}$ *A. thaliana* mutant background.**

HR assays by *Pf0*-infiltration at $OD_{600}$ = 0.2 in 4/5-week-old *A. thaliana* leaves at 1 dpi. These two *Pf0* strains are either delivering the unrecognized *Pseudomonas* type III effector AvrRps4$^{EEAA}$ (**A**) (Ma et al., 2018) or the recognized AvrRps4 (**B**). *Pf0* carrying AvrRps4 infiltration shows HR in wild-type Ws-2 leaves. Indeed, the effector protein AvrRps4 is recognized by the Arabidopsis NLR pair RPS4/RRS1 (Le Roux et al., 2015, Sarris et al., 2015). Each leaf corresponds to an individual (10 plants were used per treatment).

| mCherry vs EDS1 (Ac2V infection)<br>spectral count of Ac2V_proteins > 2 & present in EDS1 but not in mCherry | | | | |
|---|---|---|---|---|
| Protein | rep 1 | rep 2 | rep 3 | Total spectral counts |
| CCG82 | 5 | NA | 15 | 20 |
| Ac2vTS10G116 | 7 | NA | 10 | 17 |
| Ac2vTS27G121 | 4 | NA | 6 | 10 |
| Ac2vTS4G145 | 8 | NA | 2 | 10 |
| Ac2vTS42G33 | 7 | NA | 2 | 9 |
| Ac2vTS94G55 | 3 | NA | 5 | 8 |
| Ac2vTS8G249 | 3 | NA | 5 | 8 |
| Ac2vTS112G37 | 4 | NA | 3 | 7 |
| Ac2vTS29G162 | 3 | NA | 4 | 7 |
| CCG32 | 4 | NA | 3 | 7 |
| Ac2vTS82G21 | 4 | NA | 3 | 7 |
| Ac2vTS8G116 | 2 | NA | 4 | 6 |
| Ac2vTS5G197 | 4 | NA | 2 | 6 |
| Ac2vTS34G12 (+1) | 4 | NA | 2 | 6 |
| Ac2vTS23G16 | 2 | NA | 3 | 5 |
| Ac2vTS54G88 | 2 | NA | 3 | 5 |
| Ac2vTS7G187 | 2 | NA | 3 | 5 |
| Ac2vTS66G26 | 2 | NA | 3 | 5 |
| Ac2vTS47G59 | 2 | NA | 3 | 5 |
| Ac2vTS55G34 | 3 | NA | 2 | 5 |
| Ac2vTS13G327 | 2 | NA | 3 | 5 |
| Ac2vTS13G365 | 2 | NA | 3 | 5 |
| Ac2vTS4G221 | 3 | NA | 2 | 5 |
| Ac2vTS22G71 | NA | 2 | 2 | 4 |
| Ac2vTS51G95 | 2 | NA | 2 | 4 |
| Ac2vTS5G53 | 2 | NA | 2 | 4 |
| Ac2vTS1G74 | 2 | NA | 2 | 4 |
| Ac2vTS17G128 | 2 | NA | 2 | 4 |
| Ac2vTS153G12 | 2 | NA | 2 | 4 |
| Ac2vTS80G107 | 2 | NA | 2 | 4 |
| Ac2vTS139G5 | 2 | NA | 2 | 4 |
| Ac2vTS12G155 | 2 | NA | 2 | 4 |
| Ac2vTS82G23 | 2 | NA | 2 | 4 |

**Supplementary Figure 5-5 List of proximal pathogen proteins identified with *At*EDS1 at 6 days post *A. candida*$^{Ac2V}$ infection in DM10 *A. thaliana*.**

Proteins are ranked by total number of spectral counts across the three replicates, with a minimum of two spectral counts detected by mass spectrometry for each protein. Only proteins uniquely detected in the *At*EDS1 samples, but absent from mCherry control samples, are included. Results from each experimental replicate are shown.

**Transgenic *A. thaliana* T3 homozygote seedlings** (7-9 days old):

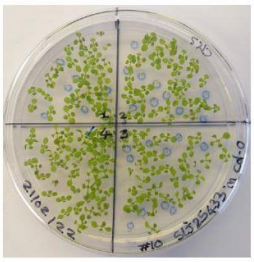

433 #10 in Col-0

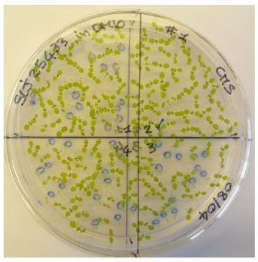

433 #1 in DM10

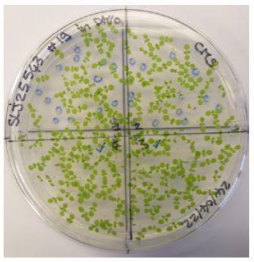

543 #19 in DM10

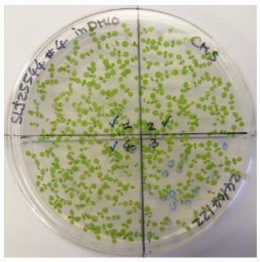

544 #4 in DM10

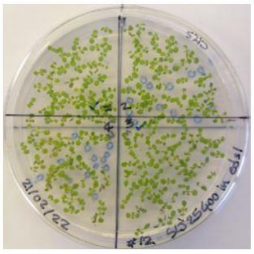

400 #12 in *eds1-12*

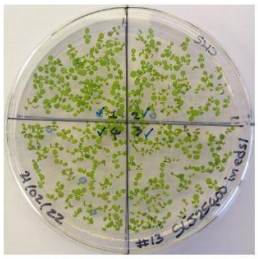

400 #13 in *eds1-12*

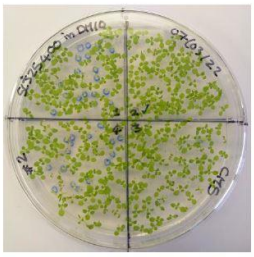

400 #2 in DM10

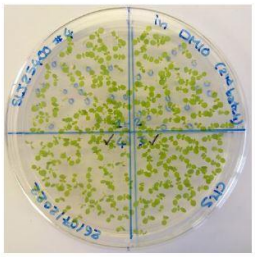

400 #4 in DM10

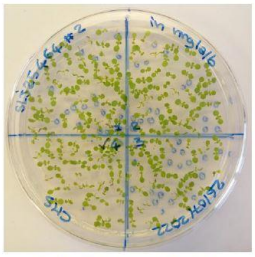

464 #2 in *nrg1-a/b*

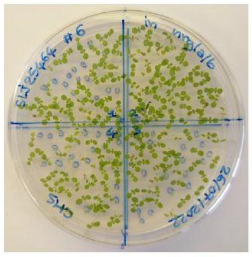

464 #6 in *nrg1-a/b*

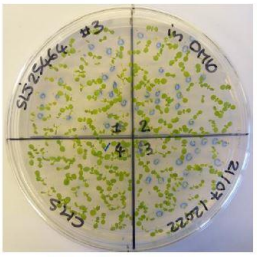

464 #3 in DM10

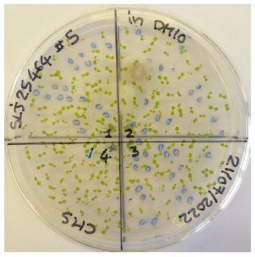

464 #5 in DM10

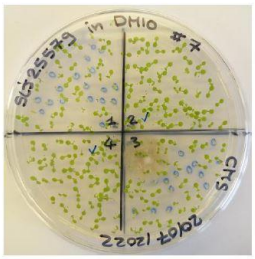

579 #7 in DM10

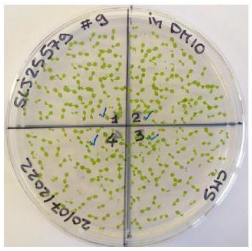

579 #9 in DM10

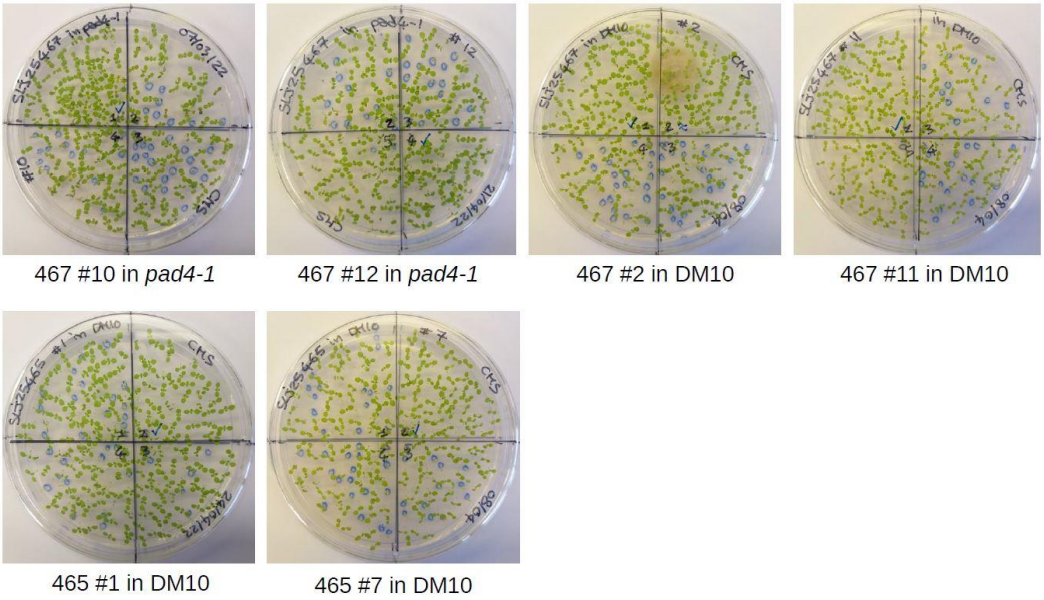


**Supplementary Figure 5-6 Identification of T3 homozygote *A. thaliana* TurboID transgenic lines by BASTA selection.**

Seeds of *pEDS1*:*EDS1*:TurboID-V5 (400), *pSAG101*:*SAG101*:TurboID-V5 (465), *pPAD4*:*PAD4*:TurboID-V5 (467), 35S:*ADR1-L1*:TurboID-V5 (579), *pNRG1.2*:*NRG1.2*:TurboID-V5 (464), 35S:*WRR4A*$^{Col-0}$:TurboID-V5 (584), pAt2:mCherry:TurboID-V5 (543), p35S:mCherry:TurboID-V5 (433) and pAt2:NLS-GFP:TurboID-V5 (544) in DM10, *eds1-12*, *sag101-2*, *pad4-1*, *nrg1-a/b*, *eds1*$^{Ws-2}$ and Col-0 *A. thaliana* backgrounds were sown on BASTA selection plates. The individuals showing 100% resistance to the antibiotic were selected and will be used to carry out TurboID experiments.

# Chapter 6

TurboID-mediated identification of NRC class helper NLRs activation through transient interaction with sensor NLRs

# 6. TurboID-mediated identification of NRC class helper NLRs activation through transient interaction with sensor NLRs

## 6.1 Introduction

### 6.1.1 The NRC network consists of sensor and helper NLRs

Many plant NLRs have functionally specialized to sense pathogen effectors and are referred to as "sensor" NLRs, while others specialize in executing immune signalling and are known as "helper" NLRs.

Some plant NLRs combine both sensing and signalling functions, and are therefore classified as "singleton" NLRs (Adachi et al., 2019b). For instance, the wheat singleton CNL Sr35 directly recognizes its cognate effector and mediates immune signalling through homo-oligomarization and complex formation, independent of other NLRs (Förderer et al., 2022, Zhao et al., 2022). Beyond singleton NLRs, many plant NLRs have functionally specialized to either sense pathogen effectors (sensor NLRs) or execute immune signalling (executor NLRs), often working together in pairs. For example, the rice sensor CNLs RGA5 and Pik-1 are genetically linked to and divergently transcribed from their respective executor CNLs, RAG4 and Pik-2 (Ashikawa et al., 2008, Okuyama et al., 2011). These sensor-executor NLR pairs form heterocomplexes to trigger immune signalling (Césari et al., 2014, Zdrzalek et al., 2020). Finally, some NLRs act as helper NLRs, serving as signalling hubs for multiple sensor NLRs. These helper NLRs create a complex network architecture that extends beyond the typical one-to-one relationship of NLR pairs, facilitating the activation of downstream immune responses (Adachi et al., 2019b).

The NLR-REQUIRED FOR CELL DEATH (NRC) proteins function as helper NLRs within the NRC network, mediating immune responses by supporting the function of various sensor NLRs in both redundant and, in some cases, specific ways (Gabriëls et al., 2007, Wu et al., 2017). In the Solanaceous model plant *Nicotiana benthamiana*, the NRCs NRC2, NRC3 and NRC4 act redundantly, yet with distinct specificities, as helper NLRs for a variety of sensor NLRs (Lin et al., 2022, Witek et al., 2021, Wu et al., 2017). For instance, the sensor NLR Rpi-blb2 activates resistance to the oomycete pathogen *Phytophthora infestans* through *Nb*NRC4 alone, while all three NRC helper *Nb*NLRs contribute redundantly to the function of Rx, a sensor NLR mediating resistance to *potato virus X* (PVX) (Wu et

al., 2017). This redundancy, along with a certain degree of specificity, suggests a co-evolutionary relationship between sensor and helper NLRs. The redundancy among helper NLRs might enhance the robustness of immune responses, protecting against pathogen effectors that may suppress key signalling nodes, as discussed in Chapter 5. Although NRCs and their associated sensor NLRs are not genetically linked and are scattered across the genomes of solanaceous plants, they form a well-supported phylogenetic clade (Contreras et al., 2023a, Wu et al., 2017).

### 6.1.2 Activation and regulation of the NRC network

The mechanism by which sensor NLRs activate helper NLRs in the NRC network remains poorly understood.

Upon effector recognition by the sensor NLRs, Rpi-amr1 and Rpi-amr3 from *Solanum americanum,* (which confer oomycete resistance), Bs2 from pepper (which confers bacterial resistance), and Rx from *Solanum tuberosum* (which confers virus resistance), studies have shown that NRC2 and NRC4 oligomerize into multiprotein complexes known as resistosomes (Ahn et al., 2023, Contreras et al., 2023b). These studies also demonstrated that sensor NLRs do not become incorporated into the NRC2 oligomer, suggesting that NRC2 transiently interacts with these sensor NLRs prior to resistosome formation, thereby triggering their activation. By “transient interaction”, we refer to the helper NRC directly interacting with or coming into close proximity to the sensor NLR to become activated, before being released to initiate the homo-oligomerization of NRCs. The molecular structure of these resistosomes has now been resolved, revealing that NRC2 and NRC4 form hexameric resistosomes and confirming that sensor NLRs are not incorporated into these oligomers (Liu et al., 2024a, Ma et al., 2024, Madhuprakash et al., 2024). Furthermore, the nucleotide-binding (NB) domains within the NB-ARC of the disease resistance proteins Rx, Rpi-amr1, Rpi-amr3, Gpa2 (which confers nematode resistance), and Sw-5b (which confers virus resistance) have been shown to be sufficient to trigger the oligomerization of their respective downstream NRCs (Contreras et al., 2024). This suggests that the NB domain serves as the minimal unit for NRC activation, undergoing conformational rearrangements within the NB-ARC domain upon effector recognition, which likely exposes the NB domain to activate NRCs.

The pre-activation stage of NRC2 has been shown to be a dimer, which contributes to immune receptor auto-inhibition and suggests a transition from homodimers to higher-order oligomeric

resistosomes upon activation (Ma et al., 2024, Selvaraj et al., 2024). Indeed, the activation of defense responses must be tightly regulated to avoid auto-immunity. NRCX, a member of the NRC family, has been reported to negatively modulate the hypersensitive cell death mediated by NRC2 and NRC3, but not by NRC4 (Adachi et al., 2023). Moreover, NRC2 does not associate with other NRC paralogs, indicating a molecular compartmentalization of helper nodes in the NRC network, likely to minimize undesired cross-activation (Selvaraj et al., 2024).

Upon activation, some helper NRCs undergo subcellular re-localization. After activation by their corresponding sensor NLRs, both NRC2 and NRC4 localize to the plasma membrane, where they form puncta (Contreras et al., 2023b, Duggan et al., 2021). In contrast, the sensor NLR Rx does not form plasma membrane-associated puncta upon activation and remains cytosolic (Contreras et al., 2023b). This observation further supports an activation-and-release mechanism for NRC activation. However, the precise mechanism by which sensor NLRs mediate signal transduction and communicate with downstream helper NLRs to trigger their oligomerization, and whether this involves a transient interaction state or other components, remains unknown.

Traditional methods for identifying protein-protein interactions (PPIs) have been unable to detect potential interactions between sensor NLRs and helper NRCs as a mode of activation. However, proximity labelling (PL) techniques, including the engineered biotin ligases TurboID and miniTurbo (Branon et al., 2018), allow us to explore an entirely new area of PPIs that corresponds to weak or transient interactions. These interactions are often missed by traditional methods unless cross-linking is used, highlighting the value of PL approaches. In this chapter, we used TurboID and miniTurbo to investigate specific and dynamic intracellular protein interactions between sensor and NRC class helper NLRs, offering new insights into the signalling pathways involved in effector-triggered immunity (ETI).

## 6.2 Results

Ahn et al. (2023) showed that sensor NLRs are not incorporated into the NRC2 oligomer, suggesting that the interaction between sensor NLRs and helper NLRs is most likely transient and occurs before resistosome formation. In line with this, Dr. Hee-Kyung Ahn attempted to test for a stable interaction between NRC2 and Rpi-amr3 using Co-IP, but the results were inconsistent. Consequently, we

decided to use TurboID and miniTurbo (miniID), which are more sensitive techniques than Co-IP, to investigate the transient interactions between sensor NLRs and their corresponding helper NLRs.

The TurboID-tagged CNLs, Rpi-amr1 and Rpi-amr3 from *Solanum americanum*, and Rpi-blb2 from *Solanum bulbocastanum*, were tested in the presence of their respective *P. infestans* effectors AVRamr1, AVRamr3, and AVRblb2, along with the helper NLRs NRC2 and NRC4 (Table 6.1 and Table 4.1 in Chapter 4) (Lin et al., 2022, Lin et al., 2020, Oh et al., 2009). Rpi-amr1 requires NRC2 or NRC3, but not NRC4, to trigger HR (Witek et al., 2021), whereas Rpi-amr3 activation can be supported by NRC2, NRC3 or NRC4 (Lin et al., 2022). In contrast, Rpi-blb2 relies exclusively on NRC4 to induce cell death (Wu et al., 2017). The helper NLR NRG1.2 (also known as NRG1-B), from *A. thaliana*, which is downstream of TNLs and thus involved in a distinct signalling pathway from that of the NRCs, was used as a negative control. *At*NRG1.2 was tested in both directions: a TurboID-tagged version was used to verify that it would not biotinylate the helper NRCs, and a Myc-tagged version was used to confirm that *At*NRG1.2 would not be biotinylated by Rpi-amr1:TurboID or Rpi-amr3:miniID. Additionally, TurboID-tagged Rpi-blb2, which relies on NRC4 but not NRC2 to trigger HR, was also included as a negative control. Since TurboID experiments are more sensitive than Co-IP experiments and can detect weaker interactions, I aimed to include as many diverse negative controls as possible. The MADA motif mutants of NRC2 ($NRC2^{EEE}$) (Kourelis et al., 2022) or NRC4 ($NRC4^{L9E}$) (Adachi et al., 2019a) were used in these experiments, as they do not trigger HR but still retain the ability to form oligomers upon effector recognition (Ahn et al., 2023, Contreras et al., 2023b, Liu et al., 2024a).

First, the functionality of all TurboID-tagged NLRs, Rpi-amr1, Rpi-amr3, Rpi-blb2 and *At*NRG1.2, was verified (Figure 6.1, Figures 4.1, 4.2 and 4.3 from Chapter 4, and Figure 5.3 from Chapter 5). This was followed by the establishment of experimental conditions to ensure the specific biotinylation of the *P. infestans* effectors AVRamr1 and AVRamr3 by their corresponding sensor CNLs, Rpi-amr1 and Rpi-amr3, respectively, as described in Chapter 4 (Figure 4.2 in Chapter 4). Only after this, I examined the potential biotinylation of $NRC2^{EEE}$ by Rpi-amr1:TurboID and Rpi-amr3:miniID.

**Table 6-1 List of the TurboID- or miniTurbo-tagged proteins generated by Golden Gate cloning and used in *N. benthamiana*.**

The MADA motif mutants of NRC2 (NRC2$^{EEE}$) or NRC4 (NRC4$^{L9E}$) do not trigger HR but maintain oligomer formation (Ahn et al., 2023, Contreras et al., 2023). The promoters and terminators that were used to perform these DNA assemblies are as follow: p35S = cauliflower mosaic virus 35S promoter, t35S = cauliflower mosaic virus 35S terminator.

| Protein | Construct |
|---|---|
| *Sb*Rpi-blb2 | p35S:Rpi-blb2:TurboID-V5:t35S |
| *Nb*NRC2$^{EEE}$ | p35S:NRC2$^{EEE}$:V5-miniID:t35S |
| *Nb*NRC4$^{L9E}$ | p35S:NRC4$^{L9E}$:Myc:t35S |

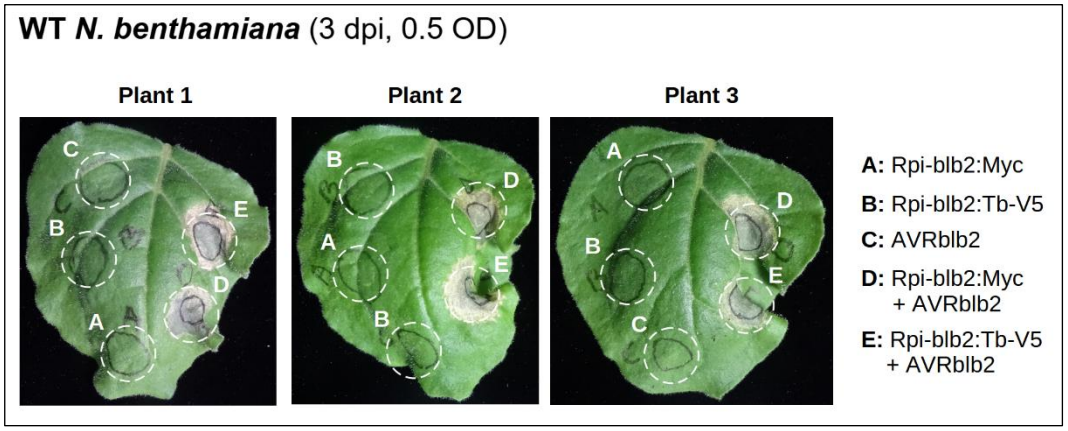


**Figure 6.1 *Sb*Rpi-blb2:TurboID-V5 supports HR in *N. benthamiana*.**

HR assays by *Agro*-infiltration at $OD_{600}$ = 0.5 in 4/5-week-old *N. benthamiana* leaves and at 3 dpi. The *P. infestans* effector AVRblb2 is recognized by the *Solanum bulbocastanum* NLR protein Rpi-blb2 (Oh et al., 2009). Co-delivery of 35S promoter-driven *Sb*Rpi-blb2:Myc or *Sb*Rpi-blb2:TurboID-V5 (Rpi-blb2:Tb-V5) with GFP:AVRblb2 triggers HR in WT *N. benthamiana* leaves.

Interestingly, NRC2$^{EEE}$ appeared to be in the vicinity of Rpi-amr1 and Rpi-amr3 in the presence of both the recognized and unrecognized *P. infestans* effector (Figures 6.2 and 6.3). As expected, no biotinylation of *At*NRG1.2:Myc by either Rpi-amr1:TurboID or Rpi-amr3:miniID was observed. NRC2$^{EEE}$ was not biotinylated by TurboID-tagged *At*NRG1.2 but was slightly biotinylated by TurboID-tagged *Sb*Rpi-blb2. *Sb*Rpi-blb2 is more closely related to Rpi-amr1 and Rpi-amr3 than *At*NRG1.2 is, which could explain this potentially weak interaction (Contreras et al., 2023a). However, even if NRC2$^{EEE}$ exhibits a weak affinity for *Sb*Rpi-blb2, it is known that *Sb*Rpi-blb2 does not trigger HR with the support of *Nb*NRC2, but does so with *Nb*NRC4, which is why it was chosen as an additional negative control (Wu et al., 2017). This underscores the fact that not every protein that comes into

proximity of another protein necessarily results in a biological output. Most importantly, NRC2$^{EEE}$ was consistently and more abundantly biotinylated by TurboID- and miniTurbo-tagged Rpi-amr1 and Rpi-amr3.

It is important to note that the biotinylation of NRC2$^{EEE}$ was only detectable when NRC2$^{EEE}$ was specifically pulled down using Myc beads, followed by blotting the membrane with HRP-conjugated streptavidin. In contrast, biotinylated NRC2$^{EEE}$ was not detectable when all biotinylated proteins were indiscriminately pulled down with streptavidin beads, and the membrane was blotted with anti-Myc antibodies, as done for detecting biotinylated cognate effectors by their corresponding sensor NLRs in Chapter 4 (Figures 4.4 and 4.17). This likely reflects that only a small fraction of the available NRC2$^{EEE}$ in the cells is in close proximity to Rpi-amr1 and Rpi-amr3, and thus, for detection, NRC2$^{EEE}$ proteins must be specifically enriched using Myc beads.

Surprisingly, a higher molecular weight band pulled-down with NRC2$^{EEE}$ was observed in the presence of Rpi-amr1 but not in the presence of Rpi-amr3 (Figures 6.2 and 6.3). This unknown interactor was Rpi-amr1 which was unintentionally “co-immunoprecipitated” with NRC2$^{EEE}$ as you would in a traditional Co-IP experiment. Therefore, NRC2$^{EEE}$ interacts directly with Rpi-amr1 and appears to have a higher interaction affinity with Rpi-amr1 than Rpi-amr3. In view of these results, our hypothesis was that NRC2 dynamically interacts with Rpi-amr1 and Rpi-amr3 in a “kiss and run” manner to continuously monitor the activated or de-activated state of these sensor NLRs to rapidly form NRC2 resistosomes upon pathogen detection (Figure 6.5). This phenomenon is not specific to NRC2; NRC4, which can support HR with Rpi-amr3 but not with Rpi-amr1, was also found to be biotinylated by Rpi-amr3:miniID in an effector-independent manner (Figure 6.4).

Notably, no significant difference in the amount of biotinylated NRC2$^{EEE}$ was detected between activated (in the presence of the recognized effector) and pre-activated (in the absence of the recognized effector) states of both Rpi-amr1 and Rpi-amr3 (Figures 6.2 and 6.3). For TurboID-tagged Rpi-amr1, an apparent reduction in the amount of biotinylated NRC2$^{EEE}$ was observed in the presence of AVRamr1 compared to the absence of the cognate effector. However, this was simply due to the lower abundance of NRC2$^{EEE}$ proteins in these samples, as shown in the input, and this trend was consistently observed across repeats (Figure 6.3).

Initially, we hypothesized that effector recognition by sensor NLRs would lead to a reduction in biotinylated NRC2, as NRC2 would dissociate from the sensor NLRs and begin oligomerizing in response. However, in this particular experimental setup, we could not observe this phenomenon. In these two experiments (Figures 6.2 and 6.3), I only examined the biotinylation of NRC2$^{EEE}$ at a single time point, 3 days post infiltration. If the protein-protein interaction between sensor and helper NLRs is dynamic, as we hypothesized, a single time point is insufficient to capture any potential changes in the affinity between these proteins over time. Moreover, as shown by Ahn et al. (2023), by this particular experimental time point, most of the available NRC2 proteins will have already formed oligomers upon effector recognition. Therefore, the similar amount of biotinylated NRC2$^{EEE}$ observed in the activated state compared to the pre-activated state likely reflects newly synthesized NRC2$^{EEE}$ proteins and/or the remaining pool of non-oligomerized NRC2$^{EEE}$. Therefore, in this experimental setup, we likely missed the moment when NRC2 is activated. To test this hypothesis, I decided to monitor the interaction between sensor and helper NLRs over a time-course (Figure 6.6), as this is the only way to capture sequential association and dissociation between these proteins.

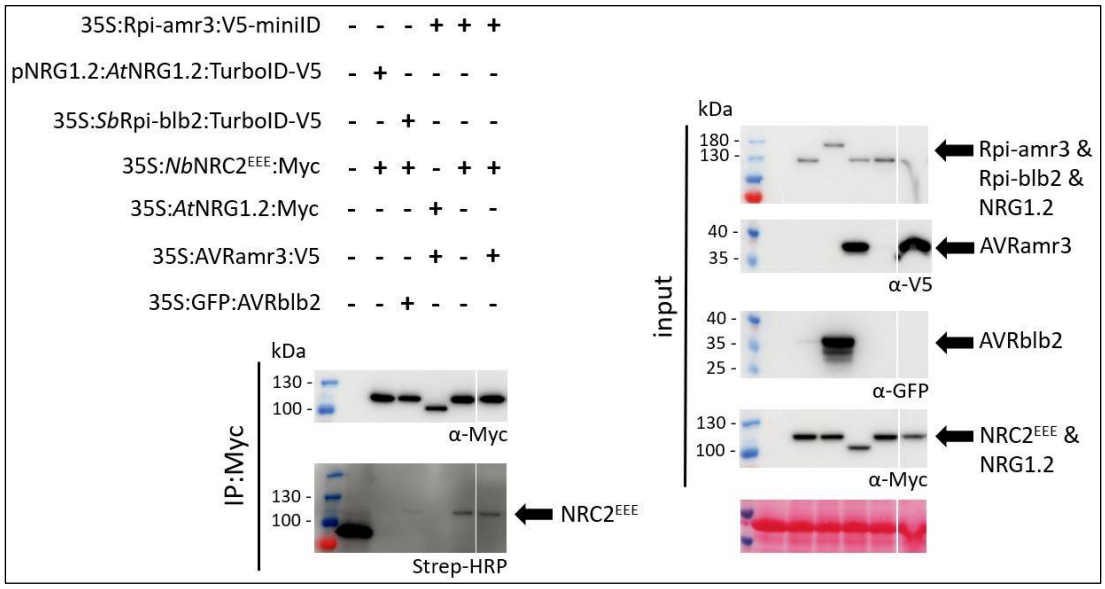


**Figure 6.2 Effector-independent biotinylation of *Nb*NRC2$^{EEE}$ by Rpi-amr3:V5-miniTurbo.**

IP and biotinylation of *Nb*NRC2$^{EEE}$:Myc by Rpi-amr3:V5-miniTurbo in *nrc2/3/4 N. benthamiana*. *At*NRG1.2:TurboID-V5, *Sb*Rpi-blb2:TurboID-V5, *At*NRG1.2:Myc were used as negative controls. *Agro*-infiltrations at $OD_{600}$ = 0.5 in 4-week-old *nrc2/3/4 N. benthamiana* leaves in the presence of p19. Biotin-infiltration (50 µM) at 3 dpi and for 30 min before tissue harvesting. IP was carried out with anti-Myc beads. Lysates were resolved by SDS-PAGE. Biotinylated proteins were detected by using HRP-conjugated streptavidin labelling. Images were cropped to facilitate understanding.

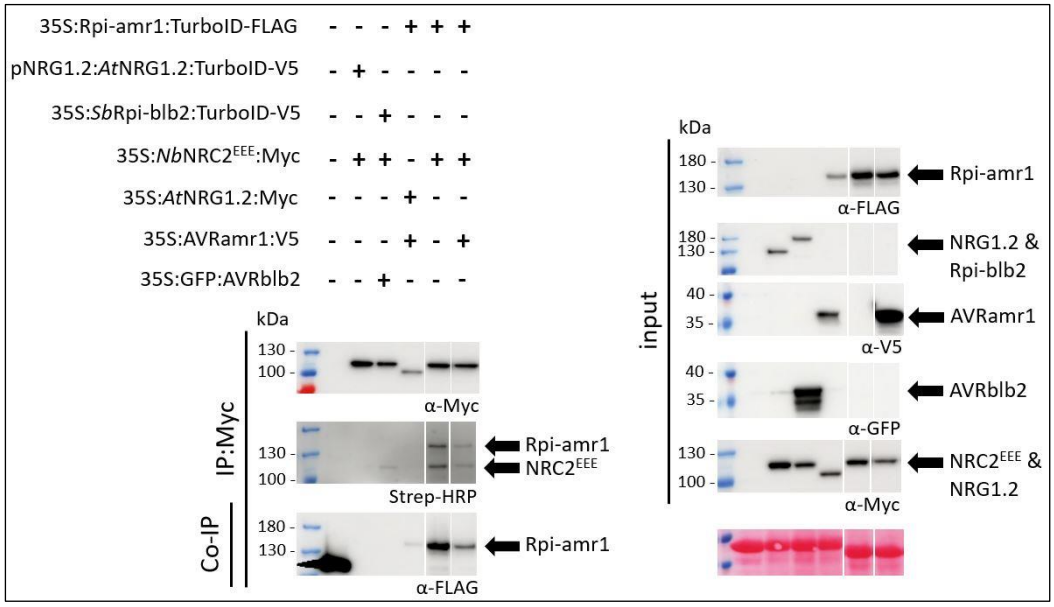


**Figure 6.3 Effector-independent biotinylation of *Nb*NRC2$^{EEE}$ by Rpi-amr1:TurboID-FLAG.**

IP and biotinylation of *Nb*NRC2$^{EEE}$:Myc by Rpi-amr1:TurboID-FLAG in *nrc2/3/4 N. benthamiana*. *At*NRG1.2:TurboID-V5, *Sb*Rpi-blb2:TurboID-V5 and *At*NRG1.2:Myc were used as negative controls. *Agro*-infiltrations at $OD_{600}$ = 0.5 in 4-week-old *nrc2/3/4 N. benthamiana* leaves in the presence of p19. Biotin-infiltration (50 µM) at 3 dpi and for 30 min before tissue harvesting. IP was carried out with anti-Myc beads. Lysates were resolved by SDS-PAGE. Biotinylated proteins were detected by using HRP-conjugated streptavidin labelling. Images were cropped to facilitate understanding.

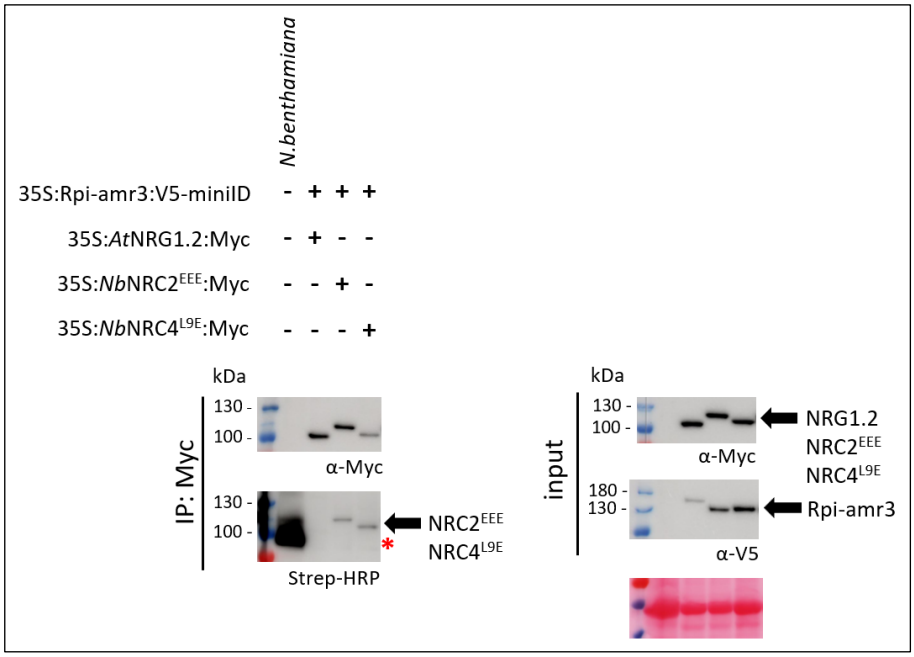


**Figure 6.4 Effector-independent biotinylation of *Nb*NRC4$^{L9E}$ by Rpi-amr3:V5-miniTurbo.**

IP and biotinylation of *Nb*NRC4$^{L9E}$:Myc by Rpi-amr3:V5-miniTurbo in *nrc2/3/4 N. benthamiana*. *At*NRG1.2:Myc was used as negative control. *Agro*-infiltrations at $OD_{600}$ = 0.5 in 4-week-old *nrc2/3/4 N. benthamiana* leaves in the presence of p19. Biotin-infiltration (50 µM) at 3 dpi and for 30 min before tissue harvesting. IP was carried out with anti-Myc beads. Lysates were resolved by SDS-PAGE. Biotinylated proteins were detected by using HRP-conjugated streptavidin labelling. Unspecific bands are indicated with a red asterisk (*).

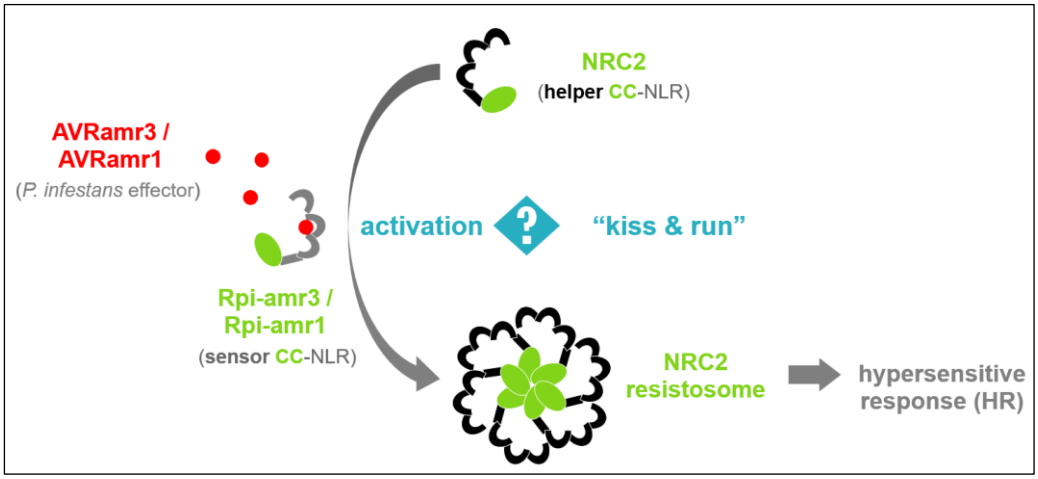


**Figure 6.5 Model for activation of NRC class helper NLRs upon detection of effectors by sensor CNLs.**

Recognition of AVRamr1 and AVRamr3 by Rpi-amr1 and Rpi-amr3, respectively, trigger the activation and oligomerization of NRC2. Sensor CNLs are not incorporated into the NRC2 oligomer, suggesting that NRCs transiently interact with sensor CNLs prior to resistosome formation. My data shows that NRCs consistently monitor sensor CNLs both before and after effector recognition and exhibit varying levels of affinity with their corresponding sensor CNLs.

For the time-course experiment, the *Pseudomonas syringae* DC3000(D36E) polymutant was used, which lacks all known bacterial type III secretion effector (T3E) genes (Bao et al., 2014). This mutant carried either an empty vector (D36E$^{EV}$) or the *P. infestans* effector AVRamr3 (D36E$^{AVRamr3}$), delivered from a pEDV construct (for effector detector vector) (Sohn et al., 2007). The pEDV construct contains the 136 amino acids that encode a type III secretion system (T3SS) and the AvrRps4 promoter. The assembled effector constructs were then transformed into the effector-less mutant *P. syringae* DC3000(D36E). These two strains were generated by my colleague, Dr. Maheen Alam. Three treatments were performed: mock ($MgCl_2$-infiltration), PTI alone (D36E$^{EV}$-infiltration) and PTI + ETI (D36E$^{AVRamr3}$-infiltration). Biotin labelling was performed at 0, 4, 6, 8 and 24 hours post mock- or D36E-infiltration, with a 30-minute labelling period before sample harvest (Figure 6.6 and Supplementary Figures 6.1, 6.2, 6.3). It is important to note that the biotin labelling at these different time points is not cumulative but corresponds to individual 30-minute labelling periods. After the initial trial (Supplementary Figures 6.1, 6.2, 6.3), only two time points were retained, 4 and 24 hours post mock- or D36E-infiltration (Figure 6.7). As expected, no change in the biotinylation pattern of NRC2$^{EEE}$ was observed in the mock-treated samples (Figure 6.7 and Supplementary Figure 6.1). In the PTI and PTI + ETI-treated samples, a significant reduction in the amount of biotinylated NRC2$^{EEE}$ was observed 6 hours post D36E-infiltration (Supplementary Figures 6.2 and 6.3). This reduction

persisted over time, despite an increase in the total amount of NRC2$^{EEE}$ present in the samples (Figure 6.7, Supplementary Figures 6.2 and 6.3). Therefore, fewer NRC2$^{EEE}$ proteins were found near Rpi-amr3 after D36E-infiltration, suggesting their dissociation from the sensor CNL. This dissociation is why the interaction is considered “transient”. Surprisingly, this phenomenon was also triggered by PTI alone.

Considering the apparent involvement of PTI in the dissociation between sensor and helper NLRs (Figure 6.7) and knowing that previous phosphoproteomic studies have identified numerous differentially phosphorylated proteins during PTI, we decided to test if NRC2 could be phosphorylated. Using the same experimental setup as in Figure 6.6, we found that NRC2$^{EEE}$ is indeed phosphorylated in a PTI-dependent manner following D36E-infiltration (Figure 6.8). Subsequently, the corresponding phosphorylation sites were identified by mass spectrometry (Figure 6.9). Phospho-variants of NRC2 are being generated to determine whether this post-translational modification could be involved in the association/dissociation between helper and sensor NLRs, and to what extent.

Intriguingly, one of these phosphorylated residues, S707, is located near some of the inositol-binding residues conserved among NRCs and identified in tomato NRC2 (Ma et al., 2024). When mutated, these residues have been shown to compromise or abolish the cell death induced by the coat protein of the potato virus X (PVX) in *N. benthamiana*, suggesting that inositol hexakisphosphate ($IP_6$) or inositol pentakisphosphate ($IP_5$) may function as cofactors of *Sl*NRC2 in recognizing activated Rx, potentially enhancing the interaction between *Sl*NRC2 and Rx (Ma et al., 2024). Notably, $IP_6$ has been shown to play a role in PTI, although its mode of action and targets in plant defense remain unknown (Murphy et al., 2008).

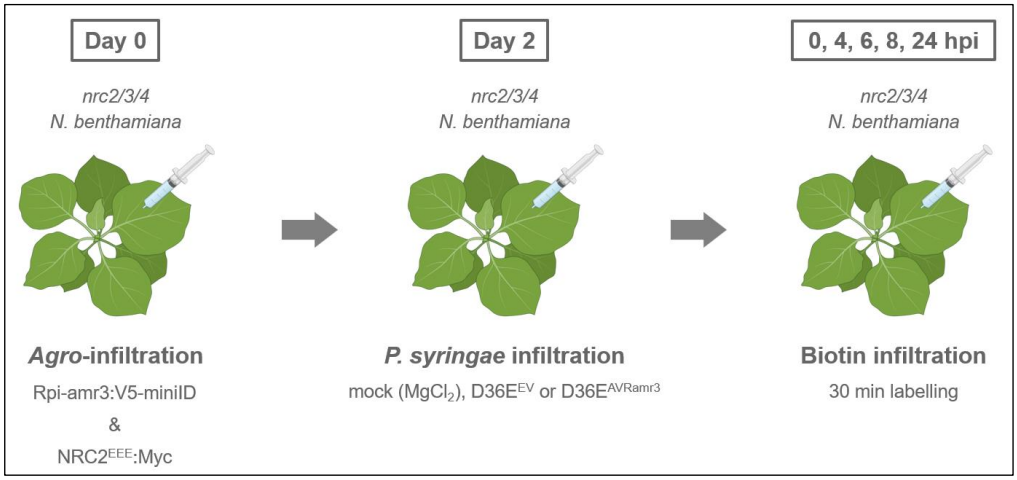


**Figure 6.6 Schematic representation of the experimental design used to capture the transient interaction between *Nb*NRC2$^{EEE}$ and Rpi-amr3.**

*Agro*-infiltrations of 35S:*Nb*NRC2$^{EEE}$:Myc and 35S:Rpi-amr3:V5-miniTurbo at $OD_{600}$ = 0.5 in 4-week-old *nrc234 N. benthamiana* and in the presence of p19, followed by *P. syringae* D36E$^{EV}$ or D36E$^{AVRamr3}$ infiltration at $OD_{600}$ = 0.2 two days later. The DC3000(D36E) polymutant lacks all known bacterial type III secretion effector (T3E) genes (Bao et al., 2014). Biotin-infiltration (50 µM) was performed at 0, 4, 6, 8 and 24 hours post *P. syringae* infiltration and for 30 min before tissue harvesting.

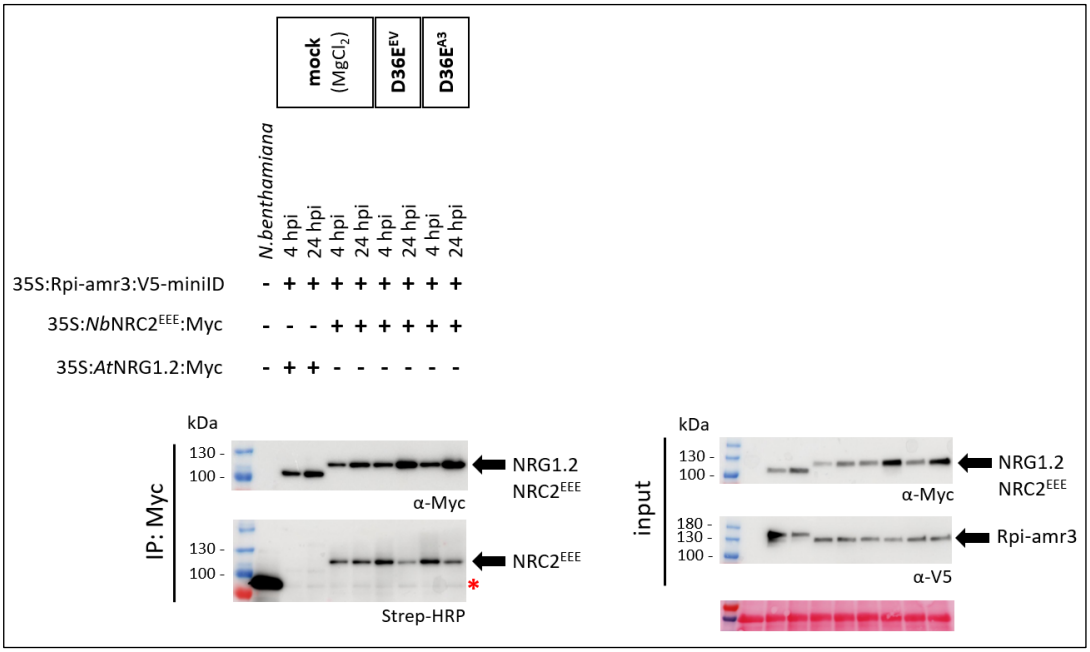


**Figure 6.7 PTI-dependent dissociation of *Nb*NRC2$^{EEE}$ from Rpi-amr3:V5-miniTurbo.**

IP and biotinylation of *Nb*NRC2$^{EEE}$:Myc by Rpi-amr3:V5-miniTurbo in *nrc2/3/4 N. benthamiana*. *Agro*-infiltrations at $OD_{600}$ = 0.5 in 4-week-old *nrc2/3/4 N. benthamiana* leaves in the presence of p19, followed by mock ($MgCl_2$), *P. syringae* D36E$^{EV}$ or D36E$^{AVRamr3}$ infiltration at $OD_{600}$ = 0.2 and two days post *Agro*-infiltration. *At*NRG1.2:Myc was used as negative control. Biotin-infiltration (50 µM) at 0, 4, 6, 8 and 24 hours post *P. syringae* infiltration and for 30 min before tissue harvesting. Only the 4 and 24 hour time points are shown here. IP was carried out with anti-Myc beads. Lysates were resolved by SDS-PAGE. Biotinylated proteins were detected by using HRP-conjugated streptavidin labelling. Unspecific bands are indicated with a red asterisk (*).

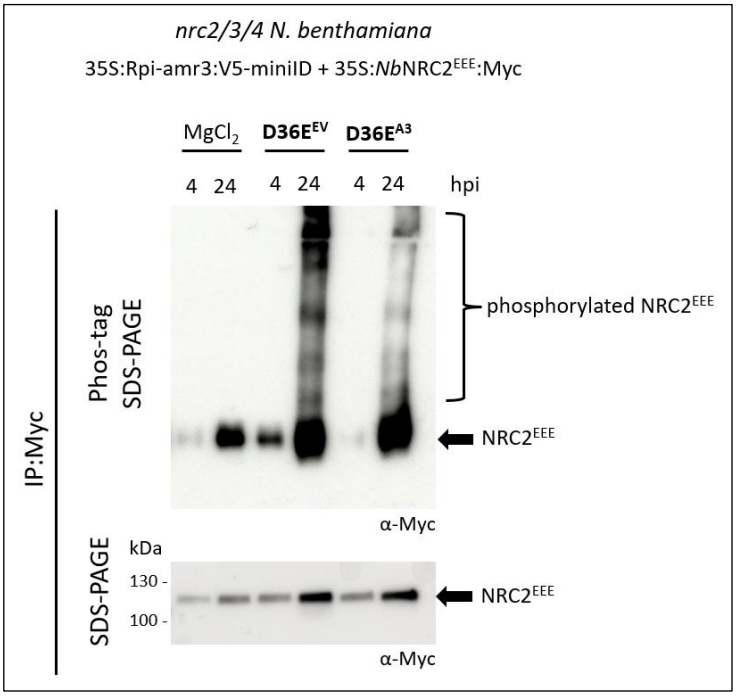


**Figure 6.8 PTI-dependent phosphorylation of *Nb*NRC2$^{EEE}$ – part 1.**

*P. syringae* D36E-induced phosphorylation patterns of *Nb*NRC2$^{EEE}$:Myc with Rpi-amr3:V5-miniTurbo in *nrc2/3/4 N. benthamiana*. *Agro*-infiltrations at $OD_{600}$ = 0.5 in 4-week-old *nrc2/3/4 N. benthamiana* leaves in the presence of p19, followed by *P. syringae* D36E$^{EV}$ or D36E$^{AVRamr3}$ infiltration at $OD_{600}$ = 0.2 and two days post *Agro*-infiltration. Tissues were harvested at 0, 4, 6, 8 and 24 hours post *P. syringae* infiltration. Only the 4 and 24 hour time points are shown here. IP was carried out with anti-Myc beads. Lysates were resolved by Phos-tag or regular SDS-PAGE. Upper and lower shifted bands were observed on Phos-tag SDS-PAGE corresponding to phosphorylated and unphosphorylated *Nb*NRC2$^{EEE}$ respectively. I prepared the samples and my colleague Renzo Villena Gaspar ran the Phos-tag gels.

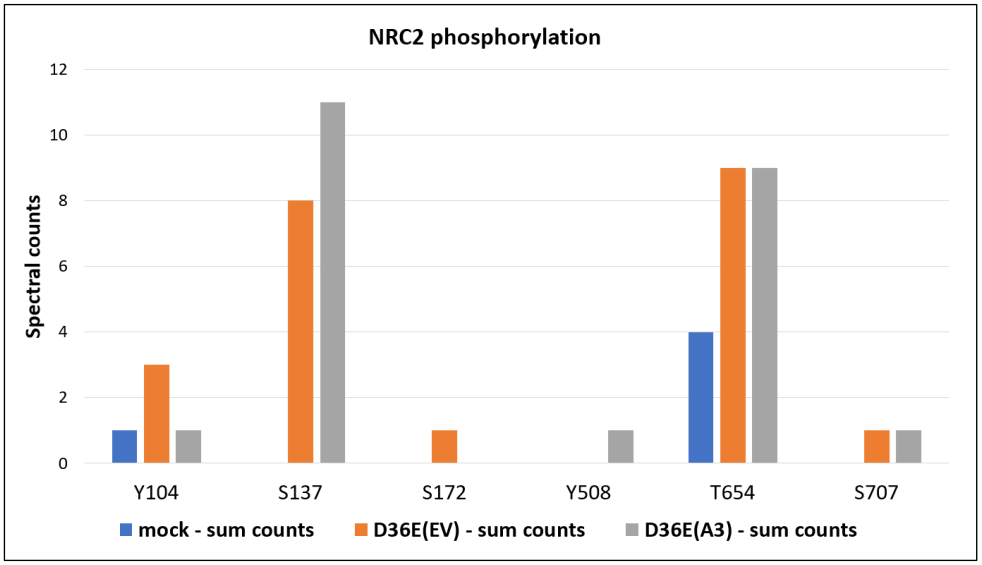


**Figure 6.9 PTI-dependent phosphorylation of *Nb*NRC2$^{EEE}$ – part 2.**

*P. syringae* D36E-induced phosphorylation sites of *Nb*NRC2$^{EEE}$:Myc with Rpi-amr3:V5-miniTurbo in *nrc2/3/4 N. benthamiana*. *Agro*-infiltrations at $OD_{600}$ = 0.5 in 4-week-old *nrc2/3/4 N. benthamiana* leaves, in the presence of p19. This was followed by *P. syringae* D36E$^{EV}$ or D36E$^{AVRamr3}$ infiltration at $OD_{600}$ = 0.2, two days post *Agro*-infiltration. Tissues were harvested at 8 hours post *P. syringae* infiltration. IP was carried out with anti-Myc beads. My colleague Renzo Villena Gaspar prepared the samples and sent them for MS analysis.

Finally, after demonstrating that helper NRCs dynamically interact with sensor NLRs in an effector-independent manner, we aimed to test whether NRC2$^{EEE}$, in the presence of multiple corresponding sensor CNLs, would preferentially associate with the effector-activated CNL and move toward its vicinity. This experiment serves as a competition assay for biotinylation (Figure 6.10). In this case, both Rpi-amr1 and Rpi-amr3 were expressed simultaneously in the presence of NRC2$^{EEE}$, with only Rpi-amr1 carrying TurboID. Either AVRamr1 or AVRamr3 was co-delivered to activate Rpi-amr1 or Rpi-amr3, respectively, with the knowledge that NRC2 supports both Rpi-amr1 and Rpi-amr3 in triggering cell death. Two days post infiltration, before NRC2 oligomer formation, biotin was infiltrated for 30 minutes. When AVRamr3 is co-delivered and activates Rpi-amr3, which does not carry TurboID, if NRC2$^{EEE}$ preferentially associates with the effector-activated CNLs, we would expect a decrease in the amount of NRC2$^{EEE}$ biotinylated by Rpi-amr1:TurboID (Figure 6.10). However, no difference in the amount of biotinylated NRC2$^{EEE}$ by Rpi-amr1:TurboID was observed when AVRamr3 was co-delivered, compared to when AVRamr1 was co-delivered (Figure 6.11). This result suggests that the available NRC2 proteins in the cells are equally distributed across their corresponding sensor NLRs. Furthermore, upon effector recognition, the recruitment of NRC2 to a given sensor NLR

remains unchanged. Additionally, it suggests that for NRC2 proteins to oligomerize, it is likely that only a few need to be activated by the sensor NLR, which can then recruit other non-activated NRC2 proteins to form oligomers. Thus, not every NRC2 protein within an oligomer needs to be activated by the sensor NLR.

I also generated a miniTurbo-tagged NRC2$^{EEE}$ and confirmed that it does not trigger HR (Supplementary Figure 6.4) but still maintains oligomer formation (Supplementary Figure 6.5). This construct could be used to further explore the mechanisms involved in the activation of NRC2 and to potentially identify the protein kinase responsible for the phosphorylation of NRC2.

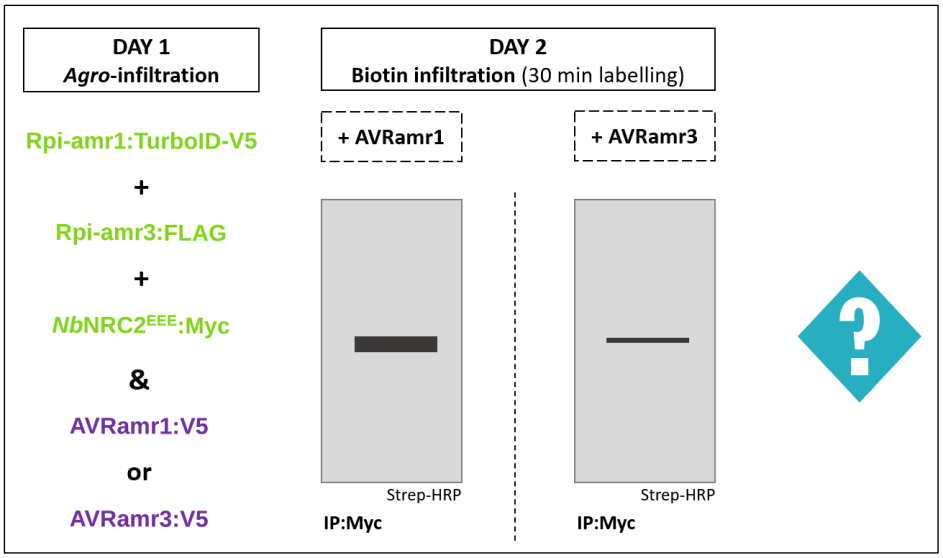


**Figure 6.10 Schematic representation of the experimental design used to test whether *Nb*NRC2$^{EEE}$ preferentially associates with effector-activated CNLs.**

Two CNLs, Rpi-amr1 and Rpi-amr3, are simultaneously expressed in the presence of *Nb*NRC2$^{EEE}$, but only Rpi-amr1 is tagged with TurboID. Either AVRamr1:V5 or AVRamr3:V5 is co-infiltrated to activate one of the two CNLs, Rpi-amr1 or Rpi-amr3, respectively. Two days later, biotin was infiltrated for 30 min before tissue harvesting. If *Nb*NRC2$^{EEE}$ preferentially associates with effector-activated CNLs, we would expect a decrease in the amount of *Nb*NRC2$^{EEE}$ biotinylated by Rpi-amr1 when Rpi-amr3 is activated.

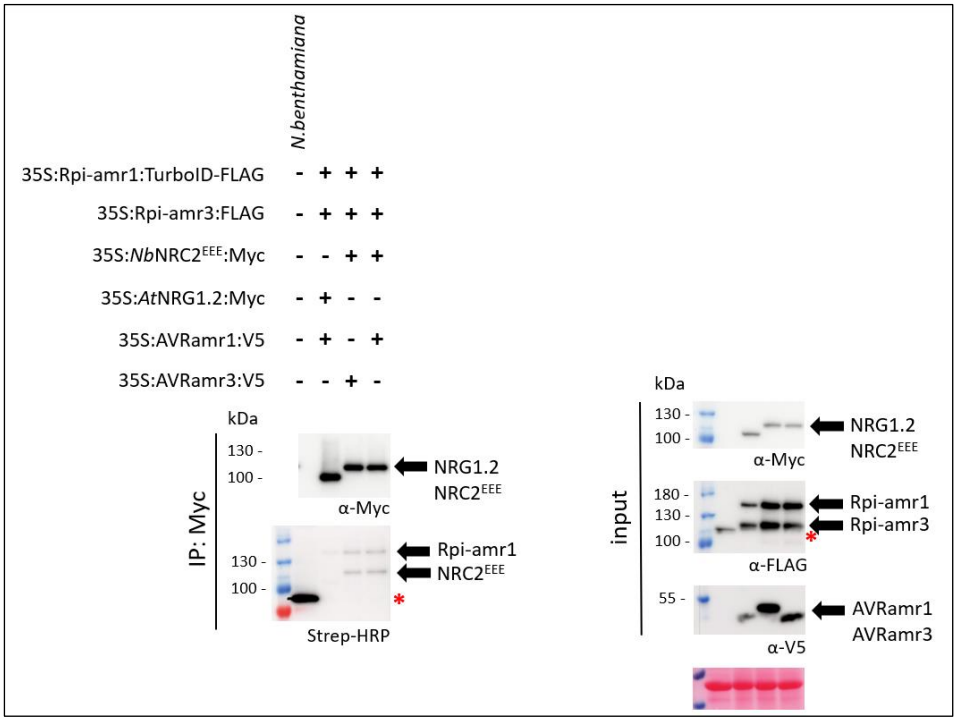


**Figure 6.11 *Nb*NRC2$^{EEE}$ does not preferentially associates with effector-activated CNLs.**

IP and biotinylation of *Nb*NRC2$^{EEE}$:Myc by Rpi-amr1:TurboID-V5 in the presence of Rpi-amr3:FLAG and AVRamr1:V5 or AVRamr3:V5 in *nrc2/3/4 N. benthamiana*. *At*NRG1.2:Myc was used as negative control. *Agro*-infiltrations at $OD_{600}$ = 0.5 in 4-week-old *nrc2/3/4 N. benthamiana* leaves in the presence of p19. Biotin-infiltration (50 µM) at 2 dpi and for 30 min before tissue harvesting. IP was carried out with anti-Myc beads. Lysates were resolved by SDS-PAGE. Biotinylated proteins were detected by using HRP-conjugated streptavidin labelling. Unspecific bands are indicated with a red asterisk (*).

## 6.3 Discussion

Compared to traditional affinity purification (AP) methods, the combination of TurboID and immunoprecipitation facilitated the detection of transient interactions between sensor NLRs and helper NRCs, offering valuable insights into the molecular mechanisms underlying their communication (Figures 6.2, 6.3 and 6.7).

AP techniques require that interacting partners remain stably bound throughout all biochemical steps of the protocol, including protein extraction, precipitation, washing, and isolation. In contrast, proximity labelling (PL) methods directly label interacting proteins within living cells. This process is

irreversible, eliminating the need to preserve the integrity of protein interactions during sample processing. Unlike AP, PL does not rely on the affinity of prey proteins for the bait protein, nor does it require the maintenance of protein complexes in their native state during affinity capture. Furthermore, the high affinity of biotinylated residues for streptavidin enables the capture of biotinylated proteins under harsh conditions, reducing the likelihood of non-specific or artefactual interactions that may occur during AP. Altogether, these advantages likely contributed to capturing the transient nature of the interaction between sensor NLRs and helper NRCs (Figures 6.2, 6.3 and 6.7).

NRC2 was found to directly interact with Rpi-amr1 and to come into proximity with Rpi-amr3 in an effector-independent manner (Figures 6.2 and 6.3), suggesting that a portion of the NRC2 proteins present in cells continuously communicates with or guards the conformational state of sensor NLRs, likely enabling the rapid activation of downstream immune responses upon detection of pathogen-triggered modifications. Interestingly, this PL approach allowed us to detect potentially different degrees of interaction affinities between sensor and helper NLRs. Indeed, Rpi-amr1 appeared to interact more stably with NRC2 than Rpi-amr3, as NRC2 was unintentionally co-immunoprecipitated with Rpi-amr1 but not with Rpi-amr3 (Figures 6.2 and 6.3). Moreover, *Nb*NRC2 was found to have a weak affinity for Rpi-blb2, even though *Nb*NRC2 does not support Rpi-blb2-mediated HR, only *Nb*NRC4 does (Figures 6.2 and 6.3). This cannot be solely explained by the possibility that TurboID is noisy, as NRG1.2, used as a negative control, was not biotinylated. This highlights that not every protein proximity necessarily translates into a biological output, and that protein-protein interactions are more complex than simply categorizing proteins as either interacting or not interacting. Instead, there is likely a gradient of interaction affinities, and a certain threshold of affinity and/or stability may need to be reached for the interaction to become biologically relevant.

In the bioRxiv paper of (Huang et al., 2024a), they used a modified version of *Nb*NRC3 that allows it to function with Rpi-blb2. Using TurboID, they found that Rpi-blb2 comes into the vicinity of this mutated *Nb*NRC3 in an AVRblb2-independent manner, which corresponds to our observations with *Nb*NRC2 and Rpi-amr1 and Rpi-amr3. They also claimed that this interaction is transient, as biotinylated Rpi-blb2 disappears 12 hours post AVRblb2 induction. However, this statement cannot be made, as under their experimental conditions, the disappearance of biotinylated Rpi-blb2 is also observed in the non-AVRblb2-induced samples, where it should have remained unchanged. In our time-course experiment, under mock conditions, the amount of biotinylated NRC2 remained the

same. A reduction in biotinylated NRC2 was observed only when defense responses were activated, either by PTI alone or by PTI plus ETI, even though the accumulation of NRC2 proteins within cells was at its maximum (Figure 6.7). This indicates that the affinity of this interaction decreased with immune activation, highlighting the transient nature of this interaction.

To our surprise, this reduction in biotinylated NRC2 was also triggered by PTI alone, which we did not expect, as PTI alone is supposedly not sufficient to trigger NRC2 oligomerization. This raises the question of how NRC2 distinguishes between PTI alone and PTI plus ETI. Moreover, this suggests that there might be another signal relayed by either sensor NLRs or other components to initiate NRC oligomerization, such as post-translational modifications like phosphorylation. Indeed, NRC2 was found to be phosphorylated in a PTI-dependent manner (Figures 6.8 and 6.9). Therefore, the detailed activation mechanisms of NRCs by sensor NLRs still needs further investigation. It would be interesting to conduct the biotinylation time-course experiment in an ETI-only setup to further dissect the interaction between sensor NLRs and helper NRCs.

An additional unanswered question is whether every single NRC2-forming oligomer needs to be activated by sensor NLRs, or if, once activated, NRC2 proteins can recruit other non-activated NRCs to oligomerize. If the first scenario is correct, we would expect to observe an increase in the amount of NRC2 proteins interacting with sensor NLRs at some point. However, in our time-course experiment, we did not detect any increase in the amount of biotinylated NRC2 proteins; it either remained unchanged or decreased (Supplementary Figures 6.1, 6.2, 6.3, Figure 6.7). Moreover, we might also expect that NRC2 would rush to effector-activated sensor NLRs to get activated and subsequently oligomerize. Yet, in the biotinylation competition assay, we again did not observe any change in the amount of biotinylated NRC2 proteins either towards or away from the effector-activated sensor NLR (Figure 6.11). All these observations suggest that the second scenario is more likely, where a fraction of the total NRC2 available is activated by sensor NLRs and can then recruit other non-activated NRCs for activation and oligomerization. This hypothesis would need to be further explored to differentiate between the two scenarios.

## 6.4 Supplementary figures

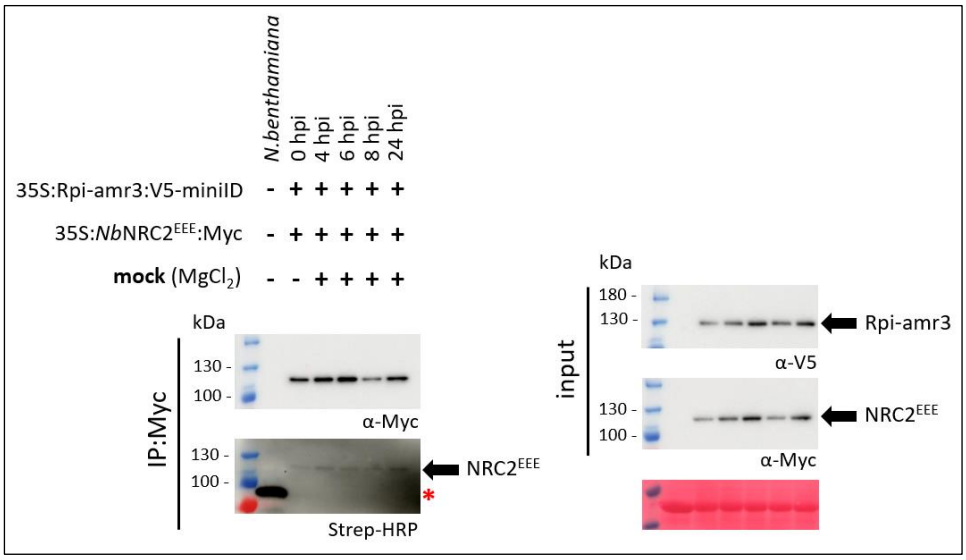


**Supplementary Figure 6-1 PTI-dependent dissociation of *Nb*NRC2$^{EEE}$ from Rpi-amr3:V5-miniTurbo – part 1.**

IP and biotinylation of *Nb*NRC2$^{EEE}$:Myc by Rpi-amr3:V5-miniTurbo in *nrc2/3/4 N. benthamiana*. *Agro*-infiltrations at $OD_{600}$ = 0.5 in 4-week-old *nrc2/3/4 N. benthamiana* leaves in the presence of p19, followed by mock ($MgCl_2$) infiltration two days post *Agro*-infiltration. Biotin-infiltration (50 µM) at 0, 4, 6, 8 and 24 hours post mock infiltration and for 30 min before tissue harvesting. IP was carried out with anti-Myc beads. Lysates were resolved by SDS-PAGE. Biotinylated proteins were detected by using HRP-conjugated streptavidin labelling. Unspecific bands are indicated with a red asterisk (*).

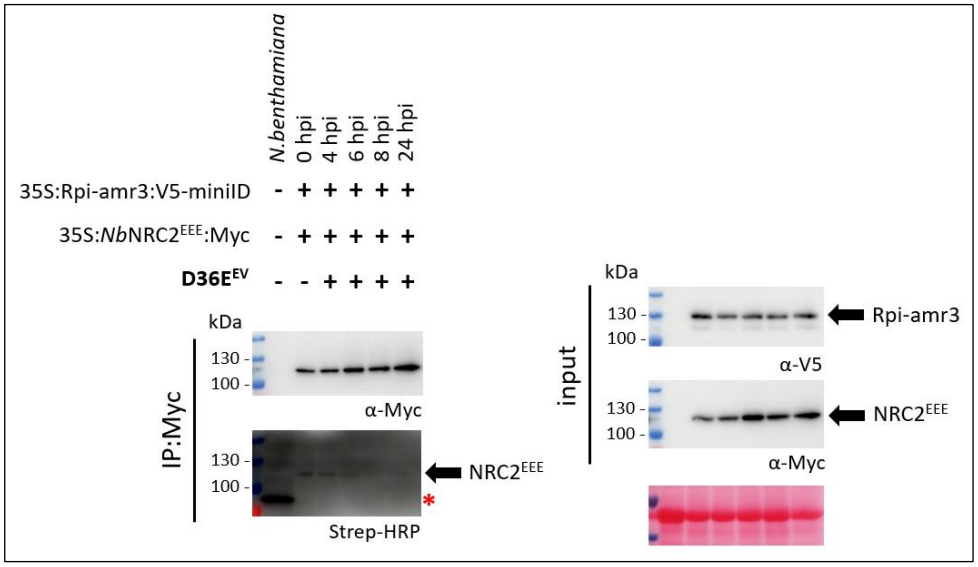


**Supplementary Figure 6-2 PTI-dependent dissociation of *Nb*NRC2$^{EEE}$ from Rpi-amr3:V5-miniTurbo – part 2.**

IP and biotinylation of *Nb*NRC2$^{EEE}$:Myc by Rpi-amr3:V5-miniTurbo in *nrc2/3/4 N. benthamiana*. *Agro*-infiltrations at $OD_{600}$ = 0.5 in 4-week-old *nrc2/3/4 N. benthamiana* leaves in the presence of p19, followed by *P. syringae* D36E$^{EV}$ infiltration at $OD_{600}$ = 0.2 and two days post *Agro*-infiltration. Biotin-infiltration (50 µM) at 0, 4, 6, 8 and 24 hours post *P. syringae* infiltration and for 30 min before tissue harvesting. IP was carried out with anti-Myc beads. Lysates were resolved by SDS-PAGE. Biotinylated proteins were detected by using HRP-conjugated streptavidin labelling. Unspecific bands are indicated with a red asterisk (*).

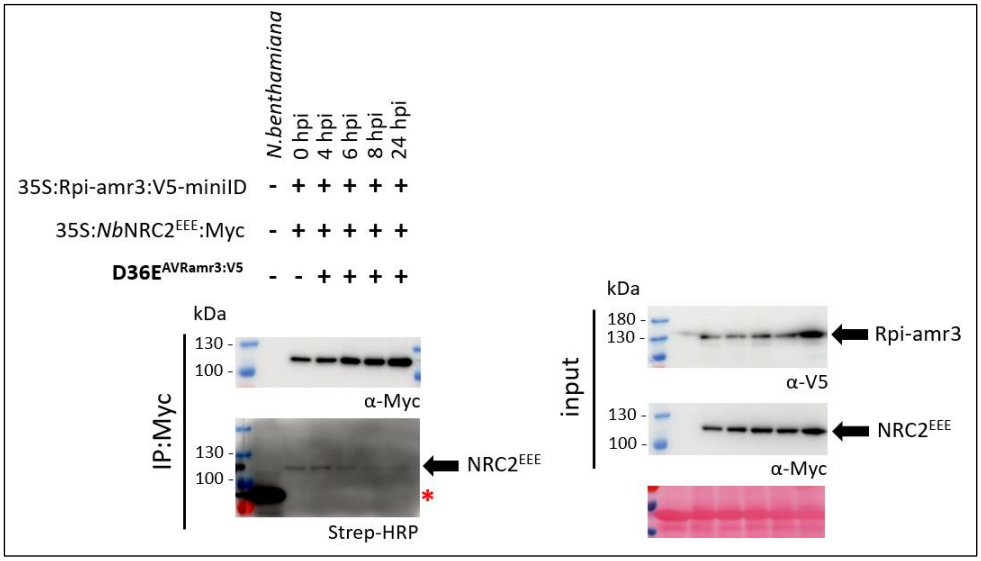


**Supplementary Figure 6-3 PTI-dependent dissociation of *Nb*NRC2$^{EEE}$ from Rpi-amr3:V5-miniTurbo – part 3.**

IP and biotinylation of *Nb*NRC2$^{EEE}$:Myc by Rpi-amr3:V5-miniTurbo in *nrc2/3/4 N. benthamiana*. *Agro*-infiltrations at $OD_{600}$ = 0.5 in 4-week-old *nrc2/3/4 N. benthamiana* leaves in the presence of p19, followed by *P. syringae* D36E$^{AVRamr3}$ infiltration at $OD_{600}$ = 0.2 and two days post *Agro*-infiltration. Biotin-infiltration (50 µM) at 0, 4, 6, 8 and 24 hours post *P. syringae* infiltration and for 30 min before tissue harvesting. IP was carried out with anti-Myc beads. Lysates were resolved by SDS-PAGE. Biotinylated proteins were detected by using HRP-conjugated streptavidin labelling. Unspecific bands are indicated with a red asterisk (*).

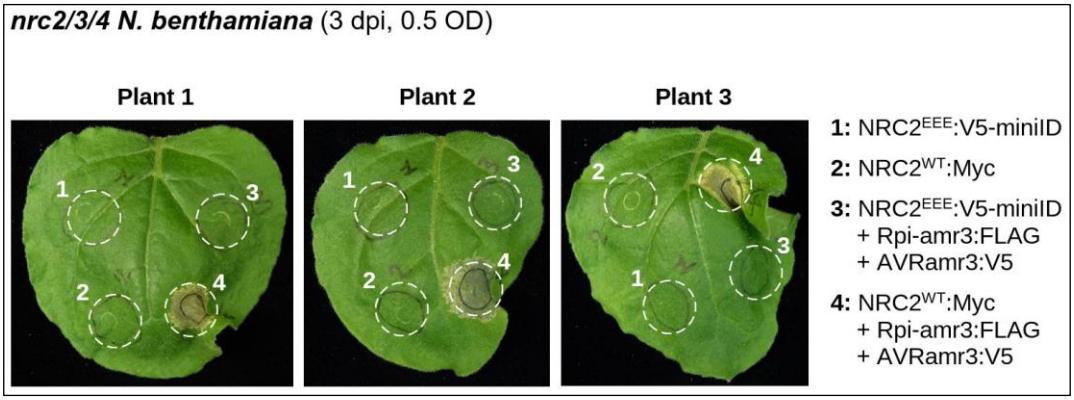


**Supplementary Figure 6-4 *Nb*NRC2$^{EEE}$:V5-miniTurbo does not trigger HR in *nrc2/3/4 N. benthamiana*.**

HR assays by *Agro*-infiltration at $OD_{600}$ = 0.5 in 4/5-week-old *nrc2/3/4 N. benthamiana* leaves and at 3 dpi. The *P. infestans* effector AVRamr3 is recognized by the *Solanum americanum* NLR protein Rpi-amr3 (Lin et al., 2022). The MADA motif mutant of NRC2 (NRC2$^{EEE}$) does not trigger HR but maintains oligomer formation (Ahn et al., 2023, Contreras et al., 2023). Co-delivery of 35S promoter-driven Rpi-amr3:FLAG and AVRamr3:V5 with *Nb*NRC2$^{WT}$:Myc triggers HR in *nrc2/3/4* mutant leaves but not with *Nb*NRC2$^{EEE}$:V5-miniTurbo (NRC2$^{EEE}$:V5-miniID).

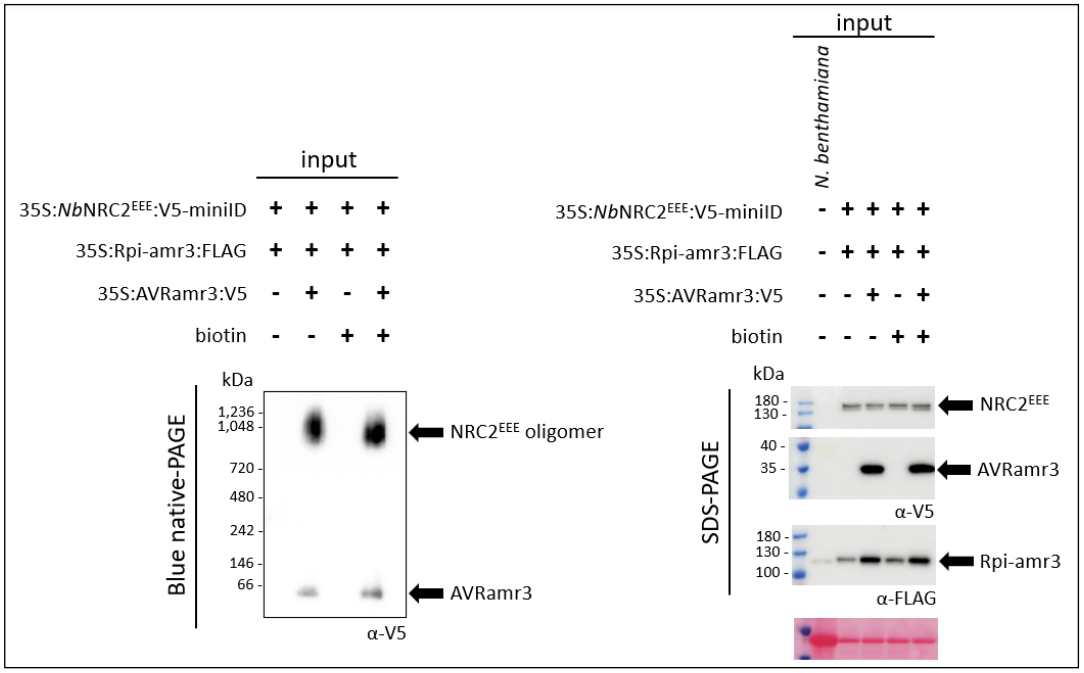


**Supplementary Figure 6-5 *Nb*NRC2$^{EEE}$:V5-miniTurbo oligomerizes upon effector detection by Rpi-amr3 in *nrc2/3/4 N. benthamiana*.**

Blue native-PAGE loading of protein extracts from *Agro*-infiltrated at $OD_{600}$ = 0.5 4/5-week-old *nrc2/3/4 N. benthamiana* leaves in the presence of p19 and harvested at 3 dpi. The *P. infestans* effector AVRamr3 is recognized by the *Solanum americanum* NLR protein Rpi-amr3 (Lin et al., 2022). The MADA motif mutant of NRC2 (NRC2$^{EEE}$) does not trigger HR but maintains oligomer formation (Ahn et al., 2023, Contreras et al., 2023). *Nb*NRC2$^{EEE}$:V5-miniTurbo oligomerizes upon effector-dependent activation of Rpi-amr3:FLAG in *nrc2/3/4* mutant leaves in the absence and presence of biotin (30 min labelling). SDS-boiled protein lysates serve as control for actual size of the different proteins.

# Chapter 7

## General discussion

# 7. General discussion

## 7.1 Future directions of this research

The identification of pathogen effectors and their interactions with host proteins is crucial for understanding plant-pathogen dynamics and developing disease resistance strategies. However, identifying a protein as an effector is a complex process that necessitates the use of various experimental techniques to determine its role in the pathogen's pathogenicity.

Firstly, genome sequencing and bioinformatics are used to sequence the pathogen's genome and identify genes encoding putative effector proteins that are homologous to known effectors. This is typically followed by mutagenesis studies, where knocking out the predicted *AVR* genes results in a reduced ability of the pathogen to infect and cause disease in plants, thereby confirming that the putative effector plays a critical role in pathogenicity. However, this approach is easier to achieve in bacteria or fungi that can be cultivated *ex planta* than in obligate pathogens, such as rusts, powdery mildews, or oomycete downy mildews. Functional screening can also assess whether the gene encoding the putative effector functions as an effector in plant systems, such as Arabidopsis or tobacco, by triggering HR. Additionally, sequence and structural analysis can identify conserved motifs associated with secretory pathways, suggesting that the putative effector may be injected into plant cells. Finally, confocal microscopy can be used to observe the localization of the effector within plant cells, further supporting its potential interaction with host proteins and indicating its role as a virulence factor. For example, the two bacterial effectors AvrRps4 from *Pseudomonas syringae* and PopP2 from *Ralstonia solanacearum* were identified based on their ability to trigger immune responses in Arabidopsis. AvrRps4 was identified for its ability to trigger a HR (Hinsch and Staskawicz, 1996), while PopP2 was identified through disruption analysis of candidate *AVR* genes (Deslandes et al., 2003). Recently, functional screening of effectors that activate immunity in resistant cultivars or wild relatives of crops has proven valuable for identifying immune receptors that can be incorporated into elite cultivars to confer disease resistance (Lin et al., 2023). However, a crucial foundation of this type of research is the accurate prediction of effector proteins. Additionally, these approaches are labour-intensive and time-consuming, as they typically require generating a library of cloned *AVR* genes or a series of disrupted *AVR* mutants and screening them individually for phenotypic changes.

Therefore, a longstanding challenge remains: how can we improve and accelerate the identification of effectors and their corresponding resistance proteins or host targets, and vice versa?

This work demonstrates that, after optimizing the TurboID protocol sufficiently, it is possible to capture native effectors *in vivo* using TurboID (Branon et al., 2018). I successfully detected two previously reported cognate effectors, AVRamr1 and AVRamr3, corresponding to the CNLs Rpi-amr1 and Rpi-amr3, respectively, by mass spectrometry (MS) under native infection conditions. Originally, these two *P. infestans* effectors were identified using traditional approaches, including cDNA pathogen enrichment sequencing for AVRamr1 (Lin et al., 2020), and screening of an RXLR effector library for AVRamr3 (Lin et al., 2022). Additionally, we identified two new cognate effectors, CCG14 and CCG41, both recognized by the same TNL, WRR4A. Previously, eight different CCG effectors were identified as being recognized by WRR4A through screening a CCG effector library, but these two newly identified effectors were not part of that screen and, therefore, were missed (Redkar et al., 2023). The interaction of these newly identified CCG effectors with TurboID-tagged WRR4A was predicted using AlphaFold, and their recognition by this TNL was validated by HR assay, demonstrating TurboID's ability to capture effectors in native settings (Chapters 3 and 4 of this thesis). The next step in confirming the direct interaction between these two CCG effectors and WRR4A would be to perform coimmunoprecipitation (Co-IP) experiments.

Through this same experimental pipeline, we identified another CCG effector, CCG82, which may interfere with EDS1-related signalling pathways. Specifically, although CCG82 was captured with TurboID-tagged EDS1, AlphaFold predicts that it primarily interacts with PAD4, one of the two lipase-like signalling partners of EDS1. Furthermore, the predicted interaction site between CCG82 and PAD4 precisely matches the binding site where ADR1 associates with PAD4 to activate downstream signalling events (Chapter 5 of this thesis). To confirm the potential interaction between CCG82 and PAD4, a Co-IP experiment could be conducted. Additionally, to assess whether CCG82 contributes to *Albugo candida* virulence, transgenic lines could be generated in wild-type Arabidopsis under both constitutive and inducible promoters. The expression of defense-related genes could then be evaluated, along with the associated bacterial growth phenotype.

Therefore, TurboID can be used for capturing effectors recognized by resistance proteins, as well as effectors potentially interfering with host defense hubs. In this study, we only TurboID-tagged the host proteins, which was particularly useful in the case of WRR4A, as it can recognize multiple

effectors (Redkar et al., 2023), enabling the discovery of new effectors. However, the reverse strategy can also be applied, where the effector itself is tagged with TurboID (Shi et al., 2023), allowing for the discovery of new host targets.

Finally, we tested the use of TurboID combined with immunoprecipitation (TurboID-directed IP) as an alternative to traditional Co-IP. Co-IP experiments often miss weak or transient interactions, and we anticipated that TurboID-directed IP might be more effective at detecting these types of interactions. Using this approach, we were able to detect the transient interaction between the helper *Nb*NRC2 and the sensor CNLs *Sa*Rpi-amr1 and *Sa*Rpi-amr3. To further characterize this dynamic interaction, we performed a time-course biotinylation assay and observed a reduction in biotinylated helper *Nb*NRC2 by the TurboID-tagged sensor *Sa*Rpi-amr3 over time post defense activation. This suggests a decrease in the affinity between these two partners, pointing toward an activation-and-release mechanism for helper NRC activation. Surprisingly, this phenomenon was observed under both PTI-alone and "PTI plus ETI" conditions, prompting us to test whether *Nb*NRC2 could be phosphorylated. Mass spectrometry analysis confirmed the phosphorylation of *Nb*NRC2, identifying several phospho-sites (Chapter 6 of this thesis). The corresponding *Nb*NRC2 phosphovariants are being generated, and it would be interesting to perform HR assays, verify oligomer formation, and conduct time-course biotinylation assays to investigate whether these phospho-sites are involved in oligomer formation and/or in regulating the interacting affinity between helper and sensor NLRs.

Therefore, TurboID-directed IP could serve as a complementary or alternative method for Co-IP when Co-IP fails to detect particularly challenging protein-protein interactions. In this context, TurboID-directed IP could aid investigate proteins involved in cell signalling pathways and enzyme-substrate interactions in the future. However, this TurboID-based approach does not replace traditional Co-IP methods; rather, it provides a different type of information. Indeed, TurboID and IP coupled with mass spectrometry (MS) were compared side by side, both techniques captured very different pools of interactors, highlighting the complementary nature of these two approaches (Moreira et al., 2023).

The main aim of this work was to explore the feasibility of capturing effectors under native infection conditions using TurboID, thereby establishing a foundation for future proximity labelling-based effector discovery. Bioinformatic pipelines and prediction software have significantly accelerated the

identification of putative effectors. The development of high-throughput functional assays, including machine-learning-based prediction tools and robotic implementations of molecular techniques, alongside lower-throughput methods such as QTL mapping, GWAS (Plissonneau et al., 2017), and TurboID (Shi et al., 2023), is poised to further enhance effector discovery and characterization. TurboID-based techniques, in particular, can improve our ability to identify or independently verify cognate effectors for *Resistance* genes, as demonstrated in Chapter 4, and susceptible host proteins or signalling hubs targeted by effectors, as explored in Chapter 5. This TurboID-based approach, when combined with artificial intelligence to predict effector-host protein interactions (Homma et al., 2023), could provide deeper insights into protein networks and their modulation by effectors. Understanding these interactions will not only enhance our mechanistic understanding of microbial pathogenesis but also open new avenues for the elucidation of effector-target interactions, offering significant potential for novel strategies in plant disease control and crop improvement.

## 7.2 Future applications of proximity labelling

Cellular activities are intricately controlled by proteins and nucleic acids, and their interactions. These interactions involve protein-protein, protein-RNA, and protein-DNA interactions. Methods that facilitate our understanding of molecular interactions on a large scale are essential for gaining deeper insights into biological processes and advancing efforts to improve plant disease resistance.

Conventional approaches like yeast two-hybrid (Y2H) and affinity purification (AP) have been widely used to discover molecular interactions. Y2H is a common method for mapping protein-protein interactions and can be high-throughput, enabling the screening of thousands of potential molecular interactions. AP, when combined with mass spectrometry (MS)-based proteomics, helps identify stable interacting partners of specific proteins of interest (POI) (Dunham et al., 2012). It can also be paired with crosslinking and nucleic acid sequencing techniques, such as chromatine immunoprecipitation sequencing (ChIP-seq) and RNA immunoprecipitation sequencing (RIP-seq), to study protein-nucleic acid interactions (Park, 2009). However, these methods often struggle to detect weak or transient PPIs, which may be lost during cell lysis and subsequent washing steps of AP. To address this, crosslinking is sometimes added to AP (Liu et al., 2015), although it can increase false positives. Additionally, AP is not always effective for studying less soluble targets, such as membrane-associated proteins.

Enzyme-catalyzed proximity labelling (PL) was developed as a complementary approach to traditional techniques (Seath et al., 2021). In PL, engineered enzymes like miniTurbo and TurboID are tagged to a POI (Branon et al., 2018). The enzyme converts a small-molecule substrate into a highly reactive species, such as an activated ester in the case of TurboID. The reactive species can then diffuse from the enzyme to covalently bond with neighbouring proteins, marking potential molecular partners (Figure 1.1 in Chapter 1). The spread of the reactive species depends on the lifetime of the reactive species and the concentration of quenchers, such as amines for TurboID, in the environment. The enzyme produces the highest concentration of reactants close to the enzyme, with decreasing levels further away from the source. Following MS analysis, a list of potential interactors can be generated. PL can detect transient PPIs, such as enzyme-substrate interactions, which are intrinsically transient due to substrate turnover, and can help dissect dynamic signalling pathways where upstream and downstream molecular partners interact transiently with the POI. Thus, PL is a powerful tool for capturing these types of interactions in native settings that were previously unexplored.

PL enzymes are commonly tagged to a POI and then use to “fish” for its molecular partners during a defined time window. Beyond the classic bait-prey paradigm, newer PL approaches have been developed to increase spatial and temporal specificity, including split PL enzymes (split-TurboID and Contact-ID), light-activated PL enzymes (LOV-Turbo), and combinations of different PL enzymes to track protein trafficking (TransitID). Split PL enzymes consist of two inactive fragments that can be reassembled into an active enzyme through PPIs or membrane apposition (Cho et al., 2020, Kwak et al., 2020). This approach allows for greater specificity in the targeting of biotinylated locations, but it has slower kinetics compared to full-length PL (Cho et al., 2020). Alternatively, LOV-Turbo combines TurboID with a light-oxygen-voltage (LOV) domain, a light-sensitive region that enables activation by light (Lee et al., 2023). Finally, TransitID combines multiple PL enzymes and can trace protein movement within cells (Qin et al., 2023). For example, TurboID and APEX2 were localized to different cellular compartments and stimulated with biotin to trigger TurboID-based labelling. One hour later, phenol alkyne probe and $H_2O_2$ were introduced to induce APEX2-based labelling. Proteins marked with both biotin and alkyne were then considered to have travelled between cellular locations.

PL can also be applied to investigate subcellular proteomes, as the function of proteins are influenced by their localization within the cell. Techniques like organelle-specific and cell-wide biochemical fractionation have been used to map proteomes of various cellular compartments

(Christopher et al., 2022, Geladaki et al., 2019). These methods usually rely on separating organelles based on their density, size, or membrane properties using multiple centrifugation or detergent steps. However, challenges such as contamination from non-target organelles, incomplete coverage or under-sampling, and inconsistent assignment of protein localization to subcellular fractions often arise. Moreover, separating membrane-less structures is particularly difficult using biochemical fractionation. PL, on the other hand, allows targeted labelling within a specific subcellular location, providing a more direct way to study protein composition in its native environment (Dionne and Gingras, 2022, Mair and Bergmann, 2022). This bypasses the need to preserve the integrity of organelles or subcellular structures during sample purification, as is required in biochemical fractionation methods. PL has been successfully used to map large-scale subcellular proteomes in human cells (Go et al., 2021), but similar approaches in plants remain largely unexplored (Mair et al., 2019). This opens new opportunities to investigate complex cellular compartments, such as membrane-less structures and other structures difficult to analyse with traditional methods.

PL can also be utilized to explore the specific functions of individual cell types, such as guard cells, various root cells, or bundle-sheath cells. Methods like laser capture microdissection, fluorescence-activated cell sorting (FACS) (Datta et al., 2015, Gallardo and Behra, 2013, Ohtsu et al., 2007), and mechanical separation coupled with sequential protoplast generation (Svozil et al., 2015), have been used for cell-type-specific proteome analysis. However, these methods are often labour-intensive and time-consuming to generate sufficient datasets. In contrast, PL enzymes can be expressed under cell-type-specific promoters, eliminating the need for extensive cell isolation and enabling high-throughput analysis of cell type-specific proteomes (Mair et al., 2019, Sun et al., 2022).

PL can also be combined with other cutting-edge techniques, like CRISPR, to study the protein-nucleic acid interactome. The integration of CRISPR and PL has proven useful for mapping local chromatin interactions comprehensively. Gene expression is regulated at specific genomic regions by the concerted action of various transcriptional regulatory proteins, which either activate or repress genes expression. A conventional method for studying these interactions is ChIP, but it is typically limited to analysing a single, pre-defined transcription factor in each experiment (Park, 2009). Chemical cross-linking, followed by precipitation of complementary DNA probes, has been used to directly analyse chromatin complexes; however, this method often suffers from the loss of cellular and chromatin context (Déjardin and Kingston, 2009). CaseID employs a nuclease-deficient dCas9 fused with a biotin ligase to target specific genomic regions, through single-guide RNAs

(sgRNAs), allowing for the biotinylation of nearby proteins (Schmidtmann et al., 2016). This approach could be adapted for plant systems to study regulatory elements of genes involved in plant immunity. A similar method, CRISPR-assisted RNA-protein interaction detection (CARPID), enables the study of RNA-protein interactions using CRISPR-CasRx-based targeting (Yi et al., 2020).

Furthermore, a novel platform called µMap (MicroMapping) has been introduced, which employs photocatalytic proximity labelling to map the protein microenvironment of small-molecule ligands with high spatiotemporal resolution (Trowbridge et al., 2022, West and Woo, 2023). Compared to enzyme-based methods, photo-proximity labelling offers tighter spatial resolutions, ranging from 50 nm to a few angstroms, depending on the half-life of the reactive substrate. This narrow labelling radius minimizes non-specific tagging, ensuring that only proteins directly bound to a target or in its immediate vicinity are detected, thereby enhancing the functional relevance of the results. The first implementation of µMap used iridium (Ir) photocatalysts, which, when exposed to blue light, convert diazirines into highly reactive carbenes with an extremely short half-life of about 1 nanosecond, due to rapid neutralization by water (Geri et al., 2020, Trowbridge et al., 2022). Carbene probes can crosslink with all amino acids, eliminating the sequence-specific labelling bias exhibited by other PL techniques. In the future, enzyme-based platforms like the foundational TurboID may evolve to incorporate photo-proximity labelling techniques (Tian et al., 2012).

While biotin ligases such as TurboID have been successfully used for *in vivo* proteomic mapping across various organisms, future improvements, like the use of non-biotin probes, could further reduce background interference and enhance the compatibility of PL *in vivo*. The continued development of more sophisticated PL technologies may expand the scope of discoveries and facilitate the resolution of more complex biological questions, such as determining the affinity, stoichiometry, and contact sites of molecular interactions. Meanwhile, AlphaFold's predictions can complement PL studies by prioritizing and refining identified PPIs, as demonstrated in Chapter 4 and 5, and by enabling the identification of potential interaction interfaces for further experimental validation (Homma et al., 2023).

In conclusion, it is reasonable to anticipate that, in the coming years, the scientific community will explore additional innovative uses of PL enzymes that have yet to be considered. In this work, by demonstrating the feasibility of capturing native effectors using PL, we propose a novel TurboID-based PL approach, which has not been explored before and has the potential to significantly

accelerate the identification of new effectors and their interacting host proteins. Ultimately, this could provide valuable insights into pathogen virulence by potentially defining the core set of effectors required for a microorganism to be pathogenic and thus revealing the key plant immune elements necessary for triggering defense mechanisms.

## Appendices

### Appendix 1: List of symbols and abbreviations

| | |
|---|---|
| ADR1 | activated disease resistance 1 |
| AP | affinity purification |
| APEX | ascorbate peroxidase |
| ATP | adenosine triphosphate |
| AVR | avirulence |
| bio-AMP | biotinyl-adenosine monophosphate |
| $Ca^{2+}$ | calcium |
| cDNA | complementary deoxyribonucleic acid |
| CNL | coiled-coil, nucleotide-binding, leucine-rich repeat |
| Co-IP | co-immunoprecipitation |
| CRISPR | clustered regularly interspaced short palindromic repeats |
| DM10 | double multi-parent advanced generation inter-cross 10 |
| dpi | days post infiltration/infection |
| EDS1 | enhanced disease susceptibility 1 |
| ETI | effector-triggered immunity |
| gDNA | genomic deoxyribonucleic acid |
| HELL | HeLo-like domain |
| $H_2O_2$ | hydrogen peroxide |
| *Hpa* | *Hyaloperonospora arabidopsidis* |
| hpi | hours post infiltration/infection |
| HR | hypersensitive response |
| ID | integrated domain |
| IP | immunoprecipitation |
| kDa | kiloDalton |
| LC-MS | liquid chromatography-mass spectrometry |
| MAGIC | multi-parent advanced generation inter-cross |
| MAMP | microbe-associated molecular pattern |
| MAPK | mitogen-activated protein kinase |
| MLKL | mixed-lineage kinase domain-like |
| MS | mass spectrometry |
| NB-ARC | nucleotide binding domain found in APAF1, R proteins and CED4 |
| NHR | non-host resistance |
| NLR | nucleotide-binding, leucine-rich repeat |
| NRC | NLR-required for cell death |
| NRG1 | N required gene 1 |
| $OD_{600}$ | optical density at a wavelength of 600 nm |

| | |
|---|---|
| PAD4 | phytoalexin deficient 4 |
| PAGE | SDS-polyacrylamide gel electrophoresis |
| PAMP | pathogen-associated molecular pattern |
| PL | proximity labelling |
| PPI | protein-protein interaction |
| PRR | pattern recognition receptor |
| PTI | pattern-triggered immunity |
| PTM | post-translational modification |
| RLK | receptor like-kinase |
| RLP | receptor like-protein |
| RNL | resistance to powdery mildew 8-like coiled-coil, nucleotide-binding, leucine-rich repeat |
| ROS | reactive oxygen species |
| SA | salicylic acid |
| SAG101 | senescence associated gene 101 |
| SAR | systemic acquired resistance |
| TNL | toll/interleukin-1 receptor/resistance, nucleotide-binding, leucine-rich repeat |
| T3SS | type-III secretion system |
| v/v | volume/volume |
| WT | wildtype |
| w/v | weight/volume |
| Y2H | yeast-two-hybrid |

**Appendix 2: List of primers**

| | |
|---|---|
| CMS3_EDS1_1F | ATGGCGTTTGAAGCTCTTACC |
| CMS3_EDS1_2F | TCCAGATGAGTTCGAAGGGG |
| CMS4_EDS1_1R | GAAGCGTAATCCACCACTTTC |
| CMS5_NRG1B_1F | ATGGTCGTGGTCGATTGGCT |
| CMS5_NRG1B_2F | TGCTTAAACTTGTTCATCTCGG |
| CMS5_NRG1B_3F | ACTTACTCCAGGACAACGGTT |
| CMS5_NRG1B_4F | GATGTCTCTAAAGCTCTATCGAAT |
| CMS6_NRG1B_1R | TCTGTTTCCTCCGTGTGAAC |
| CMS6_NRG1B_2R | TATTCCACTTCTCGACATGTGA |
| CMS7_PAD4_1F | ATGGACGATTGTCGATTCGAG |
| CMS7_PAD4_2F | CTCAATTTCACGATCACGTTTAG |
| CMS7_PAD4_4F | GCCACTCGACATTGCGAATTT |
| CMS7_PAD4_5F | ACTAATTAGTGAGTGAAACGTCAT |
| CMS8_PAD4_1R | CGCCTCCCACACACTATAAC |
| CMS8_PAD4_2R | CTGAAGAAAGAGTTTGAGTATGG |
| CMS9_SAG101_1F | ATGGAGTCTTCTTCTTCACTGT |
| CMS9_SAG101_2F | AGTATCGAACTACGGGAAGGT |
| CMS9_SAG101_3F | CCAAACGCTCAAGTCTGAGAA |

| | |
|---|---|
| CMS10_SAG101_1R | TACTTCCGGGTGTTCATAAAC |
| CMS10_SAG101_2R | AAACTTGTAGACCTGGATCATG |
| CMS25_mCherry_1F | ATCAAGGAGTTCATGCGCTTC |
| CMS28_ADR1-L1_1F | ATGGCCATCACCGATTTTTTC |
| CMS28_ADR1-L1_2F | GTCACTTTGAGAACCGGATTT |
| CMS28_ADR1-L1_3F | TGGATTGAGTTACATGATATAGATG |
| CMS28_ADR1-L1_4F | AAACCGGACTTGACGTGGCA |
| CMS29_ADR1-L1_1R | TTTGTATCTCCACGCCGTTG |
| CMS28_ADR1-L1_5F | AATGAAGACatAATGGCCATCACCGATTTTTT |
| CMS29_ADR1-L1_2R | ATTGTCTTCatGCAGAACAACATGCTGTGTC |
| CMS28_ADR1-L1_6F | AATGAAGACatCTGCGAGATCTAGCTCTTCA |
| CMS29_ADR1-L1_3R | ATTGTCTTCatCGAACCTTCGTCAAGCCAGTCTAG |
| CMS34_miniID_F | GAGCCCTGCTGCTGGAACAG |

## References


ADACHI, H., CONTRERAS, M. P., HARANT, A., WU, C. H., DEREVNINA, L., SAKAI, T., DUGGAN, C., MORATTO, E., BOZKURT, T. O., MAQBOOL, A., WIN, J. & KAMOUN, S. 2019a. An N-terminal motif in NLR immune receptors is functionally conserved across distantly related plant species. *Elife,* 8.

ADACHI, H., DEREVNINA, L. & KAMOUN, S. 2019b. NLR singletons, pairs, and networks: evolution, assembly, and regulation of the intracellular immunoreceptor circuitry of plants. *Current Opinion in Plant Biology,* 50**,** 121-131.

ADACHI, H., SAKAI, T., HARANT, A., PAI, H., HONDA, K., TOGHANI, A., CLAEYS, J., DUGGAN, C., BOZKURT, T. O., WU, C. H. & KAMOUN, S. 2023. An atypical NLR protein modulates the NRC immune receptor network in *Nicotiana benthamiana*. *Plos Genetics,* 19.

ADHIKARI, T. B., LIU, J. Q., MATHUR, S., WU, C. R. X. & RIMMER, S. R. 2003. Genetic and molecular analyses in crosses of race 2 and race 7 of *Albugo candida*. *Phytopathology,* 93**,** 959-965.

AHN, H. K., LIN, X., OLAVE-ACHURY, A. C., DEREVNINA, L., CONTRERAS, M. P., KOURELIS, J., WU, C. H., KAMOUN, S. & JONES, J. D. G. 2023. Effector-dependent activation and oligomerization of plant NRC class helper NLRs by sensor NLR immune receptors Rpi-amr3 and Rpi-amr1. *Embo Journal,* 42**,** 15.

ALBAN, C., JOB, D. & DOUCE, R. 2000. Biotin metabolism in plants. *Annual Review of Plant Physiology and Plant Molecular Biology,* 51**,** 17-47.

AMSELEM, J., CUOMO, C. A., VAN KAN, J. A. L., VIAUD, M., BENITO, E. P., COULOUX, A., COUTINHO, P. M., DE VRIES, R. P., DYER, P. S., FILLINGER, S., FOURNIER, E., GOUT, L., HAHN, M., KOHN, L. M., LAPALU, N., PLUMMER, K. M., PRADIER, J. M., QUÉVILLON, E., SHARON, A., SIMON, A., TEN HAVE, A., TUDZYNSKI, B., TUDZYNSKI, P., WINCKER, P., ANDREW, M., ANTHOUARD, V., BEEVER, R. E., BEFFA, R., BENOIT, I., BOUZID, O., BRAULT, B., CHEN, Z. H., CHOQUER, M., COLLÉMARE, J., COTTON, P., DANCHIN, E. G., DA SILVA, C., GAUTIER, A., GIRAUD, C., GIRAUD, T., GONZALEZ, C., GROSSETETE, S., GÜLDENER, U., HENRISSAT, B., HOWLETT, B. J., KODIRA, C., KRETSCHMER, M., LAPPARTIENT, A., LEROCH, M., LEVIS, C., MAUCELI, E., NEUVÉGLISE, C., OESER, B., PEARSON, M., POULAIN, J., POUSSEREAU, N., QUESNEVILLE, H., RASCLE, C., SCHUMACHER, J., SÉGURENS, B., SEXTON, A., SILVA, E., SIRVEN, C.,

SOANES, D. M., TALBOT, N. J., TEMPLETON, M., YANDAVA, C., YARDEN, O., ZENG, Q. D., ROLLINS, J. A., LEBRUN, M. H. & DICKMAN, M. 2011. Genomic Analysis of the Necrotrophic Fungal Pathogens *Sclerotinia sclerotiorum* and *Botrytis cinerea*. *Plos Genetics,* 7.

ANTONY, G., ZHOU, J. H., HUANG, S., LI, T., LIU, B., WHITE, F. & YANG, B. 2010. Rice *xa13* Recessive Resistance to Bacterial Blight Is Defeated by Induction of the Disease Susceptibility Gene Os-*11N3*. *Plant Cell,* 22**,** 3864-3876.

ARNOLD, D. L. & JACKSON, R. W. 2011. Bacterial genomes: evolution of pathogenicity. *Current Opinion in Plant Biology,* 14**,** 385-391.

ARORA, D., ABEL, N. B., LIU, C., VAN DAMME, P., YPERMAN, K., EECKHOUT, D., VU, L. D., WANG, J., TORNKVIST, A., IMPENS, F., KORBEI, B., VAN LEENE, J., GOOSSENS, A., DE JAEGER, G., OTT, T., MOSCHOU, P. N. & VAN DAMME, D. 2020. Establishment of Proximity-Dependent Biotinylation Approaches in Different Plant Model Systems. *Plant Cell,* 32**,** 3388-3407.

ASAI, S., FURZER, O. J., CEVIK, V., KIM, D. S., ISHAQUE, N., GORITSCHNIG, S., STASKAWICZ, B. J., SHIRASU, K. & JONES, J. D. G. 2018. A downy mildew effector evades recognition by polymorphism of expression and subcellular localization. *Nature Communications,* 9.

ASHIKAWA, I., HAYASHI, N., YAMANE, H., KANAMORI, H., WU, J. Z., MATSUMOTO, T., ONO, K. & YANO, M. 2008. Two Adjacent Nucleotide-Binding Site-Leucine-Rich Repeat Class Genes Are Required to Confer *Pikm*-Specific Rice Blast Resistance. *Genetics,* 180**,** 2267-2276.

ASSAAD, F. F., QIU, J. L., YOUNGS, H., EHRHARDT, D., ZIMMERLI, L., KALDE, M., WANNER, G., PECK, S. C., EDWARDS, H., RAMONELL, K., SOMERVILLE, C. R. & THORDAL-CHRISTENSEN, H. 2004. The PEN1 syntaxin defines a novel cellular compartment upon fungal attack and is required for the timely assembly of papillae. *Molecular Biology of the Cell,* 15**,** 5118-5129.

AXTELL, M. J. & STASKAWICZ, B. J. 2003. Initiation of RPS2-specified disease resistance in *Arabidopsis* is coupled to the AvrRpt2-directed elimination of RIN4. *Cell,* 112**,** 369-377.

BALDET, P., ALBAN, C., AXIOTIS, S. & DOUCE, R. 1993. Localization of free and bound biotin in cells from green pea leaves. *Archives of Biochemistry and Biophysics,* 303**,** 67-73.

BAO, Z. M., STODGHILL, P. V., MYERS, C. R., LAM, H., WEI, H. L., CHAKRAVARTHY, S., KVITKO, B. H., COLLMER, A., CARTINHOUR, S. W., SCHWEITZER, P. & SWINGLE, B. 2014. Genomic Plasticity Enables Phenotypic Variation of *Pseudomonas syringae* pv. *tomato* DC3000. *Plos One,* 9.

BELHAJ, K., CANO, L. M., PRINCE, D. C., KEMEN, A., YOSHIDA, K., DAGDAS, Y. F., ETHERINGTON, G. J., SCHOONBEEK, H. J., VAN ESSE, H. P., JONES, J. D. G., KAMOUN, S. & SCHORNACK, S. 2017. Arabidopsis late blight: infection of a nonhost plant by *Albugo laibachii* enables full colonization by *Phytophthora infestans*. *Cellular Microbiology,* 19.

BENTHAM, A. R., ZDRZALEK, R., DE LA CONCEPCION, J. C. & BANFIELD, M. J. 2018. Uncoiling CNLs: Structure/Function Approaches to Understanding CC Domain Function in Plant NLRs. *Plant and Cell Physiology,* 59**,** 2398-2408.

BERKA, M., KOPECKA, R., BERKOVA, V., BRZOBOHATY, B. & CERNY, M. 2022. Regulation of heat shock proteins 70 and their role in plant immunity. *Journal of Experimental Botany,* 73**,** 1894-1909.

BHAT, R. A., MIKLIS, M., SCHMELZER, E., SCHULZE-LEFERT, P. & PANSTRUGA, R. 2005. Recruitment and interaction dynamics of plant penetration resistance components in a plasma membrane microdomain. *Proceedings of the National Academy of Sciences of the United States of America,* 102**,** 3135-3140.

BHATTACHARJEE, S., HALANE, M. K., KIM, S. H. & GASSMANN, W. 2011. Pathogen Effectors Target *Arabidopsis* EDS1 and Alter Its Interactions with Immune Regulators. *Science,* 334**,** 1405-1408.

BI, G. Z., SU, M., LI, N., LIANG, Y., DANG, S., XU, J. C., HU, M. J., WANG, J. Z., ZOU, M. X., DENG, Y. A., LI, Q. Y., HUANG, S. J., LI, J. J., CHAI, J. J., HE, K. M., CHEN, Y. H. & ZHOU, J. M. 2021. The ZAR1 resistosome is a calcium-permeable channel triggering plant immune signaling. *Cell,* 184**,** 3528-+.

BI, G. Z. & ZHOU, J. M. 2017. MAP Kinase Signaling Pathways: A Hub of Plant-Microbe Interactions. *Cell Host & Microbe,* 21**,** 270-273.

BIERI, S., MAUCH, S., SHEN, Q. H., PEART, J., DEVOTO, A., CASAIS, C., CERON, F., SCHULZE, S., STEINBISS, H. H., SHIRASU, K. & SCHULZE-LEFERT, P. 2004. RAR1 positively controls steady state levels of barley MLA resistance proteins and enables sufficient MLA6 accumulation for effective resistance. *Plant Cell,* 16**,** 3480-3495.

BIGEARD, J., COLCOMBET, J. & HIRT, H. 2015. Signaling Mechanisms in Pattern-Triggered Immunity (PTI). *Molecular Plant,* 8**,** 521-539.

BIRCH, P. R. J., BOEVINK, P. C., GILROY, E. M., HEIN, I., PRITCHARD, L. & WHISSON, S. C. 2008. Oomycete RXLR effectors: delivery, functional redundancy and durable disease resistance. *Current Opinion in Plant Biology,* 11**,** 373-379.

BONARDI, V., TANG, S. J., STALLMANN, A., ROBERTS, M., CHERKIS, K. & DANGL, J. L. 2011. Expanded functions for a family of plant intracellular immune receptors beyond specific recognition of pathogen effectors. *Proceedings of the National Academy of Sciences of the United States of America,* 108**,** 16463-16468.

BORHAN, M. H., GUNN, N., COOPER, A., GULDEN, S., TÖR, M., RIMMER, S. R. & HOLUB, E. B. 2008. *WRR4* encodes a TIR-NB-LRR protein that confers broad-spectrum white rust resistance in *Arabidopsis thaliana* to four physiological races of *Albugo candida*. *Molecular Plant-Microbe Interactions,* 21**,** 757-768.

BORHAN, M. H., HOLUB, E. B., BEYNON, J. L., ROZWADOWSKI, K. & RIMMER, S. R. 2004. The Arabidopsis TIR-NB-LRR gene *RAC1* confers resistance to *Albugo candida* (white Rust) and is dependant on *EDS1* but not *PAD4*. *Molecular Plant-Microbe Interactions,* 17**,** 711-719.

BOTËR, M., AMIGUES, B., PEART, J., BREUER, C., KADOTA, Y., CASAIS, C., MOORE, G., KLEANTHOUS, C., OCHSENBEIN, F., SHIRASU, K. & GUEROIS, R. 2007. Structural and functional analysis of SGT1 reveals that its interaction with HSP90 is required for the accumulation of Rx, an R protein involved in plant immunity. *Plant Cell,* 19**,** 3791-3804.

BRANON, T. C., BOSCH, J. A., SANCHEZ, A. D., UDESHI, N. D., SVINKINA, T., CARR, S. A., FELDMAN, J. L., PERRIMON, N. & TING, A. Y. 2018. Efficient proximity labeling in living cells and organisms with TurboID. *Nature Biotechnology,* 36**,** 880-+.

BREEZE, E., VALE, V., MCLELLAN, H., PECRIX, Y., GODIARD, L., GRANT, M. & FRIGERIO, L. 2023. A tell tail sign: a conserved C-terminal tail-anchor domain targets a subset of pathogen effectors to the plant endoplasmic reticulum. *Journal of Experimental Botany,* 74**,** 3188-3202.

BUSTOS, R., CASTRILLO, G., LINHARES, F., PUGA, M. I., RUBIO, V., PÉREZ-PÉREZ, J., SOLANO, R., LEYVA, A. & PAZ-ARES, J. 2010. A Central Regulatory System Largely Controls Transcriptional Activation and Repression Responses to Phosphate Starvation in Arabidopsis. *Plos Genetics,* 6.

CAI, Z. Y., JITKAEW, S., ZHAO, J., CHIANG, H. C., CHOKSI, S., LIU, J., WARD, Y., WU, L. G. & LIU, Z. G. 2014. Plasma membrane translocation of trimerized MLKL protein is required for TNF-induced necroptosis. *Nature Cell Biology,* 16**,** 55-+.

CAO, Y., WEN, L. G., WANG, Z. & MA, L. G. 2015. SKIP Interacts with the Paf1 Complex to Regulate Flowering via the Activation of *FLC* Transcription in *Arabidopsis*. *Molecular Plant,* 8**,** 1816-1819.

CASTEL, B., FAIRHEAD, S., FURZER, O. J., REDKAR, A., WANG, S. S., CEVIK, V., HOLUB, E. B. & JONES, J. D. G. 2021. Evolutionary trade-offs at the Arabidopsis *WRR4A* resistance locus underpin alternate *Albugo candida* race recognition specificities. *Plant Journal,* 107**,** 1490-1502.

CASTEL, B., NGOU, P. M., CEVIK, V., REDKAR, A., KIM, D. S., YANG, Y., DING, P. T. & JONES, J. D. G. 2019. Diverse NLR immune receptors activate defence via the RPW8-NLR NRG1. *New Phytologist,* 222**,** 966-980.

CASTRILLO, G., TEIXEIRA, P., PAREDES, S. H., LAW, T. F., DE LORENZO, L., FELTCHER, M. E., FINKEL, O. M., BREAKFIELD, N. W., MIECZKOWSKI, P., JONES, C. D., PAZ-ARES, J. & DANGL, J. L. 2017. Root microbiota drive direct integration of phosphate stress and immunity. *Nature,* 543**,** 513-+.

CATANZARITI, A. M., DODDS, P. N. & ELLIS, J. G. 2007. Avirulence proteins from haustoria-forming pathogens. *Fems Microbiology Letters,* 269**,** 181-188.

CATANZARITI, A. M., DODDS, P. N., VE, T., KOBE, B., ELLIS, J. G. & STASKAWICZ, B. J. 2010. The AvrM Effector from Flax Rust Has a Structured C-Terminal Domain and Interacts Directly with the M Resistance Protein. *Molecular Plant-Microbe Interactions,* 23**,** 49-57.

CESARI, S., BERNOUX, M., MONCUQUET, P., KROJ, T. & DODDS, P. N. 2014. A novel conserved mechanism for plant NLR protein pairs: the "integrated decoy" hypothesis. *Frontiers in Plant Science,* 5.

CÉSARI, S., KANZAKI, H., FUJIWARA, T., BERNOUX, M., CHALVON, V., KAWANO, Y., SHIMAMOTO, K., DODDS, P., TERAUCHI, R. & KROJ, T. 2014. The NB-LRR proteins RGA4 and RGA5 interact functionally and physically to confer disease resistance. *Embo Journal,* 33**,** 1941-1959.

CESARI, S., THILLIEZ, G., RIBOT, C., CHALVON, V., MICHEL, C., JAUNEAU, A., RIVAS, S., ALAUX, L., KANZAKI, H., OKUYAMA, Y., MOREL, J. B., FOURNIER, E., THARREAU, D., TERAUCHI, R. & KROJ, T. 2013. The Rice Resistance Protein Pair RGA4/RGA5 Recognizes the *Magnaporthe oryzae* Effectors AVR-Pia and AVR1-CO39 by Direct Binding. *Plant Cell,* 25**,** 1463-1481.

CEVIK, V., BOUTROT, F., APEL, W., ROBERT-SEILANIANTZ, A., FURZER, O. J., REDKAR, A., CASTEL, B., KOVER, P. X., PRINCE, D. C., HOLUB, E. B. & JONES, J. D. G. 2019. Transgressive segregation reveals mechanisms of *Arabidopsis* immunity to *Brassica*-infecting races of white rust (*Albugo candida*). *Proceedings of the National Academy of Sciences of the United States of America,* 116**,** 2767-2773.

CHAKRABORTY, J., PRIYA, P., DASTIDAR, S. G. & DAS, S. 2018. Physical interaction between nuclear accumulated CC-NB-ARC-LRR protein and WRKY64 promotes EDS1 dependent *Fusarium* wilt resistance in chickpea. *Plant Science,* 276**,** 111-133.

CHEN, C. Y., LIU, Y. Q., SONG, W. M., CHEN, D. Y., CHEN, F. Y., CHEN, X. Y., CHEN, Z. W., GE, S. X., WANG, C. Z., ZHAN, S., CHEN, X. Y. & MAO, Y. B. 2019. An effector from cotton bollworm oral secretion impairs host plant defense signaling. *Proceedings of the National Academy of Sciences of the United States of America,* 116**,** 14331-14338.

CHEN, X., LI, W. J., REN, J. M., HUANG, D. L., HE, W. T., SONG, Y. L., YANG, C., LI, W. Y., ZHENG, X. R., CHEN, P. D. & HAN, J. H. 2014. Translocation of mixed lineage kinase domain-like protein to plasma membrane leads to necrotic cell death. *Cell Research,* 24**,** 105-121.

CHEN, Y. S., CHEN, L. Z., LUN, A. T. L., BALDONI, P. L. & SMYTH, G. K. 2025. edgeR v4: powerful differential analysis of sequencing data with expanded functionality and improved support for small counts and larger datasets. *Nucleic Acids Research,* 53.

CHENG, Y. T., LI, Y. Z., HUANG, S. A., HUANG, Y., DONG, X. N., ZHANG, Y. L. & LI, X. 2011. Stability of plant immune-receptor resistance proteins is controlled by SKP1-CULLIN1-F-box (SCF)-mediated protein degradation. *Proceedings of the National Academy of Sciences of the United States of America,* 108**,** 14694-14699.

CHO, K. F., BRANON, T. C., RAJEEV, S., SVINKINA, T., UDESHI, N. D., THOUDAM, T., KWAK, C., RHEE, H. W., LEE, I. K., CARR, S. A. & TING, A. Y. 2020. Split-TurboID enables contact-dependent proximity labeling in cells. *Proceedings of the National Academy of Sciences of the United States of America,* 117**,** 12143-12154.

CHOI-RHEE, E., SCHULMAN, H. & CRONAN, J. E. 2004. Promiscuous protein biotinylation by *Escherichia coli* biotin protein ligase. *Protein Science,* 13**,** 3043-3050.

CHOI, D. & PRIEST, M. J. 1995. A key to the genus Albugo. *Mycotaxon,* 53**,** 261-272.

CHOI, D. S., KIM, N. H. & HWANG, B. K. 2015. The pepper phosphoenolpyruvate carboxykinase CaPEPCK1 is involved in plant immunity against bacterial and oomycete pathogens. *Plant Molecular Biology,* 89**,** 99-111.

CHOI, Y. J., SHIN, H. D. & THINES, M. 2009. The host range of *Albugo candida* extends from Brassicaceae through Cleomaceae to Capparaceae. *Mycological Progress,* 8**,** 329-335.

CHOU, S., KRASILEVA, K. V., HOLTON, J. M., STEINBRENNER, A. D., ALBER, T. & STASKAWICZ, B. J. 2011. *Hyaloperonospora arabidopsidis* ATR1 effector is a repeat protein with distributed recognition surfaces. *Proceedings of the National Academy of Sciences of the United States of America,* 108**,** 13323-13328.

CHRISTOPHER, J. A., GELADAKI, A., DAWSON, C. S., VENNARD, O. L. & LILLEY, K. S. 2022. Subcellular Transcriptomics and Proteomics: A Comparative Methods Review. *Molecular & Cellular Proteomics,* 21.

CHU, F. X., THORNTON, D. T. & NGUYEN, H. T. 2018. Chemical cross-linking in the structural analysis of protein assemblies. *Methods,* 144**,** 53-63.

CHUA, X. E. Y., ABALLO, T., ELNEMER, W., TRAN, M. & SALOMON, A. 2021. Quantitative Interactomics of Lck-TurboID in Living Human T Cells Unveils T Cell Receptor Stimulation-Induced Proximal Lck Interactors. *Journal of Proteome Research,* 20**,** 715-726.

CONLAN, B., STOLL, T., GORMAN, J. J., SAUR, I. & RATHJEN, J. P. 2018. Development of a Rapid *in planta* BioID System as a Probe for Plasma Membrane-Associated Immunity Proteins. *Frontiers in Plant Science,* 9.

CONTRERAS, M. P., LÜDKE, D., PAI, H., TOGHANI, A. & KAMOUN, S. 2023a. NLR receptors in plant immunity: making sense of the alphabet soup. *Embo Reports,* 24.

CONTRERAS, M. P., PAI, H., THOMPSON, R., MARCHAL, C., CLAEYS, J., ADACHI, H. & KAMOUN, S. 2024. The nucleotide-binding domain of NRC-dependent disease resistance proteins is sufficient to activate downstream helper NLR oligomerization and immune signaling. *New Phytologist,* 243**,** 345-361.

CONTRERAS, M. P., PAI, H., TUMTAS, Y., DUGGAN, C., YUEN, E. L. H., CRUCES, A. V., KOURELIS, J., AHN, H. K., LEE, K. T., WU, C. H., BOZKURT, T. O., DEREVNINA, L. & KAMOUN, S. 2023b. Sensor NLR immune proteins activate oligomerization of their NRC helpers in response to plant pathogens. *Embo Journal,* 42.

COOPER, A. J., LATUNDE-DADA, A. O., WOODS-TÖR, A., LYNN, J., LUCAS, J. A., CRUTE, I. R. & HOLUB, E. B. 2008. Basic compatibility of *Albugo candida* in *Arabidopsis thaliana* and *Brassica juncea* causes broad-spectrum suppression of innate immunity. *Molecular Plant-Microbe Interactions,* 21**,** 745-756.

COURBIER, S. 2021. HOPping to defense: HOP3 contributes to plant immunity via the regulation of jasmonic acid signaling. *Plant Physiology,* 187**,** 1278-1280.

CUI, H. T., GOBBATO, E., KRACHER, B., QIU, J. D., BAUTOR, J. & PARKER, J. E. 2017. A core function of EDS1 with PAD4 is to protect the salicylic acid defense sector in Arabidopsis immunity. *New Phytologist,* 213**,** 1802-1817.

CUI, H. T., TSUDA, K. & PARKER, J. E. 2015. Effector-Triggered Immunity: From Pathogen Perception to Robust Defense. *In:* MERCHANT, S. S. (ed.) *Annual Review of Plant Biology, Vol 66.*

CUNNAC, S., LINDEBERG, M. & COLLMER, A. 2009. *Pseudomonas syringae* type III secretion system effectors: repertoires in search of functions. *Current Opinion in Microbiology,* 12**,** 53-60.

CUOMO, C. A., GUELDENER, U., XU, J. R., TRAIL, F., TURGEON, B. G., DI PIETRO, A., WALTON, J. D., MA, L. J., BAKER, S. E., REP, M., ADAM, G., ANTONIW, J., BALDWIN, T., CALVO, S., CHANG, Y. L., DECAPRIO, D., GALE, L. R., GNERRE, S., GOSWAMI, R. S., HAMMOND-KOSACK, K., HARRIS, L. J., HILBURN, K., KENNELL, J. C., KROKEN, S., MAGNUSON, J. K., MANNHAUPT, G., MAUCELI, E., MEWES, H. W., MITTERBAUER, R., MUEHLBAUER, G., MÜNSTERKÖTTER, M., NELSON, D., O'DONNELL, K., OUELLET, T., QI, W. H., QUESNEVILLE, H., RONCERO, M. I. G., SEONG, K. Y., TETKO, I. V., URBAN, M., WAALWIJK, C., WARD, T. J., YAO, J. Q., BIRREN, B. W. & KISTLER, H. C. 2007. The *Fusarium graminearum* genome reveals a link between localized polymorphism and pathogen specialization. *Science,* 317**,** 1400-1402.

DANGL, J. L. & JONES, J. D. G. 2001. Plant pathogens and integrated defence responses to infection. *Nature,* 411**,** 826-833.

DASKALOV, A., HABENSTEIN, B., SABATÉ, R., BERBON, M., MARTINEZ, D., CHAIGNEPAIN, S., COULARY-SALIN, B., HOFMANN, K., LOQUET, A. & SAUPE, S. J. 2016. Identification of a novel cell death-inducing domain

reveals that fungal amyloid-controlled programmed cell death is related to necroptosis. *Proceedings of the National Academy of Sciences of the United States of America,* 113**,** 2720-2725.

DATTA, S., MALHOTRA, L., DICKERSON, R., CHAFFEE, S., SEN, C. K. & ROY, S. 2015. Laser capture microdissection: Big data from small samples. *Histology and Histopathology,* 30**,** 1255-1269.

DEAN, R. A., TALBOT, N. J., EBBOLE, D. J., FARMAN, M. L., MITCHELL, T. K., ORBACH, M. J., THON, M., KULKARNI, R., XU, J. R., PAN, H. Q., READ, N. D., LEE, Y. H., CARBONE, I., BROWN, D., OH, Y. Y., DONOFRIO, N., JEONG, J. S., SOANES, D. M., DJONOVIC, S., KOLOMIETS, E., REHMEYER, C., LI, W. X., HARDING, M., KIM, S., LEBRUN, M. H., BOHNERT, H., COUGHLAN, S., BUTLER, J., CALVO, S., MA, L. J., NICOL, R., PURCELL, S., NUSBAUM, C., GALAGAN, J. E. & BIRREN, B. W. 2005. The genome sequence of the rice blast fungus *Magnaporthe grisea*. *Nature,* 434**,** 980-986.

DÉJARDIN, J. & KINGSTON, R. E. 2009. Purification of Proteins Associated with Specific Genomic Loci. *Cell,* 136**,** 175-186.

DEREVNINA, L., CONTRERAS, M. P., ADACHI, H., UPSON, J., CRUCES, A. V., XIE, R. R., SKLENAR, J., MENKE, F. L. H., MUGFORD, S. T., MACLEAN, D., MA, W. B., HOGENHOUT, S., GOVERSE, A., MAQBOOL, A., WU, C. H. & KAMOUN, S. 2021. Plant pathogens convergently evolved to counteract redundant nodes of an NLR immune receptor network. *Plos Biology,* 19.

DESLANDES, L., OLIVIER, J., PEETERS, N., FENG, D. X., KHOUNLOTHAM, M., BOUCHER, C., SOMSSICH, I., GENIN, S. & MARCO, Y. 2003. Physical interaction between RRS1-R, a protein conferring resistance to bacterial wilt, and PopP2, a type III effector targeted to the plant nucleus. *Proceedings of the National Academy of Sciences of the United States of America,* 100**,** 8024-8029.

DINDAS, J., DEFALCO, T. A., YU, G., ZHANG, L., DAVID, P., BJORNSON, M., THIBAUD, M. C., CUSTÓDIO, V., CASTRILLO, G., NUSSAUME, L., MACHO, A. P. & ZIPFEL, C. 2022. Direct inhibition of phosphate transport by immune signaling in *Arabidopsis*. *Current Biology,* 32**,** 488-+.

DIONNE, U. & GINGRAS, A. C. 2022. Proximity-Dependent Biotinylation Approaches to Explore the Dynamic Compartmentalized Proteome. *Frontiers in Molecular Biosciences,* 9.

DODDS, P. N. & RATHJEN, J. P. 2010. Plant immunity: towards an integrated view of plant-pathogen interactions. *Nature Reviews Genetics,* 11**,** 539-548.

DOEHLEMANN, G., WAHL, R., HORST, R. J., VOLL, L. M., USADEL, B., POREE, F., STITT, M., PONS-KÜHNEMANN, J., SONNEWALD, U., KAHMANN, R. & KÄMPER, J. 2008. Reprogramming a maize plant: transcriptional and metabolic changes induced by the fungal biotroph *Ustilago maydis*. *Plant Journal,* 56**,** 181-195.

DONG, O. X., TONG, M. X. Z., BONARDI, V., EL KASMI, F., WOLOSHEN, V., WÜNSCH, L. K., DANGL, J. L. & LI, X. 2016. TNL-mediated immunity in *Arabidopsis* requires complex regulation of the redundant *ADR1* gene family. *New Phytologist,* 210**,** 960-973.

DONG, S. M., STAM, R., CANO, L. M., SONG, J., SKLENAR, J., YOSHIDA, K., BOZKURT, T. O., OLIVA, R., LIU, Z. Y., TIAN, M. Y., WIN, J., BANFIELD, M. J., JONES, A. M. E., VAN DER HOORN, R. A. L. & KAMOUN, S. 2014. Effector Specialization in a Lineage of the Irish Potato Famine Pathogen. *Science,* 343**,** 552-555.

DONGUS, J. A., BHANDARI, D. D., PENNER, E., LAPIN, D., STOLZE, S. C., HARZEN, A., PATEL, M., ARCHER, L., DIJKGRAAF, L., SHAH, J. T., NAKAGAMI, H. & PARKER, J. E. 2022. Cavity surface residues of PAD4 and SAG101 contribute to EDS1 dimer signaling specificity in plant immunity. *Plant Journal,* 110**,** 1415-1432.

DUGGAN, C., MORATTO, E., SAVAGE, Z., HAMILTON, E., ADACHI, H., WU, C. H., LEARY, A. Y., TUMTAS, Y., ROTHERY, S. M., MAQBOOL, A., NOHUT, S., MARTIN, T. R., KAMOUN, S. & BOZKURT, T. O. 2021. Dynamic localization of a helper NLR at the plant-pathogen interface underpins pathogen recognition. *Proceedings of the National Academy of Sciences of the United States of America,* 118.

DUNHAM, W. H., MULLIN, M. & GINGRAS, A. C. 2012. Affinity-purification coupled to mass spectrometry: Basic principles and strategies. *Proteomics,* 12**,** 1576-1590.

DUPLAN, V. & RIVAS, S. 2014. E3 ubiquitin-ligases and their target proteins during the regulation of plant innate immunity. *Frontiers in Plant Science,* 5.

EISENACH, C., BAETZ, U., HUCK, N. V., ZHANG, J. B., DE ANGELI, A., BECKERS, G. J. M. & MARTINOIA, E. 2017. ABA-Induced Stomatal Closure Involves ALMT4, a Phosphorylation-Dependent Vacuolar Anion Channel of Arabidopsis. *Plant Cell,* 29**,** 2552-2569.

ENGLER, C., KANDZIA, R. & MARILLONNET, S. 2008. A One Pot, One Step, Precision Cloning Method with High Throughput Capability. *Plos One,* 3.

FALK, A., FEYS, B. J., FROST, L. N., JONES, J. D. G., DANIELS, M. J. & PARKER, J. E. 1999. *EDS1*, an essential component of *R* gene-mediated disease resistance in *Arabidopsis* has homology to eukaryotic lipases. *Proceedings of the National Academy of Sciences of the United States of America,* 96**,** 3292-3297.

FEEHAN, J. M., CASTEL, B., BENTHAM, A. R. & JONES, J. D. G. 2020. Plant NLRs get by with a little help from their friends. *Current Opinion in Plant Biology,* 56**,** 99-108.

FEEHAN, J. M., WANG, J. L., SUN, X. H., CHOI, J., AHN, H. K., NGOU, B. P. M., PARKER, J. E. & JONES, J. D. G. 2023. Oligomerization of a plant helper NLR requires cell-surface and intracellular immune receptor activation. *Proceedings of the National Academy of Sciences of the United States of America,* 120.

FEYS, B. J., MOISAN, L. J., NEWMAN, M. A. & PARKER, J. E. 2001. Direct interaction between the *Arabidopsis* disease resistance signaling proteins, EDS1 and PAD4. *Embo Journal,* 20**,** 5400-5411.

FEYS, B. J., WIERMER, M., BHAT, R. A., MOISAN, L. J., MEDINA-ESCOBAR, N., NEU, C., CABRAL, A. & PARKER, J. E. 2005. *Arabidopsis* SENESCENCE-ASSOCIATED GENE101 stabilizes and signals within an ENHANCED DISEASE SUSCEPTIBILITY1 complex in plant innate immunity. *Plant Cell,* 17**,** 2601-2613.

FÖRDERER, A., LI, E. T., LAWSON, A. W., DENG, Y. N., SUN, Y., LOGEMANN, E., ZHANG, X. X., WEN, J., HAN, Z. F., CHANG, J. B., CHEN, Y. H., SCHULZE-LEFERT, P. & CHAI, J. J. 2022. A wheat resistosome defines common principles of immune receptor channels. *Nature,* 610**,** 532-+.

FURZER, O. J., CEVIK, V., FAIRHEAD, S., BAILEY, K., REDKAR, A., SCHUDOMA, C., MACLEAN, D., HOLUB, E. B. & JONES, J. D. G. 2022. An Improved Assembly of the *Albugo candida* Ac2V Genome Reveals the Expansion of the "CCG" Class of Effectors. *Molecular Plant-Microbe Interactions,* 35**,** 39-48.

GABRIËLS, S., VOSSEN, J. H., EKENGREN, S. K., VAN OOIJEN, G., ABD-EL-HALIEM, A. M., VAN DEN BERG, G. C. M., RAINEY, D. Y., MARTIN, G. B., TAKKEN, F. L. W., DE WIT, P. & JOOSTEN, M. 2007. An NB-LRR protein required for HR signalling mediated by both extra- and intracellular resistance proteins. *Plant Journal,* 50**,** 14-28.

GALLARDO, V. E. & BEHRA, M. 2013. Fluorescent activated cell sorting (FACS) combined with gene expression microarrays for transcription enrichment profiling of zebrafish lateral line cells. *Methods,* 62**,** 226-231.

GANGAPPA, S. N. & KUMAR, S. V. 2018. DET1 and COP1 Modulate the Coordination of Growth and Immunity in Response to Key Seasonal Signals in *Arabidopsis*. *Cell Reports,* 25**,** 29-+.

GANTNER, J., ORDON, J., KRETSCHMER, C., GUEROIS, R. & STUTTMANN, J. 2019. An EDS1-SAG101 Complex Is Essential for TNL-Mediated Immunity in *Nicotiana benthamiana*. *Plant Cell,* 31**,** 2456-2474.

GARCÍA, A. V., BLANVILLAIN-BAUFUMÉ, S., HUIBERS, R. P., WIERMER, M., LI, G. Y., GOBBATO, E., RIETZ, S. & PARKER, J. E. 2010. Balanced Nuclear and Cytoplasmic Activities of EDS1 Are Required for a Complete Plant Innate Immune Response. *Plos Pathogens,* 6.

GELADAKI, A., BRITOVSEK, N. K., BRECKELS, L. M., SMITH, T. S., VENNARD, O. L., MULVEY, C. M., CROOK, O. M., GATTO, L. & LILLEY, K. S. 2019. Combining LOPIT with differential ultracentrifugation for high-resolution spatial proteomics. *Nature Communications,* 10.

GERI, J. B., OAKLEY, J. V., REYES-ROBLES, T., WANG, T., MCCARVER, S. J., WHITE, C. H., RODRIGUEZ-RIVERA, F. P., PARKER, D. L., HETT, E. C., FADEYI, O. O., OSLUND, R. C. & MACMILLAN, D. W. C. 2020. Microenvironment mapping via Dexter energy transfer on immune cells. *Science,* 367**,** 1091-+.

GILL, U. S., LEE, S. & MYSORE, K. S. 2015. Host Versus Nonhost Resistance: Distinct Wars with Similar Arsenals. *Phytopathology,* 105**,** 580-587.

GILROY, E. M., BREEN, S., WHISSON, S. C., SQUIRES, J., HEIN, I., KACZMAREK, M., TURNBULL, D., BOEVINK, P. C., LOKOSSOU, A., CANO, L. M., MORALES, J., AVROVA, A. O., PRITCHARD, L., RANDALL, E., LEES, A., GOVERS, F., VAN WEST, P., KAMOUN, S., VLEESHOUWERS, V., COOKE, D. E. L. & BIRCH, P. R. J. 2011. Presence/absence, differential expression and sequence polymorphisms between *PiAVR2* and *PiAVR2-like* in *Phytophthora infestans* determine virulence on *R2* plants. *New Phytologist,* 191**,** 763-776.

GIMENEZ-IBANEZ, S., BOTER, M., FERNÁNDEZ-BARBERO, G., CHINI, A., RATHJEN, J. P. & SOLANO, R. 2014. The Bacterial Effector HopX1 Targets JAZ Transcriptional Repressors to Activate Jasmonate Signaling and Promote Infection in *Arabidopsis*. *Plos Biology,* 12.

GINGRAS, A. C., ABE, K. T. & RAUGHT, B. 2019. Getting to know the neighborhood: using proximity-dependent biotinylation to characterize protein complexes and map organelles. *Current Opinion in Chemical Biology,* 48**,** 44-54.

GO, C. D., KNIGHT, J. D. R., RAJASEKHARAN, A., RATHOD, B., HESKETH, G. G., ABE, K. T., YOUN, J. Y., SAMAVARCHI-TEHRANI, P., ZHANG, H., ZHU, L. Y., POPIEL, E., LAMBERT, J. P., COYAUD, É., CHEUNG, S. W. T., RAJENDRAN, D., WONG, C. J., ANTONICKA, H., PELLETIER, L., PALAZZO, A. F., SHOUBRIDGE, E. A., RAUGHT, B. & GINGRAS, A. C. 2021. A proximity-dependent biotinylation map of a human cell. *Nature,* 595**,** 120-+.

GREEN, E. R. & MECSAS, J. 2016. Bacterial Secretion Systems: An Overview. *Microbiology Spectrum,* 4.

GREENBERG, J. T. & YAO, N. 2004. The role and regulation of programmed cell death in plant-pathogen interactions. *Cellular Microbiology,* 6**,** 201-211.

GRYFFROY, L., CEULEMANS, E., PEREZ, N. M., VENEGAS-MOLINA, J., JARAMILLO-MADRID, A. C., RODRIGUES, S. D., DE MILDE, L., JONCKHEERE, V., VAN MONTAGU, M., DE CONINCK, B., VANDEPOELE, K., VAN DAMME, P. & GOOSSENS, A. 2023. Rhizogenic Agrobacterium protein RolB interacts with the TOPLESS repressor proteins to reprogram plant immunity and development br. *Proceedings of the National Academy of Sciences of the United States of America,* 120.

HAAS, B. J., KAMOUN, S., ZODY, M. C., JIANG, R. H. Y., HANDSAKER, R. E., CANO, L. M., GRABHERR, M., KODIRA, C. D., RAFFAELE, S., TORTO-ALALIBO, T., BOZKURT, T. O., AH-FONG, A. M. V., ALVARADO, L., ANDERSON, V. L., ARMSTRONG, M. R., AVROVA, A., BAXTER, L., BEYNON, J., BOEVINK, P. C., BOLLMANN, S. R., BOS, J. I. B., BULONE, V., CAI, G. H., CAKIR, C., CARRINGTON, J. C., CHAWNER, M., CONTI, L., COSTANZO, S., EWAN, R., FAHLGREN, N., FISCHBACH, M. A., FUGELSTAD, J., GILROY, E. M., GNERRE, S., GREEN, P. J., GRENVILLE-BRIGGS, L. J., GRIFFITH, J., GRÜNWALD, N. J., HORN, K., HORNER, N. R., HU, C. H., HUITEMA, E., JEONG, D. H., JONES, A. M. E., JONES, J. D. G., JONES, R. W., KARLSSON, E. K., KUNJETI, S. G., LAMOUR, K., LIU, Z. Y., MA, L. J., MACLEAN, D., CHIBUCOS, M. C., MCDONALD, H., MCWALTERS, J., MEIJER, H. J. G., MORGAN, W., MORRIS, P. F., MUNRO, C. A., O'NEILL, K., OSPINA-GIRALDO, M., PINZÓN, A., PRITCHARD, L., RAMSAHOYE, B., REN, Q. H., RESTREPO, S., ROY, S., SADANANDOM, A., SAVIDOR, A., SCHORNACK, S., SCHWARTZ, D. C., SCHUMANN, U. D., SCHWESSINGER, B., SEYER, L., SHARPE, T., SILVAR, C., SONG, J., STUDHOLME, D. J., SYKES, S., THINES, M., VAN DE VONDERVOORT, P. J. I., PHUNTUMART, V., WAWRA, S., WEIDE, R., WIN, J., YOUNG, C., ZHOU, S. G., FRY, W., MEYERS, B. C., VAN WEST, P., RISTAINO, J., GOVERS, F., BIRCH, P. R. J., WHISSON, S. C., JUDELSON, H. S. & NUSBAUM, C. 2009. Genome sequence and analysis of the Irish potato famine pathogen *Phytophthora infestans*. *Nature,* 461**,** 393-398.

HAMANN, T. 2012. Plant cell wall integrity maintenance as an essential component of biotic stress response mechanisms. *Frontiers in Plant Science,* 3.

HAN, Y. F., DOU, K., MA, Z. Y., ZHANG, S. W., HUANG, H. W., LI, L., CAI, T., CHEN, S., ZHU, J. K. & HE, X. J. 2014. SUVR2 is involved in transcriptional gene silencing by associating with SNF2-related chromatin-remodeling proteins in *Arabidopsis*. *Cell Research,* 24**,** 1445-1465.

HARVEY, J. J. W., LEWSEY, M. G., PATEL, K., WESTWOOD, J., HEIMSTÄDT, S., CARR, J. P. & BAULCOMBE, D. C. 2011. An Antiviral Defense Role of AGO2 in Plants. *Plos One,* 6.

HE, Q., MCLELLAN, H., BOEVINK, P. C. & BIRCH, P. R. J. 2020. All Roads Lead to Susceptibility: The Many Modes of Action of Fungal and Oomycete Intracellular Effectors. *Plant Communications,* 1.

HE, Q., NAQVI, S., MCLELLAN, H., BOEVINK, P. C., CHAMPOURET, N., HEIN, I. & BIRCH, P. R. J. 2018. Plant pathogen effector utilizes host susceptibility factor NRL1 to degrade the immune regulator SWAP70. *Proceedings of the National Academy of Sciences of the United States of America,* 115**,** E7834-E7843.

HE, Y. H., DOYLE, M. R. & AMASINO, R. M. 2004. PAF1-complex-mediated histone methylation of *FLOWERING LOCUS C* chromatin required for the vernalization-responsive, winter-annual habit in *Arabidopsis*. *Genes & Development,* 18**,** 2774-2784.

HEATH, M. C. 2000. Nonhost resistance and nonspecific plant defenses. *Current Opinion in Plant Biology,* 3**,** 315-319.

HERR, A. J., MOLNÀR, A., JONES, A. & BAULCOMBE, D. C. 2006. Defective RNA processing enhances RNA silencing and influences flowering of *Arabidopsis*. *Proceedings of the National Academy of Sciences of the United States of America,* 103**,** 14994-15001.

HILDEBRAND, J. M., TANZER, M. C., LUCET, I. S., YOUNG, S. N., SPALL, S. K., SHARMA, P., PIEROTTI, C., GARNIER, J. M., DOBSON, R. C. J., WEBB, A. I., TRIPAYDONIS, A., BABON, J. J., MULCAIR, M. D., SCANLON, M. J., ALEXANDER, W. S., WILKS, A. F., CZABOTAR, P. E., LESSENE, G., MURPHY, J. M. & SILKE, J. 2014. Activation of the pseudokinase MLKL unleashes the four-helix bundle domain to induce membrane localization and necroptotic cell death. *Proceedings of the National Academy of Sciences of the United States of America,* 111**,** 15072-15077.

HINSCH, M. & STASKAWICZ, B. 1996. Identification of a new Arabidopsis disease resistance locus, RPS4, and cloning of the corresponding avirulence gene, avrRps4, from Pseudomonas syringae pv pisi. *Molecular Plant-Microbe Interactions,* 9**,** 55-61.

HOGENHOUT, S. A., VAN DER HOORN, R. A. L., TERAUCHI, R. & KAMOUN, S. 2009. Emerging Concepts in Effector Biology of Plant-Associated Organisms. *Molecular Plant-Microbe Interactions,* 22**,** 115-122.

HOMMA, F., HUANG, J. & VAN DER HOORN, R. A. L. 2023. AlphaFold-Multimer predicts cross-kingdom interactions at the plant-pathogen interface. *Nature Communications,* 14.

HORSEFIELD, S., BURDETT, H., ZHANG, X. X., MANIK, M. K., SHI, Y., CHEN, J., QI, T. C., GILLEY, J., LAI, J. S., RANK, M. X., CASEY, L. W., GU, W. X., ERICSSON, D. J., FOLEY, G., HUGHES, R. O., BOSANAC, T., VON ITZSTEIN, M., RATHJEN, J. P., NANSON, J. D., BODEN, M., DRY, I. B., WILLIAMS, S. J., STASKAWICZ, B. J., COLEMAN, M. P., VE, T., DODDS, P. N. & KOBE, B. 2019. $NAD^+$ cleavage activity by animal an plant TIR domains in cell death pathways. *Science,* 365**,** 793-+.

HU, L., WU, Y., WU, D., RAO, W. W., GUO, J. P., MA, Y. H., WANG, Z. Z., SHANGGUAN, X. X., WANG, H. Y., XU, C. X., HUANG, J., SHI, S. J., CHEN, R. Z., DU, B., ZHU, L. L. & HE, G. C. 2017. The Coiled-Coil and Nucleotide Binding Domains of BROWN PLANTHOPPER RESISTANCE14 Function in Signaling and Resistance against Planthopper in Rice. *Plant Cell,* 29**,** 3157-3185.

HUANG, C. Y., HUANG, Y. S., SUGIHARA, Y., WANG, H. Y., HUANG, L. T., LOPEZ-AGUDELO, J. C., CHEN, Y. F., LIN, K. Y., CHIANG, B. J., TOGHANI, A., KOURELIS, J., WANG, C. H., DEREVNINA, L. & WU, C. H. 2024a. Subfunctionalization of NRC3 altered the genetic structure of the *Nicotiana* NRC network. *Plos Genetics,* 20.

HUANG, J., LU, X. Y., WU, H. W., XIE, Y. C., PENG, Q., GU, L. F., WU, J. Y., WANG, Y. C., REDDY, A. S. N. & DONG, S. M. 2020. *Phytophthora* Effectors Modulate Genome-wide Alternative Splicing of Host mRNAs to Reprogram Plant Immunity. *Molecular Plant,* 13**,** 1470-1484.

HUANG, P. H., ZHANG, X. M., CHENG, Z. Y., WANG, X., MIAO, Y. C., HUANG, G. W., FU, Y. F. & FENG, X. Z. 2024b. The nuclear pore Y-complex functions as a platform for transcriptional regulation of FLOWERING LOCUS C in Arabidopsis. *Plant Cell,* 36**,** 346-366.

HUANG, S., CHEN, X. J., ZHONG, X. H., LI, M., AO, K. V., HUANG, J. H. & LI, X. 2016. Plant TRAF Proteins Regulate NLR Immune Receptor Turnover. *Cell Host & Microbe,* 19**,** 204-215.

HUANG, S., MONAGHAN, J., ZHONG, X. H., LIN, L., SUN, T. J., DONG, O. X. & LI, X. 2014a. HSP90s are required for NLR immune receptor accumulation in Arabidopsis. *Plant Journal,* 79**,** 427-439.

HUANG, S. J., JIA, A. L., SONG, W., HESSLER, G., MENG, Y. G., SUN, Y., XU, L. N., LAESSLE, H., JIRSCHITZKA, J., MA, S. C., XIAO, Y., YU, D. L., HOU, J., LIU, R. Q., SUN, H. H., LIU, X. H., HAN, Z. F., CHANG, J. B., PARKER, J. E. & CHAI, J. J. 2022. Identification and receptor mechanism of TIR-catalyzed small molecules in plant immunity. *Science,* 377**,** 487-+.

HUANG, S. J., WANG, J. L., SONG, R. D., JIA, A. L., XIAO, Y., SUN, Y., WANG, L., MAHR, D., WU, Z. S., HAN, Z. F., LI, X., PARKER, J. E. & CHAI, J. J. 2025. Balanced plant helper NLR activation by a modified host protein complex. *Nature*.

HUANG, Y., MINAKER, S., ROTH, C., HUANG, S., HIETER, P., LIPKA, V., WIERMER, M. & LI, X. 2014b. An E4 Ligase Facilitates Polyubiquitination of Plant Immune Receptor Resistance Proteins in *Arabidopsis*. *Plant Cell,* 26**,** 485-496.

HUBERT, D. A., TORNERO, P., BELKHADIR, Y., KRISHNA, P., TAKAHASHI, A., SHIRASU, K. & DANGL, J. L. 2003. Cytosolic HSP90 associates with and modulates the *Arabidopsis* RPM1 disease resistance protein. *Embo Journal,* 22**,** 5679-5689.

HUITEMA, E., VLEESHOUWERS, V., FRANCIS, D. M. & KAMOUN, S. 2003. Active defence responses associated with non-host resistance of *Arabidopsis thaliana* to the oomycete pathogen *Phytophthora infestans*. *Molecular Plant Pathology,* 4**,** 487-500.

INOUE, H., HAYASHI, N., MATSUSHITA, A., LIU, X. Q., NAKAYAMA, A., SUGANO, S., JIANG, C. J. & TAKATSUJI, H. 2013. Blast resistance of CC-NB-LRR protein Pb1 is mediated by WRKY45 through protein-protein interaction. *Proceedings of the National Academy of Sciences of the United States of America,* 110**,** 9577-9582.

JACOB, F., VERNALDI, S. & MAEKAWA, T. 2013. Evolution and conservation of plant NLR functions. *Frontiers in Immunology,* 4.

JACOB, P., KIM, N. H., WU, F. H., EL KASMR, F., CHI, Y., WALTON, W. G., FURZER, O. J., LIETZAN, A. D., SUNIL, S., KEMPTHORN, K., REDINBO, M. R., PEI, Z. M., WAN, L. & DANGL, J. L. 2021. Plant "helper" immune receptors are $Ca^{2+}$-permeable nonselective cation channels. *Science,* 373**,** 420-+.

JANIK, K., MITHÖFER, A., RAFFEINER, M., STELLMACH, H., HAUSE, B. & SCHLINK, K. 2017. An effector of apple proliferation phytoplasma targets TCP transcription factorsa generalized virulence strategy of phytoplasma? *Molecular Plant Pathology,* 18**,** 435-442.

JAVED, T. & GAO, S. J. 2023. WRKY transcription factors in plant defense. *Trends in Genetics,* 39**,** 787-801.

JEONG, H., MASON, S. P., BARABÁSI, A. L. & OLTVAI, Z. N. 2001. Lethality and centrality in protein networks. *Nature,* 411**,** 41-42.

JIA, A. L., HUANG, S. J., SONG, W., WANG, J. L., MENG, Y. G., SUN, Y., XU, L. N., LAESSLE, H., JIRSCHITZKA, J., HOU, J., ZHANG, T. T., YU, W. Q., HESSLER, G., LI, E. T., MA, S. C., YU, D. L., GEBAUER, J., BAUMANN, U., LIU, X. H., HAN, Z. F., CHANG, J. B., PARKER, J. E. & CHAI, J. J. 2022. TIR-catalyzed ADP-ribosylation reactions produce signaling molecules for plant immunity. *Science,* 377**,** 488-+.

JIA, Y., MCADAMS, S. A., BRYAN, G. T., HERSHEY, H. P. & VALENT, B. 2000. Direct interaction of resistance gene and avirulence gene products confers rice blast resistance. *Embo Journal,* 19**,** 4004-4014.

JIANG, R. H. Y., TRIPATHY, S., GOVERS, F. & TYLER, B. M. 2008. RXLR effector reservoir in two Phytophthora species is dominated by a single rapidly evolving superfamily with more than 700 members. *Proceedings of the National Academy of Sciences of the United States of America,* 105**,** 4874-4879.

JONES, J. D. G. & DANGL, J. L. 2006. The plant immune system. *Nature,* 444**,** 323-329.

JOUET, A., SAUNDERS, D. G. O., MCMULLAN, M., WARD, B., FURZER, O., JUPE, F., CEVIK, V., HEIN, I., THILLIEZ, G. J. A., HOLUB, E., VAN OOSTERHOUT, C. & JONES, J. D. G. 2019. *Albugo candida* race diversity, ploidy

and host-associated microbes revealed using DNA sequence capture on diseased plants in the field. *New Phytologist,* 221**,** 1529-1543.

JUBIC, L. M., SAILE, S., FURZER, O. J., EL KASMI, F. & DANGL, J. L. 2019. Help wanted: helper NLRs and plant immune responses. *Current Opinion in Plant Biology,* 50**,** 82-94.

JUMPER, J., EVANS, R., PRITZEL, A., GREEN, T., FIGURNOV, M., RONNEBERGER, O., TUNYASUVUNAKOOL, K., BATES, R., ZÍDEK, A., POTAPENKO, A., BRIDGLAND, A., MEYER, C., KOHL, S. A. A., BALLARD, A. J., COWIE, A., ROMERA-PAREDES, B., NIKOLOV, S., JAIN, R., ADLER, J., BACK, T., PETERSEN, S., REIMAN, D., CLANCY, E., ZIELINSKI, M., STEINEGGER, M., PACHOLSKA, M., BERGHAMMER, T., BODENSTEIN, S., SILVER, D., VINYALS, O., SENIOR, A. W., KAVUKCUOGLU, K., KOHLI, P. & HASSABIS, D. 2021. Highly accurate protein structure prediction with AlphaFold. *Nature,* 596**,** 583-+.

KADOTA, Y., AMIGUES, B., DUCASSOU, L., MADAOUI, H., OCHSENBEIN, F., GUEROIS, R. & SHIRASU, K. 2008. Structural and functional analysis of SGT1-HSP90 core complex required for innate immunity in plants. *Embo Reports,* 9**,** 1209-1215.

KAHMANN, R. & KÄMPER, J. 2004. *Ustilago maydis*: how its biology relates to pathogenic development. *New Phytologist,* 164**,** 31-42.

KALDE, M., NÜHSE, T. S., FINDLAY, K. & PECK, S. C. 2007. The syntaxin SYP132 contributes to plant resistance against bacteria and secretion of pathogenesis-related protein 1. *Proceedings of the National Academy of Sciences of the United States of America,* 104**,** 11850-11855.

KAMOUN, S., FURZER, O., JONES, J. D. G., JUDELSON, H. S., ALI, G. S., DALIO, R. J. D., ROY, S. G., SCHENA, L., ZAMBOUNIS, A., PANABIÈRES, F., CAHILL, D., RUOCCO, M., FIGUEIREDO, A., CHEN, X. R., HULVEY, J., STAM, R., LAMOUR, K., GIJZEN, M., TYLER, B. M., GRÜNWALD, N. J., MUKHTAR, M. S., TOMÉ, D. F. A., TÖR, M., VAN DEN ACKERVEKEN, G., MCDOWELL, J., DAAYF, F., FRY, W. E., LINDQVIST-KREUZE, H., MEIJER, H. J. G., PETRE, B., RISTAINO, J., YOSHIDA, K., BIRCH, P. R. J. & GOVERS, F. 2015. The Top 10 oomycete pathogens in molecular plant pathology. *Molecular Plant Pathology,* 16**,** 413-434.

KANG, S., LEBRUN, M. H., FARRALL, L. & VALENT, B. 2001. Gain of virulence caused by insertion of a Pot3 transposon in a *Magnaporthe grisea* avirulence gene. *Molecular Plant-Microbe Interactions,* 14**,** 671-674.

KANZAKI, H., YOSHIDA, K., SAITOH, H., FUJISAKI, K., HIRABUCHI, A., ALAUX, L., FOURNIER, E., THARREAU, D. & TERAUCHI, R. 2012. Arms race co-evolution of *Magnaporthe oryzae AVR-Pik* and rice *Pik* genes driven by their physical interactions. *Plant Journal,* 72**,** 894-907.

KEMEN, E., GARDINER, A., SCHULTZ-LARSEN, T., KEMEN, A. C., BALMUTH, A. L., ROBERT-SEILANIANTZ, A., BAILEY, K., HOLUB, E., STUDHOLME, D. J., MACLEAN, D. & JONES, J. D. G. 2011. Gene Gain and Loss during Evolution of Obligate Parasitism in the White Rust Pathogen of *Arabidopsis thaliana*. *Plos Biology,* 9.

KHAN, M., YOUN, J. Y., GINGRAS, A. C., SUBRAMANIAM, R. & DESVEAUX, D. 2018. *In planta* proximity dependent biotin identification (BioID). *Scientific Reports,* 8.

KIM, D. I., BIRENDRA, K. C., ZHU, W. H., MOTAMEDCHABOKI, K., DOYE, V. & ROUX, K. J. 2014a. Probing nuclear pore complex architecture with proximity-dependent biotinylation. *Proceedings of the National Academy of Sciences of the United States of America,* 111**,** E2453-E2461.

KIM, D. I., JENSEN, S. C., NOBLE, K. A., BIRENDRA, K. C., ROUX, K. H., MOTAMEDCHABOKI, K. & ROUX, K. J. 2016. An improved smaller biotin ligase for BioID proximity labeling. *Molecular Biology of the Cell,* 27**,** 1188-1196.

KIM, S. H., GAO, F., BHATTACHARJEE, S., ADIASOR, J. A., NAM, J. C. & GASSMANN, W. 2010. The Arabidopsis Resistance-Like Gene *SNC1* Is Activated by Mutations in *SRFR1* and Contributes to Resistance to the Bacterial Effector AvrRps4. *Plos Pathogens,* 6.

KIM, S. H., SON, G. H., BHATTACHARJEE, S., KIM, H. J., NAM, J. C., NGUYEN, P. D. T., HONG, J. C. & GASSMANN, W. 2014b. The Arabidopsis immune adaptor SRFR1 interacts with TCP transcription factors that redundantly contribute to effector-triggered immunity. *Plant Journal,* 78**,** 978-989.

KONTRA, L., CSORBA, T., TAVAZZA, M., LUCIOLI, A., TAVAZZA, R., MOXON, S., TISZA, V., MEDZIHRADSZKY, A., TURINA, M. & BURGYÁN, J. 2016. Distinct Effects of p19 RNA Silencing Suppressor on Small RNA Mediated Pathways in Plants. *Plos Pathogens,* 12.

KOURELIS, J., CONTRERAS, M. P., HARANT, A., PAI, H., LÜDKE, D., ADACHI, H., DEREVNINA, L., WU, C. H. & KAMOUN, S. 2022. The helper NLR immune protein NRC3 mediates the hypersensitive cell death caused by the cell-surface receptor Cf-4. *Plos Genetics,* 18.

KOVER, P. X., VALDAR, W., TRAKALO, J., SCARCELLI, N., EHRENREICH, I. M., PURUGGANAN, M. D., DURRANT, C. & MOTT, R. 2009. A Multiparent Advanced Generation Inter-Cross to Fine-Map Quantitative Traits in *Arabidopsis thaliana*. *Plos Genetics,* 5.

KOVERMANN, P., MEYER, S., HÖRTENSTEINER, S., PICCO, C., SCHOLZ-STARKE, J., RAVERA, S., LEE, Y. & MARTINOIA, E. 2007. The Arabidopsis vacuolar malate channel is a member of the ALMT family. *Plant Journal,* 52**,** 1169-1180.

KRASILEVA, K. V., DAHLBECK, D. & STASKAWICZ, B. J. 2010. Activation of an *Arabidopsis* Resistance Protein Is Specified by the in Planta Association of Its Leucine-Rich Repeat Domain with the Cognate Oomycete Effector. *Plant Cell,* 22**,** 2444-2458.

KUBITZ, L., BITSCH, S., ZHAO, X. Y., SCHMITT, K., DEWEID, L., ROEHRIG, A., BARAZZONE, E. C., VALERIUS, O., KOLMAR, H. & BÉTHUNE, J. 2022. Engineering of ultraID, a compact and hyperactive enzyme for proximity-dependent biotinylation in living cells. *Communications Biology,* 5.

KWAK, C., SHIN, S., PARK, J. S., JUNG, M., NHUNG, T. T. M., KANG, M. G., LEE, C., KWON, T. H., PARK, S. K., MUN, J. Y., KIM, J. S. & RHEE, H. W. 2020. Contact-ID, a tool for profiling organelle contact sites, reveals regulatory proteins of mitochondrial-associated membrane formation. *Proceedings of the National Academy of Sciences of the United States of America,* 117**,** 12109-12120.

LAM, S. S., MARTELL, J. D., KAMER, K. J., DEERINCK, T. J., ELLISMAN, M. H., MOOTHA, V. K. & TING, A. Y. 2015. Directed evolution of APEX2 for electron microscopy and proximity labeling. *Nature Methods,* 12**,** 51-54.

LANVER, D., TOLLOT, M., SCHWEIZER, G., LO PRESTI, L., REISSMANN, S., MA, L. S., SCHUSTER, M., TANAKA, S., LIANG, L., LUDWIG, N. & KAHMANN, R. 2017. *Ustilago maydis* effectors and their impact on virulence. *Nature Reviews Microbiology,* 15**,** 409-421.

LAPIN, D., KOVACOVA, V., SUN, X. H., DONGUS, J. A., BHANDARI, D., VON BORN, P., BAUTOR, J., GUARNERI, N., RZEMIENIEWSKI, J., STUTTMANN, J., BEYER, A. & PARKER, J. E. 2019. A Coevolved EDS1-SAG101-NRG1 Module Mediates Cell Death Signaling by TIR-Domain Immune Receptors. *Plant Cell,* 31**,** 2430-2455.

LAZAR, N., MESARICH, C. H., PETIT-HOUDENOT, Y., TALBI, N., LI DE LA SIERRA-GALLAY, I., ZÉLIE, E., BLONDEAU, K., GRACY, J., OLLIVIER, B., BLAISE, F., ROUXEL, T., BALESDENT, M. H., IDNURM, A., VAN TILBEURGH, H. & FUDAL, I. 2022. A new family of structurally conserved fungal effectors displays epistatic interactions with plant resistance proteins. *Plos Pathogens,* 18.

LE ROUX, C., HUET, G., JAUNEAU, A., CAMBORDE, L., TRÉMOUSAYGUE, D., KRAUT, A., ZHOU, B. B., LEVAILLANT, M., ADACHI, H., YOSHIOKA, H., RAFFAELE, S., BERTHOMÉ, R., COUTÉ, Y., PARKER, J. E. & DESLANDES, L. 2015. A Receptor Pair with an Integrated Decoy Converts Pathogen Disabling of Transcription Factors to Immunity. *Cell,* 161**,** 1074-1088.

LEE, J., MANNING, A. J., WOLFGEHER, D., JELENSKA, J., CAVANAUGH, K. A., XU, H. Q., FERNANDEZ, S. M., MICHELMORE, R. W., KRON, S. J. & GREENBERG, J. T. 2015. Acetylation of an NB-LRR Plant Immune-Effector Complex Suppresses Immunity. *Cell Reports,* 13**,** 1670-1682.

LEE, S. Y., CHEAH, J. S., ZHAO, B. X., XU, C., ROH, H., KIM, C. K., CHO, K. F., UDESHI, N. D., CARR, S. A. & TING, A. Y. 2023. Engineered allostery in light-regulated LOV-Turbo enables precise spatiotemporal control of proximity labeling in living cells. *Nature Methods,* 20**,** 908-+.

LEEGOOD, R. C. & WALKER, R. P. 2003. Regulation and roles of phospho*enol*pyruvate carboxykinase in plants. *Archives of Biochemistry and Biophysics,* 414**,** 204-210.

LEWIS, J. D., LEE, A. H. Y., HASSAN, J. A., WAN, J., HURLEY, B., JHINGREE, J. R., WANG, P. W., LO, T., YOUN, J. Y., GUTTMAN, D. S. & DESVEAUX, D. 2013. The *Arabidopsis* ZED1 pseudokinase is required for ZAR1-mediated immunity induced by the *Pseudomonas syringae* type III effector HopZ1a. *Proceedings of the National Academy of Sciences of the United States of America,* 110**,** 18722-18727.

LI, H., ZHOU, Y. & ZHANG, Z. D. 2017a. Network Analysis Reveals a Common Host-Pathogen Interaction Pattern in *Arabidopsis* Immune Responses. *Frontiers in Plant Science,* 8.

LI, P. P., LI, J. J., WANG, L. & DI, L. J. 2017b. Proximity Labeling of Interacting Proteins: Application of BioID as a Discovery Tool. *Proteomics,* 17.

LI, T. T., WANG, Q. H., FENG, R. R., LI, L. C., DING, L. W., FAN, G. J., LI, W. W., DU, Y., ZHANG, M. X., HUANG, G. Y., SCHAFER, P., MENG, Y. L., TYLER, B. M. & SHAN, W. X. 2019. Negative regulators of plant immunity derived from cinnamyl alcohol dehydrogenases are targeted by multiple *Phytophthora* Avr3a-like effectors. *New Phytologist*.

LI, Y., ZHANG, Y., WANG, Q. X., WANG, T. T., CAO, X. L., ZHAO, Z. X., ZHAO, S. L., XU, Y. J., XIAO, Z. Y., LI, J. L., FAN, J., YANG, H., HUANG, F., XIAO, S. Y. & WANG, W. M. 2018. *RESISTANCE TO POWDERY MILDEW8.1* boosts pattern-triggered immunity against multiple pathogens in Arabidopsis and rice. *Plant Biotechnology Journal,* 16**,** 428-441.

LI, Y. Z., LI, S. X., BI, D. L., CHENG, Y. T., LI, X. & ZHANG, Y. L. 2010. SRFR1 Negatively Regulates Plant NB-LRR Resistance Protein Accumulation to Prevent Autoimmunity. *Plos Pathogens,* 6.

LIN, Q. P., ZHOU, Z. J., LUO, W. B., FANG, M. C., LI, M. R. & LI, H. Q. 2017. Screening of Proximal and Interacting Proteins in Rice Protoplasts by Proximity-Dependent Biotinylation. *Frontiers in Plant Science,* 8.

LIN, X., JIA, Y. X., HEAL, R., PROKCHORCHIK, M., SINDALOVSKAYA, M., OLAVE-ACHURY, A., MAKECHEMU, M., FAIRHEAD, S., NOUREEN, A., HEO, J., WITEK, K., SMOKER, M., TAYLOR, J., SHRESTHA, R. K., LEE, Y. Y., ZHANG, C. Z., PARK, S. J., SOHN, K. H., HUANG, S. W. & JONES, J. D. G. 2023. *Solanum americanum* genome-assisted discovery of immune receptors that detect potato late blight pathogen effectors. *Nature Genetics,* 55**,** 1579-+.

LIN, X., OLAVE-ACHURY, A., HEAL, R., PAIS, M., WITEK, K., AHN, H. K., ZHAO, H., BHANVADIA, S., KARKI, H. S., SONG, T. Q., WU, C. H., ADACHI, H., KAMOUN, S., VLEESHOUWERS, V. & JONES, J. D. G. 2022. A potato late blight resistance gene protects against multiple *Phytophthora* species by recognizing a broadly conserved RXLR-WY effector. *Molecular Plant,* 15**,** 1457-1469.

LIN, X., SONG, T. Q., FAIRHEAD, S., WITEK, K., JOUET, A., JUPE, F., WITEK, A. I., KARKI, H. S., VLEESHOUWERS, V., HEIN, I. & JONES, J. D. G. 2020. Identification of *Avramr1* from *Phytophthora infestans* using long read and cDNA pathogen-enrichment sequencing (PenSeq). *Molecular Plant Pathology,* 21**,** 1502-1512.

LIN, Z. R., LIU, D., XU, Y. F., WANG, M. Y., YU, Y. Q., DIENER, A. C. & LIU, K. H. 2024. Pupylation-Based Proximity-Tagging of FERONIA-Interacting Proteins in Arabidopsis. *Molecular & Cellular Proteomics,* 23.

LINKS, M. G., HOLUB, E., JIANG, R. H. Y., SHARPE, A. G., HEGEDUS, D., BEYNON, E., SILLITO, D., CLARKE, W. E., UZUHASHI, S. & BORHAN, M. H. 2011. *De novo* sequence assembly of *Albugo candida* reveals a small genome relative to other biotrophic oomycetes. *Bmc Genomics,* 12.

LIU, F., RIJKERS, D. T. S., POST, H. & HECK, A. J. R. 2015. Proteome-wide profiling of protein assemblies by cross-linking mass spectrometry. *Nature Methods,* 12**,** 1179-+.

LIU, F. R., YANG, Z. L., WANG, C., YOU, Z., MARTIN, R., QIAO, W. J., HUANG, J., JACOB, P., DANGL, J. L., CARETTE, J. E., LUAN, S., NOGALES, E. & STASKAWICZ, B. J. 2024a. Activation of the helper NRC4 immune receptor forms a hexameric resistosome. *Cell,* 187.

LIU, Q., NEEFJES, A. C. M., KOBYLINSKA, R., MUGFORD, S. T., MARZO, M., CANHAM, J., SCHUSTER, M., VAN DER HOORN, R. A. L., CHEN, Y. & HOGENHOUT, S. A. 2024b. Aphid effectors suppress plant immunity via recruiting defence proteins to processing bodies. *bioRxiv*.

LIU, Q., ZHENG, J., SUN, W. P., HUO, Y. B., ZHANG, L. Y., HAO, P. L., WANG, H. P. & ZHUANG, M. 2018. A proximity-tagging system to identify membrane protein-protein interactions. *Nature Methods,* 15**,** 715-+.

LIU, T. Y., HUANG, T. K., YANG, S. Y., HONG, Y. T., HUANG, S. M., WANG, F. N., CHIANG, S. F., TSAI, S. Y., LU, W. C. & CHIOU, T. J. 2016. Identification of plant vacuolar transporters mediating phosphate storage. *Nature Communications,* 7.

LIU, Y. L., BURCH-SMITH, T., SCHIFF, M., FENG, S. H. & DINESH-KUMAR, S. P. 2004. Molecular chaperone Hsp90 associates with resistance protein n and its signaling proteins SGT1 and Rar1 to modulate an innate immune response in plants. *Journal of Biological Chemistry,* 279**,** 2101-2108.

LIU, Y. M., NELSON, Z. M., REDA, A. & FEHL, C. 2022. Spatiotemporal Proximity Labeling Tools to Track GlcNAc Sugar-Modified Functional Protein Hubs during Cellular Signaling. *Acs Chemical Biology,* 17**,** 2153-2164.

LO PRESTI, L., ZECHMANN, B., KUMLEHN, J., LIANG, L., LANVER, D., TANAKA, S., BOCK, R. & KAHMANN, R. 2017. An assay for entry of secreted fungal effectors into plant cells. *New Phytologist,* 213**,** 956-964.

LONG, X. G., CAI, Y. J., WANG, H. M., LIU, Y., HUANG, X. Y., XUAN, H., LI, W. J., ZHANG, X. L., ZHANG, H. Y., FANG, X. F., HE, H., XU, G. Y., DEAN, C. & YANG, H. C. 2024. Cotranscriptional splicing is required in the cold to produce COOLAIR isoforms that repress Arabidopsis FLC. *Proceedings of the National Academy of Sciences of the United States of America,* 121.

LOPEZ, J. A., SUN, Y., BLAIR, P. B. & MUKHTAR, M. S. 2015. TCP three-way handshake: linking developmental processes with plant immunity. *Trends in Plant Science,* 20**,** 238-245.

LOPEZ, V. A., PARK, B. C., NOWAK, D., SREELATHA, A., ZEMBEK, P., FERNANDEZ, J., SERVAGE, K. A., GRADOWSKI, M., HENNIG, J., TOMCHICK, D. R., PAWLOWSKI, K., KRZYMOWSKA, M. & TAGLIABRACCI, V. S. 2019. A Bacterial Effector Mimics a Host HSP90 Client to Undermine Immunity. *Cell,* 179**,** 205-+.

LUTZ, K. A., KNAPP, J. E. & MALIGA, P. 2001. Expression of *bar* in the plastid genome confers herbicide resistance. *Plant Physiology,* 125**,** 1585-1590.

LYONS, R., RUSU, A., STILLER, J., POWELL, J., MANNERS, J. M. & KAZAN, K. 2015. Investigating the Association between Flowering Time and Defense in the *Arabidopsis thaliana-Fusarium oxysporum* Interaction. *Plos One,* 10.

MA, L., LUKASIK, E., GAWEHNS, F. & TAKKEN, F. L. 2012. The use of agroinfiltration for transient expression of plant resistance and fungal effector proteins in Nicotiana benthamiana leaves. *Methods Mol Biol,* 835**,** 61-74.

MA, S. C., AN, C. P., LAWSON, A. W., CAO, Y., SUN, Y., TAN, E. Y. J., PAN, J. H., JIRSCHITZKA, J., KÜMMEL, F., MUKHI, N., HAN, Z. F., FENG, S., WU, B., SCHULZE-LEFERT, P. & CHAI, J. J. 2024. Oligomerization-mediated autoinhibition and cofactor binding of a plant NLR. *Nature,* 632.

MA, S. C., LAPIN, D., LIU, L., SUN, Y., SONG, W., ZHANG, X. X., LOGEMANN, E., YU, D. L., WANG, J., JIRSCHITZKA, J., HAN, Z. F., SCHULZE-LEFERT, P., PARKER, J. E. & CHAI, J. J. 2020. Direct pathogen-induced assembly of an NLR immune receptor complex to form a holoenzyme. *Science,* 370**,** 1184-+.

MA, Y., GUO, H. L., HU, L. X., MARTINEZ, P. P., MOSCHOU, P. N., CEVIK, V., DING, P. T., DUXBURY, Z., SARRIS, P. F. & JONES, J. D. G. 2018. Distinct modes of derepression of an *Arabidopsis* immune receptor complex by two different bacterial effectors. *Proceedings of the National Academy of Sciences of the United States of America,* 115**,** 10218-10227.

MACKEY, D., BELKHADIR, Y., ALONSO, J. M., ECKER, J. R. & DANGL, J. L. 2003. *Arabidopsis* RIN4 is a target of the type III virulence effector AvrRpt2 and modulates RPS2-mediated resistance. *Cell,* 112**,** 379-389.

MACKEY, D., HOLT, B. F., WIIG, A. & DANGL, J. L. 2002. RIN4 interacts with *Pseudomonas syringae* type III effector molecules and is required for RPM1-mediated resistance in *Arabidopsis*. *Cell,* 108**,** 743-754.

MADHUPRAKASH, J., TOGHANI, A., CONTRERAS, M. P., POSBEYIKIAN, A., RICHARDSON, J., KOURELIS, J., BOZKURT, T. O., WEBSTER, M. W. & KAMOUN, S. 2024. A disease resistance protein triggers oligomerization of its NLR helper into a hexameric resistosome to mediate innate immunity. *Science Advances,* 10.

MAIR, A. & BERGMANN, D. C. 2022. Advances in enzyme-mediated proximity labeling and its potential for plant research. *Plant Physiology,* 188**,** 756-768.

MAIR, A., XU, S. L., BRANON, T. C., TING, A. Y. & BERGMANN, D. C. 2019. Proximity labeling of protein complexes and cell-type-specific organellar proteomes in *Arabidopsis* enabled by TurboID. *Elife,* 8.

MARGETS, A., FOSTER, J., KUMAR, A., MAIER, T. R., MASONBRINK, R., MEJIAS, J., BAUM, T. J. & INNES, R. W. 2024. The Soybean Cyst Nematode Effector Cysteine Protease 1 (CPR1) Targets a Mitochondrial Soybean Branched-Chain Amino Acid Aminotransferase (GmBCAT1). *Molecular Plant-Microbe Interactions,* 37**,** 751-764.

MARTIN, R., QI, T. C., ZHANG, H. B., LIU, F. R., KING, M., TOTH, C., NOGALES, E. & STASKAWICZ, B. J. 2020. Structure of the activated ROQ1 resistosome directly recognizing the pathogen effector XopQ. *Science,* 370**,** 1185-+.

MARTÍNEZ-GARCÍA, J. F., MONTE, E. & QUAIL, P. H. 1999. A simple, rapid and quantitative method for preparing *Arabidopsis* protein extracts for immunoblot analysis. *Plant Journal,* 20**,** 251-257.

MAY, D. G., SCOTT, K. L., CAMPOS, A. R. & ROUX, K. J. 2020. Comparative Application of BioID and TurboID for Protein-Proximity Biotinylation. *Cells,* 9.

MAYOR, A., MARTINON, F., DE SMEDT, T., PETRILLI, V. & TSCHOPP, J. 2007. A crucial function of SGT1 and HSP90 in inflammasome activity links mammalian and plant innate immune responses. *Cytokine,* 39**,** 26-26.

MCMULLAN, M., GARDINER, A., BAILEY, K., KEMEN, E., WARD, B. J., CEVIK, V., ROBERT-SEILANIANTZ, A., SCHULTZ-LARSEN, T., BALMUTH, A., HOLUB, E., VAN OOSTERHOUT, C. & JONES, J. D. G. 2015. Evidence for suppression of immunity as a driver for genomic introgressions and host range expansion in races of *Albugo candida*, a generalist parasite. *Elife,* 4.

MELKONIAN, K., STOLZE, S. C., HARZEN, A. & NAKAGAMI, H. 2022. miniTurbo-based interactomics of two plasma membrane-localized SNARE proteins in *Marchantia polymorpha*. *New Phytologist,* 235**,** 786-800.

MELOTTO, M., UNDERWOOD, W. & HE, S. Y. 2008. Role of stomata in plant innate immunity and foliar bacterial diseases. *Annual Review of Phytopathology,* 46**,** 101-122.

MENDGEN, K., HAHN, M. & DEISING, H. 1996. Morphogenesis and mechanisms of penetration by plant pathogenic fungi. *Annual Review of Phytopathology,* 34**,** 367-386.

MOREIRA, C. M. D., KELEMEN, C. D., OBADO, S. O., ZAHEDIFARD, F., ZHANG, N., HOLETZ, F. B., GAUGLITZ, L., DALLAGIOVANNA, B., FIELD, M. C., KRAMER, S. & ZOLTNER, M. 2023. Impact of inherent biases built into proteomic techniques: Proximity labeling and affinity capture compared. *Journal of Biological Chemistry,* 299.

MORI, S., OYA, S., TAKAHASHI, M., TAKASHIMA, K., INAGAKI, S. & KAKUTANI, T. 2023. Cotranscriptional demethylation induces global loss of H3K4me2 from active genes in *Arabidopsis*. *Embo Journal,* 42.

MUKHTAR, M. S., CARVUNIS, A. R., DREZE, M., EPPLE, P., STEINBRENNER, J., MOORE, J., TASAN, M., GALLI, M., HAO, T., NISHIMURA, M. T., PEVZNER, S. J., DONOVAN, S. E., GHAMSARI, L., SANTHANAM, B., ROMERO, V., POULIN, M. M., GEBREAB, F., GUTIERREZ, B. J., TAM, S., MONACHELLO, D., BOXEM, M., HARBORT, C. J., MCDONALD, N., GAI, L. T., CHEN, H. M., HE, Y. J., VANDENHAUTE, J., ROTH, F. P., HILL, D. E., ECKER,

J. R., VIDAL, M., BEYNON, J., BRAUN, P., DANGL, J. L. & EUROPEAN UNION EFFECTOROMICS, C. 2011. Independently Evolved Virulence Effectors Converge onto Hubs in a Plant Immune System Network. *Science,* 333**,** 596-601.

MUÑOZ, A., SANTAMARIA, M. E., FERNÁNDEZ-BAUTISTA, N., MANGANO, S., TORIBIO, R., MARTÍNEZ, M., BERROCAL-LOBO, M., DIAZ, I. & CASTELLANO, M. M. 2021. The co-chaperone HOP3 participates in jasmonic acid signaling by regulating CORONATINE-INSENSITIVE 1 activity. *Plant Physiology,* 187**,** 1679-1689.

MURPHY, A. M., OTTO, B., BREARLEY, C. A., CARR, J. P. & HANKE, D. E. 2008. A role for inositol hexakisphosphate in the maintenance of basal resistance to plant pathogens. *Plant Journal,* 56**,** 638-652.

MYERS, S. A., WRIGHT, J., PECKNER, R., KALISH, B. T., ZHANG, F. & CARR, S. A. 2018. Discovery of proteins associated with a predefined genomic locus via dCas9-APEX-mediated proximity labeling. *Nature Methods,* 15**,** 437-+.

MZID, R., MARCHIVE, C., BLANCARD, D., DELUC, L., BARRIEU, F., CORIO-COSTET, M. F., DRIRA, N., HAMDI, S. & LAUVERGEAT, V. 2007. Overexpression of VvWRKY2 in tobacco enhances broad resistance to necrotrophic fungal pathogens. *Physiologia Plantarum,* 131**,** 434-447.

NATALE, P., BRÜSER, T. & DRIESSEN, A. J. M. 2008. Sec- and Tat-mediated protein secretion across the bacterial cytoplasmic membrane: Distinct translocases and mechanisms. *Biochimica Et Biophysica Acta-Biomembranes,* 1778**,** 1735-1756.

NGOU, B. P. M., AHN, H. K., DING, P. T. & JONES, J. D. G. 2021. Mutual potentiation of plant immunity by cell-surface and intracellular receptors. *Nature,* 592**,** 110-+.

NIELSEN, H. & KROGH, A. 1998. Prediction of signal peptides and signal anchors by a hidden Markov model. *Proceedings International Conference Intelligent Systems for Molecular Biology*.

NIKOLAU, B. J., OHLROGGE, J. B. & WURTELE, E. S. 2003. Plant biotin-containing carboxylases. *Archives of Biochemistry and Biophysics,* 414**,** 211-222.

NTOUKAKIS, V., SAUR, I. M. L., CONLAN, B. & RATHJEN, J. P. 2014. The changing of the guard: the Pto/Prf receptor complex of tomato and pathogen recognition. *Current Opinion in Plant Biology,* 20**,** 69-74.

OH, S. K., YOUNG, C., LEE, M., OLIVA, R., BOZKURT, T. O., CANO, L. M., WIN, J., BOS, J. I. B., LIU, H. Y., VAN DAMME, M., MORGAN, W., CHOI, D., VAN DER VOSSEN, E. A. G., VLEESHOUWERS, V. & KAMOUN, S. 2009. In Planta Expression Screens of *Phytophthora infestans* RXLR Effectors Reveal Diverse Phenotypes, Including Activation of the *Solanum bulbocastanum* Disease Resistance Protein Rpi-blb2. *Plant Cell,* 21**,** 2928-2947.

OHTSU, K., TAKAHASHI, H., SCHNABLE, P. S. & NAKAZONO, M. 2007. Cell type-specific gene expression profiling in plants by using a combination of laser microdissection and high-throughput technologies. *Plant and Cell Physiology,* 48**,** 3-7.

OKUYAMA, Y., KANZAKI, H., ABE, A., YOSHIDA, K., TAMIRU, M., SAITOH, H., FUJIBE, T., MATSUMURA, H., SHENTON, M., GALAM, D. C., UNDAN, J., ITO, A., SONE, T. & TERAUCHI, R. 2011. A multifaceted genomics approach allows the isolation of the rice *Pia*-blast resistance gene consisting of two adjacent NBS-LRR protein genes. *Plant Journal,* 66**,** 467-479.

ORDON, J., GANTNER, J., KEMNA, J., SCHWALGUN, L., RESCHKE, M., STREUBEL, J., BOCH, J. & STUTTMANN, J. 2017. Generation of chromosomal deletions in dicotyledonous plants employing a user-friendly genome editing toolkit. *Plant Journal,* 89**,** 155-168.

PAIS, M., YOSHIDA, K., GIANNAKOPOULOU, A., PEL, M. A., CANO, L. M., OLIVA, R. F., WITEK, K., LINDQVIST-KREUZE, H., VLEESHOUWERS, V. & KAMOUN, S. 2018. Gene expression polymorphism underpins evasion of host immunity in an asexual lineage of the Irish potato famine pathogen. *Bmc Evolutionary Biology,* 18.

PARK, C. H., CHEN, S. B., SHIRSEKAR, G., ZHOU, B., KHANG, C. H., SONGKUMARN, P., AFZAL, A. J., NING, Y. S., WANG, R. Y., BELLIZZI, M., VALENT, B. & WANG, G. L. 2012. The *Magnaporthe oryzae* Effector AvrPiz-t Targets the RING E3 Ubiquitin Ligase APIP6 to Suppress Pathogen-Associated Molecular Pattern-Triggered Immunity in Rice. *Plant Cell,* 24**,** 4748-4762.

PARK, C. H., SHIRSEKAR, G., BELLIZZI, M., CHEN, S. B., SONGKUMARN, P., XIE, X., SHI, X. T., NING, Y. S., ZHOU, B., SUTTIVIRIYA, P., WANG, M., UMEMURA, K. & WANG, G. L. 2016. The E3 Ligase APIP10 Connects the Effector AvrPiz-t to the NLR Receptor Piz-t in Rice. *Plos Pathogens,* 12.

PARK, P. J. 2009. ChIP-seq: advantages and challenges of a maturing technology. *Nature Reviews Genetics,* 10**,** 669-680.

PAXTON, J. D. 1981. Phytoalexins - a working re-definition. *Phytopathologische Zeitschrift-Journal of Phytopathology,* 101**,** 106-109.

PEART, J. R., MESTRE, P., LU, R., MALCUIT, I. & BAULCOMBE, D. C. 2005. NRG1, a CC-NB-LRR protein, together with N, a TIR-NB-LRR protein, mediates resistance against tobacco mosaic virus. *Current Biology,* 15**,** 968-973.

PENG, W., GARCIA, N., SERVAGE, K. A., KOHLER, J. J., READY, J. M., TOMCHICK, D. R., FERNANDEZ, J. & ORTH, K. 2024. *Pseudomonas* effector AvrB is a glycosyltransferase that rhamnosylates plant guardee protein RIN4. *Science Advances,* 10.

PERKEL, J. M. 2021. Proteomics at the single-cell level. *Nature,* 597**,** 580-582.

PETELSKI, A. A., EMMOTT, E., LEDUC, A., HUFFMAN, R. G., SPECHT, H., PERLMAN, D. H. & SLAVOV, N. 2021. Multiplexed single-cell proteomics using SCoPE2. *Nature Protocols,* 16**,** 5398-+.

PETRE, B. & KAMOUN, S. 2014. How do filamentous pathogens deliver effector proteins into plant cells? *PLoS Biol,* 12**,** e1001801.

PIASECKA, A., JEDRZEJCZAK-REY, N. & BEDNAREK, P. 2015. Secondary metabolites in plant innate immunity: conserved function of divergent chemicals. *New Phytologist,* 206**,** 948-964.

PLISSONNEAU, C., BENEVENUTO, J., MOHD-ASSAAD, N., FOUCHÉ, S., HARTMANN, F. E. & CROLL, D. 2017. Using Population and Comparative Genomics to Understand the Genetic Basis of Effector-Driven Fungal Pathogen Evolution. *Frontiers in Plant Science,* 8.

PLOCH, S., CHOI, Y. J., ROST, C., SHIN, H. D., SCHILLING, E. & THINES, M. 2010. Evolution of diversity in *Albugo* is driven by high host specificity and multiple speciation events on closely related Brassicaceae. *Molecular Phylogenetics and Evolution,* 57**,** 812-820.

PLOCH, S. & THINES, M. 2011. Obligate biotrophic pathogens of the genus *Albugo* are widespread as asymptomatic endophytes in natural populations of Brassicaceae. *Molecular Ecology,* 20**,** 3692-3699.

POWERS, J., ZHANG, X., REYES, A., ZAVALIEV, R., OCHAKOVSKI, R., XU, S. L. & DONG, X. N. 2024. Next-generation mapping of the salicylic acid signaling hub and transcriptional cascade. *Molecular Plant,* 17**,** 1558-1572.

PRINCE, D. C., RALLAPALLI, G., XU, D. Y., SCHOONBEEK, H. J., ÇEVIK, V., ASAI, S., KEMEN, E., CRUZ-MIRELES, N., KEMEN, A., BELHAJ, K., SCHORNACK, S., KAMOUN, S., HOLUB, E. B., HALKIER, B. A. & JONES, J. D. G. 2017. Albugo-imposed changes to tryptophanderived antimicrobial metabolite biosynthesis may contribute to suppression of non- host resistance to Phytophthora infestans in Arabidopsis thaliana. *Bmc Biology,* 15.

PUCKER, B., HOLTGRÄWE, D., STADERMANN, K. B., FREY, K., HUETTEL, B., REINHARDT, R. & WEISSHAAR, B. 2019. A chromosome-level sequence assembly reveals the structure of the *Arabidopsis thaliana* Nd-1 genome and its gene set. *Plos One,* 14.

QI, P. P., ZHANG, D., ZHANG, Y., ZHU, W. T., DU, X. Y., MA, X. S., XIAO, C. F., LIN, Y., XIE, J. T., CHENG, J. S., FU, Y. P., JIANG, D. H., YU, X. & LI, B. 2024. Ubiquitination and degradation of plant helper NLR by the Ralstonia solanacearum effector RipV2 overcome tomato bacterial wilt resistance. *Cell Reports,* 43.

QI, T., SEONG, K., THOMAZELLA, D. P. T., KIM, J. R., PHAM, J., SEO, E., CHO, M. J., SCHULTINK, A. & STASKAWICZ, B. J. 2018. NRG1 functions downstream of EDS1 to regulate TIR-NLR-mediated plant immunity in *Nicotiana benthamiana*. *Proceedings of the National Academy of Sciences of the United States of America,* 115**,** E10979-E10987.

QIN, W., CHEAH, J. S., XU, C. R., MESSING, J., FREIBAUM, B. D., BOEYNAEMS, S., TAYLOR, J. P., UDESHI, N. D., CARR, S. A. & TING, A. Y. 2023. Dynamic mapping of proteome trafficking within and between living cells by TransitID. *Cell,* 186**,** 3307-+.

RAFFAELE, S., FARRER, R. A., CANO, L. M., STUDHOLME, D. J., MACLEAN, D., THINES, M., JIANG, R. H. Y., ZODY, M. C., KUNJETI, S. G., DONOFRIO, N. M., MEYERS, B. C., NUSBAUM, C. & KAMOUN, S. 2010. Genome Evolution Following Host Jumps in the Irish Potato Famine Pathogen Lineage. *Science,* 330**,** 1540-1543.

RAFFAELE, S. & KAMOUN, S. 2012. Genome evolution in filamentous plant pathogens: why bigger can be better. *Nature Reviews Microbiology,* 10**,** 417-430.

REDKAR, A., CEVIK, V., BAILEY, K., ZHAO, H., KIM, D. S., ZOU, Z., FURZER, O. J., FAIRHEAD, S., BORHAN, M. H., HOLUB, E. B. & JONES, J. D. G. 2023. The Arabidopsis *WRR4A* and *WRR4B* paralogous NLR proteins both confer recognition of multiple *Albugo candida* effectors. *New Phytologist,* 237**,** 532-547.

REDKAR, A., HOSER, R., SCHILLING, L., ZECHMANN, B., KRZYMOWSKA, M., WALBOT, V. & DOEHLEMANN, G. 2015. A Secreted Effector Protein of *Ustilago maydis* Guides Maize Leaf Cells to Form Tumors. *Plant Cell,* 27**,** 1332-1351.

RHEE, H. W., ZOU, P., UDESHI, N. D., MARTELL, J. D., MOOTHA, V. K., CARR, S. A. & TING, A. Y. 2013. Proteomic Mapping of Mitochondria in Living Cells via Spatially Restricted Enzymatic Tagging. *Science,* 339**,** 1328-1331.

RHEE, S. Y., BIRNBAUM, K. D. & EHRHARDT, D. W. 2019. Towards Building a Plant Cell Atlas. *Trends in Plant Science,* 24**,** 303-310.

ROUX, K. J., KIM, D. I., RAIDA, M. & BURKE, B. 2012. A promiscuous biotin ligase fusion protein identifies proximal and interacting proteins in mammalian cells. *Journal of Cell Biology,* 196**,** 801-810.

SAILE, S. C., JACOB, P., CASTEL, B., JUBIC, L. M., SALAS-GONZÁLES, I., BÄCKER, M., JONES, J. D. G., DANGL, J. L. & EL KASMI, F. 2020. Two unequally redundant "helper" immune receptor families mediate *Arabidopsis thaliana* intracellular "sensor" immune receptor functions. *Plos Biology,* 18.

SAITOH, H., FUJISAWA, S., MITSUOKA, C., ITO, A., HIRABUCHI, A., IKEDA, K., IRIEDA, H., YOSHINO, K., YOSHIDA, K., MATSUMURA, H., TOSA, Y., WIN, J., KAMOUN, S., TAKANO, Y. & TERAUCHI, R. 2012. Large-Scale Gene Disruption in *Magnaporthe oryzae* Identifies MC69, a Secreted Protein Required for Infection by Monocot and Dicot Fungal Pathogens. *Plos Pathogens,* 8.

SAMAVARCHI-TEHRANI, P., SAMSON, R. & GINGRAS, A. C. 2020. Proximity Dependent Biotinylation: Key Enzymes and Adaptation to Proteomics Approaches. *Molecular & Cellular Proteomics,* 19**,** 757-773.

SÁNCHEZ-VALLET, A., FOUCHÉ, S., FUDAL, I., HARTMANN, F. E., SOYER, J. L., TELLIER, A. & CROLL, D. 2018. The Genome Biology of Effector Gene Evolution in Filamentous Plant Pathogens. *In:* LEACH, J. E. & LINDOW, S. E. (eds.) *Annual Review of Phytopathology, Vol 56.*

SANDERFOOT, A. A., PILGRIM, M., ADAM, L. & RAIKHEL, N. V. 2001. Disruption of individual members of arabidopsis syntaxin gene families indicates each has essential functions. *Plant Cell,* 13**,** 659-666.

SARRIS, P. F., DUXBURY, Z., HUH, S. U., MA, Y., SEGONZAC, C., SKLENAR, J., DERBYSHIRE, P., CEVIK, V., RALLAPALLI, G., SAUCET, S. B., WIRTHMUELLER, L., MENKE, F. L. H., SOHN, K. H. & JONES, J. D. G. 2015. A Plant Immune Receptor Detects Pathogen Effectors that Target WRKY Transcription Factors. *Cell,* 161**,** 1089-1100.

SAUNDERS, D. G. O., BREEN, S., WIN, J., SCHORNACK, S., HEIN, I., BOZKURT, T. O., CHAMPOURET, N., VLEESHOUWERS, V., BIRCH, P. R. J., GILROY, E. M. & KAMOUN, S. 2012. Host Protein BSL1 Associates with *Phytophthora infestans* RXLR Effector AVR2 and the *Solanum demissum* Immune Receptor R2 to Mediate Disease Resistance. *Plant Cell,* 24**,** 3420-3434.

SCHMIDTMANN, E., ANTON, T., ROMBAUT, P., HERZOG, F. & LEONHARDT, H. 2016. Determination of local chromatin composition by CasID. *Nucleus,* 7**,** 476-484.

SCHULTINK, A., QI, T. C., LEE, A., STEINBRENNER, A. D. & STASKAWICZ, B. 2017. Roq1 mediates recognition of the Xanthomonas and Pseudomonas effector proteins XopQ and HopQ1. *Plant Journal,* 92**,** 787-795.

SCHULZE-LEFERT, P. & PANSTRUGA, R. 2011. A molecular evolutionary concept connecting nonhost resistance, pathogen host range, and pathogen speciation. *Trends in Plant Science,* 16**,** 117-125.

SEATH, C. P., TROWBRIDGE, A. D., MUIR, T. W. & MACMILLAN, D. W. C. 2021. Reactive intermediates for interactome mapping. *Chemical Society Reviews,* 50**,** 2911-2926.

SELVARAJ, M., TOGHANI, A. A., PAI, H., SUGIHARA, Y., KOURELIS, J., YUEN, E. L. H., IBRAHIM, T., ZHAO, H., XIE, R. R., MAQBOOL, A., DE LA CONCEPCION, J. C., BANFIELD, M. J., DEREVNINA, L., PETRE, B., LAWSON, D. M., BOZKURT, T. O., WU, C. H., KAMOUN, S. & CONTRERAS, M. P. 2024. Activation of plant immunity through conversion of a helper NLR homodimer into a resistosome. *Plos Biology,* 22.

SEURING, C., GREENWALD, J., WASMER, C., WEPF, R., SAUPE, S. J., MEIER, B. H. & RIEK, R. 2012. The Mechanism of Toxicity in HET-S/HET-s Prion Incompatibility. *Plos Biology,* 10.

SHAO, Z. Q., XUE, J. Y., WU, P., ZHANG, Y. M., WU, Y., HANG, Y. Y., WANG, B. & CHEN, J. Q. 2016. Large-Scale Analyses of Angiosperm Nucleotide-Binding Site-Leucine-Rich Repeat Genes Reveal Three Anciently Diverged Classes with Distinct Evolutionary Patterns. *Plant Physiology,* 170**,** 2095-2109.

SHI, W., STOLZE, S. C., NAKAGAMI, H., VILLAMIL, J. C. M., SAUR, I. M. L. & DOEHLEMANN, G. 2023. Combination of *in vivo* proximity labeling and co-immunoprecipitation identifies the host target network of a tumor-inducing effector in the fungal maize pathogen Ustilago maydis. *Journal of Experimental Botany,* 74**,** 4736-4750.

SHIMADA, T. L., SHIMADA, T. & HARA-NISHIMURA, I. 2010. A rapid and non-destructive screenable marker, FAST, for identifying transformed seeds of *Arabidopsis thaliana*. *Plant Journal,* 61**,** 519-528.

SHIRASU, K. 2009. The HSP90-SGT1 Chaperone Complex for NLR Immune Sensors. *Annual Review of Plant Biology,* 60**,** 139-164.

SINAPIDOU, E., WILLIAMS, K., NOTT, L., BAHKT, S., TÖR, M., CRUTE, I., BITTNER-EDDY, P. & BEYNON, J. 2004. Two TIR:NB:LRR genes are required to specify resistance to *Peronospora parasitica* isolate Cala2 in *Arabidopsis*. *Plant Journal,* 38**,** 898-909.

SOHN, K. H., LEI, R., NEMRI, A. & JONES, J. D. G. 2007. The downy mildew effector proteins ATR1 and ATR13 promote disease susceptibility in *Arabidopsis thaliana*. *Plant Cell,* 19**,** 4077-4090.

SPERSCHNEIDER, J., DODDS, P. N., GARDINER, D. M., MANNERS, J. M., SINGH, K. B. & TAYLOR, J. M. 2015. Advances and Challenges in Computational Prediction of Effectors from Plant Pathogenic Fungi. *Plos Pathogens,* 11.

STEGMANN, M., MONAGHAN, J., SMAKOWSKA-LUZAN, E., ROVENICH, H., LEHNER, A., HOLTON, N., BELKHADIR, Y. & ZIPFEL, C. 2017. The receptor kinase FER is a RALF-regulated scaffold controlling plant immune signaling. *Science,* 355**,** 287-+.

STRUK, S., JACOBS, A., MARTÍN-FONTECHA, E. S., GEVAERT, K., CUBAS, P. & GOORMACHTIG, S. 2019. Exploring the protein-protein interaction landscape in plants. *Plant Cell and Environment,* 42**,** 387-409.

SUGIO, A., KINGDOM, H. N., MACLEAN, A. M., GRIEVE, V. M. & HOGENHOUT, S. A. 2011. Phytoplasma protein effector SAP11 enhances insect vector reproduction by manipulating plant development and defense hormone biosynthesis. *Proceedings of the National Academy of Sciences of the United States of America,* 108**,** E1254-E1263.

SUN, X. H., LAPIN, D., FEEHAN, J. M., STOLZE, S. C., KRAMER, K., DONGUS, J. A., RZEMIENIEWSKI, J., BLANVILLAIN-BAUFUMÉ, S., HARZEN, A., BAUTOR, J., DERBYSHIRE, P., MENKE, F. L. H., FINKEMEIER, I., NAKAGAMI, H., JONES, J. D. G. & PARKER, J. E. 2021. Pathogen effector recognition-dependent association of NRG1 with EDS1 and SAG101 in TNL receptor immunity. *Nature Communications,* 12.

SUN, X. J., SUN, H., HAN, X., CHEN, P. C., JIAO, Y., WU, Z. P., ZHANG, X., WANG, Z., NIU, M. M., YU, K. W., LIU, D. T., DEY, K. K., MANCIERI, A., FU, Y. X., CHO, J. H., LI, Y. X., POUDEL, S., BRANON, T. C., TING, A. Y. & PENG, J. M. 2022. Deep Single-Cell-Type Proteome Profiling of Mouse Brain by Nonsurgical AAV-Mediated Proximity Labeling. *Analytical Chemistry,* 94**,** 5325-5334.

SUN, Y., ZHU, Y. X., BALINT-KURTI, P. J. & WANG, G. F. 2020. Fine-Tuning Immunity: Players and Regulators for Plant NLRs. *Trends in Plant Science,* 25**,** 695-713.

SUNIL, S., BEEH, S., STÖBBE, E., FISCHER, K., WILHELM, F., MERAL, A., PARIS, C., TEASDALE, L., JIANG, Z. H., ZHANG, L. S., URBAN, M., PARRAS, E. A., NÜRNBERGER, T., WEIGEL, D., LOZANO-DURAN, R. & EL KASMI, F. 2024. Activation of an atypical plant NLR with an N-terminal deletion initiates cell death at the vacuole. *Embo Reports,* 25**,** 4358-4386.

SVOZIL, J., GRUISSEM, W. & BAERENFALLER, K. 2015. Proteasome targeting of proteins in Arabidopsis leaf mesophyll, epidermal and vascular tissues. *Frontiers in Plant Science,* 6.

TAKAHASHI, A., CASAIS, C., ICHIMURA, K. & SHIRASU, K. 2003. HSP90 interacts with RAR1 and SGT1 and is essential for RPS2-mediated disease resistance in *Arabidopsis*. *Proceedings of the National Academy of Sciences of the United States of America,* 100**,** 11777-11782.

TANG, J., WU, D. S., LI, X. X., WANG, L. F., XU, L., ZHANG, Y., XU, F., LIU, H. B., XIE, Q. J., DAI, S. J., COLEMAN-DERR, D., ZHU, S. R. & YU, F. 2022. Plant immunity suppression via PHR1-RALF-FERONIA shapes the root microbiome to alleviate phosphate starvation. *Embo Journal,* 41.

TANG, M. Z., NING, Y. S., SHU, X. L., DONG, B., ZHANG, H. Y., WU, D. X., WANG, H., WANG, G. L. & ZHOU, B. 2017. The Nup98 Homolog APIP12 Targeted by the Effector AvrPiz-t is Involved in Rice Basal Resistance Against *Magnaporthe oryzae*. *Rice,* 10.

TANG, Y., YANG, X. Y., HUANG, A. B., SEONG, K., YE, M., LI, M. T., ZHAO, Q., KRASILEVA, K. & GU, Y. N. 2024. Proxiome assembly of the plant nuclear pore reveals an essential hub for gene expression regulation. *Nature Plants,* 10.

TEUFEL, F., ARMENTEROS, J. J. A., JOHANSEN, A. R., GÍSLASON, M. H., PIHL, S. I., TSIRIGOS, K. D., WINTHER, O., BRUNAK, S., VON HEIJNE, G. & NIELSEN, H. 2022. SignalP 6.0 predicts all five types of signal peptides using protein language models. *Nature Biotechnology,* 40**,** 1023-+.

THINES, M. 2014. Phylogeny and evolution of plant pathogenic oomycetes-a global overview. *European Journal of Plant Pathology,* 138**,** 431-447.

THINES, M., CHOI, Y. J., KEMEN, E., PLOCH, S., HOLUB, E. B., SHIN, H. D. & JONES, J. D. G. 2009. A new species of *Albugo* parasitic to *Arabidopsis thaliana* reveals new evolutionary patterns in white blister rusts (*Albuginaceae*). *Persoonia,* 22**,** 123-128.

THOMAS, W. J., THIREAULT, C. A., KIMBREL, J. A. & CHANG, J. H. 2009. Recombineering and stable integration of the *Pseudomonas syringae* pv. *syringae* 61 *hrp/hrc* cluster into the genome of the soil bacterium *Pseudomonas fluorescens* Pf0-1. *Plant Journal,* 60**,** 919-928.

THOMMA, B., NÜRNBERGER, T. & JOOSTEN, M. 2011. Of PAMPs and Effectors: The Blurred PTI-ETI Dichotomy. *Plant Cell,* 23**,** 4-15.

TIAN, D., TRAW, M. B., CHEN, J. Q., KREITMAN, M. & BERGELSON, J. 2003. Fitness costs of R-gene-mediated resistance in *Arabidopsis thaliana*. *Nature,* 423**,** 74-77.

TIAN, M. Y., HUITEMA, E., DA CUNHA, L., TORTO-ALALIBO, T. & KAMOUN, S. 2004. A Kazal-like extracellular serine protease inhibitor from *Phytophthora infestans* targets the tomato pathogenesis-related protease P69B. *Journal of Biological Chemistry,* 279**,** 26370-26377.

TIAN, M. Y., VON DAHL, C. C., LIU, P. P., FRISO, G., VAN WIJK, K. J. & KLESSIG, D. F. 2012. The combined use of photoaffinity labeling and surface plasmon resonance-based technology identifies multiple salicylic acid-binding proteins. *Plant Journal,* 72**,** 1027-1038.

TROWBRIDGE, A. D., SEATH, C. P., RODRIGUEZ-RIVERA, F. P., LI, B. X., DUL, B. E., SCHWAID, A. G., BUKSH, B. F., GERI, J. B., OAKLEY, J. V., FADEYI, O. O., OSLUND, R. C., RYU, K. A., WHITE, C., REYES-ROBLES, T., TAWA,

P., PARKER, D. L. & MACMILLAN, D. W. C. 2022. Small molecule photocatalysis enables drug target identification via energy transfer. *Proceedings of the National Academy of Sciences of the United States of America,* 119.

UNGAR, D. & HUGHSON, F. M. 2003. SNARE protein structure and function. *Annual Review of Cell and Developmental Biology,* 19**,** 493-517.

ÜSTÜN, S., SHEIKH, A., GIMENEZ-IBANEZ, S., JONES, A., NTOUKAKIS, V. & BÖRNKE, F. 2016. The Proteasome Acts as a Hub for Plant Immunity and Is Targeted by *Pseudomonas* Type III Effectors. *Plant Physiology,* 172**,** 1941-1958.

VAN DE WEYER, A. L., MONTEIRO, F., FURZER, O. J., NISHIMURA, M. T., CEVIK, V., WITEK, K., JONES, J. D. G., DANGL, J. L., WEIGEL, D. & BEMM, F. 2019. A Species-Wide Inventory of NLR Genes and Alleles in *Arabidopsis thaliana*. *Cell,* 178**,** 1260-+.

VAN DER BIEZEN, E. A., FREDDIE, C. T., KAHN, K., PARKER, J. E. & JONES, J. D. G. 2002. *Arabidopsis RPP4* is a member of the *RPP5* multigene family of TIR-NB-LRR genes and confers downy mildew resistance through multiple signalling components. *Plant Journal,* 29**,** 439-451.

VAN DER BIEZEN, E. A. & JONES, J. D. G. 1998a. The NB-ARC domain: A novel signalling motif shared by plant resistance gene products and regulators of cell death in animals. *Current Biology,* 8**,** R226-R227.

VAN DER BIEZEN, E. A. & JONES, J. D. G. 1998b. Plant disease-resistance proteins and the gene-for-gene concept. *Trends in Biochemical Sciences,* 23**,** 454-456.

VAN DER HOORN, R. A. L. & KAMOUN, S. 2008. From Guard to Decoy: A new model for perception of plant pathogen effectors. *Plant Cell,* 20**,** 2009-2017.

VAN OOIJEN, G., MAYR, G., KASIEM, M. M. A., ALBRECHT, M., CORNELISSEN, B. J. C. & TAKKEN, F. L. W. 2008. Structure-function analysis of the NB-ARC domain of plant disease resistance proteins. *Journal of Experimental Botany,* 59**,** 1383-1397.

VANDEREYKEN, K., VAN LEENE, J., DE CONINCK, B. & CAMMUE, B. P. A. 2018. Hub Protein Controversy: Taking a Closer Look at Plant Stress Response Hubs. *Frontiers in Plant Science,* 9.

VANETTEN, H. D., MANSFIELD, J. W., BAILEY, J. A. & FARMER, E. E. 1994. Two classes of plant antibiotics - Phytoalexins versus phytoanticipins. *Plant Cell,* 6**,** 1191-1192.

VLEESHOUWERS, V. & OLIVER, R. P. 2014. Effectors as Tools in Disease Resistance Breeding Against Biotrophic, Hemibiotrophic, and Necrotrophic Plant Pathogens. *Molecular Plant-Microbe Interactions,* 27**,** 196-206.

VLEESHOUWERS, V., RAFFAELE, S., VOSSEN, J. H., CHAMPOURET, N., OLIVA, R., SEGRETIN, M. E., RIETMAN, H., CANO, L. M., LOKOSSOU, A., KESSEL, G., PEL, M. A. & KAMOUN, S. 2011. Understanding and Exploiting Late Blight Resistance in the Age of Effectors. *In:* VANALFEN, N. K., BRUENING, G. & LEACH, J. E. (eds.) *Annual Review of Phytopathology, Vol 49.*

VLEESHOUWERS, V., RIETMAN, H., KRENEK, P., CHAMPOURET, N., YOUNG, C., OH, S. K., WANG, M. Q., BOUWMEESTER, K., VOSMAN, B., VISSER, R. G. F., JACOBSEN, E., GOVERS, F., KAMOUN, S. & VAN DER VOSSEN, E. A. G. 2008. Effector Genomics Accelerates Discovery and Functional Profiling of Potato Disease Resistance and *Phytophthora Infestans* Avirulence Genes. *Plos One,* 3.

WAGNER, S., STUTTMANN, J., RIETZ, S., GUEROIS, R., BRUNSTEIN, E., BAUTOR, J., NIEFIND, K. & PARKER, J. E. 2013. Structural Basis for Signaling by Exclusive EDS1 Heteromeric Complexes with SAG101 or PAD4 in Plant Innate Immunity. *Cell Host & Microbe,* 14**,** 619-630.

WAN, L., ESSUMAN, K., ANDERSON, R. G., SASAKI, Y., MONTEIRO, F., CHUNG, E. H., NISHIMURA, E. O., DIANTONIO, A., MILBRANDT, J., DANGL, J. L. & NISHIMURA, M. T. 2019. TIR domains of plant immune receptors are $NAD^+$-cleaving enzymes that promote cell death. *Science,* 365**,** 799-+.

WANG, G. X., ROUX, B., FENG, F., GUY, E., LI, L., LI, N. N., ZHANG, X. J., LAUTIER, M., JARDINAUD, M. F., CHABANNES, M., ARLAT, M., CHEN, S., HE, C. Z., NOEL, L. D. & ZHOU, J. M. 2015. The Decoy Substrate

of a Pathogen Effector and a Pseudokinase Specify Pathogen-Induced Modified-Self Recognition and Immunity in Plants. *Cell Host & Microbe,* 18**,** 285-295.

WANG, J. J., PEI, G. F., WANG, Y. P., WU, D. W., LIU, X. K., LI, G. M., HE, J. F., ZHANG, X. L., SHAN, X. Y., LI, P. L. & XIE, D. X. 2023. Phase separation of the nuclear pore complex facilitates selective nuclear transport to regulate plant defense against pathogen and pest invasion. *Molecular Plant,* 16**,** 1016-1030.

WANG, J. Z., HU, M. J., WANG, J., QI, J. F., HAN, Z. F., WANG, G. X., QI, Y. J., WANG, H. W., ZHOU, J. M. & CHAI, J. J. 2019. Reconstitution and structure of a plant NLR resistosome conferring immunity. *Science,* 364**,** 44-+.

WANG, L. Y., CHEN, H., LI, J. J., SHU, H. D., ZHANG, X. X., WANG, Y. C., TYLER, B. M. & DONG, S. M. 2020. Effector gene silencing mediated by histone methylation underpins host adaptation in an oomycete plant pathogen. *Nucleic Acids Research,* 48**,** 1790-1799.

WANG, S., GU, Y. N., ZEBELL, S. G., ANDERSON, L. K., WANG, W., MOHAN, R. & DONG, X. N. 2014. A Noncanonical Role for the CKI-RB-E2F Cell-Cycle Signaling Pathway in Plant Effector-Triggered Immunity. *Cell Host & Microbe,* 16**,** 787-794.

WESSLING, R., EPPLE, P., ALTMANN, S., HE, Y. J., YANG, L., HENZ, S. R., MCDONALD, N., WILEY, K., BADER, K. C., GLÄSSER, C., MUKHTAR, M. S., HAIGIS, S., GHAMSARI, L., STEPHENS, A. E., ECKER, J. R., VIDAL, M., JONES, J. D. G., MAYER, K. F. X., VAN THEMAAT, E. V., WEIGEL, D., SCHULZE-LEFERT, P., DANGL, J. L., PANSTRUGA, R. & BRAUN, P. 2014. Convergent Targeting of a Common Host Protein-Network by Pathogen Effectors from Three Kingdoms of Life. *Cell Host & Microbe,* 16**,** 364-375.

WEST, A. V. & WOO, C. M. 2023. Photoaffinity Labeling Chemistries Used to Map Biomolecular Interactions. *Israel Journal of Chemistry,* 63.

WHISSON, S. C., BOEVINK, P. C., MOLELEKI, L., AVROVA, A. O., MORALES, J. G., GILROY, E. M., ARMSTRONG, M. R., GROUFFAUD, S., VAN WEST, P., CHAPMAN, S., HEIN, I., TOTH, I. K., PRITCHARD, L. & BIRCH, P. R. J. 2007. A translocation signal for delivery of oomycete effector proteins into host plant cells. *Nature,* 450**,** 115-+.

WHITHAM, S., DINESHKUMAR, S. P., CHOI, D., HEHL, R., CORR, C. & BAKER, B. 1994. The product of the tobacco mosaic-virus resistance gene-N - similarity to Toll and the interleukin-1 receptor. *Cell,* 78**,** 1101-1115.

WIERMER, M., FEYS, B. J. & PARKER, J. E. 2005. Plant immunity: the EDS1 regulatory node. *Current Opinion in Plant Biology,* 8**,** 383-389.

WITEK, K., JUPE, F., WITEK, A. I., BAKER, D., CLARK, M. D. & JONES, J. D. G. 2016. Accelerated cloning of a potato late blight-resistance gene using RenSeq and SMRT sequencing. *Nature Biotechnology,* 34**,** 656-660.

WITEK, K., LIN, X., KARKI, H. S., JUPE, F., WITEK, A. I., STEUERNAGEL, B., STAM, R., VAN OOSTERHOUT, C., FAIRHEAD, S., HEAL, R., COCKER, J. M., BHANVADIA, S., BARRETT, W., WU, C. H., ADACHI, H., SONG, T. Q., KAMOUN, S., VLEESHOUWERS, V., TOMLINSON, L., WULFF, B. B. H. & JONES, J. D. G. 2021. A complex resistance locus in *Solanum americanum* recognizes a conserved *Phytophthora* effector. *Nature Plants,* 7.

WU, C. H., ABD-EL-HALIEM, A., BOZKURT, T. O., BELHAJ, K., TERAUCHI, R., VOSSEN, J. H. & KAMOUN, S. 2017. NLR network mediates immunity to diverse plant pathogens. *Proceedings of the National Academy of Sciences of the United States of America,* 114**,** 8113-8118.

WU, C. H., ADACHI, H., DE LA CONCEPCION, J. C., CASTELLS-GRAELLS, R., NEKRASOV, V. & KAMOUN, S. 2020. *NRC4* Gene Cluster Is Not Essential for Bacterial Flagellin-Triggered Immunity. *Plant Physiology,* 182**,** 455-459.

WU, S. J., SHAN, L. B. & HE, P. 2014. Microbial signature-triggered plant defense responses and early signaling mechanisms. *Plant Science,* 228**,** 118-126.

WU, Z. S., LI, M., DONG, O. X., XIA, S. T., LIANG, W. W., BAO, Y. K., WASTENEYS, G. & LI, X. 2019. Differential regulation of TNL-mediated immune signaling by redundant helper CNLs. *New Phytologist,* 222**,** 938-953.

WU, Z. S., TIAN, L., LIU, X. R., HUANG, W. J., ZHANG, Y. L. & LI, X. 2022. The N-terminally truncated helper NLR *NRG1C* antagonizes immunity mediated by its full-length neighbors *NRG1A* and *NRG1B*. *Plant Cell,* 34**,** 1621-1640.

WU, Z. S., TIAN, L., LIU, X. R., ZHANG, Y. L. & LI, X. 2021. TIR signal promotes interactions between lipase-like proteins and ADR1-L1 receptor and ADR1-L1 oligomerization. *Plant Physiology,* 187**,** 681-686.

XIAO, S. Y., ELLWOOD, S., CALIS, O., PATRICK, E., LI, T. X., COLEMAN, M. & TURNER, J. G. 2001. Broad-spectrum mildew resistance in *Arabidopsis thaliana* mediated by *RPW*8. *Science,* 291**,** 118-120.

XIAO, Y. Y., WU, X. X., WANG, Z. Q., JI, K. X., ZHAO, Y., ZHANG, Y. & WAN, L. 2025. Activation and inhibition mechanisms of a plant helper NLR. *Nature*.

XU, F., KAPOS, P., CHENG, Y. T., LI, M., ZHANG, Y. L. & LI, X. 2014. NLR-Associating Transcription Factor bHLH84 and Its Paralogs Function Redundantly in Plant Immunity. *Plos Pathogens,* 10.

XU, X., SHI, X. T., YOU, X. M., HAO, Z. Y., WANG, R. Y., WANG, M., HE, F., PENG, S. S., TAO, H., LIU, Z., WANG, J. S., ZHANG, C. Y., FENG, Q., WU, W. X., WANG, G. L. & NING, Y. S. 2024. A pair of E3 ubiquitin ligases control immunity and flowering by targeting different ELF3 proteins in rice. *Developmental Cell,* 59.

YANG, L., TEIXEIRA, P., BISWAS, S., FINKEL, O. M., HE, Y. J., SALAS-GONZALEZ, I., ENGLISH, M. E., EPPLE, P., MIECZKOWSKI, P. & DANGL, J. L. 2017a. *Pseudomonas syringae* Type III Effector HopBB1 Promotes Host Transcriptional Repressor Degradation to Regulate Phytohormone Responses and Virulence. *Cell Host & Microbe,* 21**,** 156-168.

YANG, Y., LA, H. G., TANG, K., MIKI, D., YANG, L., WANG, B. S., DUAN, C. G., NIE, W. F., WANG, X. G., WANG, S. W., PAN, Y. F., TRAN, E. J., AN, L. Z., ZHANG, H. M. & ZHU, J. K. 2017b. SAC3B, a central component of the mRNA export complex TREX-2, is required for prevention of epigenetic gene silencing in *Arabidopsis*. *Nucleic Acids Research,* 45**,** 181-197.

YEATS, T. H. & ROSE, J. K. C. 2013. The Formation and Function of Plant Cuticles. *Plant Physiology,* 163**,** 5-20.

YI, H., SHI, H., MAO, W., YIN, J. J., MA, Y. Y., XU, L., JING, L. J., HE, M., ZHU, X. B., LU, X., XIONG, Q., TANG, Y. Y., HOU, Q. Q., SONG, L., WANG, L., LI, W. T., YU, H., CHEN, X. W., LI, J. Y. & WANG, J. 2024. E3 ubiquitin ligase IPI1 controls rice immunity and flowering via both E3 ligase-dependent and-independent pathways. *Developmental Cell,* 59.

YI, W. K., LI, J. Y., ZHU, X. X., WANG, X., FAN, L. G., SUN, W. J., LIAO, L. B., ZHANG, J. L., LI, X. Y., YE, J., CHEN, F. L., TAIPALE, J., CHAN, K. M., ZHANG, L. & YAN, J. 2020. CRISPR-assisted detection of RNA-protein interactions in living cells. *Nature Methods,* 17**,** 685-+.

YU, G., XIAN, L., XUE, H., YU, W. J., RUFIAN, J. S., SANG, Y. Y., MORCILLO, R. J. L., WANG, Y. R. & MACHO, A. P. 2020. A bacterial effector protein prevents MAPK-mediated phosphorylation of SGT1 to suppress plant immunity. *Plos Pathogens,* 16.

YU, H., XU, W. Y., CHEN, S. S., WU, X. X., RAO, W. W., LIU, X. X., XU, X. Y., CHEN, J. Q., NISHIMURA, M. T., ZHANG, Y. & WAN, L. 2024. Activation of a helper NLR by plant and bacterial TIR immune signaling. *Science,* 386**,** 1413-1420.

YUAN, M. H., NGOU, B. P. M., DING, P. T. & XIU-FAN, X. 2021. PTI-ETI crosstalk: an integrative view of plant immunity. *Current Opinion in Plant Biology,* 62.

ZDRZALEK, R., KAMOUN, S., TERAUCHI, R., SAITOH, H. & BANFIELD, M. J. 2020. The rice NLR pair Pikp-1/Pikp-2 initiates cell death through receptor cooperation rather than negative regulation. *Plos One,* 15.

ZEBELL, S. G. & DONG, X. N. 2015. Cell-Cycle Regulators and Cell Death in Immunity. *Cell Host & Microbe,* 18**,** 402-407.

ZHANG, D. L., YANG, X. X., WEN, Z. Y., LI, Z., ZHANG, X. Y., ZHONG, C. C., SHE, J. J., ZHANG, Q. S., ZHANG, H., LI, W. L., ZHAO, X. Y., XU, M. L., SU, Z., LI, D. W., DINESH-KUMAR, S. P. & ZHANG, Y. L. 2024. Proxitome

profiling reveals a conserved SGT1-NSL1 signaling module that activates NLR-mediated immunity. *Molecular Plant,* 17**,** 1369-1391.

ZHANG, X. C., MILLET, Y. A., CHENG, Z., BUSH, J. & AUSUBEL, F. M. 2015. Jasmonate signalling in *Arabidopsis* involves SGT1b-HSP70-HSP90 chaperone complexes. *Nature Plants,* 1.

ZHANG, X. D., YAO, J., ZHANG, Y. P., SUN, Y. J. & MOU, Z. L. 2013. The Arabidopsis Mediator complex subunits MED14/SWP and MED16/SFR6/IEN1 differentially regulate defense gene expression in plant immune responses. *Plant Journal,* 75**,** 484-497.

ZHANG, Y. L., LI, Y. Y., YANG, X. X., WEN, Z. Y., NAGALAKSHMI, U. & DINESH, S. P. 2020. TurboID-Based Proximity Labeling for In Planta Identification of Protein-Protein Interaction Networks. *Jove-Journal of Visualized Experiments*.

ZHANG, Y. L., SONG, G. Y., LAI, N. K., NAGALAKSHMI, U., LI, Y. Y., ZHENG, W. J., HUANG, P. J., BRANON, T. C., TING, A. Y., WALLEY, J. W. & DINESH-KUMAR, S. P. 2019. TurboID-based proximity labeling reveals that UBR7 is a regulator of N NLR immune receptor-mediated immunity. *Nature Communications,* 10.

ZHAO, Y. B., LIU, M. X., CHEN, T. T., MA, X. M., LI, Z. K., ZHENG, Z. C., ZHENG, S. R., CHEN, L. F., LI, Y. Z., TANG, L. R., CHEN, Q., WANG, P. Y. & OUYANG, S. Y. 2022. Pathogen effector AvrSr35 triggers Sr35 resistosome assembly *via* a direct recognition mechanism. *Science Advances,* 8.

ZHOU, E. X., JIA, Y. L., SINGH, P., CORRELL, J. C. & LEE, F. N. 2007. Instability of the *Magnaporthe oryzae* avirulence gene *AVR-Pita* alters virulence. *Fungal Genetics and Biology,* 44**,** 1024-1034.

ZHOU, H. B., LIN, J. A., JOHNSON, A., MORGAN, R. L., ZHONG, W. W. & MA, W. B. 2011. *Pseudomonas syringae* Type III Effector HopZ1 Targets a Host Enzyme to Suppress Isoflavone Biosynthesis and Promote Infection in Soybean. *Cell Host & Microbe,* 9**,** 177-186.

ZHU, C., LIU, J. H., ZHAO, J. H., LIU, T., CHEN, Y. Y., WANG, C. H., ZHANG, Z. H., GUO, H. S. & DUAN, C. G. 2022. A fungal effector suppresses the nuclear export of AGO1-miRNA complex to promote infection in plants. *Proceedings of the National Academy of Sciences of the United States of America,* 119.

ZHU, Z. H., XU, F., ZHANG, Y. X., CHENG, Y. T., WIERMER, M., LI, X. & ZHANG, Y. L. 2010. Arabidopsis resistance protein SNC1 activates immune responses through association with a transcriptional corepressor. *Proceedings of the National Academy of Sciences of the United States of America,* 107**,** 13960-13965.

ZULUAGA, A. P., VEGA-ARREGUÍN, J. C., FEI, Z. J., PONNALA, L., LEE, S. J., MATAS, A. J., PATEV, S., FRY, W. E. & ROSE, J. K. C. 2016. Transcriptional dynamics of *Phytophthora infestans* during sequential stages of hemibiotrophic infection of tomato. *Molecular Plant Pathology,* 17**,** 29-41.